Bauhaus-
Universität
Weimar

Bauhaus-University Weimar
Institute of Structural Mechanics
Structural Analysis and Component Strength

BAM
Bundesanstalt für
Materialforschung
und -prüfung

A multiscale numerical framework for the simulation of anistropic material response of additively manufactured stainless steel 316L undergoing large plastic deformation

Ein numerisches Multiskalenverfahren zur Simulation des anisotropen Materialverhaltens des additiv gefertigten Stahls 316L für große plastische Verformungen

DISSERTATION

Zur Erlangung des akademischen Grades
Doktor-Ingenieur (Dr.-Ing.)
an der Fakultät Bauingenieurwesen
der Bauhaus-Universität Weimar

vorgelegt von:
Amir Charmi
(externer Doktorand)
geboren am 14.04.1992 in Teheran, Iran

Betreuer: Prof. Dr.-Ing. habil. Carsten Könke
Dr.-Ing. Rainer Falkenberg (BAM)

Gutachter: Prof. Dr.-Ing. habil. Carsten Könke
Prof. Dr.-Ing. Matthias Kraus
Prof. Dr. Giovanni Bruno

Tag der Disputation: 11. Januar 2024

Acknowledgements

This work was completed during my employment as a Ph.D. student at Bundesanstalt für Materialforschung und -prüfung (BAM). I am very thankful for this opportunity and the funding provided during my employment. Next, I would like to convey my appreciation and gratitude to the following individuals.

I would like to express my heartfelt thanks to my advisor in BAM, Dr. Rainer Falkenberg, who guided me through different stages of my work and at the same time gave me the freedom to explore my own research ideas. His support, encouragement, and expertise were instrumental during the research and writing phase of my thesis.

I would also like to express my sincere gratitude to my advisor at Bauhaus-Universität Weimar, Professor Carsten Könke, for his invaluable support, feedback, and his warm and welcoming character. It was always a pleasure to present and discuss my results with him and to be under his supervision.

I am particularly grateful to Professor Birgit Skrotzki as the head of the division in BAM and as my boss. The completion of this work wouldn't be possible without her kind support, willingness to help me, and without her having an open ear for all my concerns and requests.

Next, I would like to extend my appreciation to Professor Giovanni Bruno and Dr. Alexander Evans as the coordinators of the AGIL project who supported me, showed interest in my work, and encouraged me to explore new and fruitful ideas. I would also like to thank all people involved in AGIL project who helped with different aspects of my work, inspired me with new ideas, and strengthened my motivation to continue my work. I want to especially thank Dr. Luis Ávila, Dr. Birgit Rehmer, Patrick Uhlemann, Dr. Maximilian Sprengel, Dr. Gunther Mohr, Dr. Alexander Ulbricht, and Konstantin Sommer who helped me with the experimental part of my work. I am indebted to all my colleagues and friends at BAM and especially to Dr. Bernard Fedelich who introduced me into the world of academia and whom I learned a lot from. I am also grateful to Dr. Vitaliy Kindrachuck and Cetin Haftaoglu for being a source of inspiration, collaboration, and fun.

I am also grateful to the members of my dissertation committee, including Professor Matthias Kraus and Professor Tom Lahmer, for their willingness to review my dissertation and for their constructive comments and suggestions.

Last but not least, I would like to express my deepest and heartfelt gratitude to my beloved parents and sister who supported me my whole life with everything they had and helped me get through difficult phases of my life with their unconditional love and encouragement. My warmest and sincere appreciation goes also to my wife for her love, patience, and unwavering support and for all the difficulties she endured throughout my Ph.D. journey. This dissertation is dedicated to all of them.

Contents

List of Figures **III**

List of Tables **V**

Nomenclature **VI**

Latin symbols VI

Greek symbols IX

Abbreviations XI

1 Introduction **1**

2 Experimental material characterization **9**

2.1 Material and laser powder bed fusion processing conditions 9

2.2 Machining of test specimens 11

2.3 Mechanical testing 14

2.4 Dynamic Young’s modulus determination 15

2.5 Porosity and defects analysis 15

2.6 Residual stress measurements 16

2.7 Electron backscatter diffraction measurements 18

2.8 In-situ neutron diffraction tensile experiments 19

3 Multiscale modeling of anisotropic yield behavior **21**

3.1 A brief introduction of some basic concepts used in continuum mechanics . 21

3.2 Crystal plasticity framework for the microscale simulations 25

3.2.1 Crystalline metals 25

3.2.2 Defects and dislocations in a crystalline material 26

3.2.3 Material model 28

3.2.4 Texture evolution 29

3.2.5 Calculation of lattice strain 30

3.2.6 Mechanical equilibrium - spectral solver 31

3.2.7 Creation of representative volume elements 34

3.2.8 A summary of the crystal plasticity model equations 35

3.2.8.1 Numerical solution scheme of the mechanical equilibrium . 36

3.2.8.2 Time integration procedure for the constitutive model . . . 36

3.3 Rate independent hypoelastic plasticity framework for the macroscale . . . 37

3.3.1 Weak formulation of BVP and the FEM solver 38

3.3.2 Rate independent plasticity framework 41

3.3.3 Hypoelastic plasticity models 43

3.3.4 Incrementally objective integration algorithm 46

3.3.5 Anisotropic yield functions 48

3.3.6 Hardening law 51

3.3.7 Evolution of microstructure and the plastic spin 52

3.3.7.1 Existing models 54
3.3.7.2 Proposed model 56
3.3.8 Return mapping algorithm 62
3.3.9 Consistent elasto-plastic tangent operator 64
3.3.10 Complete Abaqus/UMAT implementation 65
3.3.11 A summary of the macroscale model equations 67
3.3.11.1 Incremental form 68
3.3.11.2 Return mapping algorithm 69
3.3.11.3 The incremental finite element formulation 70
3.4 Scale bridging approach and the calibration procedure 71
3.4.1 Estimating the elastic properties of a polycrystal 71
3.4.2 Parameter identification procedure 73
3.4.2.1 Parameters of the crystal plasticity model 73
3.4.2.2 Parameters of the Barlat yield function Yld2004-18p 75
3.4.2.3 Parameters of the macroscopic hardening model 77
3.4.2.4 Parameters for the novel plastic spin model 80

4 Final results and discussion 93
4.1 Defects and residual stresses 93
4.2 Texture analysis 99
4.3 Understanding the mechanical anisotropy in LPBF316L 103
4.3.1 Tensile test results 103
4.3.2 Elastic anisotropy 106
4.3.3 Numerical modeling of anisotropic yield behavior 108
4.4 Micromechanical validation 111
4.4.1 Numerical simulation of the lattice strain evolution 112
4.4.2 Optimized single crystal elastic constants 114
4.5 Macromechanical validation 119
4.5.1 Abaqus model creation 119
4.5.2 Torsion test: comparison between simulation and experiment 122
4.5.3 Shear test: comparison between simulation and experiment 125
4.6 Influence of anisotropy, numerical algorithm, and plastic spin 128
4.6.1 Virtual torsion experiments 129
4.6.2 Virtual shear experiments 130
4.7 Conclusion and outlook 133

References 137

List of Figures

1.1 Schematic portrayal of LPBF process. 2
2.1 Schematic portrayal of all geometries and the corresponding scan strategies. 11
2.2 Position of extracted tensile and Young's modulus specimens. 12
2.3 Technical sketch used for the machining of tensile specimens. 13
2.4 Technical sketch used for the machining of torsion specimen. 13
2.5 Technical sketch used for the machining of shear specimens. 13
2.6 Measurement positions used during neutron diffraction experiments. 17
2.7 Location of different regions used during EBSD analysis. 19
2.8 Labeling of normal and radial direction for the in-situ tensile experiments. . 20
3.1 Movement of a material point. 22
3.2 Multiplicative decomposition of the total deformation gradient. 23
3.3 Simplified crystal structure in the three dimensional space. 26
3.4 {111} plane family in an face-centered cubic (FCC) crystal together with ⟨110⟩ direction vectors. 26
3.5 Line defects in a crystalline material. 27
3.6 Slip of an edge dislocation by moving few atoms at a time. 28
3.7 Representative volume elements used for crystal plasticity simulations . . . 35
3.8 Non-uniqueness of the intermediate configuration. 53
3.9 Geometrical representation of the Lode parameter μ_L and the Lode angle θ_L. 58
3.10 Representation of the eigenvectors $\mathbf{e}_i^\mathrm{p}$ in different coordinate systems. 60
3.11 Stress-strain curves obtained experimentally and from the CP model. 74
3.12 Experimental and numerical stress-strain curves (30 µm). 75
3.13 Calibration of the Barlat yield function. 77
3.14 Extrapolation of the stress-strain curves beyond the necking instability. . . 78
3.15 Extrapolated stress-strain curves and the calibrated hardening models. . . . 79
3.16 Loading directions are defined using the angles φ^p and θ^p. 82
3.17 Pole figures corresponding to texture evolution results. 85
3.18 Pole figures corresponding to texture evolution results. 86
3.19 Calibrated plastic spin model $\hat{\mathbf{W}}^\mathrm{p}_\mathrm{TC}$. 87
3.20 Comparison between different plastic spin components of $\hat{\mathbf{W}}^\mathrm{p}_\mathrm{TC}$ and $\tilde{\mathbf{W}}^\mathrm{p}_\mathrm{TC}$. . 88
3.21 Calibrated plastic spin model $\hat{\mathbf{W}}^\mathrm{p}_\mathrm{S}$. 89
3.22 Comparison between different plastic spin components of $\hat{\mathbf{W}}^\mathrm{p}_\mathrm{S12}$ and $\tilde{\mathbf{W}}^\mathrm{p}_\mathrm{S}$. . . 90
4.1 Residual stresses in the normal direction ($\overline{\mathrm{Z}}$). 96
4.2 Residual stresses in the transverse direction ($\overline{\mathrm{X}}$). 97
4.3 Residual stresses in the longitudinal direction ($\overline{\mathrm{Y}}$). 98
4.4 EBSD measurements from 50 µm specimens. 100
4.5 Pole figures corresponding to EBSD measurements from 50 µm specimens. . 101
4.6 Grain size distributions determined from five 50 µm EBSD measurements. . 101
4.7 EBSD measurements from 30 µm specimens. 102
4.8 Pole figures corresponding to EBSD measurements from 30 µm specimens. . 102

4.9 Grain size distributions determined from five 30 µm EBSD measurements. . 103
4.10 Stress-strain curves obtained during the tensile tests (50 µm). 104
4.11 Stress-strain curves obtained during the tensile tests (30 µm and 50 µm). . . 105
4.12 Experimentally measured and numerically estimated Young's moduli. . . . 107
4.13 Comparison between experimental and numerical stress-strain response. . . 109
4.14 Stress-strain response for all crystallographic textures. 110
4.15 Deviation between the experimental and numerical stress-strain curves. . . 110
4.16 Crystal plasticity model calibration results for the Tower 45° specimen. . . 111
4.17 Experimental and numerical lattice strains for the 90 ° specimen. 113
4.18 Experimental and numerical lattice strains for the 0 ° specimen. 114
4.19 Measured and numerically calculated lattice strains for the 90 ° specimen. . 116
4.20 Measured and numerically calculated lattice strains for the 0 ° specimen. . . 117
4.21 Error analysis between original and re-calibrated SCEC. 118
4.22 Abaqus geometry and mesh for the torsion specimen 120
4.23 Abaqus geometry and mesh for the shear specimen 121
4.24 Experimentally measured and numerically calculated torsion moment. . . . 123
4.25 Error analysis for all torsion simulations. 124
4.26 The results of the convergence study for torsion tests. 124
4.27 Experimentally measured and numerically calculated shear force. 126
4.28 The error analysis for all shear simulations. 127
4.29 The results of the convergence study for shear tests. 127
4.30 Orientation of three torsion specimens shown relative to each other. 128
4.31 Orientation of three shear specimens shown relative to each other. 129
4.32 Torsion simulation results for the test orientation 1. 130
4.33 Torsion simulation results for the test orientation 2. 130
4.34 Shear simulation results for the test orientation 1. 131
4.35 Shear simulation results for the test orientation 2. 132

List of Tables

2.1 Overview of all test specimens. 14
3.1 Calibrated parameters of the crystal plasticity (CP) model for the 50 µm specimens. 74
3.2 Calibrated parameters of the crystal plasticity model for the 30 µm specimens. 74
3.3 Calibrated parameters of the yield function Yld2004-18p. 76
3.4 Calibrated parameters of the macroscopic hardening models. 80
3.5 Calibrated parameters of the plastic spin model $\tilde{\mathbf{W}}^{\mathrm{p}}_{\mathrm{TC}}$. 91
3.6 Calibrated parameters of the plastic spin model $\tilde{\mathbf{W}}^{\mathrm{p}}_{\mathrm{S}}$. 91
4.1 Porosity measured by µCT for six tensile specimens. 94
4.2 Maximum residual stress range measured in 6 tensile specimens. 95
4.3 Tensile test results for the 50 µm specimens according to DIN EN ISO 6892-1.104
4.4 Results from resonance method according to ASTM E1876. 106
4.5 Recalibrated single crystal elastic constants. 116

Nomenclature

Latin symbols

Symbol	Description
a	Hardening exponent in the crystal plasticity model
$\boldsymbol{b}$	Burgers vector
$\mathscr{B}_0$	Configuration of a body at time $t = 0$
$\mathscr{B}_t$	Configuration of a body at time t
C_{11}, C_{12}, C_{44}	Single crystal elastic constants
$\mathbf{C}^{\mathrm{e}}_{\mathrm{I}}$	Elastic right Cauchy-Green tensor
$\mathbb{C}_{\mathrm{I}}$	Elastic stiffness tensor in intermediate configuration
$\mathbb{C}^{\mathrm{ep}}$	Consistent elasto-plastic tangent operator
$\boldsymbol{d}^{\mathrm{reflection}}$	Diffraction vector
$\hat{\mathbf{D}}$	Rate of deformation in a rotating coordinate frame
$\hat{\mathbf{D}}^{\mathrm{p}}$	Rate of plastic deformation in a rotating coordinate frame
$\mathbf{D}^{\mathrm{p}}$	Rate of plastic deformation in current configuration
$\mathbf{D}^{\mathrm{p}}_{\mathrm{I}}$	Rate of plastic deformation in intermediate configuration
$\tilde{\mathbf{E}}^{\mathrm{e}}_{\{\}}$	Averaged lattice strain tensor
$E^{\mathrm{e}}_{\{\}}$	Numerically estimated lattice strain for specific diffraction direction
$\mathbf{E}^{\mathrm{e}}_{\mathrm{I}}$	Elastic Green-Lagrange strain tensor in intermediate configuration
E^{hkl}	Lattice plane specific Young's modulus
$\boldsymbol{f}^{\mathrm{ext}}$	External global force vector
$\mathbf{F}$	Deformation gradient
$\mathbf{F}^{\mathrm{e}}$	Elastic part of the deformation gradient
$\mathbf{F}^{\mathrm{p}}$	Plastic part of the deformation gradient
$\boldsymbol{g}$	Volumetric force
$\mathbf{G}$	Plastic strain residual
$h^{\alpha\beta}$	Instantaneous strain hardening in the crystal plasticity model
h_0	Reference self-hardening coefficient in the crystal plasticity model

Symbol	Description
$\boldsymbol{H}$	Generalized hardening modulus
$H_{(k)}{}'$	Slope of hardening curve
$\mathbf{I}$	Identity tensor
J	Determinant of the total deformation gradient
$\mathbf{K}^{\mathrm{e}}$	Element stiffness
$\mathbf{K}_{\mathrm{T}}$	Global tangent stiffness matrix
$\mathbf{L}$	Velocity gradient
$\mathscr{L}^{(k)}$	Hessian of the return mapping algorithm
$\mathbf{L}_{\mathrm{I}}^{\mathrm{p}}$	Plastic part of the velocity gradient
$\boldsymbol{m}_0^{\alpha}$	Slip direction vector
$\boldsymbol{n}_0^{\alpha}$	Normal of the slip plane
n	Microscopic strain rate sensitivity in the crystal plasticity model
$\boldsymbol{n}$	Normal at the surface
$\boldsymbol{n}_{\{\}}^{\mathrm{current}}$	Current orientation of the normal vector fo a specific grain family
$\boldsymbol{n}_{\{\}}^{0}$	Initial orientation of the normal vector fo a specific grain family
$\boldsymbol{N}$	Flow vector
N	Number of slip systems
$\mathbf{P}$	First Piola-Kirchhoff stress tensor
q	latent-hardening coefficient in the crystal plasticity model
$\boldsymbol{r}$	Residual vector
$\underline{\mathbf{R}}$	Rotational part of the deformation gradient
$\mathbf{R}^{\mathrm{crytsal}}$	Rotation matrix for rotating the normal vectors of grains
$\mathbf{R}^{\mathrm{e}}$	Rotational part of the elastic part of the deformation gradient
$\mathbf{R}^{\mathrm{p}}$	Rotational part of the plastic part of the deformation gradient
$\mathbf{R}_{\mathrm{Pol}}$	Rotation matrix for spherical polar coordinates
$\mathbf{R}$	Rotation matrix for the locally rotating Cartesian coordinate frame
$\mathbf{R}^{\mathrm{C}}$	Rotation matrix used for rotating the elastic stiffness tensor

Symbol	**Description**
$\mathbf{S}_\mathrm{I}$	Second Piola-Kirchhoff stress tensor
t	Time
$\boldsymbol{u}$	Global nodal displacement vector
$\mathbf{U}$	Right stretch tensor
$\mathbf{U}^\mathrm{e}$	Stretching part of the elastic part of the deformation gradient
$\mathbf{U}^\mathrm{p}$	Stretching part of the plastic part of the deformation gradient
$\boldsymbol{v}$	Speed of the material points of the body
$\mathbf{V}$	Left stretch tensor
$\dot{w}$	Rate of total power per unit volume
$\dot{w}^\mathrm{e}$	Elastic part of rate of total power per unit volume
$\dot{w}^\mathrm{p}$	Plastic part of rate of total power per unit volume
$\boldsymbol{w}$	Speed of the region $\Omega(t)$
$\mathbf{W}$	Spin tensor
$\mathbf{W}^\mathrm{p}$	Plastic spin tensor in the current configuration
$\mathbf{W}^\mathrm{p}_\mathrm{I}$	Plastic spin tensor in the intermediate configuration
$\hat{\mathbf{W}}^\mathrm{p}$	Plastic spin tensor in a locally rotating Cartesian coordinate frame
$\hat{\mathbf{W}}^\mathrm{p}_\mathrm{TC}$	Plastic spin contribution from tension/compression
$\hat{\mathbf{W}}^\mathrm{p}_\mathrm{S}$	Plastic spin contribution from generalized shear
$\tilde{\mathrm{W}}^\mathrm{p}_{\theta r}$, $\tilde{\mathrm{W}}^\mathrm{p}_{\varphi r}$, $\tilde{\mathrm{W}}^\mathrm{p}_{\varphi\theta}$	Plastic spin components in the spherical polar coordinate frame
$\boldsymbol{x}$	Position vector in body $\mathscr{B}_t$
$\boldsymbol{X}$	Position vector in body $\mathscr{B}_0$

Greek symbols

Symbol	Description
$\alpha^{(k)}$	Modified step size in the line search algorithm
$\dot{\gamma}_0$	Reference shearing rate in the crystal plasticity model
$\dot{\gamma}^{\alpha}$	Slip rate in the crystal plasticity model
$\dot{\gamma}$	Plastic multiplier
$\Delta\boldsymbol{\varepsilon}$	Strain increment
$\Delta\gamma$	Incremental consistency parameter
$\Delta(\Delta\gamma)$	Incremental change for the consistency parameter
$\Delta\boldsymbol{\varepsilon}^{\mathrm{p}}$	Plastic strain increment
$\bar{\varepsilon}^{\mathrm{p}}$	Equivalent plastic strain
ε^{hkl}	Lattice strain
$\boldsymbol{\varepsilon}$	Total strain tensor
$\boldsymbol{\varepsilon}^{\mathrm{e}}$	Elastic part of the strain tensor
$\boldsymbol{\varepsilon}^{\mathrm{p}}$	Plastic part of the strain tensor
ζ	Volumetric sources inside the region $\Omega(t)$
θ^{p}	Polar angle in a spherical polar coordinate frame
θ_{L}	Lode angle
$\theta^{\,\mathrm{cut\ off}}$	Cut off angle for choosing the normal vectors
λ_1^{p}, λ_2^{p}, λ_3^{p}	Principal components of the rate of plastic deformation tensor
μ_{L}	Lode parameter
ν^{hkl}	Lattice plane specific Poisson's ratio
ρ	Mass density
$\boldsymbol{\sigma}$	Cauchy stress tensor
$\overset{\bullet}{\boldsymbol{\sigma}}$	Objective rate of Cauchy stress tensor
$\overset{\triangledown}{\boldsymbol{\sigma}}$	Jaumann rate of Cauchy stress tensor
$\dot{\hat{\boldsymbol{\sigma}}}$	Rate of Cauchy stress tensor in a rotating Cartesian coordinate frame
$\hat{\boldsymbol{\sigma}}$	Cauchy stress tensor in a rotating Cartesian coordinate frame
σ_{y}	Hardening function

Symbol	Description
σ_1, σ_2, σ_3	Principal components of the Cauchy stress tensor
$\boldsymbol{\sigma}^{\mathrm{tr}}$	Trial stress
$\boldsymbol{\sigma}^{n}$	Stress tensor at the start of the increment
τ^{α}	Schmid stress
$\uptau_0$	Initial value of the slip resistance in the crystal plasticity model
$\uptau_\infty$	Saturation value of the slip resistance in the crystal plasticity model
$\uptau_{\mathrm{c}}^{\alpha}$	Slip resistance in the crystal plasticity model
$\boldsymbol{\varphi}$	Non-convective flux through the surface
φ^{p}	Azimuth in a spherical polar coordinate frame
Φ	Yield surface
$\boldsymbol{\chi}(t, \boldsymbol{X})$	Mapping of the material points on the current configuration.
ψ	Conserved quantity

Abbreviations

Abbreviation	Description
AM	*Additive manufacturing*
BCC	*Body-centered cubic*
CCO	*Cartesian coordinates*
CEPT	*Consistent elasto-plastic tangent operator*
CP	*Crystal plasticity*
µCT	*Micro computed tomography*
EBSD	*Electron backscatter diffraction*
EDM	*Electrical discharge machining*
FCC	*Face-centered cubic*
FEM	*Finite element method*
FDM	*Finite difference method*
FFT	*Fast fourier transform*
HCP	*Hexagonal close packed*
IBVP	*Initial boundary value problem*
LPBF	*Laser powder bed fusion*
LPBF316L	*Stainless steel 316L produced via laser powder bed fusion*
RS	*Residual stress*
RVE	*Representative volume element*
SEM	*Scanning electron microscope*
SCEC	*Single crystal elastic constants*
SPC	*Spherical polar coordinates*
TOF	*Time-of-flight*
UMAT	*User-defined mechanical material behavior*

1 Introduction

Additive manufacturing (AM) is a collective term used for production processes during which the final part is built layer by layer, such as material extrusion, material jetting, material droplet printing, binder jetting, sheet lamination, powder bed fusion, directed energy deposition, and wire arc additive manufacturing. These AM processes differ regarding the utilized feedstock materials and deposition techniques. However, all of them have one thing in common. They all offer significantly greater freedom of design than conventional manufacturing processes since AM generally allows for the production of parts with complex geometries, whereas other manufacturing processes would have failed. Moreover, AM offers other advantages with the potential for improved efficiency and functionality, such as rapid prototyping, which shortens the time needed for testing the design ideas and reduces overall manufacturing costs by, for example, eliminating the need for expensive molds or decreasing the amount of wasted material. In this work, the main focus is on the metal AM processes, also known as metal 3D printing. It should be noted that AM, as of now, is not a replacement for conventional manufacturing processes and is best used in conjunction with them. Metal AM is best suited for producing parts where mass production is not needed, rendering them financially not feasible. However, as time goes by, the AM processes become more mature and widespread, which could potentially be used to replace some of the traditional manufacturing processes. However, despite the technological advancements made during the last few years, several aspects of the AM process are not fully understood. They are, thus, a hindrance to mass adoption, specifically in safety-critical environments. Some of these challenges are, for example, the rough surface finish, slow production time, microstructural defects, residual stresss (RSs), mechanical anisotropy, and, more importantly, the lack of understanding of the process-property-performance relationship. [1–6]

From all existing AM processes, laser powder bed fusion (LPBF), in particular, has gained more traction both among researchers and in the industry due to its overall capabilities for producing parts with high-quality and near full density. Moreover, under optimized conditions, it is possible to produce materials with mechanical properties superior to conventional manufacturing techniques [6, 7]. Furthermore, LPBF also offers the possibility of combining different feedstock materials to obtain a microstructure tailored for a specific use case. LPBF works by melting different regions of a thin layer of metallic powder via a high-power laser source according to the predefined part geometry and scan strategy. The molten areas are then rapidly solidified as the energy source moves to other regions. After that, another thin layer of metallic powder is deposited on top of the previous layer by the recoater. These steps are repeated until the final structure is complete. At the end of the production process, the component is made of fused powder particles [8, 9]. This layerwise process is schematically illustrated in fig. 1.1. LPBF systems offer a wide range of process parameters, which can substantially change the resulting microstructure. These parameters include laser scan strategy, scanning velocity, laser power, inter-layer time, layer thickness, and hatch distance.

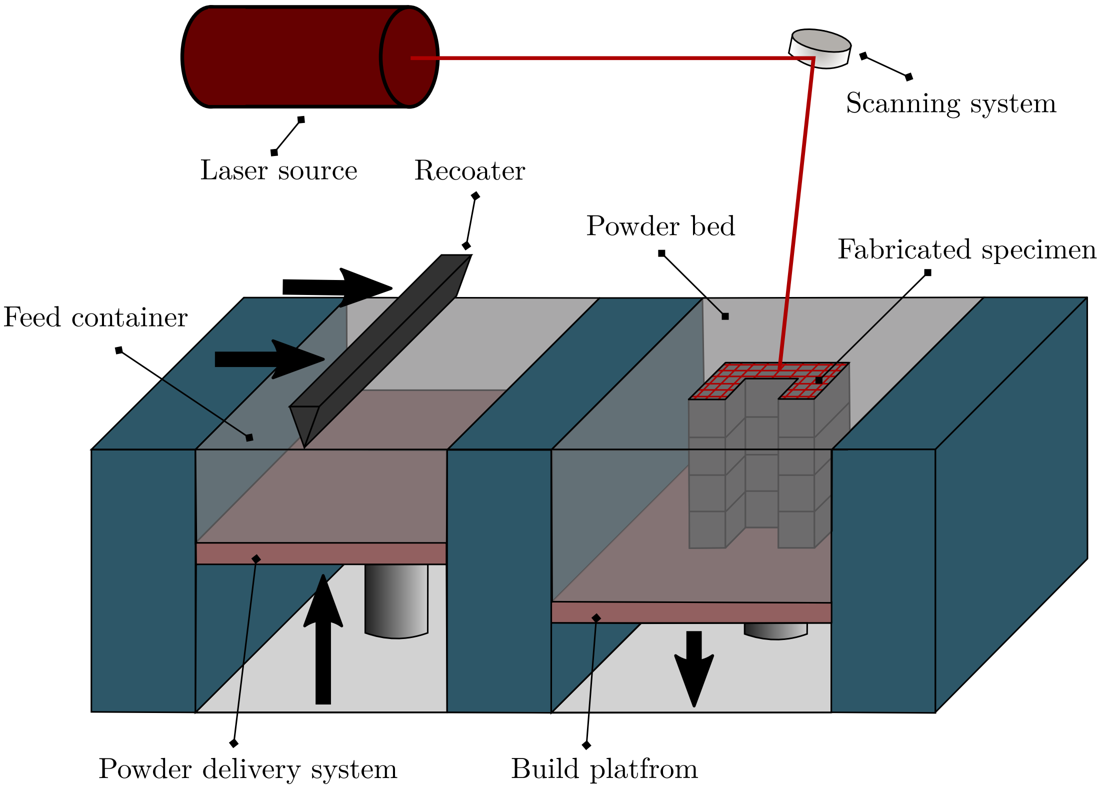

Figure 1.1: Schematic portrayal of LPBF process.

Different commercial alloys can be used as feedstock materials in the LPBF systems. Ni-, Fe-, Cu-, Al-, and Ti-base alloys are some of the popular alloys widely utilized in commercial LPBF systems. Final parts made by many of these alloys in the LPBF systems have a layered morphology consisting of many different features spanning over a large spectrum of length scales [10, 11], which have a significant impact on the final mechanical properties. However, as explained before, the connection between these process-specific features and the final material properties is not yet fully understood. One of such aspects is the resulting mechanical anisotropy in LPBF parts, and in particular, in stainless steel 316L produced via laser powder bed fusion (LPBF316L), which is the material of choice in this work for the production of all test specimens. In the context of this work, mechanical anisotropy refers to the property of certain materials, where the mechanical behavior is dependent on the orientation of the material or specimen as opposed to isotropic behavior, where the orientation has no effect on the material properties. The cause of the resulting mechanical anisotropy in LPBF316L has been attributed to different features [12], such as the interface between the layers. The explanation for this argument is that oxidation, foreign particle inclusions, and defects are more frequent in the vicinity of these interfaces due to the layerwise manufacturing process [13–15]. Other frequently mentioned factors include the grain size, grain shape, and grain aspect ratio in conjunction with the Hall-Petch effect [15–18]. This explanation may seem logical at first glance since, in conventional materials, the high angle grain boundaries are a major hindrance to dislocation glide [19,20]. Therefore, if in LPBF316L, dislocations have to cross a different number of such barriers in various directions, then anisotropy could be attributed to this phenomenon. However, several authors believe that the mechanical properties of LPBF316L are directly linked to its subgrain structure, predominately its fine-scaled dendritic and cellular substructure, and not to the high angle grain boundaries [10, 21, 22]. The usually higher ultimate tensile strength and strain at breakage have also been attributed to these unusual and highly oriented cellular substructures [23], which were also reported by many separate research groups and for a variety of different processing parameters [10,13,22,24–28]. It is also speculated that RSs [29–33] and melt pool boundaries [34] might play a role regarding the mechanical anisotropy of LPBF316L. The microstructure of as-built AM parts usually displays a preferred crystallographic orientation. Therefore, similar to the findings for conventional metallic materials [35–37], the crystallographic texture has been repeatedly linked to the mechanical anisotropy of LPBF316L [3, 18, 38, 39]. Some researchers [16, 22, 25, 40, 41] believe that the crystallographic texture combined with different deformation mechanisms, such as dislocation slip and twinning, is the underlying cause for the observed directional dependency of material properties. The authors explain this behavior by arguing that depending on the crystallographic texture and loading direction, the deformation conditions become more favorable for either twinning, dislocation slip, or any other competing mechanisms. Moreover, the reported directional dependency of LPBF316L differs significantly and is even contradictory in various studies [32].

All these mentioned factors indicate that the underlying cause of anisotropy in LPBF316L isn't fully understood and that further analysis is required to eliminate these uncertainties. More importantly, based on the state of the research, the numerical modeling aspect of the anisotropic response of LPBF316L also calls for more attention, which is beneficial in understanding and isolating the main contributing factors. Accurate numerical models are also necessary for designing parts and ensuring that they meet the required standards. This is even more crucial for parts to be used in safety-critical domains. The issue of anisotropy is relevant for many different applications like topology optimization [42–45], designing of lattice structures [44,46–48], simulation of thermophysical processes during the AM process for the determination of the residual stress state [45,49–52], predicting the machinability and tool wear [53], fabrication of functional medical implants [1,54,55], and aero engines [1,56–58]. It is emphasized that anisotropy isn't only crucial for the listed use cases. It plays a vital role in every scenario, where the mechanical response of the final part has to be calculated. Thus, it is clear that having a better understanding of the origin of the mechanical anisotropy in LPBF316L and having an accurate and reliable numerical framework for predicting the material response for any desired loading condition is very beneficial to the additive manufacturing community for the successful fabrication of metallic components and for facilitating faster adoption rate.

The LPBF316L material is experimentally characterized utilizing several different methods. Tensile, torsion, and shear tests, together with dynamic Young's modulus measurement, are used to determine the mechanical response of LPBF316L under various loading conditions. Neutron diffraction experiments are employed to determine the RS state inside different LPBF316L specimens and are also used to measure the lattice strain evolution during tensile tests. Furthermore, the porosity and defect analysis is conducted with X-ray micro computed tomography (µCT). Lastly, electron backscatter diffraction (EBSD) measurements determine the morphological and crystallographic textures present in several different LPBF316L specimens.

The numerical modeling of the deformation behavior of a polycrystalline material, on the other hand, can be pursued on different length scales. The first group belongs to the atomistic simulations [59–62, 62–64], which offer valuable insight into the underlying physical phenomena, such as the formation of dislocations, defects, their interaction with each other, and mechanisms related to the plastic deformation of crystalline materials. However, these simulations are computationally very costly and can, therefore, be used in very small regions, which usually embody a single or very few grains. On the next logical length scale, a few hundred or thousand grains are included in the simulation, usually in the form of a representative volume element (RVE). Using a RVE, it is possible to create a statistically representative replacement of the actual material with all the necessary features, such as the grain morphology, the phase decomposition, and the crystallographic texture [65–67]. This step allows for the utilization of numerical models, often referred to as crystal plasticity models [68–73], which can be used to both analyze the underlying physical phenomena and also predict the average macroscopic response of the material by making use of various homogenization techniques [68, 71, 74]. Such models are more popular among researchers since they are computationally more efficient than atomistic simulations and offer a greater range of applications. Although these models can accurately predict the average material response under different loading conditions, they also suffer from the same limitation similar to the atomistic simulations, which is the overall high computational cost, preventing them from being used for the simulation of actual components.

Phenomenological analytical yield functions have the highest numerical efficiency, enabling them to be used to simulate large structures containing many millions of grains [75–78]. However, these improvements come at a cost, which in some cases renders these models impractical on their own. The first limitation is that using these models alone makes it impossible to directly include the effect of different microstructural features in the simulation. The second limitation concerns the fact that these models require many constitutive parameters to capture the complex underlying physical phenomena and retain the high simulation accuracy observed in the crystal plasticity simulations. And the calibration of these constitutive parameters requires experimental data obtained from many different types of mechanical tests. Such an experimental characterization campaign is not feasible and renders most of these models unsuitable for many scenarios. On the other hand, lowering the number of experiments often substantially reduces simulation accuracy.

Multiscale simulation frameworks were developed to solve these issues by combining numerical methods on different length scales [68, 79–81]. One of the main advantages of this approach is that it offers the possibility of simultaneously reducing the number of actual experiments and retaining high simulation accuracy. This is possible by using virtual experiments to replace real experiments, whereby the constitutive material parameters of the models on the larger length scale are extracted from the virtual experiments conducted on lower length scales. Virtual experiments make it also possible to realize boundary conditions, which are physically not achievable. This approach doesn't completely eliminate the need for actual experiments. However, the experimental efforts could be reduced substantially by employing this approach. However, there isn't a perfect solution covering all use cases, and there are many different possible ways to combine these various models to create a multiscale simulation framework. Therefore, the pursued goals determine the structure and requirements of the final numerical framework. The multiscale simulation approach utilized in this work combines a micro and macroscale model. It is highlighted that the terms nano, micro, meso, and macroscale aren't strictly defined and are sometimes used interchangeably. In this work, the terms micro and macroscale are used to separate the crystal plasticity model from the analytical yield function, respectively. This approach is chosen based on its success in the simulation of the sheet metal forming process, where virtual experiments on the microscale are used to extract the constitutive parameters of the macroscale model [68, 82–92]. More importantly, in this framework, the micro and macroscale simulations are run separately from each other, unlike some two-scale methods [74, 93–96], where during the entire simulation, the material response in an integration point of the macroscopic model is determined from the homogenized response of the underlying full-field crystal plasticity simulations. These methods offer excellent simulation accuracy, especially for large deformations, but are computationally much more expensive and require special care during the numerical implementation.

The necessary steps required for utilizing the multiscale framework used in this work are roughly as follows. First, the underlying physical mechanisms responsible for the plastic deformation of the analyzed material have to be identified. Based on this information, an appropriate crystal plasticity model has to be chosen. Third, a RVE has to be created based on the extracted statistical data from the microstructure. Fourth, the crystal plasticity model must be calibrated and validated using mechanical testing data. Fifth, the parameters of the macroscale model are calibrated using virtual experiments conducted with the CP model. Optionally and in the sixth step, the macroscale model is validated using data obtained from mechanical tests on standard test specimens or actual components. These steps describe this process in a very simplified manner. Many issues and difficulties have to be addressed with care to avoid numerical errors and ensure the reliability and accuracy of the final framework, which are discussed in detail in this work. Moreover, some aspects of this subject require additional modeling efforts, such as the microstructure evolution and its connection to the plastic spin [97–99].

It should be noted that the AM process offers exceptional flexibility and has many parameters that can be varied to create a microstructure with unique features and properties. However, such optimization isn't part of this present work. The following main objectives define the scope of this work:

- Characterization of the mechanical anisotropy in LPBF316L using various experimental methods.
- Accurately modeling and predicting the mechanical response of LPBF316L on the microscale using a crystal plasticity model and also determination of the deformation mechanism or mechanisms, which dictate the material behavior on the microscale.
- Isolating the main contributing factors that have the highest impact on the mechanical anisotropy of LPBF316L.
- Creating a multiscale simulation framework to transfer the micromechanical simulation results to the macroscale by means of virtual experiments and by utilizing appropriate homogenization and scale-bridging techniques.
- Addressing the numerical modeling aspect of microstructure evolution during large plastic deformation by formulating a novel constitutive model for the plastic spin in 3D.

In essence, the final goals can be summarized as isolating and understanding the root cause of anisotropy in LPBF316L and also accurately modeling and predicting the deformation behavior of actual AM parts on the macroscale undergoing large plastic deformations. These goals are achieved by using various experimental characterization techniques and also by creating an efficient and reliable multiscale simulation framework, where the effects of the microstructure evolution on the material behavior are captured using a novel constitutive model for the plastic spin. For this purpose, this present work is split into different chapters to cover the necessary topics required for fulfilling these objectives.

In chapter 2, various experimental methods used for material characterization are explained. The data obtained from these techniques are used for different purposes, such as defect, residual stress, texture analysis, and calibration and validation of the numerical models.

In chapter 3, first, the building blocks of the multiscale simulation framework are formulated separately. After that, the scale-bridging approach connecting these two length scales together is presented.

In chapter 4, first, the experimental findings are analyzed. After that, the simulation results for the microscale model and their implications regarding the anisotropy of LPBF316L are discussed and, furthermore, validated using in-situ neutron diffraction results. Moreover, the macroscale model is validated using the data obtained from shear and torsion tests. Lastly, various vital aspects of the macroscale model are analyzed using different virtual experiments.

In chapter 4.7, a complete summary of the findings and identified shortcomings are presented.

Disclaimer: Please note that the experimental results presented in this work are part of a much bigger project in Bundesanstalt für Materialforschung und -prüfung (BAM), where different aspects of the AM process and the LPBF316L material are investigated by several researchers and PhD students. Most importantly, the experiments weren't carried out by the author himself. However, these experiments were either conducted with the request of the author and the author was involved in the planning of the them.

2 Experimental material characterization

For a numerical model to be successful in accurately predicting the mechanical response of a material under different loading conditions, it is crucial in the first place to have a clear understanding of the underlying phenomena, which are mainly responsible for the observed material behavior. Moreover, the AM process parameters and subsequent post-processing of the specimens significantly influence the material properties and have to be taken into account when analyzing such materials. Therefore, all required steps for producing the LPBF316L specimens and the employed characterization methods are explained in this chapter and are as follows:

- In section 2.1, the processing conditions of LPBF system for the production of test specimens are described. Moreover, all different specimen geometries and the corresponding scan strategies are illustrated.
- In section 2.2, the required post-processing steps for the machining of the test specimens are described, which include the Young's moduli, tensile, torsion, and shear specimens.
- In section 2.3, the test conditions during the mechanical testing of tensile, shear, and torsion specimens are explained.
- In section 2.4, the measurement of dynamic Young's moduli and its advantages over conventional methods are discussed.
- In section 2.5, it is shown why and how µCT is employed to analyze the defects inside of the LPBF316L specimens.
- In section 2.6, the details of the experimental residual stress measurement are laid out.
- In section 2.7, the EBSD measurements and their importance for the texture analysis are described.
- In section 2.8, it is clarified how the in-situ neutron diffraction experiments are used for the determination of the lattice strain evolution during tensile deformation.

2.1 Material and laser powder bed fusion processing conditions

The most important parameters to be specified during the AM process are the laser scan strategy, scanning velocity, laser power, inter-layer time, layer thickness, and hatch distance. The LPBF316L specimens for this work were all produced using a commercial LPBF system SLM280HL (SLM Solutions Group AG, Germany), equipped with a single 400 W continuous wave ytterbium fiber laser. The feedstock material was commercially available gas atomized 316L raw powder with spherical particle morphology and an apparent density of 4.58 g/cm^3, and a mean diameter of 34.69 µm, according to the information provided by the supplier. The cumulative mass values of the particle size distribution were: $D_{10} = 18.22\,\mu m$, $D_{50} = 30.50\,\mu m$, and $D_{90} = 55.87\,\mu m$. More details about the powder are available in [100, 101]. Argon gas was used during the process as the shielding gas with an oxygen content below 0.1 %. Moreover, during the whole process, it is ensured that a gas flow is present from the right to the left side of the building chamber, whereby the gas flow is adjusted to be slightly above the powder bed with a flow velocity between $19\,\frac{m}{s}$ and $21\,\frac{m}{s}$. Before the start of the AM process, the base plates were heated to 100 °C and kept at this temperature. The process parameters were chosen as follows: scanning velocity of 700 mm/s, laser power of 275 W, and hatch distance of 0.12 mm. An alternating meander stripe scanning strategy was applied. The scanning pattern was rotated by 90 ° from layer to layer. Two different values for the layer thickness were used for the production of the samples: 30 µm and 50 µm.

In total, three types of specimens were manufactured: towers of the dimensions $(13 \times 20 \times 112)\,mm^3$ with 50 µm layer thickness, walls of the dimensions $(13 \times 80 \times 80)\,mm^3$ with 50 µm layer thickness, and walls of the dimensions $(13 \times 80 \times 80)\,mm^3$ with 30 µm layer thickness, see fig. 2.1. The dimension of the vertically produced walls in the build direction (Z-Axis) was 82.5 mm for the compensation of the cutting waste during the removal of the walls from base plates. The tower specimens were produced in three different inclinations: 0 ° (Z-Axis dimension 22.5 mm), 45 ° (Z-Axis dimension 90.9 mm), and 90 ° (Z-Axis dimension 114.5 mm) relative to the build plate. The scan vectors used for the production of the 45 ° and 90 ° towers were parallel to the edges of the specimens and were not split into different sections. For the walls and 0 ° towers, the scan vectors were rotated about 45 ° along the build axis in order to avoid high RSs and splitting of scanning vectors into stripes. The different types of geometries produced during the AM process and the corresponding scan strategies are shown in fig. 2.1. For the purpose of having a comparable microstructure in all of the specimens, the inter-layer time was kept constant at a value of approximately 65 s, according to [100]. Before removing the specimens from the base plate, all the specimens were heat-treated at 450 °C for 4 h under argon gas atmosphere to reduce the RSs. This temperature was chosen in order to avoid substantial changes in the microstructure.

The 30 µm and 50 µm walls, together with the 50 µm towers, were used for producing different test specimens. The manufacturing process is explained in detail in the next section. In summary, the in-situ neutron diffraction specimens were extracted from the 30 µm walls, which are used to analyze the evolution of lattice strains during tensile tests. All normal tensile specimens were manufactured from 50 µm towers and walls. Similarly, the dynamic Young's moduli specimens were extracted from a single 50 µm wall. Lastly, the torsion and shear specimens were manufactured from 0 ° towers with 50 µm layer thickness. However, the scan strategy for these specimens was rotated in comparison to the 0 ° towers used for the manufacturing of the tensile specimens, as illustrated in fig. 2.1. This adjustment is made mainly to validate the macroscale model and demonstrate the capabilities of the multiscale simulation approach employed in this work.

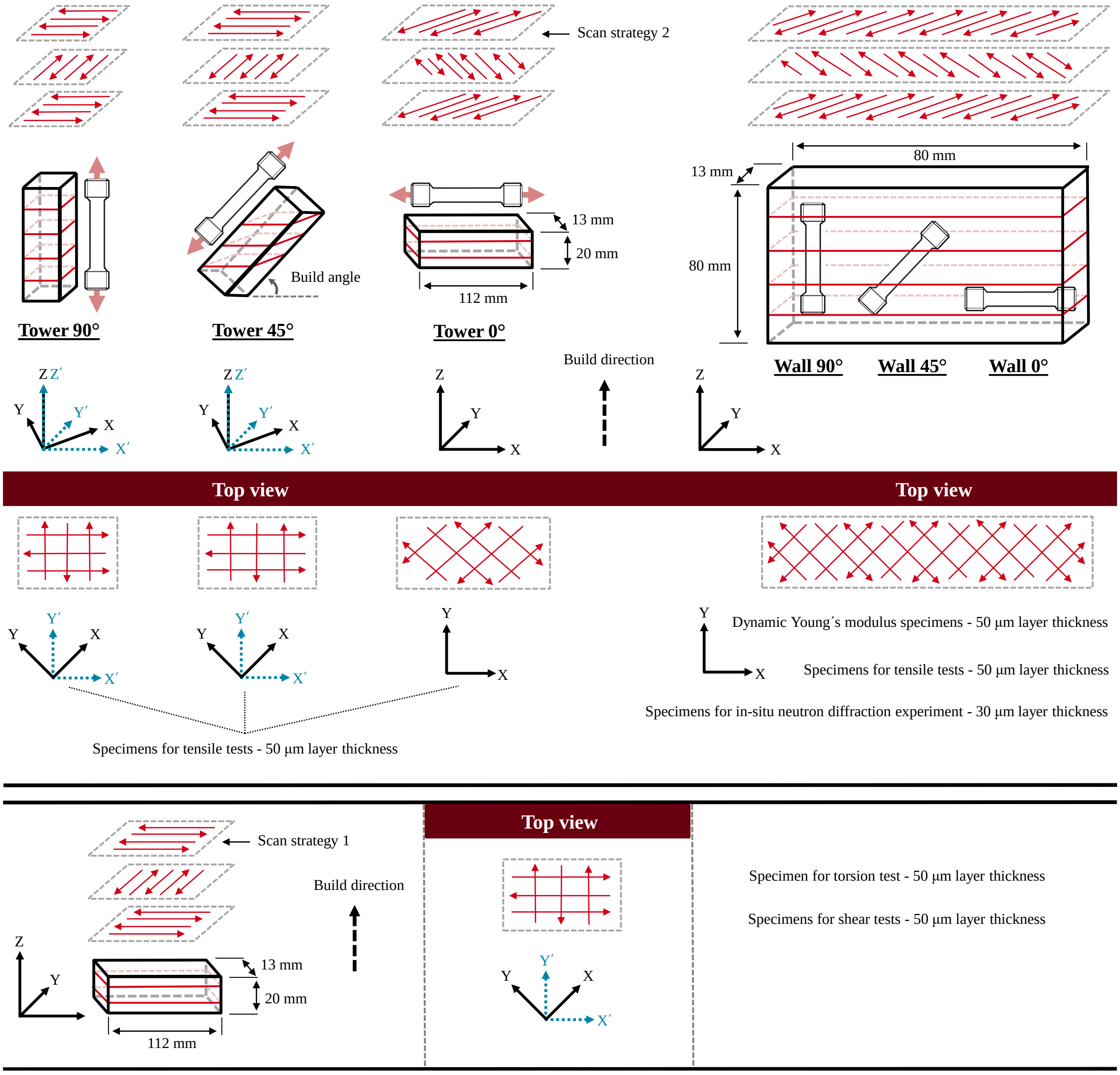
Scan strategy 2
13 mm
80 mm
80 mm
13 mm
20 mm
112 mm
Build angle
Tower 90°
Tower 45°
Tower 0°
Build direction
Wall 90°
Wall 45°
Wall 0°
Z Z′
Y Y′ X X′
Z Y X
Top view
Top view
Dynamic Young´s modulus specimens - 50 µm layer thickness
Specimens for tensile tests - 50 µm layer thickness
Specimens for in-situ neutron diffraction experiment - 30 µm layer thickness
Specimens for tensile tests - 50 µm layer thickness
Scan strategy 1
Build direction
13 mm
20 mm
112 mm
Top view
Specimen for torsion test - 50 µm layer thickness
Specimens for shear tests - 50 µm layer thickness

Figure 2.1: Schematic portrayal of all geometries and the corresponding scan strategies. Note that in total three different types of specimens were produced: towers with 50 µm layer thickness, walls with 50 µm layer thickness, and walls with 30 µm layer thickness.

2.2 Machining of test specimens

The characterization of the material properties of LPBF316L in this work is achieved by using different types of mechanical testing. For this purpose, dynamic Young’s modulus, tensile, shear, and torsion specimens were manufactured from the towers and walls produced using LPBF. All manufactured test specimens are listed in table 2.1. Tensile specimens made from towers were turned and subsequently ground from the middle section of each tower. Two additional steps were required for the production of tensile specimens and Young’s modulus from the wall. In the first step, the walls were symmetrically plane ground to a thickness of 12 mm. In the second step, blocks were cut out from the walls using electrical discharge machining (EDM), which were then used for the machining of tensile specimens. In fig. 2.2, the extraction positions of these blocks are shown. Moreover, milling and surface grinding were the last machining steps for producing the Young's modulus specimen. The Young's modulus specimens come with a rectangular cross-section and a dimension of $(3 \times 6 \times 64)\,\mathrm{mm}^3$. The planes of Young's modulus specimen are parallel with a ±1 % accuracy. For the calculation of the dynamic Young's moduli, the exact dimensions and weight of the test specimens are needed, which were determined by a caliper gauge (Model CD-20D, accuracy: ±10 µm, Mitutoyo Deutschland GmbH, Germany) and an outside micrometer (Model 232871, accuracy: ±1 µm, Vogel Germany GmbH, Germany) and with a precision balance (accuracy: ±0.001 g, Sartorius AG, Germany), respectively. One torsion and two shear specimens were machined from the 0 ° towers, additively manufactured using the scan strategy 1. The torsion specimen was turned and subsequently ground from the middle section of the tower. The shear specimens were cut from the towers using EDM, with the flat side of the specimen being parallel to the top surface of 0 ° towers. The exact geometries used for the tensile, torsion, and shear specimens are shown in figs. 2.3, 2.4, and 2.5. The tensile specimens used for the in-situ neutron diffraction experiments were manufactured from the 30 µm walls. The manufacturing process was similar to the tensile specimens. However, the neutron diffraction specimens were slightly larger than the specimens used for the conventional tensile testing.

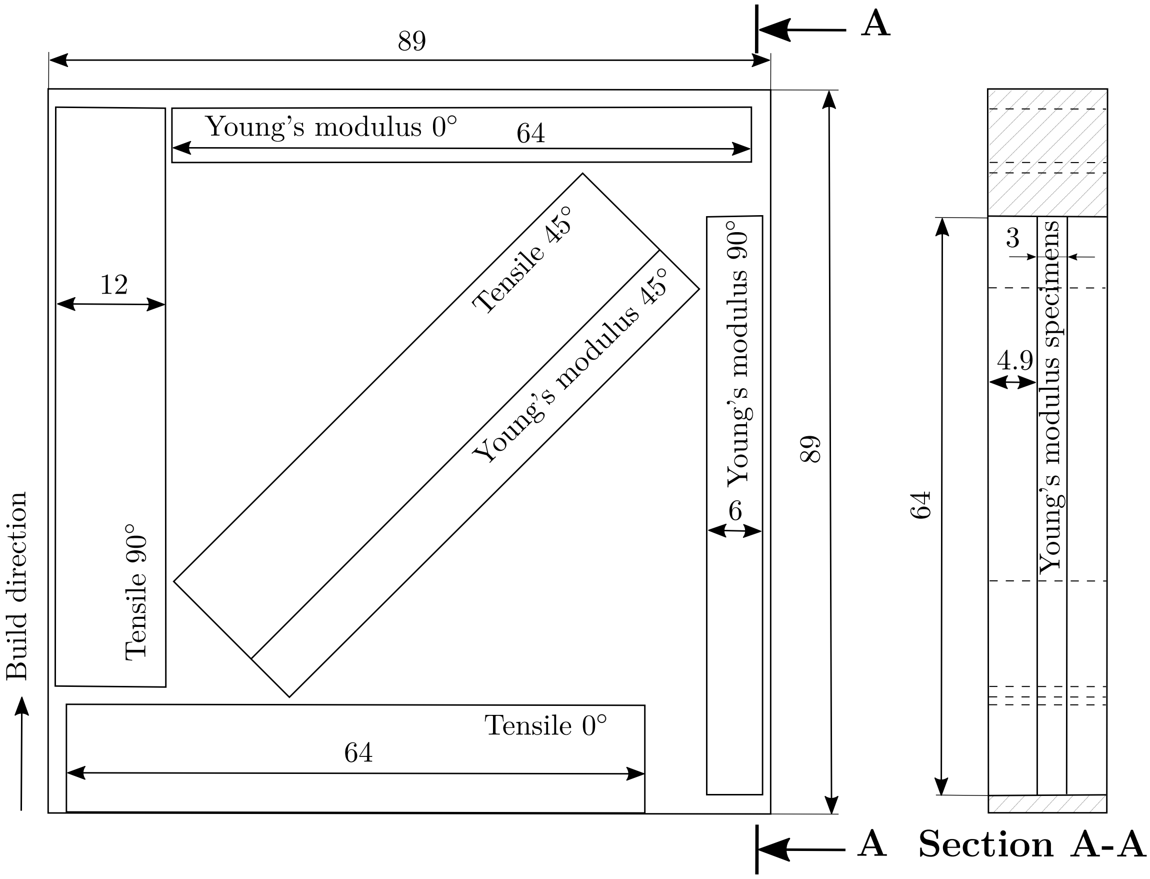

Figure 2.2: Position of extracted tensile and Young's modulus specimens in the wall.

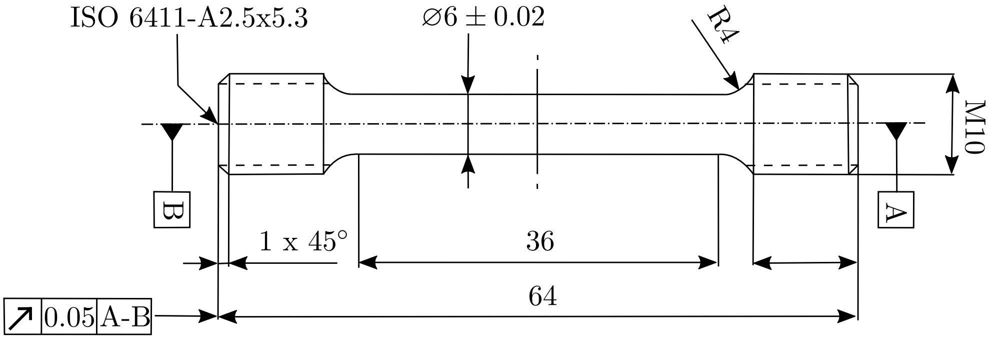
ISO 6411-A2.5x5.3
⌀6 ± 0.02
R4
M10
B
A
1 x 45°
36
64
↗ 0.05 A-B

Figure 2.3: Technical sketch used for the machining of tensile specimens.

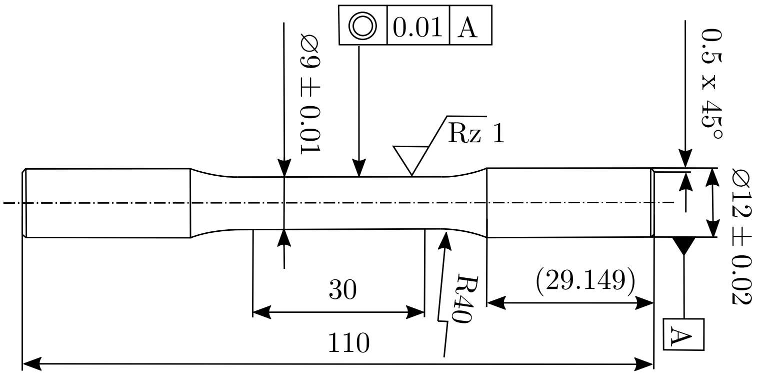
◎ 0.01 A
⌀9 ± 0.01
0.5 x 45°
Rz 1
⌀12 ± 0.02
30
R40
(29.149)
110
A

Figure 2.4: Technical sketch used for the machining of torsion specimen.

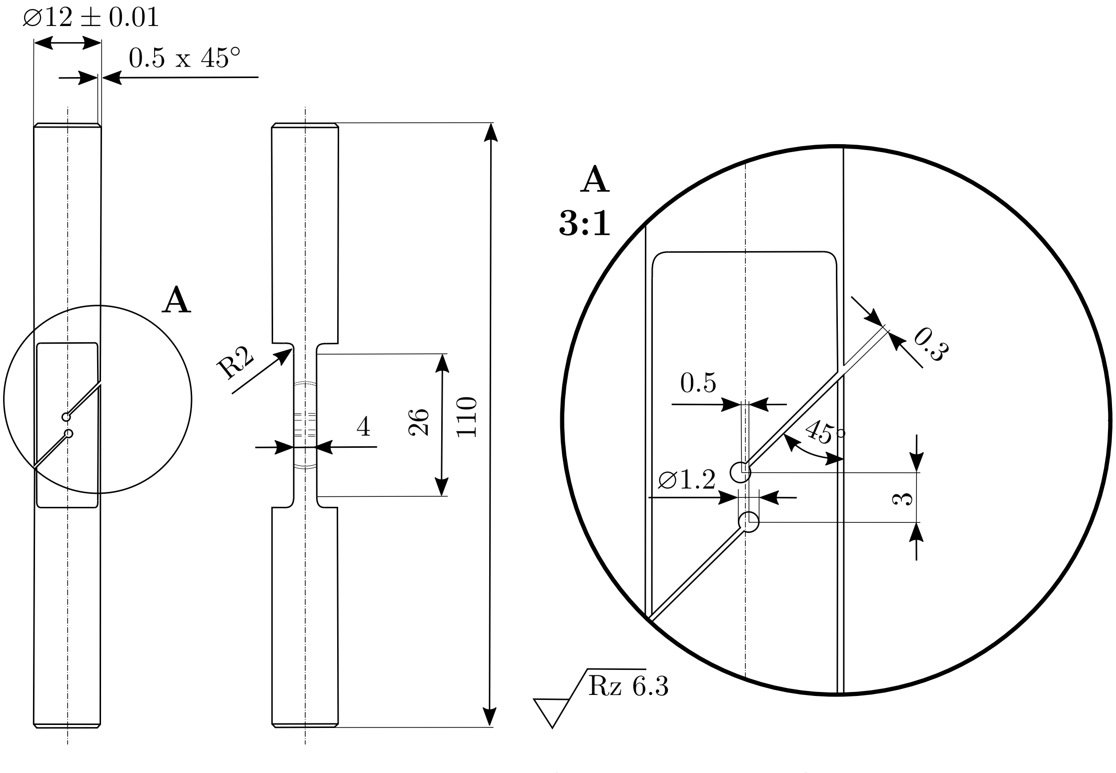
⌀12 ± 0.01
0.5 x 45°
A
R2
4
26
110
A
3:1
0.3
0.5
45°
⌀1.2
3
Rz 6.3

Figure 2.5: Technical sketch used for the machining of shear specimens.

Table 2.1: Overview of all test specimens.

	0° scan strat. 1	**0° scan strat. 2**	**45°**	**90°**
Tower 50 µm Tensile	-	2	2	1
Wall 50 µm Tensile	-	2	2	2
Tower 50 µm Young's modulus	-	1	1	1
Tower 50 µm Shear	2	-	-	-
Tower 50 µm Torsion	1	-	-	-
Wall 30 µm Tensile	-	2	-	2

2.3 Mechanical testing

Tensile tests provide the stress-strain curves that characterize the material's mechanical performance and are required in this work for the calibration and validation of the micromechanical model. These tests were conducted according to DIN EN ISO 6892-1 [102] (Method A, strain rate range 2) at room temperature, whereby a 100 kN Instron testing machine (Model: 4505, Instron GmbH, Germany) was used, which was calibrated according to DIN EN ISO 7500-1 [103] (Force, class 1) and DIN EN ISO 9513 [104] (Displacement, class 1). The tensile tests were strain-controlled. Switching to crosshead speed control was not necessary since all specimens failed before exceeding the maximum range of the extensometer. An extensometer (Model: 632.12C-21, MTS Systems GmbH, Germany) with 25 mm gauge length was used to obtain the experimental strain values. The extensometer was calibrated according to DIN EN ISO 9513 [104] (class 0.5) between $-10\,\%$ and $50\,\%$ strain.

The torsion and shear tests were conducted using a custom-made universal 100 kN/1000 Nm testing machine in order to obtain the torsional moment-angle and shear force-displacement curves necessary for validating the macroscale model. All test data are obtained using the built-in sensors of the testing machine. Torsion and shear tests provide important information regarding the microstructure evolution during large deformations overlapped with large rotations since both of them represent a simple shear.

2.4 Dynamic Young's modulus determination

The Young's modulus is of fundamental importance when dealing with metallic materials in engineering and science, especially in areas such as buckling analysis, fracture mechanics, lattice defects, and creep [105]. The Young's moduli can also be used for validation purposes. In this work, the experimentally measured Young's moduli are used to analyze the accuracy of the single crystal elastic constants of the stainless steel 316L and also the quality of the determined crystallographic textures. The Young's moduli can be experimentally measured using different techniques. In this work, both tensile tests and the resonance method are employed for this purpose. However, dynamic techniques offer an overall higher accuracy when compared to static methods. Moreover, ease of specimen preparation and a wide variety of allowed specimen shapes and sizes are other advantages of the dynamic techniques [106, 107]. The dynamic Young's moduli were determined at room temperature according to ASTM E1876 [108] using an Industrial testing machine (Model: GrindoSonic MK5, GrindoSonic BVBA, Belgium) and a network analyzer (Model: HP8751A, Agilent Technologies, Inc., United States). When using the resonance method, fundamental resonance frequency, dimensions, and mass of the test specimens are required to determine the dynamic Young's moduli. Oscillatory displacements with small strains and relatively high strain rates are used to measure the elastic properties. It should be noted that the elastic properties determined using dynamic methods are also called adiabatic constants, which exhibit slightly higher values compared to the isothermal elastic properties determined using slow or static loadings [109]. A singular strike with an impulse tool is used to excite the specimen and measure the resonance frequency. Furthermore, a transducer is used to convert the mechanical vibrations into electrical signals, which are then analyzed in subsequent steps.

2.5 Porosity and defects analysis

The role of microstructural defects in AM is not yet fully understood. In the case of mechanical anisotropy, some researchers believe that microstructural defects are a contributing factor [13–15]. To assess the plausibility of this claim for the employed process parameters and analyze the overall quality of the produced specimens, six tensile specimens we examined for porosity by µCT. Three of these specimens were extracted from a wall, and three were from the towers. The chosen specimens were of three different inclinations in both cases: 0°, 45°, and 90°. A commercial µCT scanner (Model: GE v|tome|x 180/300, Baker Hughes, United States) was used to analyze the specimens. The following parameters were used during the analysis: voltage of 200 kV, a current of 50 µA, and a silver prefilter of 0.25 mm thickness. The acquired data were post-processed using the commercial software VG Studio MAX Version 3.2 (Volume Graphics GmbH, Germany). The gauge volume where the pores were detected had a length of 16 mm around the center of the specimens. During the experiments, only defects larger than 20 µm were detected since the achieved voxel size was 10 µm.

2.6 Residual stress measurements

To have a better understanding of the role of RSs, they are often categorized by different length scales and into three main groups. Type I, II, and III refer to RSs on macro, micro, and nanoscale, respectively. Type II and III RSs have a minimal impact on the mechanical properties of the final part. However, type I RSs could influence the material performance and integrity of the final part [110]. Thus, only the Type I RSs are analyzed in this work to identify their impact on the mechanical anisotropy observed in LPBF316L specimens. Moreover, this analysis will determine if RSs have to be included in the numerical simulations or if they can be ignored. Different methods are available for the measurement of RSs. X-ray and neutron diffraction are the most common non-destructive methods for measuring the RSs near the surface and in the bulk material, respectively.

The type I RSs in this work were measured in the bulk of six tensile specimens with the neutron diffraction method using the angular-dispersive diffractometer E3 at the Helmholtz Zentrum Berlin, Germany. Details of the measuring instrument are outlined in [111]. The Fe-311 reflection was recorded using a wavelength of $\approx 1.476\,\text{Å}$ and the corresponding 2θ angle of 86°. The {311} reflection was chosen since, in literature, it is reported that it behaves similar to the bulk material in the elastic region, and it has a lower tendency to form intergranular strains [112–114]. The strains were measured along three orthogonal orientations, which were parallel to the edges of the tower and wall. These measured strains were then used to calculate the triaxial RSs. It is highlighted that for the determination of the strains, the stress-free reference lattice spacing has to be known. For this purpose, small cubes of dimension $(3 \times 3 \times 3)\,\text{mm}^3$ were cut by wire EDM in the vicinity of the gauge length of the tensile specimens extracted from the wall. The lattice spacing measured for these small cubes is then used as the stress-free reference since it is assumed that the macroscopic RSs are fully relaxed in these small cubes [113, 115]. Moreover, it is assumed that using wire EDM prevents the insertion of additional RSs into these small cubes and that it only has an influence on a thin layer near the surface, which does not play a role during the bulk measurements using neutron diffraction. Following this approach, the stress-free reference values were determined for the three orthogonal directions. Subsequently, these values were averaged to minimize the influence of microscopic RSs. With the stress-free reference lattice spacing and the lattice spacing measured in the tensile specimens, it is possible to calculate the strains, which in turn can be used to calculate the RSs. The RSs in this work are calculated using Hooke's law:

$$\sigma_{ij} = \lambda^{hkl} \varepsilon_{kk}^{hkl} \delta_{ij} + 2\mu^{hkl} \varepsilon_{ij}^{hkl} \,, \tag{2.1}$$

σ_{ij} and ε_{ij}^{hkl} are the stress and the measured lattice strain, respectively. The Lamé constants λ^{hkl} and μ^{hkl} are calculated using lattice plane specific Young's modulus E^{hkl} and Poisson's ratio ν^{hkl}. It should be noted that the data needed for the calculation of the RS for the Tower 90 ° tensile specimen were acquired during two separate measurements. For the subsequent data analysis and merging, an angular offset of approximately

0.02 ° was applied due to different experimental conditions. The Young's modulus and Poisson's ratio, which were used for the calculation of the RSs, were determined in [116] for the {311} reflection. The calculations were based on the model of Kröner [117], whereby a random texture and measured single crystal elastic constants (SCEC) were used. The resulting Young's modulus of 184 GPa and Poisson's ratio of 0.294 were used in this work for the calculation of the RSs. By using these values, isotropic material behavior is assumed, similar to recently reported work on LPBF316L [116]. However, it is noted that the LPBF316L in this work exhibits anisotropic material behavior, which results in anisotropy of the diffraction elastic constants (DECs). This is caused by the non-random crystallographic texture present in LPBF316L and influences the calculated RSs. The anisotropic DECs were omitted for the calculation of the RSs since the isotropic condition is sufficient for the analysis of the RSs in this work. Moreover, the experimental determination of the anisotropic DECs requires a lot of work.

For the determination of the RSs in each specimen, three planes were chosen, which were distributed 18 mm away from each other and along the height of the specimen. And on each plane, five measurement positions were used for the determination of the RSs. Hence, for each specimen, in total, fifteen measurement positions were experimentally investigated, see fig. 2.6. The gauge volume during the neutron diffraction experiments was $(2 \times 2 \times 2)\,\mathrm{mm}^3$. The data analysis software for these experiments was StressTexCalculator [118].

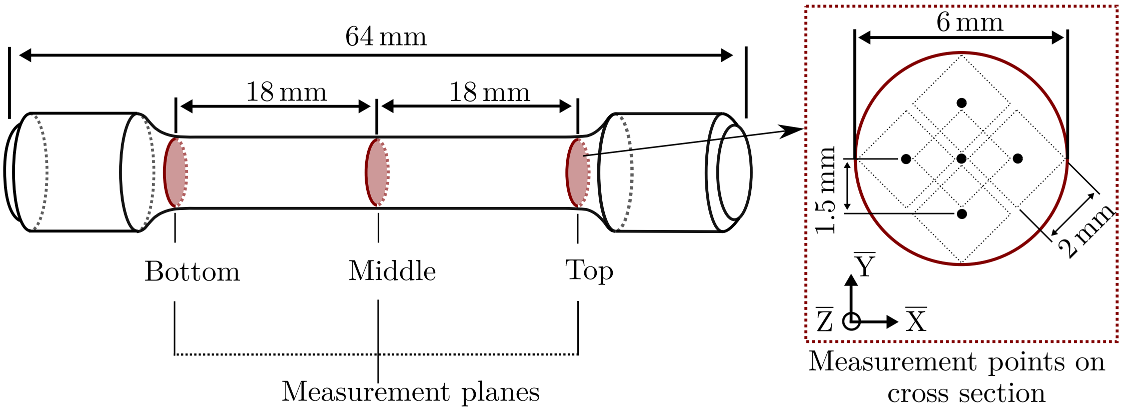

Figure 2.6: Three planes along the height of each specimen labeled as Bottom, Middle, and Top, were used to measure the RSs during neutron diffraction experiments. And on each plane, five positions were specified for these measurements, which are shown on the right side. It is highlighted that the sample coordinate system $(\overline{\mathrm{X}}, \overline{\mathrm{Y}}, \overline{\mathrm{Z}})$ is different from the coordinate system in fig. 2.1 and this cartesian coordinates (CCO) is used to analyze the residual stresses in section 4.1. For an easier comparison, the coordinate system is chosen such that $\overline{\mathrm{X}}$ and $\overline{\mathrm{Y}}$ are always parallel to the edges of the as-built specimens irrespective of the employed scan strategy. Furthermore, $\overline{\mathrm{Z}}$ has always the same alignment as the loading axis.

2.7 Electron backscatter diffraction measurements

The mechanical performance of a metallic specimen is directly linked to its microstructure. Hence, having reliable and representative data about the microstructure can significantly improve the modeling effort. Electrons are ideal for extracting microstructural information from a specimen since, by using them, the probe size becomes much smaller than the microstructural units. Thus, up until the 1980s, transmission electron microscopy (TEM) was the primary method used for analyzing the microstructure. However, in recent years, an enhanced scanning electron microscope (SEM)-based technique has been extensively developed for texture analysis, known as electron backscatter diffraction or EBSD. Using EBSD, it is also possible to identify phases and do strain measurements. One of the main advantages of this method is the rapid automated diffraction analysis, which is used to obtain high-resolution spatial information about the grain morphology and crystallographic texture. The EBSD technique works by using the patterns, which are created by the backscattered electrons. These electrons are diffracted from the surface of the specimen, which is positioned within the SEM sample chamber and with a certain orientation relative to the electron beam source. Computer algorithms then extract the crystallographic orientation from the experimentally obtained diffraction patterns [119].

To have high-quality orientation maps, it is necessary to prepare the surface of the specimen. For this purpose, all specimens were ground using emery papers with 180, 320, 600, and 1200 grits. This was followed by a polishing step using clothes with 3 µm and 1 µm particle suspensions. In the final surface preparation phase, the specimens were electro-polished on Struers Lectropol-5 (Struers GmbH, Germany) device using standard electrolyte A2. Leo Gemini 1530 VP (Carl Zeiss Microscopy GmbH, Germany) was used as the SEM machine, equipped with a high-resolution EBSD detector $\mathrm{e^{-}Flash^{HR+}}$ (Bruker Corporation, United States). The software package ESPRIT 1.94 (Bruker Corporation, United States) was used for the subsequent data analysis. Different specimens and regions were used for the data acquisition, which are listed as follows: the middle section of a Tower 90 ° specimen, the top section of a Tower 45 ° specimen, and specimens extracted from one of the 30 µm walls and the 50 µm walls. In total, nine different regions were used during the EBSD measurements for the extraction of the representative microstructural data, see fig. 2.7. The samples were orientated with an angle of 70 ° inside the SEM machine. The measurements were done using electrons of 20 kV energy, 11.9 µm pixel size, 17 ms exposure time, 10 nA beam current, and pattern size of 160 × 120 pixels.

It is worth noting that the EBSD maps play a crucial role in this work since they are used for different tasks, such as analyzing the grain morphology and the crystallographic texture, which are directly linked to the material behavior. Moreover, these results are used as an input to the CP model and also for the calibration of the plastic spin model.

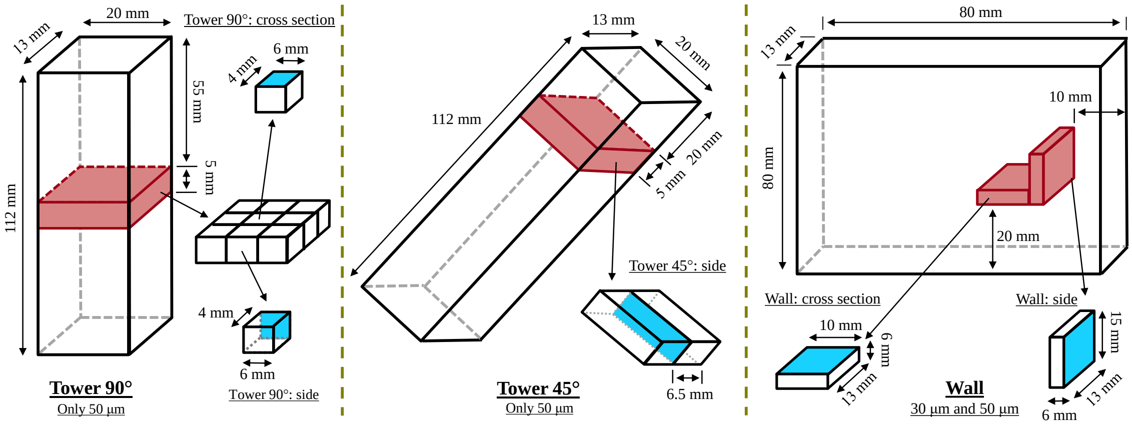

Figure 2.7: Location of different regions used during EBSD analysis (blue surfaces). Two $(3 \times 4)\,\mathrm{mm}^2$ EBSD measurements are from the middle section of a Tower 90 ° specimen, one $(3 \times 4)\,\mathrm{mm}^2$ EBSD measurement from the top section of a Tower 45 ° specimen, eight $(3 \times 4)\,\mathrm{mm}^2$ measurements from one of the 50 µm walls, and sixteen $(3 \times 4)\,\mathrm{mm}^2$ measurements from one of the 30 µm walls.

2.8 In-situ neutron diffraction tensile experiments

In-situ neutron diffraction experiments can be used to investigate important aspects of the deformation at the micromechanical level. Like the SEM measurements, neutron diffraction analysis uses diffraction patterns to obtain the desired pieces of information. However, instead of an electron beam, a neutron beam is employed, which is capable of penetrating the bulk material contrary to the electron beam, which is diffracted from the surface of the specimen. This makes the in-situ neutron diffraction experiments very useful for analyzing the bulk of the specimens. After obtaining the diffraction profiles for different crystallographic grain families, they can be used to track and examine the evolution of lattice strain during the deformation of these crystallographic grain families. The in-situ neutron diffraction experiments to determine lattice strain evolution during tensile tests are conducted using the time-of-flight (TOF) instrument ENGIN-X at the spallation source, ISIS Neutron, and Muon Source at Harwell, UK. An idealized TOF transmission instrument uses a pulsed point neutron source and a point detector to determine the wavelength of a neutron at the detector based on its TOF t from the neutron source. Moreover, this wavelength can be linked to the lattice spacing of a crystallographic plane family by using Bragg's law [120] and the diffraction angle. This measured lattice spacing is then used to calculate the residual strains for a specific crystallographic grain family similar to the to the type I residual stress measurements described in section 2.6. However, instead of only measuring the lattice spacing for the {311} grain family, other grain families of interest are also analyzed. This is possible since the beam of neutrons going through a polycrystal is diffracted at different angles. Therefore, each diffraction peak is related to a single crystallographic grain family. [121–123]

In the TOF experiments, the gauge volume was $4\,\mathrm{mm} \times 4\,\mathrm{mm} \times 4\,\mathrm{mm}$. After these experiments, the acquired data sets were subjected to a Pawley refinement and single peak fitting over the six most intense lattice reflections, {420}, {331}, {311}, {220}, {200}, and {111} [124, 125]. This post-processing analysis was conducted using the Open GENIE software suite [126, 127]. The ENGIN-X detector coverage is 28° – (±14°) in the diffraction plane and 42° – (±21°) perpendicular to the diffraction plane. These ranges have to be accounted for in the crystal plasticity simulations and are labeled as normal and radial direction, see fig. 2.8. A 100 kN Instron testing machine (Instron GmbH, Germany) was used for the in-situ tensile tests. Moreover, the reference lattice spacing for calculating the residual strains was determined at a load of 5 MPa, which doesn't account for the initial residual strains possibly present in the test specimens at the beginning of the experiment. Tensile tests were conducted for two 30 µm specimens with 0° and 90° inclinations. An Instron (Instron GmbH, Germany) extensometer with 12.5 mm gauge length was used to measure the macroscopic strains at a frequency of 1 Hz. The experiments were conducted in load control up until 390 MPa and 355 MPa for the 0° and 90° specimens, respectively. After reaching these stress levels, the tests were continued in displacement control mode. The time for acquiring the neutron diffraction pattern was approximately 10 minutes. Finer details about the experimental setup are shown in [123].

The results of the neutron diffraction experiments are important in this work since they offer an insight into the deformation behavior of different grain families during tensile tests and are thus, complimentary to the conventional tensile test results, where the average elasto-plastic behavior of all different grain families is analyzed. These results will be used for the validation of the CP model and, more specifically, for the validation of the assumptions made about the dominating deformation mechanism at the microscale.

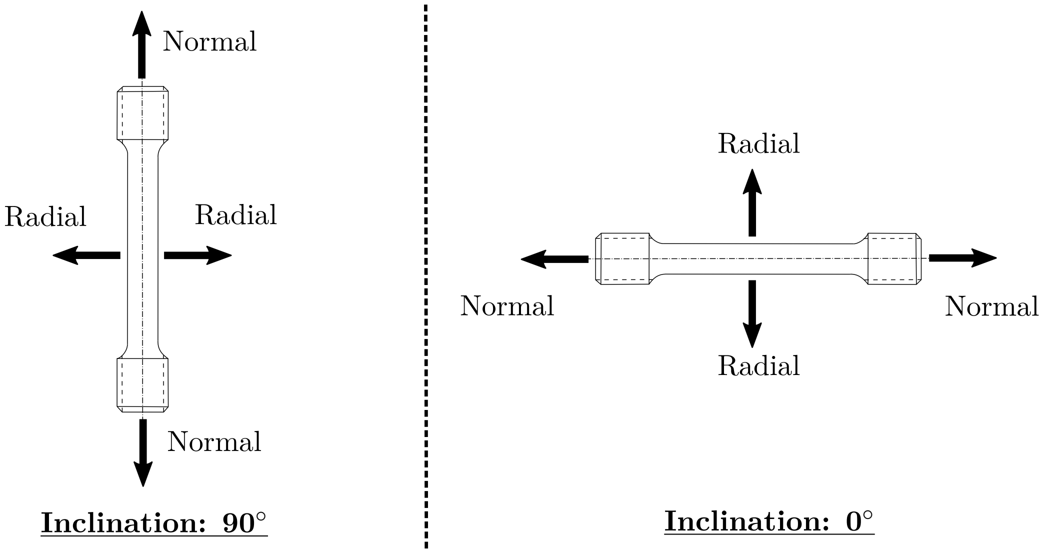

Figure 2.8: Labeling of normal and radial direction for the in-situ tensile experiments.

3 Multiscale modeling of anisotropic yield behavior

The modeling approach taken in this work consists of two separate scales. On the microscale, a CP model is employed to capture the physical phenomena which dominate the anisotropic material behavior. This is done for two main purposes. First, the CP simulation results will give insight into the main underlying factor contributing to the mechanical anisotropy of LPBF316L. Second, the CP model is used to conduct virtual experiments, which can fully replace costly and time-consuming real experiments in order to calibrate the macroscale model. This approach is beneficial for the macroscale model since it allows for the implementation of complex constitutive models with a higher number of material parameters, which are very cumbersome to calibrate experimentally. Thus, the modeling aspect of this work is split as follows:

1. In section 3.1, the basic mathematical requirements and assumptions are presented, which are valid for both the micro and macroscale.
2. In section 3.2, the modeling approach at the microscale is presented, which includes the CP model formulation combined with the most important numerical aspects.
3. In section 3.3, the macroscale model is derived in a co-rotational framework using a Barlat-type yield function, a modified Ludwik hardening law, and a constitutive model for the description of plastic spin to account for the effects of large deformations and also the evolution of the microstructure under different types of boundayr conditions. Furthermore, a robust algorithm is developed satisfying the strict requirements, such as incremental objectivity, necessary for the correct numerical implementation.
4. In section 3.4, the procedures for the calibration of these two models combined with the scale-bridging approach connecting them together are explained fully in detail.

3.1 A brief introduction of some basic concepts used in continuum mechanics

Mathematical models are needed to describe the changes made to a material point of the body when external loads are applied. This can be achieved by means of conservation laws, which describe the temporal and spatial evolution of conserved quantities like mass, momentum, and energy [128]. The balance equations can be written both in spatial and material configuration and are one of the foundations of numerical simulations [129]. In this section, the Einstein notation and a Cartesian coordinate system are used. To distinguish between the spatial and material configuration, we look at a material body $\mathscr{B}$. We assume that this body is made of an infinite number of material points. This body can occupy regions in the three-dimensional space at different times. Thus, it can have different configurations, see fig. 3.1. $\mathscr{B}_0$ displays the configuration at time $t = 0$ and is called reference configuration. For solids, it is helpful to choose the undeformed state as the reference configuration. $\mathscr{B}_t$ describes the current configuration of the material body [130, 131].

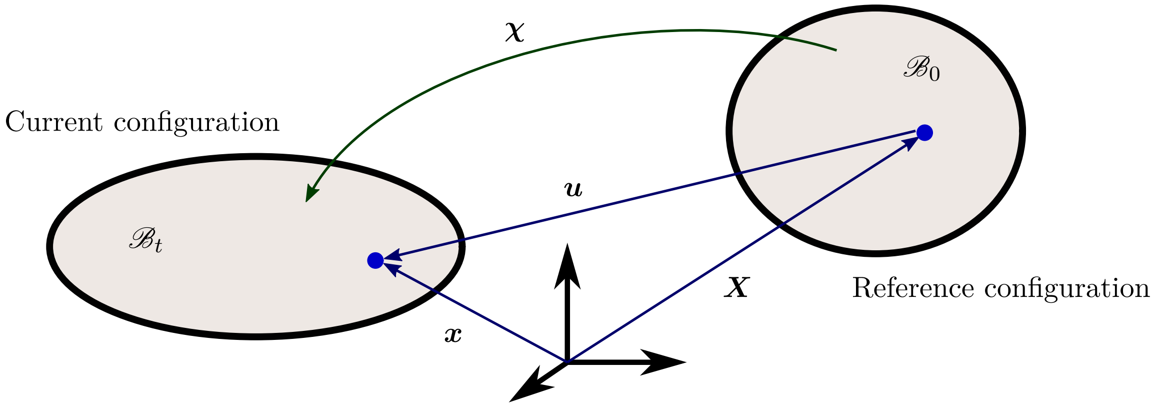

Figure 3.1: Movement of a material point.

Each material point of the body $\mathscr{B}_0$ in the reference configuration can be uniquely identified using a position vector $\boldsymbol{X}$. The position vector $\boldsymbol{x}(t, \boldsymbol{X})$ describes the position of the material points of the body $\mathscr{B}_t$ in the current configuration. Thus, it is a function of the position vector $\boldsymbol{X}$ and time t. The mapping $\boldsymbol{\chi}(t, \boldsymbol{X})$ maps the material points of the body $\mathscr{B}_0$ on the current configuration $\mathscr{B}_t$. The opposite is also possible with:

$$\boldsymbol{x} = \boldsymbol{\chi}(t, \boldsymbol{X})\,, \qquad \boldsymbol{X} = \boldsymbol{\chi}^{-1}(t, \boldsymbol{x})\,. \tag{3.1}$$

Here, it is assumed that this mapping is reversible. This condition is satisfied if the determinant of the deformation gradient is greater than zero:

$$\det(F_{ij}) > 0\,, \qquad F_{ij} = \frac{\partial \chi_i}{\partial X_j}\,. \tag{3.2}$$

The deformation gradient tensor $\mathbf{F}$ describes the local deformation at a material point of the body $\mathscr{B}_0$ with position vector $\boldsymbol{X}$. The deformation is characterized by means of homogeneously mapping the material lines, which consist of the same material points, from reference configuration $\mathscr{B}_0$ onto the current configuration $\mathscr{B}_t$ [130, 131]. Any invertible deformation gradient $\mathbf{F}$ which is the primary quantity used for calculating various different stress and strain measures, can be uniquely decomposed into two separate tensors [130]:

$$\mathbf{F} = \underline{\mathbf{R}} \cdot \mathbf{U} = \mathbf{V} \cdot \underline{\mathbf{R}}\,. \tag{3.3}$$

The tensor $\underline{\mathbf{R}}$ is a proper orthogonal tensor which is often called the rotational part of the deformation gradient since it describes a rigid-body rotation. $\mathbf{U}$ and $\mathbf{V}$ are positive definite symmetric tensors and are called the right and left stretch tensors, respectively. Many other essential quantities are calculated using the deformation gradient $\mathbf{F}$. One of them is the velocity gradient $\mathbf{L}$, which is used to quantify the relative velocity of two neighboring positions in the current configuration:

$$\mathbf{L} = \dot{\mathbf{F}} \cdot \mathbf{F}^{-1}\,. \tag{3.4}$$

To successfully describe the plastic deformation of a deformable body using a material model, one has to have a mathematical concept of the plastic deformation in the first step. Two different approaches are available when dealing with the plasticity of crystalline metals. One of them is the additive decomposition of the strain measure into elastic and plastic parts, which is usually used when dealing with small deformations:

$$\boldsymbol{\varepsilon} = \boldsymbol{\varepsilon}^{\mathrm{e}} + \boldsymbol{\varepsilon}^{\mathrm{p}} \,. \tag{3.5}$$

$\boldsymbol{\varepsilon}$, $\boldsymbol{\varepsilon}^{\mathrm{e}}$, and $\boldsymbol{\varepsilon}^{\mathrm{p}}$ are the total strain, the elastic part of the strain, and the plastic part of the strain, respectively. The other approach, called finite strain plasticity, is more suitable for large deformations [132–134]. In the finite strain plasticity, it is assumed that the deformation gradient $\mathbf{F}$ and the velocity gradient $\mathbf{L}$ contain both the elastic and plastic parts of the deformation. The first assumption is that there exists an intermediate configuration that corresponds to a state of the body in which the elastic part of deformation is unloaded, and only the plastic part of the deformation remains. In this state, it is assumed that the lattice coordinate system coincides with the fixed laboratory system [130]. Based on these assumptions in the work of [135] the multiplicative decomposition of the total deformation gradient is proposed:

$$\mathbf{F} = \mathbf{F}^{\mathrm{e}} \cdot \mathbf{F}^{\mathrm{p}}. \tag{3.6}$$

In this framework, it is assumed that the transformation from the reference configuration to the intermediate configuration is described by the plastic part of the deformation gradient $\mathbf{F}^{\mathrm{p}}$, which does not alter the crystal orientation or the lattice frame. The plastic part of the deformation gradient $\mathbf{F}^{\mathrm{p}}$ can itself be decomposed into a plastic shape change and a rotational part, similar to eq. (3.3). The mapping from the intermediate configuration to the current configuration is made possible by the elastic part of the deformation gradient $\mathbf{F}^{\mathrm{e}}$, which describes the stretching of the crystal lattice and the potential rotation of it, see fig. 3.2.

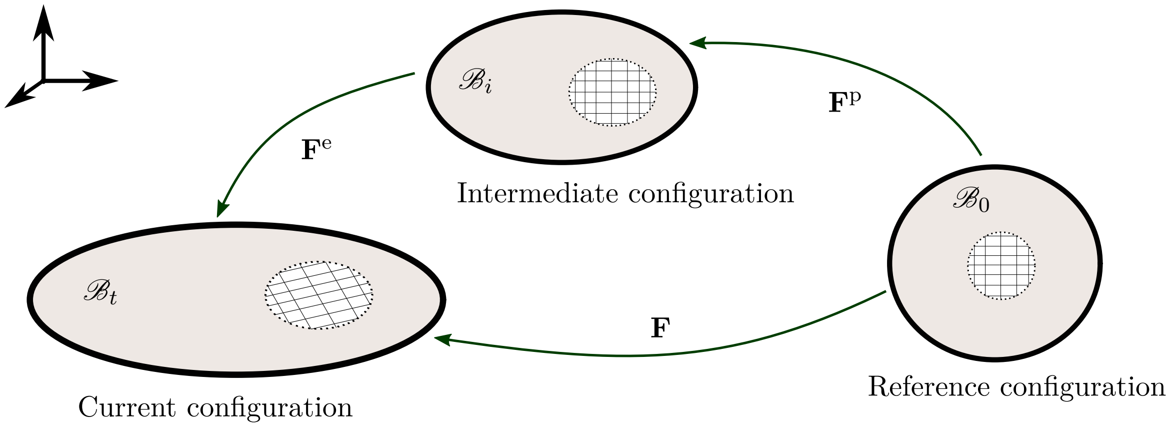

Figure 3.2: Multiplicative decomposition of the total deformation gradient.

It should be noted that, in reality, there is no way to uniquely decompose the total deformation gradient $\mathbf{F}$ into its elastic and plastic parts. This results from the spatial heterogeneity of plastic deformation, which causes the elastic and plastic parts of the deformation gradient to have equal and opposite incompatibilities [130]. Thus, it is impossible to have a stress-free intermediate configuration in which the elastic deformation is completely unloaded. However, these assumptions are still very useful when formulating a material model to describe the plastic deformation of crystalline metals caused by dislocation slip. Following the multiplicative decomposition of the total deformation gradient **F** one can also derive an expression for the velocity gradient **L**:

$$\begin{aligned}\mathbf{L} &= \dot{\mathbf{F}} \cdot \mathbf{F}^{-1} \\ &= \frac{\partial\left(\mathbf{F}^{\mathrm{e}} \cdot \mathbf{F}^{\mathrm{p}}\right)}{\partial t} \cdot \mathbf{F}^{\mathrm{p}-1} \cdot \mathbf{F}^{\mathrm{e}-1} = \dot{\mathbf{F}}^{\mathrm{e}} \cdot \mathbf{F}^{\mathrm{p}} \cdot \mathbf{F}^{\mathrm{p}-1} \cdot \mathbf{F}^{\mathrm{e}-1} + \mathbf{F}^{\mathrm{e}} \cdot \dot{\mathbf{F}}^{\mathrm{p}} \cdot \mathbf{F}^{\mathrm{p}-1} \cdot \mathbf{F}^{\mathrm{e}-1} \\ &= \dot{\mathbf{F}}^{\mathrm{e}} \cdot \mathbf{F}^{\mathrm{e}-1} + \mathbf{F}^{\mathrm{e}} \cdot \dot{\mathbf{F}}^{\mathrm{p}} \cdot \mathbf{F}^{\mathrm{p}-1} \cdot \mathbf{F}^{\mathrm{e}-1} = \mathbf{L}^{\mathrm{e}} + \mathbf{F}^{\mathrm{e}} \cdot \mathbf{L}^{\mathrm{p}}_{\mathrm{I}} \cdot \mathbf{F}^{\mathrm{e}-1} \,. \end{aligned} \tag{3.7}$$

It should be noted that despite the multiplicative decomposition of the total deformation gradient **F**, the decomposition of the total velocity gradient **L** becomes additive [130].

The conservation equations describe the temporal and spatial changes of a conserved quantity based on the fluxes through the surface of the body and the sources in the body itself. When dealing with a conserved quantity, it is assumed that it is additive and continuous inside the body. Conservation laws can be formulated both in their local or global form [129]. The general global form of a conservation law for open volumes can be formulated as follows [136]:

$$\frac{\mathrm{d}}{\mathrm{d}t} \int\limits_{\Omega(t)} \psi \,\mathrm{d}V - \oint\limits_{\partial\Omega(t)} \psi(\boldsymbol{w} - \boldsymbol{v}) \cdot \boldsymbol{n} \,\mathrm{d}A + \oint\limits_{\partial\Omega(t)} \boldsymbol{\varphi} \cdot \boldsymbol{n} \,\mathrm{d}A - \int\limits_{\Omega(t)} \zeta \,\mathrm{d}V = 0 \,. \tag{3.8}$$

The above conservation law is formulated in the current configuration. ψ, $\boldsymbol{v}$, $\boldsymbol{w}$, $\boldsymbol{n}$, $\boldsymbol{\varphi}$, and ζ are the conserved quantity, speed of the material points of the body, speed of the region $\Omega(t)$, normal at the surface, the non-convective flux through the surface, and the volumetric sources inside the region $\Omega(t)$, respectively. The local form of the conservation law is then obtained by transforming the surface integrals into volume integrals using Gauss and Reynolds transport theorem and then imposing the condition that the derived expression must hold for each volumina:

$$\frac{\partial \psi}{\partial t} + \nabla \cdot (\psi \,\boldsymbol{v}) + \nabla \cdot \boldsymbol{\varphi} - \zeta = 0 \,. \tag{3.9}$$

ψ, $\boldsymbol{\varphi}$, and ζ in the eq. (3.9) can be replaced by appropriate conserved quantities. In case of $\psi = \rho$, $\boldsymbol{\varphi} = 0$ and $\zeta = 0$ one obtains the law of conservation of mass:

Invariant form: $$\frac{\partial \rho}{\partial t} + \nabla \cdot (\rho \boldsymbol{v}) = 0 \,,$$

Index notation: $$\frac{\partial \rho}{\partial t} + \frac{\partial}{\partial x^k}\left(\rho v^k\right) = 0 \,. \tag{3.10}$$

With $\psi = \rho\boldsymbol{v}$, $\boldsymbol{\varphi} = -\boldsymbol{\sigma}$, and $\zeta = \rho\boldsymbol{g}$ the law of conservation of momentum is obtained:

Invariant form: $$\frac{\partial \rho\boldsymbol{v}}{\partial t} + \nabla \cdot (\rho\boldsymbol{v} \otimes \boldsymbol{v} - \boldsymbol{\sigma}) = \rho\boldsymbol{g}\,,$$

Index notation: $$\frac{\partial \rho v^i}{\partial t} + \frac{\partial}{\partial x^k}\left(\rho v^i v^k - \sigma^{ik}\right) = \rho g^i\,. \tag{3.11}$$

Both of the conservation laws are formulated in the current configuration. ρ, $\boldsymbol{v}$, $\boldsymbol{\sigma}$, and $\boldsymbol{g}$ are the mass density, speed, Cauchy stress tensor, and the volumetric force, respectively [136]. The most important conservation law for this work is the conservation of momentum, since it is required to calculate the stresses within a body. Assuming a quasi-static state ($|\rho\dot{\boldsymbol{v}}| \ll |\boldsymbol{\nabla} \cdot \boldsymbol{\sigma}|$ and $|\rho\boldsymbol{g}| \ll |\boldsymbol{\nabla} \cdot \boldsymbol{\sigma}|$) then eq. (3.11) reduces to:

$$\nabla \cdot \boldsymbol{\sigma} = 0\,. \tag{3.12}$$

Similarly, the local form of the conservation of momentum can be derived for the reference configuration [130]:

$$\nabla \cdot \mathbf{P} = 0\,. \tag{3.13}$$

$\mathbf{P}$ is the first Piola-Kirchhoff stress and is related to the Cauchy stress by:

$$\mathbf{P} = J\boldsymbol{\sigma} \cdot \mathbf{F}^{-\mathrm{T}}\,. \tag{3.14}$$

J is the determinant of the total deformation gradient $\mathbf{F}$. The main tasks remaining for the numerical calculation of stresses inside a body are first formulating a proper material model and employing a suited numerical method for solving the arising differential equations. In this work, two separate methods are employed for solving the differential equations. For the microscale model, an FFT-based solver is chosen [71]. For the macroscale model, a finite element method (FEM) solver is employed [132–134].

3.2 Crystal plasticity framework for the microscale simulations

3.2.1 Crystalline metals

CP is a collective term used for describing the microstructural defects and deformation mechanisms that contribute to the elastic-plastic behavior of metals. Dislocation slip, martensite formation, and mechanical twinning are the main contributing mechanisms to the plastic deformation of crystalline metals at ambient temperature. However, mechanical twinning and martensite formation have a more substantial impact on hardening and flow stress behavior than plastic shape change. Thus, the dislocations become the most important lattice defects and the primary focus when investigating the plastic deformation of crystalline metals on the microscale since they are the primary carriers of plastic deformation [130].

The arrangement of the atoms in a crystalline metal is not random. It follows a periodic structure, which can be visualized in a very simplified form using lines in a three-dimensional space, see fig. 3.3. Using this approach, the space is divided into parallelepipeds which are the building blocks of a defect-free crystalline metal and are also called unit cells. Moreover, the unit cell can be used to define the crystallographic directions and planes, which are very helpful when analyzing the crystallographic textures and also conducting CP simulations. FCC, body-centered cubic (BCC) and hexagonal close packed (HCP) crystals are the most common crystal structures among the metals. LPBF316L in this work has a FCC crystal structure. In a FCC crystal we have: $a^{\mathrm{z}} = b^{\mathrm{z}} = c^{\mathrm{z}}$ and $\alpha^{\mathrm{z}} = \beta^{\mathrm{z}} = \gamma^{\mathrm{z}} = 90°$. Moreover, Miller indices are used to specify certain crystallographic planes and directions. In cubic crystal, the Miller indices (111), $(11\bar{1})$, $(1\bar{1}1)$, and $(\bar{1}11)$ build a crystallographic plane family which is referred to as $\{111\}$ and has the closest packing of the atoms, see fig. 3.4. Similarly, the direction vectors $[11\bar{1}]$, $[\bar{1}11]$, $[\bar{1}1\bar{1}]$, and $[\bar{1}\bar{1}\bar{1}]$ build the crystallographic group $\langle 111\rangle$. The importance of these crystallographic direction vectors and planes becomes clear when defining the slip direction and planes for the dislocations. Going forward, the crystallographic plane families and direction vectors are designated by $\{\,\}$ and $\langle\,\rangle$, respectively. [137]

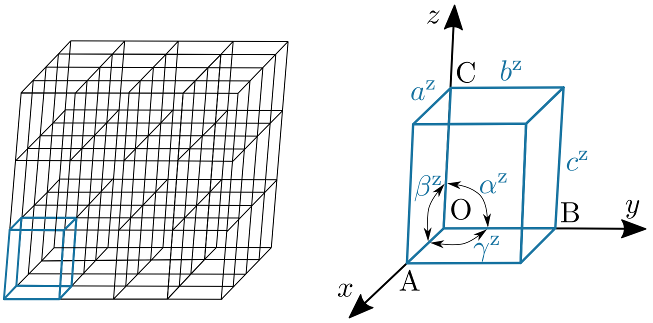

Figure 3.3: Simplified crystal structure in the three dimensional space, based on [137].

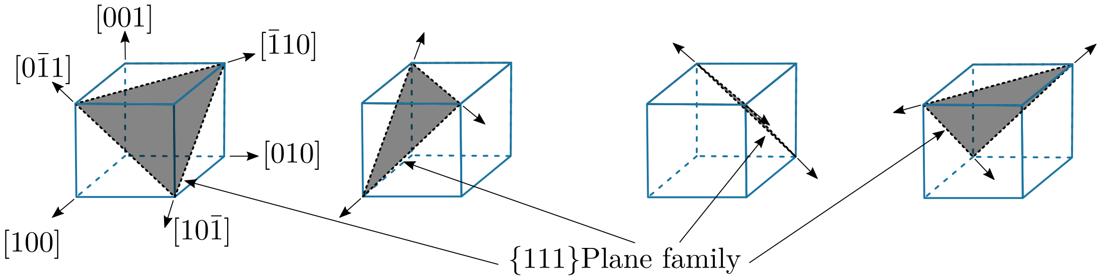

Figure 3.4: $\{111\}$ plane family in an FCC crystal together with $\langle 110\rangle$ direction vectors.

3.2.2 Defects and dislocations in a crystalline material

A crystalline material without any imperfections shown in the last section is a strong idealization. In reality, the crystalline materials used in real life contain many imperfections that substantially impact the mechanical behavior of these materials. These imperfections are strongly coupled with the manufacturing process and can be categorized through their dimensions. Vacancies, dislocations, grain boundaries, and pores are examples of point, line, and two-dimensional and three-dimensional defects, respectively. In this work, only dislocations are considered during the CP simulations. In a perfect crystalline material, the shearing of the material must happen simultaneously along the slip plane. The shear stress necessary for this is much higher than the observed shear stresses in real experiments. However, if the dislocations are present in the material, the shearing process can happen incrementally through the glide of the dislocations on their slip plane. In fig. 3.5 two, different types of dislocations can be seen, namely the edge and screw dislocation. It should be noted that in a real crystal, the dislocations are usually a mix between these two types of dislocations [137].

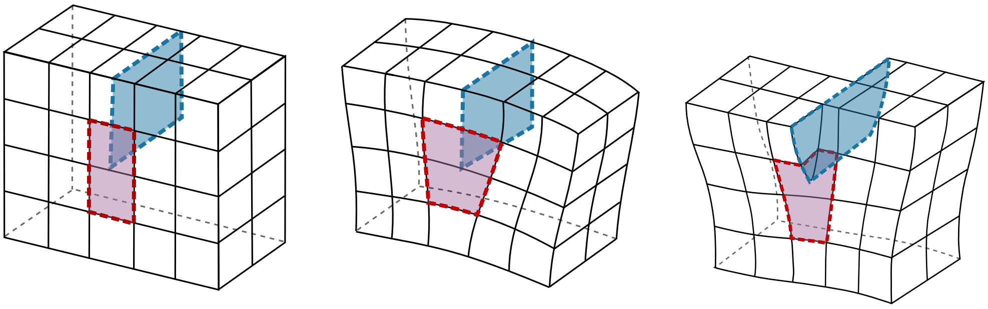

(a) Perfect crystal. **(b)** Edge dislocation. **(c)** Screw dislocation.

Figure 3.5: Line defects in a crystalline material, based on [137].

The CP is often the consequence of the slip of many mobile dislocations on their respective slip planes. The plastic deformation causes a permanent shape change of the material but without any volume changes. Moreover, the slip planes are often the planes with the closest packing of the atoms, and the slip direction is usually the shortest lattice vector. In an FCC crystal, the slip planes and slip directions are generally the $\{111\}$ planes and the $\langle 110 \rangle$ direction vectors, see fig. 3.4. Thus, in a FCC crystal, the plastic deformation is caused by the slip activity in 12 slip systems [137]. It should be noted that the plastic deformation can also be caused by the climb of the dislocations instead of the slip. However, this mechanism is not relevant at room temperature [138] and thus, won't play a role in this work. The movement of a dislocation is only possible if a driving force is present. For the dislocation slip, the driving force is the shear stress acting on the dislocation in its slip plane. This shear stress is also called the Schmid stress and is calculated as follows:

$$\tau^{\alpha} = \boldsymbol{m}_0^{\alpha} \cdot \boldsymbol{\sigma} \cdot \boldsymbol{n}_0^{\alpha} \, . \tag{3.15}$$

$\boldsymbol{m}_0^{\alpha}$ and $\boldsymbol{n}_0^{\alpha}$ are the slip direction vector and the normal of the slip plane, respectively. The incremental movement of a dislocation is illustrated in fig. 3.6, which causes the crystal to be sheared over the slip plane by the Burgers vector $\boldsymbol{b}$ in the slip direction $\boldsymbol{m}_0^{\alpha}$. Thus, the shearing process is possible by only moving a few atoms at a time. This reduces the needed theoretical stress values significantly.

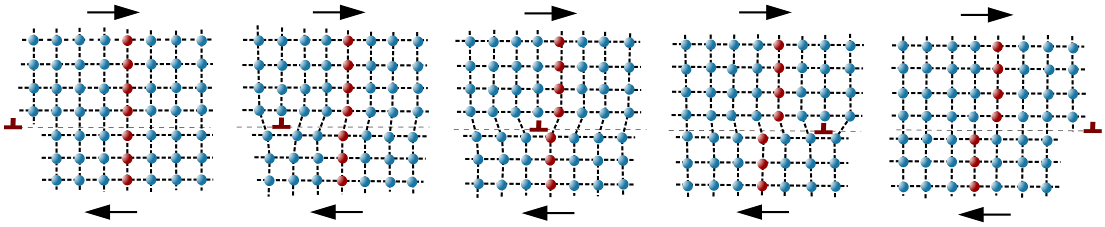

Figure 3.6: Slip of an edge dislocation by moving few atoms at a time, based on [137].

3.2.3 Material model

To analyze the anisotropic yield behavior of LPBF316L utilizing CP, first, we have to couple the dislocation slip with the plastic deformation caused in the material. For simple edge dislocations, this can be achieved by assuming that the total plastic deformation in a crystalline metal is the sum of the plastic deformations in the active slip systems. The material constitutive model required for describing the dislocation slip are derived in this section. The quantities in the intermediate configuration are marked with the letter I. The intermediate configuration represents a reference configuration for the elastic part of the deformation, and is obtained when the elastic part of deformation is relaxed, see fig. 3.2. The stress measure $\mathbf{S}_\mathrm{I}$, also called the second Piola-Kirchhoff stress, is calculated as follows:

$$\mathbf{S}_\mathrm{I} = \mathbb{C}_\mathrm{I} : \mathbf{E}^\mathrm{e}_\mathrm{I}, \tag{3.16}$$

with

$$\mathbf{E}^\mathrm{e}_\mathrm{I} = \frac{1}{2}\left((\mathbf{F}^\mathrm{e})^\mathrm{T} \cdot \mathbf{F}^\mathrm{e} - \mathbf{I}\right) = \frac{1}{2}\left(\mathbf{C}^\mathrm{e}_\mathrm{I} - \mathbf{I}\right), \tag{3.17}$$

where $\mathbb{C}_\mathrm{I}$ is the fourth order tensor of elastic constants, $\mathbf{C}^\mathrm{e}_\mathrm{I}$ is the elastic right Cauchy-Green tensor and $\mathbf{I}$ is the identity tensor. The elastic stiffness tensor $\mathbb{C}_\mathrm{I}$ for a FCC crystal is determined using three elastic constants C_{11}, C_{12} and C_{44}, which are also called the SCEC. Moreover, the elastic and plastic parts of the total power per unit volume are decomposed as follows [139]:

$$\dot{w} = \dot{w}^\mathrm{e} + \dot{w}^\mathrm{p} = \mathbf{S}_\mathrm{I} : \dot{\mathbf{E}}^\mathrm{e}_\mathrm{I} + (\mathbf{C}^\mathrm{e}_\mathrm{I} \cdot \mathbf{S}_\mathrm{I}) : \mathbf{L}^\mathrm{p}_\mathrm{I}, \tag{3.18}$$

where $\mathbf{L}^\mathrm{p}_\mathrm{I}$ is the plastic velocity gradient in the intermediate configuration. By assuming that the total plastic deformation caused by dislocation glide is the sum of the plastic deformations in the active slip systems, $\mathbf{L}^\mathrm{p}_\mathrm{I}$ can be determined using

$$\mathbf{L}^\mathrm{p}_\mathrm{I} = \dot{\mathbf{F}}^\mathrm{p} \cdot (\mathbf{F}^\mathrm{p})^{-1} = \sum_{\alpha=1}^{N} \dot{\gamma}^\alpha \mathbf{m}^\alpha_0 \otimes \mathbf{n}^\alpha_0, \tag{3.19}$$

where $\mathbf{m}^\alpha_0$ and $\mathbf{n}^\alpha_0$ are unit vectors representing the slip direction and the normal of the slip plane for the slip system α, respectively. The plastic power per unit volume is calculated by adding the product of the resolved shear stress τ^α with the slip rate $\dot{\gamma}^\alpha$ in all slip systems

$$\dot{w}^{\mathrm{p}} = \sum_{\alpha=1}^{N} \tau^\alpha \dot{\gamma}^\alpha, \tag{3.20}$$

with N being the number of slip systems. Thus, by using the eqs. (3.18-3.20) an exact expression for the resolved shear stress τ^α acting on slip system α can be derived:

$$\tau^\alpha = (\mathbf{C}_{\mathrm{I}}^{\mathrm{e}} \cdot \mathbf{S}_{\mathrm{I}}) : (\mathbf{m}_0^\alpha \otimes \mathbf{n}_0^\alpha)\,. \tag{3.21}$$

Most CP models utilize the above relations for the formulation of their respective constitutive models. What sets them apart is the calculation of the shear rate. The employed phenomenological model in this work is characterized by a rate-dependent power-law function used to calculate the slip rate $\dot{\gamma}^\alpha$ [140]

$$\dot{\gamma}^\alpha = \dot{\gamma}_0 \left| \frac{\tau^\alpha}{\tau_{\mathrm{c}}^\alpha} \right|^n \operatorname{sgn}(\tau^\alpha), \tag{3.22}$$

with $\dot{\gamma}_0$ being the reference shearing rate, n the microscopic strain rate sensitivity, and τ_{c}^α the slip resistance, which evolves asymptotically from τ_0 towards τ_∞ [88]. Moreover, work-hardening is incorporated into the constitutive material model by making the slip resistance $\dot{\tau}_{\mathrm{c}}^\alpha$ a function of the shear rate

$$\dot{\tau}_{\mathrm{c}}^\alpha = \sum_{\beta}^{N} h^{\alpha\beta} \dot{\gamma}^\beta. \tag{3.23}$$

$h^{\alpha\beta}$ describes the instantaneous strain hardening, and is calculated by a saturation-type law [88]

$$h^{\alpha\beta} = h_0 \left[q + (1-q)\delta^{\alpha\beta} \right] \left| 1 - \tau_{\mathrm{c}}^\beta / \tau_\infty \right|^a \operatorname{sgn}(1 - \tau_{\mathrm{c}}^\beta / \tau_\infty). \tag{3.24}$$

The parameters q, h_0, τ_∞ and a are the latent-hardening, the reference self-hardening coefficient, saturation value of the slip resistance and the hardening exponent, respectively.

3.2.4 Texture evolution

One of the advantages of using a CP model is the possibility of predicting crystallographic texture changes during deformation. This capability is instrumental since it can be used to validate the CP model by comparing the predicted crystallographic texture with the actual texture from an EBSD map, i.e., in a tensile specimen. On the other hand, this capability can be used to easily predict the crystallographic texture for many different loading conditions by removing the need for timely and costly experimental determination. Furthermore, these predicted crystallographic textures can be used to investigate the evolution of mechanical properties, which are heavily dependent on crystallographic texture. For example, in the case of an anisotropic material, both the elastic properties and the yield surface are directly coupled with the crystallographic texture. In DAMASK [71], the evolution of crystallographic texture is obtained by rotating and updating the lattice orientation of each grain in the RVE. To determine the proper rotation matrix, DAMASK makes use of the multiplicative decomposition shown in the eq. 3.6. As explained in section 3.1, the plastic part of the deformation gradient $\mathbf{F}^{\mathrm{p}}$ does not alter the lattice orientation of a crystal. The elastic part of the deformation gradient $\mathbf{F}^{\mathrm{e}}$, on the other hand, is responsible for the changes in the lattice structure of the crystal. As a consequence of this assumption, the texture evolution is governed by the elastic part of the deformation gradient $\mathbf{F}^{\mathrm{e}}$, and more precisely, by the rotational part of it. Thus, texture evolution can be interpreted and linked the rotations of the grains in a RVE. For obtaining the rotational part of $\mathbf{F}^{\mathrm{e}}$, one can make use of the polar decomposition showed in the eq. (3.3) [130]:

$$\mathbf{F}^{\mathrm{e}} = \mathbf{R}^{\mathrm{e}} \cdot \mathbf{U}^{\mathrm{e}} \, , \tag{3.25}$$

which requires the elastic part of the deformation gradient $\mathbf{F}^{\mathrm{e}}$ to be invertible. The rotation part of the eq. (3.25), $\mathbf{R}^{\mathrm{e}}$, is used in DAMASK to update the current crystallographic orientations [71].

3.2.5 Calculation of lattice strain

The in-situ neutron diffraction experiments, which are explained in section 2.8, can be used to validate the CP model on the micro-mechanical level. In such experiments, the lattice strain is measured for different crystallographic grain families during a tensile test. To compare the experimentally measured values to their numerical counterparts, one has to extract the lattice strain from the simulation results. The following steps are required for this purpose. The first step is finding the grains which belong to the same crystallographic grain family inside the RVE. To achieve this goal, the grain families of interest have to be specified. The crystallographic grain families, which were experimentally investigated, are the {100}, {110}, {111}, and {311} grain families. Each grain inside the RVE has a specific orientation, which can be characterized by the three Euler angles. Furthermore, these angles can be converted into a rotation matrix $\mathbf{R}^{\mathrm{crytsal}}$, which is then used to determine the actual normal vectors belonging to the grain families of interest [141]:

$$\boldsymbol{n}_{\{\}}^{\mathrm{current}} = \mathbf{R}^{\mathrm{crytsal}} \cdot \boldsymbol{n}_{\{\}}^{0} \, . \tag{3.26}$$

During the simulation, the rotation matrix $\mathbf{R}^{\mathrm{crytsal}}$ has to be updated to account for the rotation of the crystal lattice as a consequence of deformation, see section 3.2.4. After that, the diffraction vector has to be specified $\boldsymbol{d}^{\mathrm{reflection}}$. This vector can, for example, be the loading direction, transverse direction, or any other direction of interest. Following these steps, one has to determine the angle between the normal vectors of the crystallographic grain families in the current configuration of the grains with the specified diffraction vector using the scalar product. If the angle is smaller than a cut-off angle, then the grain is used to calculate the lattice strain. Thus, for each grain inside the RVE, one has to check the following condition:

$$\text{If } \angle\left(\boldsymbol{n}_{\{\}}^{\mathrm{current}}, \boldsymbol{d}^{\mathrm{reflection}}\right) \leq \theta^{\mathrm{cut\ off}} \rightarrow \text{This grain is selected.} \tag{3.27}$$

Following this procedure for all grains and all crystallographic grain families, one can determine the group of grains, which have to be used for the calculation of lattice strains. For each of the selected grains, the lattice strain tensor is calculated using the elastic part of the deformation gradient $\mathbf{F}^{\mathrm{e}}$ [142]:

$$\mathbf{E}_{\mathrm{I}}^{\mathrm{e}} = \frac{1}{2}\left((\mathbf{F}^{\mathrm{e}})^{\mathrm{T}} \cdot \mathbf{F}^{\mathrm{e}} - \mathbf{I}\right) = \frac{1}{2}\left(\mathbf{C}_{\mathrm{I}}^{\mathrm{e}} - \mathbf{I}\right) . \tag{3.28}$$

The lattice strain tensor is then averaged over all grains belonging to the same crystallographic grain family. In the final step, the averaged lattice strain tensor $\tilde{\mathbf{E}}_{\{\}}^{\mathrm{e}}$ is projected in the direction of the diffraction vector [143]:

$$E_{\{\}}^{\mathrm{e}} = \boldsymbol{d}^{\text{reflection}} \cdot \tilde{\mathbf{E}}_{\{\}}^{\mathrm{e}} \cdot \boldsymbol{d}^{\text{reflection}} . \tag{3.29}$$

$E_{\{\}}^{\mathrm{e}}$ is the numerically estimated lattice strain for specific diffraction direction and crystallographic grain family, which can be compared to the experimental results.

3.2.6 Mechanical equilibrium - spectral solver

Different algorithms like FEM, finite difference method (FDM), and spectral methods are available to solve the partial differential equations. The difference between them is that spectral methods take a global approach for numerically estimating the solution, while the FEM and FDM use a local one. For example, when FEM is employed, the region is discretized into elements that contain the interpolation functions. The interpolation function is constructed from polynomials with a low degree and is only nonzero in their corresponding element. Using the FEM, one converts the partial differential equations into algebraic equations by assembling the emerging element matrices into a global matrix. Since the interpolation functions are only nonzero in their corresponding element, the resulting global matrix is sparse. One of the significant advantages of FEM is that it allows the discretization of regions with complex geometries, since the interpolation functions are defined locally. To compensate for the low accuracy of the low degree polynomials, the FEM offers two remedies. The first one is called the h-refinement, where the number of elements is increased in the whole region to improve the numerical accuracy. The second one is called the p-refinement, where the degree of the polynomials is increased.

Spectral methods, however, use a different approach where the approximation of the whole region is achieved by one large set of basis functions. These interpolation functions are usually either high degree polynomials or trigonometric polynomials, which are nonzero over the entire approximation region. The numerical results are extracted in the sampling points N when using the spectral methods. Increasing the number of sampling points N results in an h- and p-refinement simultaneously, which gives the spectral methods a superior convergence behavior over the FEM. If the interpolation functions are chosen to be the trigonometric polynomials, then the approximation is equal to the case where Fourier series are employed. One of the disadvantages of the spectral methods is that nonsmooth solutions are much harder to handle since the high gradients are concentrated locally, and the spectral methods use a global approach. By employing a linear combination of the global interpolation functions $\phi_n(\boldsymbol{x})$, one can approximate the function $u(x)$ as follows:

$$u(x) \approx \sum_{n=0}^{N} a_n \phi_n(\boldsymbol{x}) \,. \tag{3.30}$$

a_n are the coefficients of the interpolation functions. Using the differential or integral operator L on the eq. (3.30), one gets:

$$Lu(x) = f(x) \,. \tag{3.31}$$

One possible way of approximating the unknown function $u(x)$ is by making use of fixed-point iteration schemes. For this purpose it is necessary to define the residual R:

$$R(\boldsymbol{x}, a_0, a_1, ..., a_N) = L\left(\sum_{n=0}^{N} a_n \phi_n(\boldsymbol{x})\right) - f(x) \,. \tag{3.32}$$

The most critical aspect of approximating the unknown function $u(x)$ is finding the coefficients a_n of the interpolation functions $\phi_n(\boldsymbol{x})$ such that the residual R is minimized. Spectral methods can be categorized as either interpolating or non-interpolating. The interpolating methods, which are also called pseudospectral methods, require those differential equations to be exactly satisfied in the grid points, which are also called collocation or interpolation points. On the other hand, the non-interpolating algorithms, which include Galerkin's method, have no grid or interpolation points. These methods compute the unknown coefficients by multiplying the known function $f(x)$ with the interpolation functions and integrating it [144, 145].

The spectral method formulation described in this section is taken from [144]. The first assumption is that the deformation map $\boldsymbol{\chi}(t, \boldsymbol{X})$ is composed of a homogeneous deformation in the form of a constant deformation gradient $\bar{\mathbf{F}}$ and a superimposed deformation fluctuation field $\bar{w}(t, \boldsymbol{X})$:

$$\boldsymbol{\chi}(t, \boldsymbol{X}) = \bar{\mathbf{F}} \cdot \boldsymbol{X} + \bar{w}(t, \boldsymbol{X}) \,. \tag{3.33}$$

The eq. (3.33) satisfies the periodicity condition and can be used to split the total deformation gradient $\mathbf{F}$ into a spatially homogeneous $\bar{\mathbf{F}}$ and a locally fluctuating part $\tilde{\mathbf{F}}$:

$$\mathbf{F} = \bar{\mathbf{F}} + \tilde{\mathbf{F}} \,. \tag{3.34}$$

To reach the equilibrium state, one has to find a deformation field that satisfies the law of conservation of momentum:

$$\nabla \cdot \mathbf{P}(\boldsymbol{X}) = \mathbf{0} \,. \tag{3.35}$$

The eq. (3.35) describes the static equilibrium in real space. For the spectral methods, it is more beneficial to express the static equilibrium in the Fourier space:

$$\nabla \cdot \mathbf{P}(\boldsymbol{X}) = \mathscr{F}^{-1}\left[\mathbf{P}(\boldsymbol{k})\, i\boldsymbol{k}\right] = \mathbf{0} \,. \tag{3.36}$$

The eq. (3.46) can also be interpreted as finding the root of the residual body force:

$$\mathbf{P}(\boldsymbol{k})\, i\boldsymbol{k} = \mathbf{0}\,. \tag{3.37}$$

However, solving the above differential equation is not an easy task because of its high condition number. Following the suggestions made in [144], one can reformulate the eq. (3.37) using a linear reference material of stiffness $\mathbb{D}$:

$$\mathbb{D}\left[\boldsymbol{\chi}(\boldsymbol{k}) \otimes i\boldsymbol{k}\right]\, i\boldsymbol{k} = \mathbf{A}(\boldsymbol{k})\boldsymbol{\chi}(\boldsymbol{k}) = \mathbf{0}\,. \tag{3.38}$$

The acoustic tensor $\mathbf{A}(\boldsymbol{k})$ is defined as

$$\mathbf{A}(\boldsymbol{k})\boldsymbol{a}(\boldsymbol{k}) = \mathbb{D}\left[\boldsymbol{a}(\boldsymbol{k}) \otimes i\boldsymbol{k}\right]\, i\boldsymbol{k}\,, \tag{3.39}$$

for a given vector field $\boldsymbol{a}(\boldsymbol{k})$. With the inverse of the acoustic tensor $\mathbf{A}^{-1}$, it is possible to calculate the deformation map, which corresponds to the known body force field in the reference material. If the static equilibrium is reached, then the deformation map vanishes with the body force field. The next step would be the definition of an operator which maps the body force field from the reference material to the original material, which results in the following equation:

$$\mathbf{A}^{-1}\mathbf{P}(\boldsymbol{k})\, i\boldsymbol{k} = \mathbf{0}\,. \tag{3.40}$$

To obtain the deformation gradient field, one can use the gradient in real space:

$$\mathbb{\Gamma}(\boldsymbol{k})\, \mathbf{P}(\boldsymbol{k}) = \mathbf{0}\,. \tag{3.41}$$

$\mathbb{\Gamma}(\mathbf{k})$ is the Gamma operator, which is defined as:

$$\mathbb{\Gamma}(\boldsymbol{k})\mathbf{T}(\boldsymbol{k}) = \left[\mathbf{A}^{-1}(\boldsymbol{k})\mathbf{T}(\boldsymbol{k})\, i\boldsymbol{k}\right] \otimes i\boldsymbol{k}\,. \tag{3.42}$$

Thus, the mechanical boundary value problem is defined by the following system of equations [71, 88, 144]:

$$\mathscr{F}_{\text{basic}}\left[\mathbf{F}(\boldsymbol{X})\right] := \mathscr{F}^{-1}\left[\begin{cases} \mathbb{\Gamma}(\boldsymbol{k})\, \mathbf{P}(\boldsymbol{k}) = \mathbf{0} & \text{if } \boldsymbol{k} \neq 0 \\ \Delta\mathbf{F}_{\text{BC}} & \text{if } \boldsymbol{k} = 0 \end{cases}\right]. \tag{3.43}$$

$\boldsymbol{X}$ and $\boldsymbol{k}$ stand for position in real space and frequency vector in Fourier space, respectively. By solving the system of equations (3.43), one obtains the desired deformation gradient field. With $\mathbf{F}_{\text{BC}}$, the necessary boundary conditions are prescribed. In the case of a RVE, one has:

$$\Delta\mathbf{F}_{\text{BC}} = \hat{\mathbf{F}} - \mathbf{F}_{\text{BC}}\,. \tag{3.44}$$

In DAMASK [71], it is also possible to define mixed boundary conditions to avoid non-volume preserving loads for very large deformations. For example, to simulate the tension in 11 direction, one can make use of the following mixed boundary condition:

$$\dot{\mathbf{F}}_{\text{BC}} = \begin{pmatrix} a & 0 & 0 \\ 0 & * & 0 \\ 0 & 0 & * \end{pmatrix} \text{ and } \mathbf{P}_{\text{BC}} = \begin{pmatrix} * & * & * \\ * & 0 & * \\ * & * & 0 \end{pmatrix}. \tag{3.45}$$

a stands for the loading rate. Furthermore, rotation matrices can be applied to the eq. (3.45) to define other loading directions.

3.2.7 Creation of representative volume elements

To use the spectral solver with the CP model explained in sections 3.2.6 and 3.2.3, periodic boundary conditions are required since the spectral method in this work makes use of the trigonometric ansatz functions. When using such boundary conditions, the implication is that the domain of interest is repeated infinitely. The advantages of employing such boundary conditions is that a large domain can be replaced by its representative counterpart. This is a very useful tool when conducting the CP simulation since a crystalline material contains a considerable number of grains that can not be included in a simulation at the same time because of the enormous computational cost. However, a crystalline material can be represented using a fraction of these grains by employing a RVE. To successfully simulate the material behavior using a RVE, it has to be ensured that the statistical properties of the crystalline material, such as the grain morphology and crystallographic texture, are correctly captured. Usually, this is achieved by extracting these pieces of information from EBSD scans of the specimens. In this work, the CP model is mainly used to investigate the influence of the crystallographic texture on mechanical behavior. Thus, instead of the actual grain size distribution, the RVE uses a cubic grain having a dimension of $(70 \times 70 \times 70)\,\mu\mathrm{m}^3$, see fig. 3.7. This grain size and grain aspect ratio are adopted based on the observations made using the EBSD measurements. The actual grain size distribution is shown in fig. 4.6. Moreover, the chosen grain size is based on the mean value obtained from the grain size distributions. It is worth noting, that for the chosen CP model, the actual grain size does not influence the simulation results, as long as the grain aspect ratio remains constant since the parameters of the chosen phenomenological CP model don't depend on the length scale. Furthermore, the simulations are conducted using three different RVEs. Afterward, the results of the simulations are compared to ensure numerical convergence.

The synthetic RVEs used in this work are created using the software Neper [146]. Moreover, the software MTEX [147] is used to extract the orientation distribution function (ODF) intensity data from the EBSD measurements. The ODFs are determined using a $4.5\,°$ halfwidth. In the final step, discrete orientations have to be extracted from the ODF to be assigned to the grains inside of the RVE. One possible solution is randomly choosing orientations matching the number of grains in each. However, if the RVE does not contain a large number of grains, this reduces the simulation accuracy significantly since the crystallographic texture of the RVE will measurably differ from the actual texture. Another solution is finding a set of discrete orientations to minimize this error. This can be achieved by using the hybridIA scheme [148]. After finding these discrete orientations, they are randomly assigned to the grains inside the RVEs.

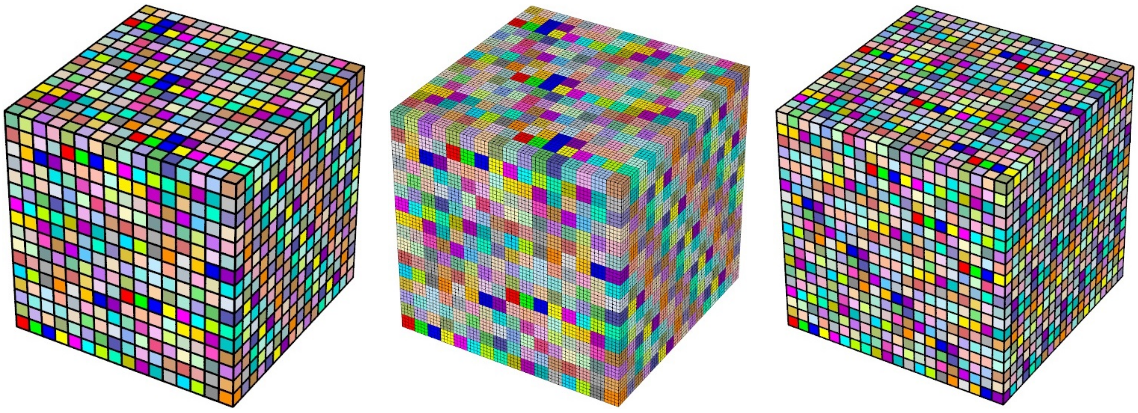

(a) 4096 grains, 1 Fourier point per grain **(b)** 4096 grains, 64 Fourier points per grain **(c)** 8000 grains, 1 Fourier point per grain

Figure 3.7: RVEs used for CP simulations. It should be noted that the grain colors don't represent the grain orientation. The coloring scheme is used in the software Neper [146] to separate different grains.

3.2.8 A summary of the crystal plasticity model equations

The crystal plasticity model consists of the following system of governing equations

$$\begin{cases} \mathbf{F} = \mathbf{F}^{\mathrm{e}} \cdot \mathbf{F}^{\mathrm{p}} & \text{Multiplicative decomposition} \\ \nabla \cdot \mathbf{P}(\boldsymbol{X}) = \mathscr{F}^{-1}\left[\mathbf{P}(\boldsymbol{k})\, i\boldsymbol{k}\right] = \mathbf{0} & \text{Equilibrium condition} \\ \Delta\mathbf{F}_{\mathrm{BC}} = \hat{\mathbf{F}} - \mathbf{F}_{\mathrm{BC}} & \text{Boundary conditions} \\ \mathbf{L}_{\mathrm{I}}^{\mathrm{p}} = \dot{\mathbf{F}}^{\mathrm{p}} \cdot (\mathbf{F}^{\mathrm{p}})^{-1} = \sum_{\alpha=1}^{N} \dot{\gamma}^{\alpha} \mathbf{m}_0^{\alpha} \otimes \mathbf{n}_0^{\alpha} & \text{Flow rule} \\ \dot{\tau}_{\mathrm{c}}^{\alpha} = \sum_{\beta}^{N} h^{\alpha\beta} \dot{\gamma}^{\beta} & \text{Hardening rule} \\ h^{\alpha\beta} = h_0 \left[q + (1-q)\delta^{\alpha\beta}\right] \left|1 - \tau_{\mathrm{c}}^{\beta}/\tau_{\infty}\right|^{a} \operatorname{sgn}(1 - \tau_{\mathrm{c}}^{\beta}/\tau_{\infty}) & \text{Hardening coefficients} \end{cases} \tag{3.46}$$

leading to the following expressions to be solved:

(a) for the mechanical equilibrium part of the system

$$\mathscr{F}_{\mathrm{basic}}\left[\mathbf{F}(\boldsymbol{X})\right] := \mathscr{F}^{-1}\left[\begin{cases} \mathbb{\Gamma}(\boldsymbol{k})\,\mathbf{P}(\boldsymbol{k}) = \mathbf{0} & \text{if } \boldsymbol{k} \neq 0 \\ \Delta\mathbf{F}_{\mathrm{BC}} & \text{if } \boldsymbol{k} = 0 \end{cases}\right], \tag{3.47}$$

with Gamma operator defined as:

$$\mathbb{\Gamma}(\boldsymbol{k})\mathbf{T}(\boldsymbol{k}) = \left[\mathbf{A}^{-1}(\boldsymbol{k})\mathbf{T}(\boldsymbol{k})\, i\boldsymbol{k}\right] \otimes i\boldsymbol{k}\,. \tag{3.48}$$

$\boldsymbol{X}$ and $\boldsymbol{k}$ stand for position in real space and frequency vector in Fourier space, respectively. and

(b) for the prescribed boundary conditions

$$\Delta \mathbf{F}_{\mathrm{BC}} = \hat{\mathbf{F}} - \mathbf{F}_{\mathrm{BC}} \,. \tag{3.49}$$

3.2.8.1 Numerical solution scheme of the mechanical equilibrium

The resulting system of equations can be solved for using a fix-point iteration scheme:

$$\{\mathbf{F}(\boldsymbol{X})\}_{n+1} = \{\mathbf{F}(\boldsymbol{X})\}_{n} - \mathscr{F}^{-1}\left[\begin{cases}\mathbb{\Gamma}(\boldsymbol{k})\ \{\mathbf{P}(\boldsymbol{k})\}_n = \mathbf{0} & \text{if } \boldsymbol{k} \neq 0 \\ \left\{\hat{\mathbf{F}}\right\}_n - \left\{\hat{\mathbf{F}}_{\mathrm{BC}}\right\}_{n+1} & \text{if } \boldsymbol{k} = 0\end{cases}\right] , \tag{3.50}$$

with the mixed boundary condition term defined as:

$$\left\{\hat{\mathbf{F}}_{\mathrm{BC}}\right\}_{n+1} = \left\{\hat{\mathbf{F}}\right\}_0 + \dot{\mathbf{F}}_{\mathrm{BC}}\,\Delta t - \left\{\frac{\partial \hat{\mathbf{F}}}{\partial \mathbf{P}}\right\}_n \left(\left\{\hat{\mathbf{P}}\right\}_n - \{\mathbf{P}\}_{\mathrm{BC}}\right) . \tag{3.51}$$

However, DAMASK uses more advanced solution strategies implemented in the Portable, Extensible Toolkit for Scientific Computation (PETSc) package, which consist of the non-linear Richardson method, the non-linear GMRES method, and the inexact Newton-GMRES method. To get the solution $\{\mathbf{F}(\boldsymbol{X})\}_{n+1}$, these employed solution strategies improve an existing solution $\{\mathbf{F}(\boldsymbol{X})\}_{n}$ iteratively until the convergence criteria are satisfied. [71, 144, 149]

3.2.8.2 Time integration procedure for the constitutive model

$$\dot{\mathbf{F}}^{\mathrm{p}} = \mathbf{L}^{\mathrm{p}}_{\mathrm{I}} \cdot (\mathbf{F}^{\mathrm{p}}) \,. \tag{3.52}$$

Time integration in an implicit manner:

$$\frac{\mathbf{F}^{\mathrm{p}}_{n+1} - \mathbf{F}^{\mathrm{p}}_{n}}{\Delta t} = (\mathbf{L}^{\mathrm{p}}_{\mathrm{I}})_{n+1} \cdot \mathbf{F}^{\mathrm{p}}_{n+1} \,, \tag{3.53}$$

$$\mathbf{F}^{\mathrm{p}}_{n+1} = \left(\mathbf{I} - \Delta t\,(\mathbf{L}^{\mathrm{p}}_{\mathrm{I}})_{n+1}\right)^{-1} \cdot \mathbf{F}^{\mathrm{p}}_{n} \,. \tag{3.54}$$

Using the above equation and $\mathbf{F}_{n+1}$ and $\mathbf{F}^{\mathrm{p}}_{n}$ as input, it is possible to determine $\mathbf{F}^{\mathrm{p}}_{n+1}$ and $\mathbf{F}^{\mathrm{e}}_{n+1}$ using the following strategy:

(i) Initialize:

$$(\tilde{\mathbf{L}}^{\mathrm{p}}_{\mathrm{I}})_{n+1} = (\mathbf{L}^{\mathrm{p}}_{\mathrm{I}})_{n} \,. \tag{3.55}$$

(ii) While $||\mathbf{R}^{\mathrm{p}}|| \geq \varepsilon^{Tol}$ do:

$$\mathbf{F}^{\mathrm{p}}_{n+1} = \left(\mathbf{I} - \Delta t\,(\tilde{\mathbf{L}}^{\mathrm{p}}_{\mathrm{I}})_{n+1}\right)^{-1} \cdot \mathbf{F}^{\mathrm{p}}_{n} \,, \tag{3.56}$$

$$\mathbf{F}^{\mathrm{e}}_{n+1} = \mathbf{F}_{n+1} \cdot \left(\mathbf{F}^{\mathrm{p}}_{n+1}\right)^{-1} \,, \tag{3.57}$$

$$(\mathbf{S}_{\mathrm{I}})_{n+1} = \mathrm{Function}(\mathbf{F}^{\mathrm{e}}_{n+1}) \,, \tag{3.58}$$

$$\mathbf{R}^{\mathrm{p}} = (\tilde{\mathbf{L}}^{\mathrm{p}}_{\mathrm{I}})^{k}_{n+1} - \mathbf{L}^{\mathrm{p}}_{\mathrm{I}}((\mathbf{S}_{\mathrm{I}})_{n+1}) \,, \tag{3.59}$$

$$(\tilde{\mathbf{L}}^{\mathrm{p}}_{\mathrm{I}})^{k+1}_{n+1} = (\tilde{\mathbf{L}}^{\mathrm{p}}_{\mathrm{I}})^{k}_{n+1} - \alpha^{\mathrm{p}} \left(\frac{\partial \mathbf{R}^{\mathrm{p}}}{\partial \tilde{\mathbf{L}}^{\mathrm{p}}_{\mathrm{I}}}\right)^{-1} \mathbf{R}^{\mathrm{p}} \,, \tag{3.60}$$

$$k = k + 1 \,. \tag{3.61}$$

3.3 Rate independent hypoelastic plasticity framework for the macroscale

The numerical aspects required for the simulation of the anisotropic yield behavior of the LPBF316L on the macroscale are discussed in this section. The simulations are conducted using the FEM software Abaqus. The most important topics are divided and explained in different sections for a better understanding of the proposed model.

- The starting point is the formulation of boundary value problem (BVP) and the FEM solver. This aspect of the framework is handled by the employed FEM software Abaqus and is only described briefly in section 3.3.1 for the sake of completeness.

The material constitutive model, on the other hand, is implemented using the user-defined mechanical material behavior (UMAT) interface of the FEM software Abaqus. For the successful implementation of any material model in UMAT, extensive development and testing are inseparable parts of the process. The following sections are chosen and ordered in a way to better distinguish between the different requirements and assumptions needed for formulating the material constitutive model at the macroscale:

- In section 3.3.2, the rate-independent plasticity framework for small strains is presented. This formulation is then expanded upon in the following sections to correctly describe the effects of large deformations and also deal with the different rotations during the simulation. The small strains formulation is chosen as the first building block because the general requirements remain unchanged even for large strains and the further extensions of the model. This approach makes it possible to present the underlying ideas and assumptions in a more clear and compact structure.
- In section 3.3.3, the small strain formulation is expanded upon using a hypoelastic constitutive model. This extended formulation can be safely used for simulations where large deformations occur, including large rotations.
- In section 3.3.4, the numerical aspects for the correct implementation and integration of a hypoelastic constitutive model are handled.
- In section 3.3.5, the Barlat yield function Yld2004-18p is presented, which is an essential part of capturing the anisotropic yield behavior of LPBF316L at the macroscale. Moreover, this particular yield function's first and second derivatives are derived, which are necessary for the numerical implementation in UMAT.
- In section 3.3.6, several different hardening laws are presented, which are required to calculate the yield stress of the material at desired equivalent plastic strain levels.
- In section 3.3.7, the underlying idea behind the texture evolution and its link to different quantities, such as plastic spin tensor $\mathbf{W}^{\mathrm{p}}$, are established. Furthermore, the implementation aspect of the texture evolution is presented, whereby different mathematical expressions are derived.

- In section 3.3.8, the return mapping algorithm and its modification required for the numerical integration of the presented hypoelastic constitutive model are formulated.
- In section 3.3.9, the consistent elasto-plastic tangent operator (CEPT) is derived, which has to be returned as an output variable in UMAT, and is required to preserve the quadratic rate convergence.
- In the last section 3.3.10, the complete numerical scheme implemented in Abaqus UMAT is presented, which makes use of all the building blocks explained in the former sections.

3.3.1 Weak formulation of BVP and the FEM solver

The local form of the conservation law of momentum has been derived in section 3.1. For a quasi-static problem in the current configuration, it reads:

$$\nabla \cdot \boldsymbol{\sigma} = 0\,. \tag{3.62}$$

The principle of virtual work is applied to arrive at the weak formulation of the above equation. In the first step, the eq. (3.62) is multiplied with a compatible displacement field $\delta\tilde{\boldsymbol{u}}$ and integrated over the entire domain Ω:

$$\int\limits_{\Omega} \nabla \cdot \boldsymbol{\sigma}\, \delta\tilde{\boldsymbol{u}}\, \mathrm{d}V = 0\,, \qquad \forall\, \delta\tilde{\boldsymbol{u}} \in \mathbb{V}\,, \tag{3.63}$$

where $\mathbb{V}$ is the space of virtual displacements of the body [132]. Applying the partial integration rule to the eq. (3.63) delivers:

$$-\int\limits_{\Omega} \nabla \cdot \left(\boldsymbol{\sigma}\, \delta\tilde{\boldsymbol{u}}\right)\, \mathrm{d}V + \int\limits_{\Omega} \boldsymbol{\sigma} : \nabla\delta\tilde{\boldsymbol{u}}\, \mathrm{d}V = 0\,, \qquad \forall\, \delta\tilde{\boldsymbol{u}} \in \mathbb{V}\,. \tag{3.64}$$

Using the Gauss theorem, one can convert the first volume integral in the eq. (**??**) into a surface integral:

$$-\oint\limits_{\partial\Omega} \left(\boldsymbol{\sigma} \cdot \boldsymbol{n}\right)\, \delta\tilde{\boldsymbol{u}}\, \mathrm{d}A + \int\limits_{\Omega} \boldsymbol{\sigma} : \nabla\delta\tilde{\boldsymbol{u}}\, \mathrm{d}V = 0\,, \qquad \forall\, \delta\tilde{\boldsymbol{u}} \in \mathbb{V}\,. \tag{3.65}$$

$\boldsymbol{n}_0$ is the normal vector on the surface $\partial\Omega_0$. Furthermore, using the Cauchy relation

$$\boldsymbol{t} = \boldsymbol{\sigma} \cdot \boldsymbol{n}_0\,, \tag{3.66}$$

one can transform the eq. (3.65) to:

$$\int\limits_{\Omega} \boldsymbol{\sigma} : \nabla\delta\tilde{\boldsymbol{u}}\, \mathrm{d}V = \oint\limits_{\partial\Omega} \boldsymbol{t} \cdot \delta\tilde{\boldsymbol{u}}\, \mathrm{d}A\,, \qquad \forall\, \delta\tilde{\boldsymbol{u}} \in \mathbb{V}\,. \tag{3.67}$$

The traction vector $\boldsymbol{t}$ can be used to define the Neumann boundary condition. On the other hand, if the displacement is prescribed, one speaks of the Dirichlet boundary condition. Both these boundary conditions can be present simultaneously if the integrals are separated accordingly using $\partial\Omega = \partial\Omega_\mathrm{N} \cup \partial\Omega_\mathrm{D}$. In a displacement-based FEM, the displacement field is the unknown quantity that has to be determined. The Cauchy stress tensor $\boldsymbol{\sigma}$ in the eq. (3.67) is coupled with the displacement field through the following equation:

$$\boldsymbol{\sigma} = \mathbb{C} : \boldsymbol{\varepsilon}^{\mathrm{e}} = \mathbb{C} : \left(\boldsymbol{\varepsilon} - \boldsymbol{\varepsilon}^{\mathrm{p}}\right) . \tag{3.68}$$

$\boldsymbol{\varepsilon}$, $\boldsymbol{\varepsilon}^{\mathrm{e}}$, $\boldsymbol{\varepsilon}^{\mathrm{p}}$, and $\mathbb{C}$ are the total strain, the elastic part of the strain, the plastic part of the strain, and the elastic stiffness tensor, respectively. It should be noted that the additive decomposition of the total strain is employed for brevity. It is also possible to reformulate the eq. (3.67) using the multiplicative decomposition of the total deformation gradient $\mathbf{F}$. Furthermore, in the case of small deformations, the strain tensor $\boldsymbol{\varepsilon}$ can be calculated as follows [150]:

$$\boldsymbol{E} \approx \boldsymbol{e} \approx \boldsymbol{\varepsilon} = \frac{1}{2}\left(\nabla \boldsymbol{u} + (\nabla \boldsymbol{u})^{\mathrm{T}}\right) = \nabla^{\mathrm{s}} \boldsymbol{u} . \tag{3.69}$$

The small strain is only used to simply show the dependency of the Cauchy stress tensor on the displacement field:

$$\boldsymbol{\sigma} = \boldsymbol{\sigma}\left(\varepsilon(\boldsymbol{u})\right) = \boldsymbol{\sigma}\left(\nabla^{\mathrm{s}} \boldsymbol{u}\right) . \tag{3.70}$$

Thus, the eq. (3.67) reads:

$$\int\limits_{\Omega} \boldsymbol{\sigma}\left(\nabla^{\mathrm{s}} \boldsymbol{u}\right) : \nabla \tilde{\boldsymbol{u}} \, \mathrm{d}V = \oint\limits_{\partial\Omega} \boldsymbol{t} \cdot \delta \tilde{\boldsymbol{u}} \, \mathrm{d}A , \qquad \forall \, \delta \tilde{\boldsymbol{u}} \in \mathbb{V} . \tag{3.71}$$

In the next step, the domain Ω is discretized by replacing the Hilbert space $\mathbb{V}$ with the discrete approximation subset $\mathbb{V}_{\mathrm{h}}$. Furthermore, the ansazt functions

$$\boldsymbol{u}_{\mathrm{h}} = \sum_{j} \boldsymbol{u}_j \varphi_j , \tag{3.72}$$

are employed to approximate the displacements, which are also the unknown quantity. $\{\boldsymbol{u}_j\}$ and $\{\varphi_j\}$ are the vector containing the unknown nodal values and the shape functions, respectively. Using the eq. (3.72) in eq. (3.71) one has:

$$\int\limits_{\Omega_{\mathrm{h}}} \boldsymbol{\sigma}\left(\nabla^{\mathrm{s}} \boldsymbol{u}_{\mathrm{h}}\right) : \nabla \tilde{\boldsymbol{u}}_{\mathrm{h}} \, \mathrm{d}V = \oint\limits_{\partial\Omega_{\mathrm{h}}} \boldsymbol{t} \cdot \delta \tilde{\boldsymbol{u}}_{\mathrm{h}} \, \mathrm{d}A , \qquad \forall \, \delta \tilde{\boldsymbol{u}} \in \mathbb{V}_{\mathrm{h}} . \tag{3.73}$$

It should be noted that in eq. (3.73) the same ansatz function is employed for both $\boldsymbol{u}_{\mathrm{h}}$ and $\delta \tilde{\boldsymbol{u}}$, which is also called the isoparametric formulation [151]. After discretizing the domain, the integral terms in eq. (3.73) have to be numerically evaluated for each element inside the domain. This is usually achieved by using the Gaussian quadratures. After the numerical integration, the global stiffness matrix $\mathbf{K}$ is assembled from the resulting element stiffness $\mathbf{K}^{\mathrm{e}}$. For a linear elastic material the problem reduces to solving the following linear system of algebraic equations [132]:

$$\mathbf{K} \boldsymbol{u} = \boldsymbol{f}^{\mathrm{ext}} . \tag{3.74}$$

$\boldsymbol{u}$ and $\boldsymbol{f}^{\text{ext}}$ are the global nodal displacement vector and the external global force vector, respectively. It should be emphasized that the eq. (3.74) is only valid if the material behavior is linear and path independent. If this is not the case, then one has to resort to the incremental finite element procedure [132]. The Newton-Raphson algorithm is often employed when solving the nonlinear incremental equations since it has a quadratic rate of asymptotic convergence. For this particular method, the discretized incremental equations have to be linearized. Moreover, in each iteration of the Newton-Raphson method, the solution of the linearized equations is obtained. To have a better understanding of this procedure, the required steps are demonstrated in the box 3.1 in a simplified form. These steps are necessary for a FEM software to solve the linearized equations and are repeated in each iteration until the desired solution is obtained. In this work, the macro scale model, which is explained in the following sections, is implemented in the UMAT interface of the software Abaqus. The steps listed in the box 3.1 are not required when working with the UMAT interface. These steps are taken care of by the main program. The displacements are supplied at the beginning of the increment. Only the stresses with the corresponding tangent stiffness operator have to be returned at the end of the increment.

Box. 3.1: Newton-Raphson procedure for solving the nonlinear FEM equations [132]

1. At the beginning of the iteration $k = 0$, the initial displacement values and the resulting residual vector $\boldsymbol{r}$ are calculated using the prescribed load factor λ_{n+1}:

$$\boldsymbol{u}_{n+1}^{(0)} = \boldsymbol{u}_n \,, \qquad \boldsymbol{r} = \boldsymbol{f}^{\text{int}}(\boldsymbol{u}_n) - \lambda_{n+1}\boldsymbol{f}^{\text{ext}}(\boldsymbol{u}_n)\,. \tag{3.75}$$

2. In the next step, the consistent tangent operator is determined:

$$\boldsymbol{D} = \frac{\partial \Delta \boldsymbol{\sigma}}{\partial \Delta \boldsymbol{\varepsilon}} \tag{3.76}$$

3. Using the consistent tangent operator, the element tangent stiffness matrices are calculated and assembled in the global stiffness matrix $\mathbf{K}_{\text{T}}$. For $k = k+1$ the increment for updating the displacement vector is calculated solving the following equation:

$$\mathbf{K}_{\text{T}}\, \delta \boldsymbol{u}^k = -\boldsymbol{r}^{(k-1)} \,, \qquad \boldsymbol{u}_{n+1}^{(k)} = \boldsymbol{u}_{n+1}^{(k-1)} + \boldsymbol{u}^k \,. \tag{3.77}$$

4. Using the new displacement vector $\boldsymbol{u}_{n+1}^{(k)}$ the strains and stresses can be updated. With the updated quantities, the global internal force vector is recalculated. The residual vector is then updated as follows:

$$\boldsymbol{r} = \boldsymbol{f}^{\text{int}} - \lambda_{n+1}\boldsymbol{f}^{\text{ext}}(\boldsymbol{u}_n)\,. \tag{3.78}$$

5. In the last step, the convergence is checked:

$$\text{IF } \frac{||\boldsymbol{r}||}{||\boldsymbol{f}^{\text{ext}}||} \leq \varepsilon_{\text{tol}} \text{ THEN } (.)_{n+1} = (.)_{n+1}^{k} \text{ ELSE GOTO } 2\,. \tag{3.79}$$

3.3.2 Rate independent plasticity framework

To mathematically describe the plastic deformation of a material on the macroscale certain assumptions have to be made. This is where the theory of plasticity comes into play. The framework employed in this work can be used to model the plastic deformation of materials for which the rate of the deformation does not affect the end results. The term rate-independent is used to describe such material models. Under certain conditions which also apply to LPBF316L in this work, metals, concrete, rocks, clays, and soils can usually be modeled using this framework. The most important phenomenological aspects are as follows [132]:

1. All stresses which do not cause any plastic deformation belong to the elastic domain. The yield surface of the material encloses this so-called elastic domain.

2. Stresses outside of the elastic domain or the yield surface cause plastic deformation. This is also called plastic yielding, which further causes the plastic strains to evolve.
3. As a consequence of the plastic deformation and evolution of plastic strains, the yield surface changes its shape. This phenomenon can be modeled using an appropriate hardening rule.

As evident from the assumptions listed above, unlike the CP model in section 3.2.3, the underlying microphysical causes are not of importance when using these phenomenological models. To have a better understanding of such a phenomenological framework, it is easier to start with the small strain formulation, see box 3.2.

Box. 3.2: Small strain rate-independent plasticity framework [132].

1. In this framework the total strain is additively decomposed into its elastic and plastic part:

$$\boldsymbol{\varepsilon} = \boldsymbol{\varepsilon}^{\mathrm{e}} + \boldsymbol{\varepsilon}^{\mathrm{p}}\,. \tag{3.80}$$

The above equation can also be written in its rate form:

$$\dot{\boldsymbol{\varepsilon}} = \dot{\boldsymbol{\varepsilon}}^{\mathrm{e}} + \dot{\boldsymbol{\varepsilon}}^{\mathrm{p}}\,. \tag{3.81}$$

2. Following on, the next assumption is that there exists a free energy ψ which is a function of total strain and a set of hardening internal variables $\boldsymbol{\alpha}$ (including the plastic strain). This free energy potential can be used to determine the contribution of elastic deformation ψ^{e} and of plastic deformation through hardening ψ^{p}. Furthermore, using the Clausius-Duhem inequality and the framework of thermodynamics, a general elastic law, and the plastic dissipation function can be derived. Moreover, the constitutive equations for the Cauchy stress $\boldsymbol{\sigma}$ and the hardening thermodynamic forces $\boldsymbol{A}$ become:

$$\boldsymbol{\sigma} = \bar{\rho}\frac{\partial\psi}{\partial\boldsymbol{\varepsilon}^{\mathrm{e}}}\,, \qquad \boldsymbol{A} = \bar{\rho}\frac{\partial\psi}{\partial\boldsymbol{\alpha}}\,. \tag{3.82}$$

3. As explained before, a yield function $\Phi(\boldsymbol{\sigma}, \boldsymbol{A})$ can be used to determine if plastic deformation has occurred. This yield function is negative for any possible elastic deformation and reaches zero on the onset of plastic flow. This yield function Φ can be used to define the yield locus as a hypersurface in the space of stresses. The hypersurface is also called the yield surface and is determined through:

$$\Phi(\boldsymbol{\sigma}, \boldsymbol{A}) = 0\,. \tag{3.83}$$

4. To completely characterize the general plasticity framework, evolution laws are required for the internal variables, which describe the hardening behavior

of the yield function and are responsible for the energy dissipation. The evolution laws include the plastic flow rule and the hardening law:

$$\dot{\boldsymbol{\varepsilon}}^{\mathrm{p}} = \dot{\gamma}\boldsymbol{N}(\boldsymbol{\sigma}, \boldsymbol{A})\,, \qquad \dot{\boldsymbol{\alpha}} = \dot{\gamma}\boldsymbol{H}(\boldsymbol{\sigma}, \boldsymbol{A})\,. \tag{3.84}$$

$\dot{\gamma}$, $\boldsymbol{N}$, and $\boldsymbol{H}$ are the plastic multiplier, the flow vector, and the generalized hardening modulus, respectively. It is often postulated that $\boldsymbol{N}$ and $\boldsymbol{H}$ can be determined using a flow potential $\Psi(\boldsymbol{\sigma}, \boldsymbol{A})$ which is required to be a non-negative convex function of its arguments:

$$\boldsymbol{N} = \frac{\partial \Psi}{\partial \boldsymbol{\sigma}}\,, \qquad \boldsymbol{H} = -\frac{\partial \Psi}{\partial \boldsymbol{A}}\,. \tag{3.85}$$

In this work, the associative plasticity framework will be used. In this case, the yield function Φ serves also as the flow potential:

$$\Phi = \Psi\,. \tag{3.86}$$

5. With the following loading/unloading conditions, it is possible to determine when the plastic deformation occurs:

$$\Phi \leq 0\,, \qquad \dot{\gamma} \geq 0 \qquad \Phi\dot{\gamma} = 0\,. \tag{3.87}$$

6. It should be noted that during plastic flow, the value of the yield function remains constant $\Phi = 0$. Using this observation, it is possible to formulate the following complementary condition:

$$\dot{\Phi}\dot{\gamma} = 0\,. \tag{3.88}$$

The above equation implicates that the rate of Φ becomes zero during plastic deformation $(\dot{\gamma}) \neq 0$:

$$\dot{\Phi} = 0\,. \tag{3.89}$$

This is also called the consistency condition and can be used for the determination of the plastic multiplier:

$$\dot{\Phi} = \frac{\partial \Phi}{\partial \boldsymbol{\sigma}} : \dot{\boldsymbol{\sigma}} + \frac{\partial \Phi}{\partial \boldsymbol{A}} * \dot{A}\,. \tag{3.90}$$

3.3.3 Hypoelastic plasticity models

In the last section, the basic building blocks of the plasticity framework were introduced. However, the equations derived in the previous section are appropriate for applications where the strains are small. One of the goals in this work is modeling the anisotropic yield behavior for large deformations. For this purpose, the small strain framework has to be modified. This is where finite strain elastoplasticity comes into play, which is the extension of the infinitesimal elastoplasticity described in the last section. In the finite strain elastoplasticity framework, two different approaches are available for modeling the plastic deformation, namely hypoelastic and hyperelastic models. For both of them, the primary underlying assumption is that the total deformation gradient can be multiplicatively decomposed into elastic and plastic parts, as explained in section 3.1. With this decomposition, it is assumed that a local unstressed configuration exists, which can be mapped by the plastic part of the deformation gradient $\mathbf{F}^{\mathrm{p}}$. This concept fails in reality for multiaxially deformed bodies that have been plastically deformed. Compatible unstressed configurations can not be found for all points inside such a body. To have a better understanding of the implications of the multiplicative decomposition for the modeling of the plastic deformation, it is useful to start with the decomposition of the velocity gradient $\mathbf{L}$:

$$\mathbf{L} = \dot{\mathbf{F}}^{\mathrm{e}} \cdot \mathbf{F}^{\mathrm{e}-1} + \mathbf{F}^{\mathrm{e}} \cdot \dot{\mathbf{F}}^{\mathrm{p}} \cdot \mathbf{F}^{\mathrm{p}-1} \cdot \mathbf{F}^{\mathrm{e}-1} = \mathbf{L}^{\mathrm{e}} + \mathbf{F}^{\mathrm{e}} \cdot \mathbf{L}_{\mathrm{I}}^{\mathrm{p}} \cdot \mathbf{F}^{\mathrm{e}-1} \,. \tag{3.91}$$

Most often, the formulation of the plastic flow rule is achieved by using the plastic part of the velocity gradient $\mathbf{L}_{\mathrm{I}}^{\mathrm{p}}$, which can also be decomposed into its symmetric and anti-symmetric components:

$$\mathbf{D}_{\mathrm{I}}^{\mathrm{p}} = \operatorname{sym}\left[\mathbf{L}_{\mathrm{I}}^{\mathrm{p}}\right] , \qquad \mathbf{W}_{\mathrm{I}}^{\mathrm{p}} = \operatorname{skew}\left[\mathbf{L}_{\mathrm{I}}^{\mathrm{p}}\right] \,. \tag{3.92}$$

$\mathbf{D}_{\mathrm{I}}^{\mathrm{p}}$ and $\mathbf{W}_{\mathrm{I}}^{\mathrm{p}}$ are also called the plastic stretching (or rate of plastic deformation) and the plastic spin tensor, respectively. $\mathbf{D}_{\mathrm{I}}^{\mathrm{p}}$ describes the instantaneous rate of plastic straining in the intermediate configuration. $\mathbf{W}_{\mathrm{I}}^{\mathrm{p}}$, on the other hand, is the instantaneous rate of rigid rotation of the intermediate configuration, which is most often ignored during the modeling of metal plasticity at the macroscale, see section 3.3.7. A hyperelastic-based elastoplastic material model can be postulated using [132]:

1. A free energy potential, which is used to derive the hyperelastic law and calculate the stresses resulting from the elastic strains.
2. A yield function, which encloses the elastic domain.
3. A dissipation potential to define the plastic flow rule and the evolution equations necessary for the internal variables.

The hypoelastic constitutive models, on the other hand, do not require a free-energy potential to model the elastic behavior of the material, which drastically reduces the complexity of the modeling aspect. This is the main reason for the adoption of such models in this work. Moreover, the equations are formulated using objective stress rates. However, these models require special care to preserve the objectivity of the rate forms. One of the most critical modeling aspects for these models is the definition of objective stress rates. A stress rate is called objective if under a change of observer, the following relation holds:

$$\overset{\bullet}{\boldsymbol{\sigma}} = \mathbf{Q} \cdot \overset{\bullet}{\boldsymbol{\sigma}} \cdot \mathbf{Q}^{\mathrm{T}} \,. \tag{3.93}$$

In this context, the material time derivative of the Cauchy stress tensor does not satisfy this condition and is thus, not an objective stress rate:

$$\dot{\boldsymbol{\sigma}} = \mathbf{Q} \cdot \dot{\boldsymbol{\sigma}} \cdot \mathbf{Q}^{\mathrm{T}} + \dot{\mathbf{Q}} \cdot \boldsymbol{\sigma} \cdot \mathbf{Q}^{\mathrm{T}} + \mathbf{Q} \cdot \boldsymbol{\sigma} \cdot \dot{\mathbf{Q}}^{\mathrm{T}} . \tag{3.94}$$

The material objectivity is satisfied if the material constitutive model is postulated using the objective stress rates. Many different objective stress rates exist. Some of these rates are more suitable for certain applications. In this work, the Jaumann rate of Cauchy stress tensor $\overset{\triangledown}{\boldsymbol{\sigma}}$ is used, which satisfies the objectivity condition [132]:

$$\overset{\triangledown}{\boldsymbol{\sigma}} = \dot{\boldsymbol{\sigma}} - \mathbf{W} \cdot \boldsymbol{\sigma} + \boldsymbol{\sigma} \cdot \mathbf{W} , \qquad \mathbf{W} = \operatorname{skew}[\mathbf{L}] . \tag{3.95}$$

$\mathbf{W}$ is called the spin tensor and is the antisymmetric part of the velocity gradient $\mathbf{L}$. With the objective stress rate, it is then possible to formulate a hypoelastic-based plasticity model, which takes the following form:

$$\overset{\triangledown}{\boldsymbol{\sigma}} = \mathbb{C} : (\mathbf{D} - \mathbf{D}^{\mathrm{p}}) . \tag{3.96}$$

Interestingly, the above equation closely resembles the small strain formulation shown in the eq. (3.68), which clearly shows the similarity between these two models. Furthermore, the rate of plastic deformation is usually calculated using the following flow rule, see box 3.2:

$$\mathbf{D}^{\mathrm{p}} = \dot{\gamma} \frac{\partial \Phi}{\partial \boldsymbol{\sigma}} , \qquad \dot{\boldsymbol{\alpha}} = \dot{\gamma} \boldsymbol{H}(\boldsymbol{\sigma}, \boldsymbol{A}) . \tag{3.97}$$

There is still one big problem remaining. By requiring the eq. (3.96) to satisfy the frame indifference, it forces the elastic tensor $\mathbb{C}$ to become isotropic [134]. Motivated by this strong limitation, the model is reformulated in a rotated configuration, which results in a rotating CCO. The resulting formulation removes the restriction to isotropy and improves the numerical stability. The new formulation has been adopted by several commercial FE softwares [134] and is explained in detail in the next section. The modified equations are as follows:

$$\dot{\hat{\boldsymbol{\sigma}}} = \mathbb{C} : \left[\hat{\mathbf{D}} - \hat{\mathbf{D}}^{\mathrm{p}}\right] , \qquad \hat{\boldsymbol{\sigma}} = \mathbf{R} \cdot \boldsymbol{\sigma} \cdot \mathbf{R}^{\mathrm{T}} , \qquad \hat{\mathbf{D}} = \mathbf{R} \cdot \mathbf{D} \cdot \mathbf{R}^{\mathrm{T}} ,$$

$$\hat{\mathbf{D}}^{\mathrm{p}} = \dot{\gamma} \frac{\partial \Phi}{\partial \hat{\boldsymbol{\sigma}}} , \qquad \dot{\boldsymbol{\alpha}} = \dot{\gamma} \hat{\boldsymbol{H}} . \tag{3.98}$$

The formulation of the constitutive model in a rotating CCO is directly coupled with the choice of the objective stress rate since it determines the calculation of the rotation matrix $\mathbf{R}$ in the above equation. For example, if the Jaumann rate of Cauchy stress tensor $\overset{\triangledown}{\boldsymbol{\sigma}}$ is used, then the rotation matrix is calculated using the spin tensor $\mathbf{W}$, which is explained in detail in the next section. Rotation matrices for other rate measures, such as Green-Naghdi, are calculated using other quantities. In summary, two approaches are available, which are closely related to each other. One makes use of an objective stress rate such as $\overset{\triangledown}{\boldsymbol{\sigma}}$ in a global CCO with the restriction of isotropic elastic stiffness tensor $\mathbb{C}$.

In the other approach, a locally rotating CCO is chosen to remove this restriction. More importantly, the rotating CCO is determined based on chosen objective stress rate.

It should be noted that choosing the appropriate objective stress rate is not an easy task. For example, for specific problems and in certain conditions, the Jaumann rate of the Cauchy stress tensor can result in spurious stress oscillations. Irrespective of the chosen objective stress rates, some limitations and drawbacks remain. However, most of these inconsistencies and problems occur when the elastic part of the deformation becomes very large and thus, can be ignored when dealing with the plastic deformation of metals since in metal plasticity, the arising elastic deformations remain much lower compared to the plastic part deformation. More importantly, the objective stress rates can not be swapped with each other and should not be compared together using the same parameters for the constitutive material model since each of the objective stress rates define, in fact, a unique material model with different behavior [132, 134].

3.3.4 Incrementally objective integration algorithm

The most important step when dealing with a hypoelastic constitutive model is the definition of an objective integration algorithm, where constitutive equations are transformed into their correct incremental forms. Objectivity and incremental objectivity should be separated from each other. The eq. (3.96) is objective. However, using the wrong framework for integrating the stress rates will result in an algorithm that does not satisfy the requirements of incremental objectivity, see [132, 134]. The possible solutions when dealing with this issue are described in [134]. In this work, the local rotated representation is adopted. The underlying idea is as follows:

1. First, the evolution equations are formulated in a constructed locally rotating CCO, where the rotated quantities all satisfy the objectivity condition and remain unchanged under superposed rigid body motion. The rotational speed of this particular coordinate system has to be chosen in a way to ensure the objectivity of the rotated quantities.
2. In the second step, the constitutive equations are integrated using the rotated quantities.

As explained in [134], this approach is suited when employing a rotational-like objective stress rate, such as the Jaumann rate of the Cauchy stress tensor. The crucial aspect of this approach is the determination of the local rotated configuration, which can be achieved by solving the following initial value problem:

$$\dot{\mathbf{R}} = \mathbf{W} \cdot \mathbf{R} \qquad \text{with} \qquad \mathbf{R}|_{t=0} = \mathbf{I}\,. \tag{3.99}$$

The above equation is formulated using the spin tensor $\mathbf{W}$ suited for the Jaumann rate. After determining the tensor $\mathbf{R}$ the stress and strain tensors can be rotated:

$$\hat{\boldsymbol{\sigma}} = \mathbf{R}^{\mathrm{T}} \cdot \boldsymbol{\sigma} \cdot \mathbf{R}\,, \qquad \hat{\mathbf{D}} = \mathbf{R}^{\mathrm{T}} \cdot \mathbf{D} \cdot \mathbf{R}\,. \tag{3.100}$$

Using the rotated quantities, it can be shown that:

$$\dot{\hat{\boldsymbol{\sigma}}} = \mathbf{R}^{\mathrm{T}} \cdot [\dot{\boldsymbol{\sigma}} + \boldsymbol{\sigma} \cdot \mathbf{W} - \mathbf{W} \cdot \boldsymbol{\sigma}] \cdot \mathbf{R} = \mathbf{R}^{\mathrm{T}} \cdot \overset{\triangledown}{\boldsymbol{\sigma}} \cdot \mathbf{R}\,. \tag{3.101}$$

Thus, the eq. (3.96) can be rewritten in the following form inside the elastic domain:

$$\dot{\hat{\boldsymbol{\sigma}}} = \mathbb{C} : \hat{\mathbf{D}}\,. \tag{3.102}$$

The eq. (3.102) is rigid motion insensitive and satisfies the objectivity requirements [132, 134]. Thus, this concludes the first step, where the equations are formulated in a locally rotating coordinate system. In the second step, the integration algorithm is formulated using the eq. (3.102). It should be noted that by employing this approach, it is automatically assumed that the microstructure and the related properties of each material point rotate with the locally constructed coordinate system. This is evident from the fact that the elastic stiffness tensor $\mathbb{C}$ remains unaltered in the eq. (3.102). The implications, limitations, and extension of this assumption will be discussed in detail in section 3.3.7. Following step two, the eq. (3.102) is integrated applying the midpoint rule

$$\hat{\boldsymbol{\sigma}}_{n+1} = \hat{\boldsymbol{\sigma}}_n + \Delta t\, \mathbb{C} : \hat{\mathbf{D}}_{n+\frac{1}{2}}\,, \tag{3.103}$$

with

$$\hat{\boldsymbol{\sigma}}_{n+1} = \mathbf{R}^{\mathrm{T}}_{n+1} \cdot \boldsymbol{\sigma}_{n+1} \cdot \mathbf{R}_{n+1}\,, \quad \hat{\boldsymbol{\sigma}}_n = \mathbf{R}^{\mathrm{T}}_n \cdot \boldsymbol{\sigma}_n \cdot \mathbf{R}_n\,, \quad \hat{\mathbf{D}}_{n+\alpha} = \mathbf{R}^{\mathrm{T}}_{n+\frac{1}{2}} \cdot \mathbf{D}_{n+\frac{1}{2}} \cdot \mathbf{R}_{n+\frac{1}{2}}\,. \tag{3.104}$$

The rotation tensors $\mathbf{R}_n$, $\mathbf{R}_{n+\frac{1}{2}}$, and $\mathbf{R}_{n+1}$ are calculated using the exponential map integrators [132, 134]:

$$\mathbf{R}_{n+\frac{1}{2}} = \exp\left[\frac{\Delta t}{2}\mathbf{W}_{n+\frac{1}{2}}\right] \cdot \mathbf{R}_n\,, \qquad \mathbf{R}_{n+1} = \exp\left[\Delta t \mathbf{W}_{n+\frac{1}{2}}\right] \cdot \mathbf{R}_n\,. \tag{3.105}$$

$\mathbf{R}_n$ is equal to the identity matrix $\mathbf{I}$ in the first iteration, see eq. (3.99). Since $\mathbf{W}$ is an antisymmetric tensor, then the exponential map can be numerically evaluated using the Rodrigues formula [132]:

$$\exp\left[\mathbf{W}\right] = \mathbf{I} + \frac{\sin\left(||\boldsymbol{x}||\right)}{||\boldsymbol{x}||}\mathbf{W} + \frac{1}{2}\left[\frac{\sin\left(||\boldsymbol{x}||\right)}{||\boldsymbol{x}||}\right]^2 \mathbf{W}^2\,. \tag{3.106}$$

It should be noted that the rotation tensors $\mathbf{R}$ are sometimes approximated using the Hughes-Winget algorithm. This is the case in the software Abaqus. In the Hughes-Winget algorithm, the exponential map is approximated as follows:

$$\exp\left[\frac{\Delta t}{2}\mathbf{W}_{n+\frac{1}{2}}\right] \approx \left[\mathbf{I} + \frac{\Delta t}{2}\mathbf{W}_{n+\frac{1}{2}}\right]\,, \quad \exp\left[-\frac{\Delta t}{2}\mathbf{W}_{n+\frac{1}{2}}\right]^{-1} \approx \left[\mathbf{I} - \frac{\Delta t}{2}\mathbf{W}_{n+\frac{1}{2}}\right]^{-1}\,. \tag{3.107}$$

By multiplying the above expressions, the relative rotation between two increments can then be calculated according to the Hughes-Winget algorithm:

$$\tilde{\mathbf{R}}_{\Delta} = \left[\mathbf{I} - \frac{\Delta t}{2}\mathbf{W}_{n+\frac{1}{2}}\right]^{-1} \cdot \left[\mathbf{I} + \frac{\Delta t}{2}\mathbf{W}_{n+\frac{1}{2}}\right]\,. \tag{3.108}$$

This, in turn, is used in the software Abaqus for the integration algorithm:

$$\boldsymbol{\sigma}_{n+1} = \tilde{\mathbf{R}}_\Delta \cdot \boldsymbol{\sigma}_n \cdot \tilde{\mathbf{R}}_\Delta^{\mathrm{T}} + \Delta t \, \mathbb{C} : \mathbf{D}_{n+\frac{1}{2}} \, . \tag{3.109}$$

The approximation used in Abaqus is not sufficient for the approach employed in this work. Thus, the eq. (3.109) is used to correct the input quantities supplied by the software.

3.3.5 Anisotropic yield functions

Modeling the anisotropic yield behavior of the LPBF316L is one of the most critical aspects of this work. On the micro-mechanical scale, this was achieved by employing a CP model, see section 3.2.3. However, it is not feasible to use a CP model to conduct simulations on the macroscale since the computational cost is very high. That is the reason why the micro-mechanical models usually employ a RVE. Analytical yield functions are a possible solution for this limitation [86,88,139]. There are many different analytical yield functions available to choose from [78]. A Barlat yield function [76] is employed in this work, which is often used when dealing with aluminum alloys. It can accurately capture the shape of the yield surface, and its first and second derivatives are also known, which makes the numerical implementation less cumbersome. One of the features of this model is that the formulation is based on the principal stresses. Furthermore, this model is suited when working with an associated flow rule [152] since the plastic flow direction can be calculated using the first derivatives available in analytical form. The hardening law is not included in this model and can be chosen separately. The Barlat yield function Yld2004-18p is a homogeneous function of degree one and is defined as follows:

$$f\left(\boldsymbol{\sigma}, \bar{\varepsilon}^{\mathrm{p}}\right) = \Phi\left(\boldsymbol{\sigma}\right) - \sigma_{\mathrm{y}}\left(\bar{\varepsilon}^{\mathrm{p}}\right) \, . \tag{3.110}$$

$\boldsymbol{\sigma}$, $\bar{\varepsilon}^{\mathrm{p}}$, Φ, and σ_{y} are the Cauchy stress tensor, equivalent plastic strain, Barlat effective stress, and the hardening function, respectively. The Barlat yield function Yld2004-18p, which defines the yield surface, has 18 parameters. Two necessary linear transformations on the deviator $\mathbf{s}$ of the Cauchy stress tensor $\boldsymbol{\sigma}$ are needed to incorporate the parameters into the model:

$$\mathbf{s}' = \mathbf{C}' : \mathbf{s} \, , \qquad \mathbf{s}'' = \mathbf{C}'' : \mathbf{s} \, , \qquad \mathbf{s} = \sigma - \frac{1}{3}(\mathbf{I} : \sigma)\mathbf{I}. \tag{3.111}$$

By employing these transformations, the components of the deviatoric part of the stress tensor $\mathbf{s}$ can be weighted differently, by which the anisotropic yield surface can be represented. By using the Voigt notation, the fourth-order tensors $\mathbf{C}'$ and $\mathbf{C}''$ can be written in the following form:

$$\mathbf{C}' = \begin{bmatrix} 0 & -c'_{12} & -c'_{13} & 0 & 0 & 0 \\ -c'_{21} & 0 & -c'_{23} & 0 & 0 & 0 \\ -c'_{31} & -c'_{32} & 0 & 0 & 0 & 0 \\ 0 & 0 & 0 & c'_{44} & 0 & 0 \\ 0 & 0 & 0 & 0 & c'_{55} & 0 \\ 0 & 0 & 0 & 0 & 0 & c'_{66} \end{bmatrix} , \tag{3.112}$$

and

$$\mathbf{C}'' = \begin{bmatrix} 0 & -c''_{12} & -c''_{13} & 0 & 0 & 0 \\ -c''_{21} & 0 & -c''_{23} & 0 & 0 & 0 \\ -c''_{31} & -c''_{32} & 0 & 0 & 0 & 0 \\ 0 & 0 & 0 & c''_{44} & 0 & 0 \\ 0 & 0 & 0 & 0 & c''_{55} & 0 \\ 0 & 0 & 0 & 0 & 0 & c''_{66} \end{bmatrix} . \tag{3.113}$$

With the transformed tensors $\mathbf{s}'$ and $\mathbf{s}''$, the effective stress can be calculated:

$$\begin{aligned} \Phi(\boldsymbol{\sigma}) = & \left\{ \frac{1}{4} \Big[|s'_1 - s''_1|^a + |s'_1 - s''_2|^a + |s'_1 - s''_3|^a + |s'_2 - s''_1|^a + \right. \\ & \left. |s'_2 - s''_2|^a + |s'_2 - s''_3|^a + |s'_3 - s''_1|^a + |s'_3 - s''_2|^a + |s'_3 - s''_3|^a \Big] \right\}^{1/a} . \end{aligned} \tag{3.114}$$

where s'_i and s''_j $(i, j = 1, 2, 3)$ are the principal values of tensors $\mathbf{s}'$ and $\mathbf{s}''$. The exponent a is often chosen to be 8 for FCC crystals. To calculate the first and second derivatives of the Barlat yield function Yld2004-18p, in the first step, two fourth-order tensors, $\mathbf{L}'$ and $\mathbf{L}''$, are defined, which map the Cauchy stress tensor to the transformed deviatoric tensors:

$$\mathbf{L}' = \mathbf{C}' : \Pi , \quad \mathbf{L}'' = \mathbf{C}'' : \Pi \quad \text{with} \quad \Pi_{ijkl} = \frac{1}{2} \left(\delta_{ik}\delta_{jl} + \delta_{il}\delta_{jk} \right) - \frac{1}{3}\delta_{ij}\delta_{kl} . \tag{3.115}$$

The first derivative of the yield function is obtained by employing the chain rule [153]:

$$\frac{\partial \Phi}{\partial \boldsymbol{\sigma}} = \sum_{i=1}^{3} \left(\frac{\partial \Phi}{\partial s'_i} \frac{\partial s'_i}{\partial \mathbf{s}'} : \mathbf{L}' + \frac{\partial \Phi}{\partial s''_i} \frac{\partial s''_i}{\partial \mathbf{s}''} : \mathbf{L}'' \right) . \tag{3.116}$$

By using the relations

$$\frac{\partial s'_i}{\partial \mathbf{s}'} = \hat{\boldsymbol{e}}'_i \otimes \hat{\boldsymbol{e}}'_i \qquad \text{and} \qquad \frac{\partial s''_i}{\partial \mathbf{s}''} = \hat{\boldsymbol{e}}''_i \otimes \hat{\boldsymbol{e}}''_i , \tag{3.117}$$

where there is no summation over the repeated indices, the first derivative can be written as:

$$\frac{\partial \Phi}{\partial \boldsymbol{\sigma}} = \sum_{i=1}^{3} \left(\frac{\partial \Phi}{\partial s'_i} \left(\hat{\boldsymbol{e}}'_i \otimes \hat{\boldsymbol{e}}'_i \right) : \mathbf{L}' + \frac{\partial \Phi}{\partial s''_i} \left(\hat{\boldsymbol{e}}''_i \otimes \hat{\boldsymbol{e}}''_i \right) : \mathbf{L}'' \right) . \tag{3.118}$$

The second derivative is obtained by continuing the chain rule:

$$\begin{aligned} \frac{\partial^2 \Phi}{\partial \boldsymbol{\sigma} \partial \boldsymbol{\sigma}} = & \sum_{i=1}^{3} \left\{ \sum_{i=1}^{3} \Bigg[\right. \\ & \frac{\partial^2 \Phi}{\partial s'_i \partial s'_j} \left(\frac{\partial s'_i}{\partial \boldsymbol{s}'} : \mathbf{L}' \right) \otimes \left(\frac{\partial s'_j}{\partial \boldsymbol{s}'} : \mathbf{L}' \right) + \frac{\partial^2 \Phi}{\partial s''_i \partial s''_j} \left(\frac{\partial s''_i}{\partial \mathbf{s}''} : \mathbf{L}'' \right) \otimes \left(\frac{\partial s''_j}{\partial \mathbf{s}''} : \mathbf{L}'' \right) \\ & + \frac{\partial^2 \Phi}{\partial s'_i \partial s''_j} \left(\frac{\partial s'_i}{\partial \mathbf{s}'} : \mathbf{L}' \right) \otimes \left(\frac{\partial s''_j}{\partial \mathbf{s}''} : \mathbf{L}'' \right) + \frac{\partial^2 \Phi}{\partial s''_i \partial s'_j} \left(\frac{\partial s''_i}{\partial \mathbf{s}''} : \mathbf{L}'' \right) \otimes \left(\frac{\partial s'_j}{\partial \mathbf{s}'} : \mathbf{L}' \right) \Bigg] \\ & \left. + \frac{\partial \Phi}{\partial s'_i} \left(\mathbf{L}'^{\mathrm{T}} : \frac{\partial^2 s'_i}{\partial \mathbf{s}' \partial \mathbf{s}'} : \mathbf{L}' \right) + \frac{\partial \Phi}{\partial s''_i} \left(\mathbf{L}''^{\mathrm{T}} : \frac{\partial^2 s''_i}{\partial \mathbf{s}'' \partial \mathbf{s}''} : \mathbf{L}'' \right) \right\} . \end{aligned} \tag{3.119}$$

To avoid numerical overflow, the effective stress is evaluated after scaling the principal stresses with the von Mises stress $\bar{\sigma}_{\mathrm{vm}}$ [153]:

$$\bar{s}_i' = \frac{s_i'}{\bar{\sigma}_{\mathrm{vm}}}\,, \qquad \bar{s}_i'' = \frac{s_i''}{\bar{\sigma}_{\mathrm{vm}}}\,,$$

$$\begin{aligned}\Phi\left(\boldsymbol{\sigma}\right) =& \bar{\sigma}_{\mathrm{vm}}\Bigg\{\frac{1}{4}\Big[\left|\bar{s}_1' - \bar{s}_1''\right|^a + \left|\bar{s}_1' - \bar{s}_2''\right|^a + \left|\bar{s}_1' - \bar{s}_3''\right|^a + \left|\bar{s}_2' - \bar{s}_1''\right|^a + \\ & \left|\bar{s}_2' - \bar{s}_2''\right|^a + \left|\bar{s}_2' - \bar{s}_3''\right|^a + \left|\bar{s}_3' - \bar{s}_1''\right|^a + \left|\bar{s}_3' - \bar{s}_2''\right|^a + \left|\bar{s}_3' - \bar{s}_3''\right|^a\Big]\Bigg\}^{1/a}\,. \end{aligned} \tag{3.120}$$

For the calculation of the derivatives, the principal stresses are scaled with the effective stress Φ, and it is assumed that $a \geq 4$ to eliminate the possible singularities [153]:

$$\tilde{s}_i' = \frac{s_i'}{\Phi}\,, \qquad \tilde{s}_i'' = \frac{s_i''}{\Phi}\,,$$

$$\begin{aligned}\frac{\partial \Phi}{\partial s_1'} &= \frac{1}{4}\left[\left(\tilde{s}_1' - \tilde{s}_1''\right)\left|\tilde{s}_1' - \tilde{s}_1''\right|^{a-2} + \left(\tilde{s}_1' - \tilde{s}_2''\right)\left|\tilde{s}_1' - \tilde{s}_2''\right|^{a-2} + \left(\tilde{s}_1' - \tilde{s}_3''\right)\left|\tilde{s}_1' - \tilde{s}_3''\right|^{a-2}\right]\,,\\ \frac{\partial^2 \Phi}{\partial s_1' \partial s_1'} &= \frac{a-1}{\Phi}\left\{\frac{1}{4}\left[\left|\tilde{s}_1' - \tilde{s}_1''\right|^{a-2} + \left|\tilde{s}_1' - \tilde{s}_2''\right|^{a-2} + \left|\tilde{s}_1' - \tilde{s}_3''\right|^{a-2}\right] - \frac{\partial \Phi}{\partial s_1'}\frac{\partial \Phi}{\partial s_1'}\right\}\,,\\ \frac{\partial^2 \Phi}{\partial s_1' \partial s_2'} &= -\frac{a-1}{\Phi}\frac{\partial \Phi}{\partial s_1'}\frac{\partial \Phi}{\partial s_2'}\,,\\ \frac{\partial^2 \Phi}{\partial s_1' \partial s_1''} &= \frac{a-1}{\Phi}\left\{-\frac{1}{4}\left|\tilde{s}_1' - \tilde{s}_1''\right|^{a-2} - \frac{\partial \Phi}{\partial s_1'}\frac{\partial \Phi}{\partial s_1''}\right\}\,,\end{aligned}$$

$$\begin{aligned}\sum_{i=1}^{3}\frac{\partial \Phi}{\partial s_i'}\frac{\partial^2 s_i'}{\partial \mathbf{s}' \partial \mathbf{s}'} =& \frac{1}{2}\Bigg[\frac{\partial \Phi/\partial s_1' - \partial \Phi/\partial s_2'}{s_1' - s_2'}\tilde{\mathbf{E}}_{1212} + \frac{\partial \Phi/\partial s_2' - \partial \Phi/\partial s_3'}{s_2' - s_3'}\tilde{\mathbf{E}}_{2323}\\ & + \frac{\partial \Phi/\partial s_3' - \partial \Phi/\partial s_1'}{s_3' - s_1'}\tilde{\mathbf{E}}_{3131}\Bigg]\,,\end{aligned} \tag{3.121}$$

with

$$\begin{aligned}\tilde{\mathbf{E}}_{1212} =& \hat{\boldsymbol{e}}_1' \otimes \hat{\boldsymbol{e}}_2' \otimes \hat{\boldsymbol{e}}_1' \otimes \hat{\boldsymbol{e}}_2' + \hat{\boldsymbol{e}}_1' \otimes \hat{\boldsymbol{e}}_2' \otimes \hat{\boldsymbol{e}}_2' \otimes \hat{\boldsymbol{e}}_1'\\ & + \hat{\boldsymbol{e}}_2' \otimes \hat{\boldsymbol{e}}_1' \otimes \hat{\boldsymbol{e}}_1' \otimes \hat{\boldsymbol{e}}_2' + \hat{\boldsymbol{e}}_2' \otimes \hat{\boldsymbol{e}}_1' \otimes \hat{\boldsymbol{e}}_2' \otimes \hat{\boldsymbol{e}}_1'\,.\end{aligned} \tag{3.122}$$

All other components are calculated similarly. For the case $s_1' = s_2'$, the singularity is eliminated by taking the limit as $s_1' \to s_2'$ [153]:

$$\lim_{s_1' \to s_2'}\left[\frac{\partial \Phi/\partial s_1' - \partial \Phi/\partial s_2'}{s_1' - s_2'}\right] = \frac{\partial^2 \Phi}{\partial s_1' \partial s_1'} - \frac{\partial^2 \Phi}{\partial s_1' \partial s_2'}\,. \tag{3.123}$$

3.3.6 Hardening law

The Barlat yield function Yld2004-18p is not sufficient on its own to capture the anisotropic yield behavior of LPBF316L. A separate hardening law is required to calculate the yield stress of the material at any given equivalent plastic strain level. Depending on the hardening behavior of the material observed during tensile tests, different hardening laws can be employed for modeling purposes. Three of the commonly used models are as follows [154]:

- Swift model:

  $$\sigma_{\mathrm{y}}\left(\bar{\varepsilon}^{\mathrm{p}}\right)=K\left(\varepsilon_0+\bar{\varepsilon}^{\mathrm{p}}\right)^n \ , \tag{3.124}$$

  $$\frac{\partial \sigma_{\mathrm{y}}\left(\bar{\varepsilon}^{\mathrm{p}}\right)}{\partial \bar{\varepsilon}^{\mathrm{p}}}=n K\left(\varepsilon_0+\bar{\varepsilon}^{\mathrm{p}}\right)^{n-1} \ , \tag{3.125}$$

  with K, ε_0, and n as the material parameters.

- Voce model:

  $$\sigma_{\mathrm{y}}\left(\bar{\varepsilon}^{\mathrm{p}}\right)=\sigma_{\mathrm{s}}-\left(\sigma_{\mathrm{s}}-\sigma_1\right) e^{n \bar{\varepsilon}^{\mathrm{p}}} \ , \tag{3.126}$$

  $$\frac{\partial \sigma_{\mathrm{y}}\left(\bar{\varepsilon}^{\mathrm{p}}\right)}{\partial \bar{\varepsilon}^{\mathrm{p}}}=-n \bar{\varepsilon}^{\mathrm{p}}\left(\sigma_{\mathrm{s}}-\sigma_1\right) e^{\left(n \bar{\varepsilon}^{\mathrm{p}}-1\right)} , \tag{3.127}$$

  with σ_{s}, σ_1, and n as the material parameters.

- Ludwik model:

  $$\sigma_{\mathrm{y}}\left(\bar{\varepsilon}^{\mathrm{p}}\right)=\sigma_0+K\left(\bar{\varepsilon}^{\mathrm{p}}\right)^n \ , \tag{3.128}$$

  $$\frac{\partial \sigma_{\mathrm{y}}\left(\bar{\varepsilon}^{\mathrm{p}}\right)}{\partial \bar{\varepsilon}^{\mathrm{p}}}=-n K(\bar{\varepsilon}^{\mathrm{p}})^{n-1} , \tag{3.129}$$

  with σ_0, K, and n as the material parameters.

However, it should be noted that neither of these models is usually capable of capturing the hardening behavior of the metallic materials for a wide range of plastic strain. In most cases, the calibrated model predicts the yield stress accurately either near initial yielding or at the later stage of the plastic deformation, which causes the estimated yield stress to be inaccurate. To remedy this problem, one solution is to use different models for different stages of deformation. This can be achieved by combining one of the three presented models with another hardening behavior, for example, a linear or even a quadratic function of the equivalent plastic strain. In this work, the Ludwik law is used to capture the hardening behavior of LPBF316L since it was able to reproduce the observed material behavior more accurately. Moreover, it was also extended using different linear and non-linear functions to extrapolate the results beyond their experimental limit. A more detailed explanation and the exact calibration procedure are presented in section 3.4.2.3.

3.3.7 Evolution of microstructure and the plastic spin

To better understand the influence of plastic spin $\mathbf{W}^{\mathrm{p}}$ and its relation to the microstructure evolution, it is helpful to start with the multiplicative decomposition:

$$\mathbf{F} = \mathbf{F}^{\mathrm{e}} \cdot \mathbf{F}^{\mathrm{p}}. \tag{3.130}$$

The plastic part of the deformation gradient $\mathbf{F}^{\mathrm{p}}$ maps the initial configuration to the intermediate configuration, which is also called the isoclinic configuration. As explained in section 3.1, this mapping does not alter the crystal orientation or the lattice frame. This can also be applied to the orthonormal vectors of a coordinate frame $\boldsymbol{e}_i^0$ at each material point which characterizes the material anisotropy. The crystallographic texture of a material can be determined using EBSD measurements. This texture represents the initial texture of the material before any deformation. One can assign the coordinate system $\boldsymbol{e}_i^0$ to this texture at each material point and call it material axes. If this coordinate system is rotated during the deformation, then the texture has to be rotated accordingly. By knowing the orientation of this coordinate system, the material properties such as the elastic stiffness tensor can be correctly calculated using the same rotation, similar to the CP framework. Thus, the main goal becomes the determination of the correct rotation in each material point of the body during the deformation.

However, this is not a trivial task since the rotation arising from the multiplicative decomposition is not unique. This is demonstrated by decomposing the elastic and plastic part of the deformation gradient using the polar decomposition:

$$\mathbf{F}^{\mathrm{p}} = \mathbf{R}^{\mathrm{p}} \cdot \mathbf{U}^{\mathrm{p}}\,, \qquad \mathbf{F}^{\mathrm{e}} = \mathbf{V}^{\mathrm{e}} \cdot \mathbf{R}^{\mathrm{e}}\,. \tag{3.131}$$

Using these relations, it can be shown that the intermediate configuration is only determined up to an arbitrary rotation $\mathbf{Q}$, see fig. 3.8:

$$\mathbf{F} = \mathbf{F}^{\mathrm{e}} \cdot \mathbf{F}^{\mathrm{p}} = \tilde{\mathbf{F}}^{\mathrm{e}} \cdot \tilde{\mathbf{F}}^{\mathrm{p}} \quad \text{with} \quad \tilde{\mathbf{F}}^{\mathrm{p}} = \mathbf{Q} \cdot \mathbf{R}^{\mathrm{p}} \cdot \mathbf{U}^{\mathrm{p}}\,, \quad \tilde{\mathbf{F}}^{\mathrm{e}} = \mathbf{V}^{\mathrm{e}} \cdot \mathbf{R}^{\mathrm{e}} \cdot \mathbf{Q}^{\mathrm{T}}\,. \tag{3.132}$$

The deformation gradient $\mathbf{F}$ then becomes:

$$\mathbf{F} = \mathbf{V}^{\mathrm{e}} \cdot \underline{\mathbf{R}} \cdot \mathbf{U}^{\mathrm{p}}\,. \tag{3.133}$$

The above equations confirm the fact that the intermediate configuration is not uniquely determined since the rotation tensor $\underline{\mathbf{R}} = \mathbf{R}^{\mathrm{e}} \cdot \mathbf{R}^{\mathrm{p}}$ is not unique. If the elastic and plastic rotation tensors $\mathbf{R}^{\mathrm{e}}$ and $\mathbf{R}^{\mathrm{p}}$ are not precisely known, then the correct orientation of the material axes in the current configuration can not be identified, see fig. 3.8. The reason for that is that the plastic rotation $\mathbf{R}^{\mathrm{p}}$ is a rigid body motion, which rotates the initial configuration into the intermediate configuration without changing the orientation of the material axes. Thus, for any rotation tensor $\mathbf{R}^{\mathrm{p}}$ the material axes remains unchanged in the intermediate configuration. The body and the material axes are mapped into the current configuration by the elastic rotation tensor $\mathbf{R}^{\mathrm{e}}$. For the final shape of the body in the current configuration, the intermediate configuration does not play any role since the arbitrary rotation is canceled out for the total deformation gradient $\mathbf{F}$. However, this is not the case for the material axes since those are decoupled from the shape of the body. Thus, if $\mathbf{R}^{\mathrm{e}}$ and $\mathbf{R}^{\mathrm{p}}$ aren't calculated correctly, then the actual orientation of the material axes in the current configuration can't be determined. Consequently, the material properties can't be updated adequately.

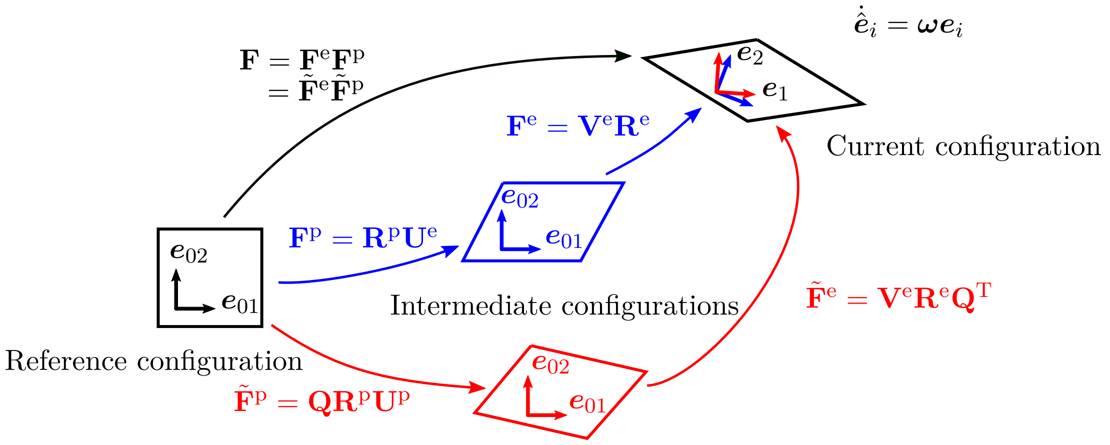
$\dot{\boldsymbol{e}}_i = \boldsymbol{\omega}\boldsymbol{e}_i$
$\mathbf{F} = \mathbf{F}^{\mathrm{e}}\mathbf{F}^{\mathrm{p}}$
$= \tilde{\mathbf{F}}^{\mathrm{e}}\tilde{\mathbf{F}}^{\mathrm{p}}$
$\boldsymbol{e}_2$
$\boldsymbol{e}_1$
$\mathbf{F}^{\mathrm{e}} = \mathbf{V}^{\mathrm{e}}\mathbf{R}^{\mathrm{e}}$
Current configuration
$\boldsymbol{e}_{02}$
$\boldsymbol{e}_{01}$
$\mathbf{F}^{\mathrm{p}} = \mathbf{R}^{\mathrm{p}}\mathbf{U}^{\mathrm{e}}$
$\boldsymbol{e}_{02}$
$\boldsymbol{e}_{01}$
Intermediate configurations
$\tilde{\mathbf{F}}^{\mathrm{e}} = \mathbf{V}^{\mathrm{e}}\mathbf{R}^{\mathrm{e}}\mathbf{Q}^{\mathrm{T}}$
Reference configuration
$\tilde{\mathbf{F}}^{\mathrm{p}} = \mathbf{Q}\mathbf{R}^{\mathrm{p}}\mathbf{U}^{\mathrm{p}}$
$\boldsymbol{e}_{02}$
$\boldsymbol{e}_{01}$

Figure 3.8: Non-uniqueness of the intermediate configuration [98].

To remedy this problem the evolution law for the material axes has to be determined. One way to achieve this is by employing a corotational formulation for the constitutive material model, as explained in section 3.3.4, where the material constitutive model is formulated in the rotating coordinate frame of the material axes. In that particular formulation, it is assumed that the material axes are rotating with the spin tensor $\mathbf{W}$, which results in the following evolution law for the coordinate frame:

$$\dot{\boldsymbol{e}}_i = \mathbf{W} \cdot \boldsymbol{e}_i \,, \qquad\qquad i = 1, 3 \,. \tag{3.134}$$

This assumption results in the objective Jaumann rate of the Cauchy stress tensor:

$$\overset{\triangledown}{\boldsymbol{\sigma}} = \dot{\boldsymbol{\sigma}} - \mathbf{W} \cdot \boldsymbol{\sigma} + \boldsymbol{\sigma} \cdot \mathbf{W} \,, \qquad\qquad \mathbf{W} = \operatorname{skew}\left[\mathbf{L}\right] \,. \tag{3.135}$$

However, this assumption is incorrect for anisotropic materials, particularly when the strains become large. This has been experimentally investigated using tensile tests, and it has been shown that the material axes can evolve even when the spin tensor $\mathbf{W}$ is zero [155]. In [97, 156–158], it has been mathematically demonstrated that the material axes do not necessarily evolve according to the spin tensor $\mathbf{W}$ and that the plastic spin $\mathbf{W}^{\mathrm{p}}$ is required to model their evolution. To derive an expression for the calculation of the plastic spin $\mathbf{W}^{\mathrm{p}}$, it is useful to start with the velocity gradient $\mathbf{L}$:

$$\mathbf{L} = \dot{\mathbf{F}}^{\mathrm{e}} \cdot \mathbf{F}^{\mathrm{e}-1} + \mathbf{F}^{\mathrm{e}} \cdot \dot{\mathbf{F}}^{\mathrm{p}} \cdot \mathbf{F}^{\mathrm{p}-1} \cdot \mathbf{F}^{\mathrm{e}-1} = \mathbf{L}^{\mathrm{e}} + \mathbf{F}^{\mathrm{e}} \cdot \mathbf{L}^{\mathrm{p}}_{\mathrm{I}} \cdot \mathbf{F}^{\mathrm{e}-1} \,. \tag{3.136}$$

The velocity gradient $\mathbf{L}$ can also be split into its symmetric and antisymmetric parts:

$$\mathbf{L} = \mathbf{D} + \mathbf{W} \,, \qquad \mathbf{D} = \operatorname{sym}\left[\mathbf{L}\right] \,, \qquad \mathbf{W} = \operatorname{skew}\left[\mathbf{L}\right] \,. \tag{3.137}$$

The rate of deformation tensor $\mathbf{D}$ and the spin tensor $\mathbf{W}$ can further be broken down into their elastic and plastic parts:

$$\mathbf{D} = \mathbf{D}^{\mathrm{e}} + \mathbf{D}^{\mathrm{p}}\,, \qquad \mathbf{W} = \mathbf{W}^{\mathrm{e}} + \mathbf{W}^{\mathrm{p}}\,. \tag{3.138}$$

The equations (3.136), (3.136), and (3.137) can be further utilized to define the rate of plastic deformation $\mathbf{D}^{\mathrm{p}}$ and the plastic spin tensor $\mathbf{W}^{\mathrm{p}}$ both in the intermediate and current configuration:

$$\mathbf{D}^{\mathrm{p}}_{\mathrm{I}} = \mathrm{sym}\left[\mathbf{L}^{\mathrm{p}}_{\mathrm{I}}\right]\,, \qquad \mathbf{W}^{\mathrm{p}}_{\mathrm{I}} = \mathrm{skew}\left[\mathbf{L}^{\mathrm{p}}_{\mathrm{I}}\right]\,,$$

$$\mathbf{D}^{\mathrm{p}} = \mathrm{sym}\left[\mathbf{F}^{\mathrm{e}}\mathbf{L}^{\mathrm{p}}_{\mathrm{I}}\mathbf{F}^{\mathrm{e}-1}\right]\,, \qquad \mathbf{W}^{\mathrm{p}} = \mathrm{skew}\left[\mathbf{F}^{\mathrm{e}}\mathbf{L}^{\mathrm{p}}_{\mathrm{I}}\mathbf{F}^{\mathrm{e}-1}\right]\,. \tag{3.139}$$

$\mathbf{D}^{\mathrm{p}}_{\mathrm{I}}$ and $\mathbf{D}^{\mathrm{p}}$ describe the instantaneous rate of plastic straining in the intermediate and current configuration. $\mathbf{W}^{\mathrm{p}}_{\mathrm{I}}$ and $\mathbf{W}^{\mathrm{p}}$, on the other hand, are the instantaneous rate of rigid rotation of the intermediate and current configuration. Depending on the modeling assumption, both the intermediate and current configuration can be used to formulate the material constitutive models. Irrespective of the configuration, in most metal plasticity models at the macroscale, only the symmetric part of the plastic deformation ($\mathbf{D}^{\mathrm{p}}_{\mathrm{I}}$ or $\mathbf{D}^{\mathrm{p}}$) is modeled. This is usually achieved by employing a flow rule like:

$$\mathbf{D}^{\mathrm{p}}_{\mathrm{I}} = \dot{\gamma}\frac{\partial\Phi}{\partial\boldsymbol{\sigma}_{\mathrm{I}}} \qquad \text{or} \qquad \mathbf{D}^{\mathrm{p}} = \dot{\gamma}\frac{\partial\Phi}{\partial\boldsymbol{\sigma}}\,. \tag{3.140}$$

$\boldsymbol{\sigma}_{\mathrm{I}}$ denotes the stress measure in the intermediate configuration. The antisymmetric part of the plastic deformation is most often ignored by assuming $\mathbf{W}^{\mathrm{p}}_{\mathrm{I}} = \mathbf{W}^{\mathrm{p}} = \mathbf{0}$. As explained before, this assumption is not correct when dealing with anisotropic materials and large deformation. This statement can also be verified by looking at the CP model described in section 3.2.3. Such a model is often employed to predict the crystallographic texture changes during the deformation accurately [71]. The central modeling assumption in this model is that:

$$\mathbf{L}^{\mathrm{p}}_{\mathrm{I}} = \dot{\mathbf{F}}^{\mathrm{p}} \cdot (\mathbf{F}^{\mathrm{p}})^{-1} = \sum_{\alpha=1}^{N} \dot{\gamma}^{\alpha}\mathbf{m}^{\alpha}_{0} \otimes \mathbf{n}^{\alpha}_{0}, \tag{3.141}$$

By closer inspection, it is evident that by using the above equation, both the symmetric and antisymmetric parts of the plastic deformation are modeled, which results in an accurate prediction of the microstructure evolution.

3.3.7.1 Existing models

To overcome this shortcoming at the macroscale, different models were developed for the evolution of the plastic spin [97–99, 155–160]. The models are derived by using the representation theory for tensor-valued functions of tensors [161, 162]. The process mainly consists of the following steps:

- Depending on the degree of anisotropy and dimensionality of the problem, a set of rank-one orientation tensors has to be chosen, which are purely orientational and act as the structure variables [97]. These variables, along with some other variables, are then used for formulating the constitutive equations for $\mathbf{D}^{\mathrm{p}}_{\mathrm{I}}$ and $\mathbf{W}^{\mathrm{p}}_{\mathrm{I}}$. For an orthotropic material, the set of structure variables is reduced to a single symmetric rank-one orientation tensor [162].
- Furthermore, it is postulated that $\mathbf{W}^{\mathrm{p}}_{\mathrm{I}}$ also depends on $\boldsymbol{\sigma}_{\mathrm{I}}$ in a similar manner to $\mathbf{D}^{\mathrm{p}}_{\mathrm{I}}$, shown in eq. (3.140) [97,98,163].
- Depending on the number of variables (in this case, the structure variables and $\boldsymbol{\sigma}_{\mathrm{I}}$), a specific set of scalar-valued invariants and generators can be derived, which are only valid for the chosen variables. The generators are second-order tensors that can be further split into symmetric and anti-symmetric groups [162].
- With the set of invariants and generators at hand, the general constitutive equation for $\mathbf{D}^{\mathrm{p}}_{\mathrm{I}}$ is postulated by adding up the symmetric generators multiplied with different scalar-valued functions, which can only depend on the defined set of invariants above. The equations for $\mathbf{W}^{\mathrm{p}}_{\mathrm{I}}$ are derived in a similar way, whereby the symmetric generators are swapped with the anti-symmetric ones.
- In the final step, the derived expressions for both $\mathbf{D}^{\mathrm{p}}_{\mathrm{I}}$ and $\mathbf{W}^{\mathrm{p}}_{\mathrm{I}}$ are compared to each other, and it is concluded that $\mathbf{W}^{\mathrm{p}}_{\mathrm{I}}$ is related to the components of $\mathbf{D}^{\mathrm{p}}_{\mathrm{I}}$ by [97,98]:

  $$\mathrm{W}^{\mathrm{p}}_{\mathrm{I}\,12} = \eta_3\,\mathrm{D}^{\mathrm{p}}_{\mathrm{I}\,12}\,, \qquad \mathrm{W}^{\mathrm{p}}_{\mathrm{I}\,13} = \eta_2\,\mathrm{D}^{\mathrm{p}}_{\mathrm{I}\,13}\,, \qquad \mathrm{W}^{\mathrm{p}}_{\mathrm{I}\,23} = \eta_1\,\mathrm{D}^{\mathrm{p}}_{\mathrm{I}\,23}\,. \tag{3.142}$$

  The scalar-valued functions η_i depend on scalar-structure variables, which include the set invariants mentioned before or any other scalar-structure variable such as equivalent plastic strain rate $\dot{\varepsilon}^{\mathrm{p}}$.

This model was successfully used in [98] to predict the microstructure evolution, which was experimentally determined for rolled metal sheets [155]. More recently, the same model was successfully adopted in [99] in a plane stress framework to investigate the influence of microstructure evolution observed in shear tests. The primary objectives in both [98] and [99] were modeling the microstructure evolution in sheet metals. As a result of their success in accurately predicting the microstructural evolution, a similar approach is employed in this work for the LPBF316L. The steps and efforts listed above are mainly required to reduce the complexity and consequently the required parameters of the final constitutive model, which is due to the fact that the parameters were calibrated using experimental data [98,163]. Hence, having a complex model with many parameters usually requires a lot of experimental effort for its calibration, which is counterproductive and could result in completely neglecting this aspect of modeling. In [99], the parameters of the plastic spin model were calibrated using virtual experiments to remedy this problem. However, the following limitations of the model were not addressed. Thus, the following points are emphasized once more to summarize the main ideas behind the approach taken in [97–99, 157, 158, 163] for the derivation of the expressions in eq. (3.142) and further, highlight the limitations of the models:

- The constitutive equations for the plastic spin $\mathbf{W}_{\mathrm{I}}^{\mathrm{p}}$ in eq. (3.142) were derived with the final goal of having a compact model with the least required number of material parameters. Furthermore, the models mainly depend on the non-coaxiality between $\mathbf{D}_{\mathrm{I}}^{\mathrm{p}}$ and the initial orthotropic axes of the material defined by $\boldsymbol{e}_i$ in eq. (3.134).
- Moreover, these relations are derived based on the assumption that the orthonormal material symmetry persists during the deformation, which is not necessarily true in the case of large deformations since texture evolution could change the initial symmetry depending on the loading condition. Moreover, additively manufactured parts could exhibit complete anisotropic texture depending on the processing parameters.
- The expressions in eq. (3.142) were mainly developed for their final application in sheet metal forming simulations [97–99, 163], which reduces the problem to a 2D scenario. This allows for a simpler model where many of the coupling effects can be ignored since only one component of the plastic spin tensor has to be modeled. However, these assumptions are not necessarily valid for an additively manufactured metallic material since the final parts often require simulations in 3D.
- Finally, it will be shown that it is not possible to address the texture evolution with a simple and universal expression as in eq. (3.142), since different loading conditions drastically influence the final texture of the material. This aspect has to be included in the final model.

3.3.7.2 Proposed model

The modeling efforts in this work will be concentrated on addressing the limitations mentioned above. Two of the most important ones are the extension of these models to the 3D case and addressing the influence of different loading conditions such as uni-axial tension and shear. It should be noted that in contrast to the approach described before, the priority in this work is not the simplicity of the final model but rather the accuracy of it during full 3D simulations. Hence, a general solution will be presented, which will result in a more complex constitutive model having a higher number of material parameters. However, this is not an issue when employing a multi-scale simulation approach since the parameters are calibrated using virtual experiments. Thus, the approach taken in [97, 98, 163] is modified as follows. Instead of using the reduced set of generators and invariants described before, the starting point becomes the following relation in the current configuration, more specifically, in the locally rotating CCO, as described in section 3.3.4:

$$\hat{\mathbf{W}}^{\mathrm{p}} = \hat{\mathbf{H}} : \hat{\mathbf{D}}^{\mathrm{p}} \,. \tag{3.143}$$

$\hat{\mathbf{H}}$ is a fourth-order tensor, which establishes the connection between $\hat{\mathbf{D}}^{\mathrm{p}}$ and $\hat{\mathbf{W}}^{\mathrm{p}}$ [163]. Similar to the η_i in eq. (3.142) the components of the $\hat{\mathbf{H}}$ tensor depend on some functional set of invariants. Thus, the eq. (3.142) can be replaced by the following expression:

$$\begin{aligned}
\hat{\mathrm{W}}^{\mathrm{p}}_{12} = &\hat{\eta}_{1211}\,\hat{\mathrm{D}}^{\mathrm{p}}_{11} + \hat{\eta}_{1222}\,\hat{\mathrm{D}}^{\mathrm{p}}_{22} + \hat{\eta}_{1233}\,\hat{\mathrm{D}}^{\mathrm{p}}_{33} + \\
&\hat{\eta}_{1212}\,\hat{\mathrm{D}}^{\mathrm{p}}_{12} + \hat{\eta}_{1213}\,\hat{\mathrm{D}}^{\mathrm{p}}_{13} + \hat{\eta}_{1223}\,\hat{\mathrm{D}}^{\mathrm{p}}_{23} + \\
&\hat{\eta}_{1221}\,\hat{\mathrm{D}}^{\mathrm{p}}_{21} + \hat{\eta}_{1231}\,\hat{\mathrm{D}}^{\mathrm{p}}_{31} + \hat{\eta}_{1232}\,\hat{\mathrm{D}}^{\mathrm{p}}_{32}\,, \\
\\
\hat{\mathrm{W}}^{\mathrm{p}}_{13} = &\hat{\eta}_{1311}\,\hat{\mathrm{D}}^{\mathrm{p}}_{11} + \hat{\eta}_{1322}\,\hat{\mathrm{D}}^{\mathrm{p}}_{22} + \hat{\eta}_{1333}\,\hat{\mathrm{D}}^{\mathrm{p}}_{33} + \\
&\hat{\eta}_{1312}\,\hat{\mathrm{D}}^{\mathrm{p}}_{12} + \hat{\eta}_{1313}\,\hat{\mathrm{D}}^{\mathrm{p}}_{13} + \hat{\eta}_{1323}\,\hat{\mathrm{D}}^{\mathrm{p}}_{23} + \\
&\hat{\eta}_{1321}\,\hat{\mathrm{D}}^{\mathrm{p}}_{21} + \hat{\eta}_{1331}\,\hat{\mathrm{D}}^{\mathrm{p}}_{31} + \hat{\eta}_{1332}\,\hat{\mathrm{D}}^{\mathrm{p}}_{32}\,, \\
\\
\hat{\mathrm{W}}^{\mathrm{p}}_{23} = &\hat{\eta}_{2311}\,\hat{\mathrm{D}}^{\mathrm{p}}_{11} + \hat{\eta}_{2322}\,\hat{\mathrm{D}}^{\mathrm{p}}_{22} + \hat{\eta}_{2333}\,\hat{\mathrm{D}}^{\mathrm{p}}_{33} + \\
&\hat{\eta}_{2312}\,\hat{\mathrm{D}}^{\mathrm{p}}_{12} + \hat{\eta}_{2313}\,\hat{\mathrm{D}}^{\mathrm{p}}_{13} + \hat{\eta}_{2323}\,\hat{\mathrm{D}}^{\mathrm{p}}_{23} + \\
&\hat{\eta}_{2321}\,\hat{\mathrm{D}}^{\mathrm{p}}_{21} + \hat{\eta}_{2331}\,\hat{\mathrm{D}}^{\mathrm{p}}_{31} + \hat{\eta}_{2332}\,\hat{\mathrm{D}}^{\mathrm{p}}_{32}\,.
\end{aligned} \tag{3.144}$$

These expressions may seem much more complicated than those of eq. (3.142). However, the eq. (3.144) can be presented in a much simpler way by using the fact that in [97–99, 155–158, 163], the functions $\hat{\eta}_i$ only depend on $\hat{\mathbf{D}}^{\mathrm{p}}$ and the equivalent plastic strain rate $\dot{\bar{\varepsilon}}^{\mathrm{p}}$. The same assumption is also made in this work, and thus, the general expressions become:

$$\hat{\mathrm{W}}^{\mathrm{p}}_{12} = \hat{\eta}_{12}\left(\hat{\mathbf{D}}^{\mathrm{p}}, \dot{\bar{\varepsilon}}^{\mathrm{p}}\right)\,, \qquad \hat{\mathrm{W}}^{\mathrm{p}}_{13} = \hat{\eta}_{13}\left(\hat{\mathbf{D}}^{\mathrm{p}}, \dot{\bar{\varepsilon}}^{\mathrm{p}}\right)\,, \qquad \hat{\mathrm{W}}^{\mathrm{p}}_{23} = \hat{\eta}_{23}\left(\hat{\mathbf{D}}^{\mathrm{p}}, \dot{\bar{\varepsilon}}^{\mathrm{p}}\right)\,. \tag{3.145}$$

The functions η_i in the equations above have to be further concretized to be applicable to the problems presented in the following sections. To accomplish this goal, the first problem which has to be addressed is the differentiation between different loading conditions, which manifest themselves in different stress states. One possible solution to this problem is using the Lode invariants such as stress triaxiality and Lode angle, which are often employed in fracture mechanics to distinguish between different stress states and incorporate that into the constitutive model [164–168]. The Lode invariants are closely related to the Haigh–Westergaard coordinates, and the kinematic invariants of the stress tensor, often referred to as first, second, and third invariant [164]. In this work, only the Lode parameter μ_{L} or equivalently the Lode angle θ_{L} is used to characterize the stress state:

$$\mu_{\mathrm{L}} = \frac{2\sigma_2 - \sigma_1 - \sigma_3}{\sigma_1 - \sigma_3}\,, \qquad \theta_{\mathrm{L}} = \tan^{-1}\left(\frac{1}{\sqrt{3}}\mu_{\mathrm{L}}\right) \qquad \text{for} \qquad -\frac{\pi}{6} < \theta_{\mathrm{L}} < \frac{\pi}{6}\,, \tag{3.146}$$

where $\sigma_1 \geq \sigma_2 \geq \sigma_3$ are the ordered set of principal components of the stress tensor $\boldsymbol{\sigma}$, using Lode parameter μ_{L}, it is easily possible to distinguish between different stress states, such as generalized tension for $\mu_{\mathrm{L}} = -1$, generalized shear for $\mu_{\mathrm{L}} = 0$, and generalized compression for $\mu_{\mathrm{L}} = 1$, see fig. 3.9. There are also other slightly different definitions for the Lode parameter μ_{L} in literature. But all of them are equivalent and can be converted into each other with ease [167, 168]. However, it should be noted that not all stress states can be uniquely identified using the Lode parameter μ_L since, for example, bi-axial tension and shear states result in the same Lode parameter $\mu_\mathrm{L} = 0$. However, in this particular case, this doesn't pose an issue since the final texture of the material under both of these stress states is identical [169]. Similarly, simple shear and pure shear stress states can't be distinguished from each other. However, it is assumed that both of them have the same effect since simple shear is a superposition of pure shear with a rigid body rotation during the deformation. Moreover, in [167, 168] it is shown that for the von Mises yield surface it is also possible to reformulate the eq. (3.146) using the principal components of the rate of plastic deformation tensor $\hat{\mathbf{D}}^\mathrm{p}$, see fig. 3.9. This is possible since the von Mises yield surface is isotropic and that the rate of plastic deformation tensor is directly coupled with the deviatoric part of the stress tensor. It is worth noting that the Barlat type yield functions fulfill these conditions only in very special cases (isotropy) and that the transition from stress to strain space doesn't result in the exact same values for the lode parameters. The lode parameters calculated in the stress and strain space will vary depending on the anisotropy of the material. The difference is zero in case of isotropy and will increase as the anisotropy gets stronger. However, this doesn't pose an issue for the formulation of the plastic spin model in the plastic strain space since this choice can be viewed as a modeling assumption. Moreover, the constitutive parameters of the phenomenological plastic spin model can be used to fine tune and adjust the model behavior for different loading conditions. Thus, in this work the lode parameters calculated in the plastic strain space will be used for the formulation of the plastic spin model:

$$\mu_\mathrm{L} = \frac{2\lambda_2^\mathrm{p} - \lambda_1^\mathrm{p} - \lambda_3^\mathrm{p}}{\lambda_1^\mathrm{p} - \lambda_3^\mathrm{p}}\,, \qquad \text{with} \qquad \lambda_1^\mathrm{p} \geq \lambda_2^\mathrm{p} \geq \lambda_3^\mathrm{p}\,. \tag{3.147}$$

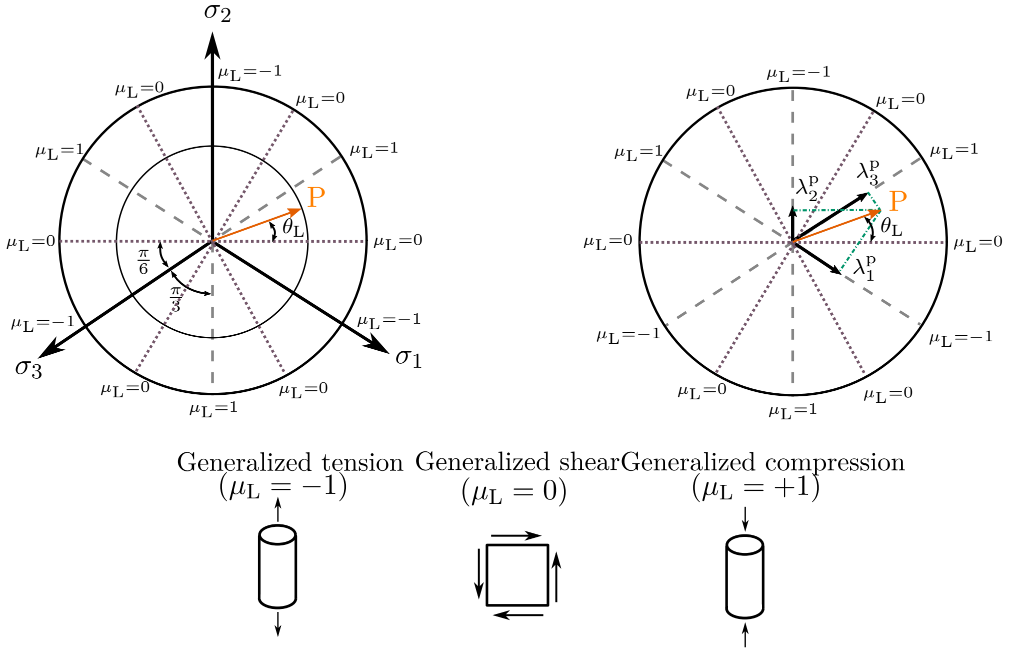

Figure 3.9: Geometrical representation of the Lode parameter μ_L and the Lode angle θ_L on the deviatoric plane. On the left, the parameters for the point P are shown in the principal stress space. On the right, the same parameters are determined in the principal plastic strain components [164–168].

Following the eq. (3.145) and the main idea of separating the different stress states, it is then postulated that the constitutive model for the plastic spin has the following general form:

$$\hat{\mathbf{W}}^{\mathrm{p}} = \mu_{\mathrm{L}}\hat{\mathbf{W}}^{\mathrm{p}}_{\mathrm{TC}} + (1 - |\mu_{\mathrm{L}}|)\left(\hat{\mathbf{W}}^{\mathrm{p}}_{\mathrm{S}}\right) , \tag{3.148}$$

with $\hat{\mathbf{W}}^{\mathrm{p}}_{\mathrm{TC}}$ and $\hat{\mathbf{W}}^{\mathrm{p}}_{\mathrm{S}}$, being the plastic spin contributions from tension/compression and generalized shear, respectively. It should be highlighted that these newly introduced plastic spin tensors depend on the same invariants as in eq. (3.145) and will have a very similar structure. However, the expressions for calculating the contribution of the different stress states are not exactly the same and may differ depending on the results of the virtual experiments. This approach offers a flexible solution, universally applicable to many different materials. Moreover, each of these contributions can be adjusted according to the priorities and complexity of the problem. For example, if a particular stress state is more dominant during a deformation process, then the expression for this exact contribution can be adjusted to have higher accuracy. Now that the contributions from the different stress states to the final plastic spin tensor $\hat{\mathbf{W}}^{\mathrm{p}}$ are determined, it is necessary to find a way to correctly calculate each of the separate tensors $\hat{\mathbf{W}}^{\mathrm{p}}_{\mathrm{TC}}$ and $\hat{\mathbf{W}}^{\mathrm{p}}_{\mathrm{S}}$.

The next logical step is determining the exact set of variables, which are then used to formulate the expression in eq. (3.148). In [98, 99, 163], the expressions for calculating the plastic spin tensor depend directly on the components of the tensor $\mathbf{D}^{\mathrm{p}}_{\mathrm{I}}$. However, in this work, the invariants of the tensor $\hat{\mathbf{D}}^{\mathrm{p}}$ are used, in particular the eigenvalues and eigenvectors. $\lambda^{\mathrm{p}}_1 \geq \lambda^{\mathrm{p}}_2 \geq \lambda^{\mathrm{p}}_3$ are the ordered set of principal components of the tensor $\hat{\mathbf{D}}^{\mathrm{p}}$, and $\mathbf{e}^{\mathrm{p}}_1$, $\mathbf{e}^{\mathrm{p}}_2$, and $\mathbf{e}^{\mathrm{p}}_3$ are corresponding eigenvectors, which are graphically shown in fig. 3.9. The eigenvectors in combination with the eigenvalues can be used to construct the constitutive equations required for the calculation of $\hat{\mathbf{W}}^{\mathrm{p}}_{\mathrm{TC}}$ and $\hat{\mathbf{W}}^{\mathrm{p}}_{\mathrm{S}}$. For example, a strain state corresponding to a uni-axial tension experiment will have one positive and two negative eigenvalues and a corresponding Lode parameter of $\mu_{\mathrm{L}} = -1$. Most importantly, the eigenvector belonging to the positive eigenvalue shows the pulling direction of the material with respect to the initial material frame, which is characterized by the vectors $\mathbf{e}_1$, $\mathbf{e}_2$, and $\mathbf{e}_3$. Moreover, for one negative, one positive, and one zero eigenvalue, the Lode parameter becomes $\mu_{\mathrm{L}} = 0$, which is an indication of a shear state. Again, the eigenvector belonging to the positive eigenvalue can be used to extract the necessary information required for the constitutive model. One eigenvector is also sufficient for the compression case. However, instead of the eigenvector belonging to the biggest positive eigenvalue, the eigenvector corresponding to the negative eigenvalue is selected since the sign of the eigenvalues are reversed when compared to the generalized tension. In summary, it is clear that one eigenvector is sufficient to determine the plastic spin tensors.

To reduce the modeling complexity, the constitutive equations are formulated using spherical polar coordinates (SPC), see fig. 3.10, which has two main advantages. First: since the eigenvectors are normalized, then using SPC, the radius r is always equal to 1, which automatically reduces the number of variables to two, namely θ^{p} and φ^{p}, instead of 3 when using CCO. The second main advantage is that when the texture has symmetrical properties, then the constitutive model is easily formulated using SPC and trigonometric functions, which significantly reduces the overall complexity of the model and the calibration efforts.

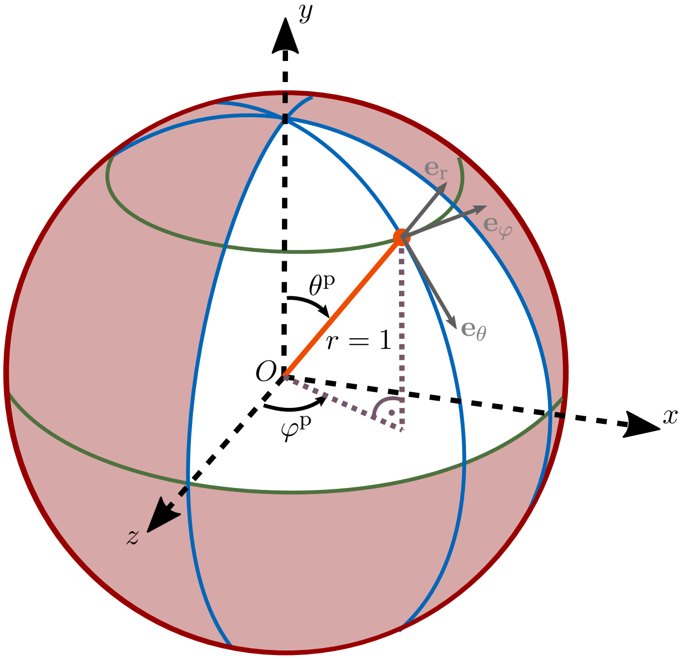

Figure 3.10: Representation of the eigenvectors $\mathbf{e}_i^{\mathrm{p}}$ in CCO and SPC.

To use these properties, the following transformation matrices can be used to perform the change of the coordinate frame between SPC and CCO:

$$\mathbf{R}_{\mathrm{Pol}} = \begin{bmatrix} \sin(\theta^{\mathrm{p}})\sin(\varphi^{\mathrm{p}}) & \cos(\theta^{\mathrm{p}}) & \sin(\theta^{\mathrm{p}})\cos(\varphi^{\mathrm{p}}) \\ \cos(\theta^{\mathrm{p}})\sin(\varphi^{\mathrm{p}}) & -\sin(\theta^{\mathrm{p}}) & \cos(\theta^{\mathrm{p}})\cos(\varphi^{\mathrm{p}}) \\ \cos(\varphi^{\mathrm{p}}) & 0 & -\sin(\varphi^{\mathrm{p}}) \end{bmatrix}, \tag{3.149}$$

$$\mathbf{R}_{\mathrm{Pol}}^{\mathrm{T}} = \begin{bmatrix} \sin(\theta^{\mathrm{p}})\sin(\varphi^{\mathrm{p}}) & \cos(\theta^{\mathrm{p}})\sin(\varphi^{\mathrm{p}}) & \cos(\varphi^{\mathrm{p}}) \\ \cos(\theta^{\mathrm{p}}) & -\sin(\theta^{\mathrm{p}}) & 0 \\ \sin(\theta^{\mathrm{p}})\cos(\varphi^{\mathrm{p}}) & \cos(\theta^{\mathrm{p}})\cos(\varphi^{\mathrm{p}}) & -\sin(\varphi^{\mathrm{p}}) \end{bmatrix}. \tag{3.150}$$

With the transformations described above, the eigenvectors $\mathbf{e}_1^{\mathrm{p}}$, $\mathbf{e}_2^{\mathrm{p}}$, and $\mathbf{e}_3^{\mathrm{p}}$ corresponding to the eigenvalues $\lambda_1^{\mathrm{p}} \geq \lambda_2^{\mathrm{p}} \geq \lambda_3^{\mathrm{p}}$ of the tensor $\hat{\mathbf{D}}^{\mathrm{p}}$ can be characterized with θ^{p} and φ^{p}, see fig. 3.10. It should be highlighted that in this work, it is assumed that the axes of the CCO frame coincide with the material axes. Thus, $\mathbf{e}_1$, $\mathbf{e}_2$, and $\mathbf{e}_3$ are the unit vectors corresponding to the CCO, which also characterize the initial material texture.

With the transformation matrices $\mathbf{R}_{\mathrm{Pol}}$ and $\mathbf{R}_{\mathrm{Pol}}^{\mathrm{T}}$ in eq. (3.150) it is then easily possible to perform a change of coordinate frame for the components of the plastic spin tensor $\hat{\mathbf{W}}^{\mathrm{p}}$. More specifically, the eq. (3.148) will be used in the SPC frame to calculate the components of the plastic spin tensor, which are then transformed back to the CCO frame by the derived transformation matrices. In the SPC frame, the contributing tensors from tension/compression $\hat{\mathbf{W}}_{\mathrm{TC}}^{\mathrm{p}}$ and shear deformation $\hat{\mathbf{W}}_{\mathrm{S}}^{\mathrm{p}}$ are simply calculated by an expression consisting of trigonometric functions, which only take θ^{p} and φ^{p} as the input variables. Moreover, each component of the tensors $\hat{\mathbf{W}}_{\mathrm{TC}}^{\mathrm{p}}$ and $\hat{\mathbf{W}}_{\mathrm{S}}^{\mathrm{p}}$ can have a very distinct behavior, which is ultimately dependent on the initial texture of the material. Thus, the final expressions for these tensors are derived based on the results obtained from virtual experiments and are presented in section 3.4.2.4. After the plastic spin tensor $\hat{\mathbf{W}}^{\mathrm{p}}$ is calculated, it is then possible to uniquely determine the material axes rotation by making the following adjustments. First, the initial value problem in eq. (3.134)

$$\dot{\boldsymbol{e}}_i = \mathbf{W} \cdot \boldsymbol{e}_i \,, \qquad\qquad i = 1,3 \,, \tag{3.151}$$

is modified using the eq. (3.138)

$$\mathbf{W}^{\mathrm{e}} = \mathbf{W} - \mathbf{W}^{\mathrm{p}} \,, \tag{3.152}$$

as follows:

$$\dot{\boldsymbol{e}}_i = \mathbf{W}^{\mathrm{e}} \cdot \boldsymbol{e}_i \,, \qquad\qquad i = 1,3 \,. \tag{3.153}$$

Please note that the constitutive equations for the plastic spin tensor $\hat{\mathbf{W}}^{\mathrm{p}}$ are defined in the locally rotating CCO frame. Thus, $\hat{\mathbf{W}}^{\mathrm{p}}$ has to be transformed back to the global frame to obtain $\mathbf{W}^{\mathrm{p}}$ used in the eq. (3.152). However, this is straightforward by making use of the incrementally objective integration algorithm presented in section 3.3.4. The complete implementation procedure with all the necessary steps is described in section 3.3.10. It is also important to see that the original corotational formulation described in section 3.3.4 is easily retrieved if the plastic spin $\mathbf{W}^{\mathrm{p}}$ vanishes, which is the case for an isotropic material.

The whole procedure for calculating the plastic spin tensor $\hat{\mathbf{W}}^{\mathrm{p}}$ can be summarized as follows. 1. After any plastic deformation has occurred, the Eigensystem of rate of plastic deformation tensor $\hat{\mathbf{D}}^{\mathrm{p}}$ is determined. 2. The eigenvector belonging to the largest eigenvalue is chosen. 3. The polar angles θ^{p} and φ^{p} of the chosen eigenvector are calculated. 4. The angles θ^{p} and φ^{p} combined with the equivalent plastic strain rate $\dot{\bar{\varepsilon}}^{\mathrm{p}}$ are then used to calculate the tensors $\hat{\mathbf{W}}_{\mathrm{TC}}^{\mathrm{p}}$ and $\hat{\mathbf{W}}_{\mathrm{S}}^{\mathrm{p}}$, which are the plastic spin tensors for tension/compression and shear deformations. 5. The lode parameter μ_{L} is calculated using the previously determined eigenvalues of $\hat{\mathbf{D}}^{\mathrm{p}}$. 6. With the lode parameter μ_{L} and the calculated tensors $\hat{\mathbf{W}}_{\mathrm{TC}}^{\mathrm{p}}$ and $\hat{\mathbf{W}}_{\mathrm{S}}^{\mathrm{p}}$, the final plastic spin tensor $\hat{\mathbf{W}}^{\mathrm{p}}$ is determined by simply inserting these terms in eq. (3.148).

3.3.8 Return mapping algorithm

In order to numerically integrate the equations of the material model, a return mapping algorithm is implemented, which is taken from [153]. This return mapping algorithm makes use of the backward Euler formulation and employs a Newton-Raphson method which is modified with a line search algorithm. The variables at the time t_n, which is the start of the increment, are denoted with n. t_{n+1} marks the time at the end of the increment. The purpose of this algorithm is to return the correct quantities at the end of the increment t_{n+1} by using the values from the start of the increment t_n as input data.

Box. 3.3: Return mapping algorithm.

1. Here it is assumed that the strain increment $\Delta\boldsymbol{\varepsilon}$ and the stresses $\boldsymbol{\sigma}^n$ at the start of the increment are known. In the first step, the trial stress $\boldsymbol{\sigma}^{\text{tr}}$ is calculated using the elastic stiffness tensor $\mathbb{C}$:

$$\boldsymbol{\sigma}^{\text{tr}} = \boldsymbol{\sigma}^n + \mathbb{C} : \Delta\boldsymbol{\varepsilon}\,. \tag{3.154}$$

2. After calculating the trial stress $\boldsymbol{\sigma}^{\text{tr}}$, the yield condition is checked:

$$f(\boldsymbol{\sigma}^{\text{tr}}, \bar{\varepsilon}^{\text{p}}_n) = \Phi\left(\boldsymbol{\sigma}^{\text{tr}}\right) - \sigma_{\text{y}}\left(\bar{\varepsilon}^{\text{p}}_n\right)\,. \tag{3.155}$$

   If $f(\boldsymbol{\sigma}^{\text{tr}}, \bar{\varepsilon}^{\text{p}}_n) \leq 0$, then the strain increment is elastic. In such a case, the end of increment is reached, and the quantities can be updated as follows $\boldsymbol{\sigma}^{n+1} = \boldsymbol{\sigma}^{\text{tr}}$ and $\bar{\varepsilon}^{\text{p}}_{n+1} = \bar{\varepsilon}^{\text{p}}_n$. If $f(\boldsymbol{\sigma}^{\text{tr}}, \bar{\varepsilon}^{\text{p}}_n) > 0$ holds true, then plastic deformation has occurred, and the next step is required.

3. This return mapping algorithm makes use of two residuals. The first residual is the yield function $f(\boldsymbol{\sigma}, \Delta\gamma)$. The second one is the plastic strain residual $\mathbf{G}(\boldsymbol{\sigma}, \Delta\gamma)$. Both are defined as follows:

$$f(\boldsymbol{\sigma}, \Delta\gamma) = \Phi\left(\boldsymbol{\sigma}\right) - \sigma_{\text{y}}\left(\Delta\gamma\right)\,, \quad \mathbf{G}(\boldsymbol{\sigma}, \Delta\gamma) = \Delta\boldsymbol{\varepsilon}^{\text{p}}(\boldsymbol{\sigma}) - \Delta\gamma\frac{\partial f}{\partial\boldsymbol{\sigma}}\,. \tag{3.156}$$

   $\Delta\gamma = \Delta t\dot{\gamma}$ is the incremental consistency parameter. The main goal here is to find a $\boldsymbol{\sigma}$ and $\Delta\gamma$, which reduce the calculated residuals. This is achieved in an iterative procedure:

$$\boldsymbol{\sigma}^{(k+1)} = \boldsymbol{\sigma}^{(k)} + \Delta\boldsymbol{\sigma}\,, \qquad \Delta\gamma^{(k+1)} = \Delta\gamma^{(k)} + \Delta(\Delta\gamma)\,. \tag{3.157}$$

4. The achieve the above goal, the correct incremental consistency parameter $\Delta\gamma$, has to be found, which is in turn used to update all of the other quantities. The incremental change for the consistency parameter $\Delta(\Delta\gamma)$ is found by linearizing the residuals:

$$\Delta(\Delta\gamma) = \frac{f^{(k)} - \mathbf{G}^{(k)} : \mathscr{L}^{(k)} : \frac{\partial\Phi^{(k)}}{\partial\boldsymbol{\sigma}}}{\frac{\partial\Phi^{(k)}}{\partial\boldsymbol{\sigma}} : \mathscr{L}^{(k)} : \frac{\partial\Phi^{(k)}}{\partial\boldsymbol{\sigma}} + {H_{(k)}}'} \tag{3.158}$$

The inverse of the Hessian of the return mapping algorithm $\mathscr{L}^{(k)}$ is calculated as follows:

$$\mathscr{L}^{(k)^{-1}} = \mathbb{C}^{-1} + \Delta\gamma^{(k)} \frac{\partial \Phi^{(k)}}{\partial \boldsymbol{\sigma} \partial \boldsymbol{\sigma}} \,. \tag{3.159}$$

The plastic strain increment $\Delta\boldsymbol{\varepsilon}^{\mathrm{p}}$ and the slope of hardening curve ${H_{(k)}}'$ at $\bar{\varepsilon}^{\mathrm{p}}_{(k)} = \bar{\varepsilon}^{\mathrm{p}}_{n} + \Delta\gamma^{(k)}$ are defined to be:

$$\Delta\boldsymbol{\varepsilon}^{\mathrm{p}}_{(k)} = -\mathbb{C}^{-1} : (\boldsymbol{\sigma}^{(k)} - \boldsymbol{\sigma}^{\mathrm{tr}}) \,, \qquad {H_{(k)}}' = \frac{\mathrm{d}\sigma_{\mathrm{y}}}{\mathrm{d}\bar{\varepsilon}^{\mathrm{p}}} \left(\bar{\varepsilon}^{\mathrm{p}}_{(k)} \right) . \tag{3.160}$$

5. The next step consists of updating the stress increment:

$$\Delta\boldsymbol{\sigma} = -\mathscr{L}^{(k)} : \left(\mathbf{G}^{(k)} + \Delta(\Delta\gamma) \frac{\partial \Phi^{(k)}}{\partial \boldsymbol{\sigma}} \right) . \tag{3.161}$$

6. The iterative process stops when convergence is reached. For this purpose, the measure $\psi^{(k)}$ is constructed, which is the combination of the two residuals:

$$\psi^{(k)} = \frac{1}{2} \left[\mathbf{G}^{(k)} : \mathbf{G}^{(k)} + \left(\frac{f^{(k)}}{2\mu} \right)^2 \right] \tag{3.162}$$

$\psi^{(k)}$ is non-dimensional since it is scaled with the shear modulus μ and is used to check if the results are within the desired tolerance. If this is the case, then the end of increment is reached, and all quantities are updated. On the other hand, if the total residual is still not within the tolerance, then the iteration is repeated from step 3.

The algorithm demonstrated in the box 3.3 uses the full step size determined in the Newton-Raphson iteration. However, it has been observed and shown numerous times that the Newton-Raphson algorithm does not always converge for non-quadratic yield functions. To remedy this problem, in [153], it is suggested to adopt the line search modification, which modifies the step size based on a merit function. The employed line search method is explained in the box 3.4.

Box. 3.4: Line search method adopted to improve the convergence behavior of the return mapping algorithm [153].

1. As explained above, the main difference is that the line search method does not always use the full step size determined in the Newton-Raphson iteration for updating the quantities. Instead, the modified step size $\alpha^{(k)}$ is used:

$$\boldsymbol{\sigma}^{(k+1)} = \boldsymbol{\sigma}^{(k)} + \alpha^{(k)} \Delta\boldsymbol{\sigma} \,, \qquad \Delta\gamma^{(k+1)} = \Delta\gamma^{(k)} + \alpha^{(k)} \Delta(\Delta\gamma) \,. \tag{3.163}$$

Thus, the goal becomes the determination of the proper step size $\alpha^{(k)}$. This can be achieved by finding a step size $\alpha^{(k)}$ that minimizes $\psi^{(k)}(\alpha^{(k)})$. This is not an easy task. However, instead of the exact function $\psi^{(k)}$, it is also possible to make use of an approximation and make sure that the new step size $\alpha^{(k)}$ sufficiently improves the results.

2. In the proposed method, the residual function $\psi^{(k)}$ is approximated as a quadratic function. With this assumption, the minimum is calculated as follows:

$$\alpha^{(k)} = \frac{\psi^{(k)}(0)}{\psi^{(k)}(0) + \psi^{(k)}(1)} \tag{3.164}$$

$\psi^{(k)}(0)$ and $\psi^{(k)}(1)$ are the residual for $\alpha^{(k)} = 0$ and $\alpha^{(k)} = 1$, respectively. If the newly determined step size $\alpha^{(k)}$ does not result in a sufficient decrease of the residual $\psi^{(k)}$, then subsequent iterations are needed:

$$\alpha^{(k)}_{(j+1)} = \frac{\psi^{(k)}(0)}{\psi^{(k)}(0) + \psi^{(k)}(\alpha^{(k)}_{(j)})} \tag{3.165}$$

3. A sufficient decrease of the residual function $\psi^{(k)}$ is obtained if the following conditions are satisfied:

$$\psi^{(k)}_{(j+1)} < \left(1 - 2\beta\alpha^{(k)}_{(j)}\right)\psi^{(k)}_{(j)}\,, \qquad \alpha^{(k)}_{(j+1)} = \max\left\{\eta\alpha^{(k)}_{(j)}, \alpha^{(k)}_{(j+1)}\right\}\,. \tag{3.166}$$

In this work, the parameters β and η are set to be 10^{-4} and 0.1, respectively.

3.3.9 Consistent elasto-plastic tangent operator

To preserve the quadratic rate of asymptotic convergence of Newton's method, it is essential to use the CEPT during the numerical integration, which is sometimes referred to as the algorithmic tangent [134]. The starting point for the derivation of the CEPT is the following equation [132, 134, 170], similar to eq. 3.161:

$$\mathrm{d}\boldsymbol{\sigma}^{n+1} = \mathscr{L}^{n+1} : \left(\mathrm{d}\boldsymbol{\varepsilon}^{n+1} - \Delta(\Delta\gamma)\frac{\partial\Phi^{n+1}}{\partial\boldsymbol{\sigma}}\right)\,. \tag{3.167}$$

By enforcing the consistency condition

$$\mathrm{d}f(\boldsymbol{\sigma}^{n+1}) = \frac{\partial\Phi^{n+1}}{\partial\boldsymbol{\sigma}}\mathrm{d}\boldsymbol{\sigma}^{n+1} - {H_{n+1}}'\Delta(\Delta\gamma) = 0\,, \tag{3.168}$$

and substituting eq. (3.167) in eq. (3.168) it is possible to obtain the incremental change of the consistency parameter:

$$\Delta(\Delta\gamma) = \frac{\frac{\partial\Phi^{n+1}}{\partial\boldsymbol{\sigma}} : \mathscr{L}^{n+1} : \mathrm{d}\boldsymbol{\varepsilon}^{n+1}}{\frac{\partial\Phi^{n+1}}{\partial\boldsymbol{\sigma}} : \mathscr{L}^{n+1} : \frac{\partial\Phi^{n+1}}{\partial\boldsymbol{\sigma}} + {H_{n+1}}'} \tag{3.169}$$

In the next step, the incremental change of the consistency parameter in eq. (3.167) is replaced with the eq. (3.169):

$$\mathrm{d}\boldsymbol{\sigma}^{n+1} = \mathscr{L}^{n+1} : \left(\mathrm{d}\boldsymbol{\varepsilon}^{n+1} - \frac{\frac{\partial \Phi^{n+1}}{\partial \boldsymbol{\sigma}} : \mathscr{L}^{n+1} : \mathrm{d}\boldsymbol{\varepsilon}^{n+1}}{\frac{\partial \Phi^{n+1}}{\partial \boldsymbol{\sigma}} : \mathscr{L}^{n+1} : \frac{\partial \Phi^{n+1}}{\partial \boldsymbol{\sigma}} + {H_{n+1}}'} \frac{\partial \Phi^{n+1}}{\partial \boldsymbol{\sigma}} \right) . \tag{3.170}$$

The results of the last step are rearranged using the following expression:

$$\mathrm{d}\boldsymbol{\sigma}^{n+1} = \mathbb{C}^{\mathrm{ep}} : \mathrm{d}\boldsymbol{\varepsilon}^{n+1} . \tag{3.171}$$

Thus, the CEPT reads:

$$\frac{\mathrm{d}\boldsymbol{\sigma}^{n+1}}{\mathrm{d}\boldsymbol{\varepsilon}^{n+1}} = \mathbb{C}^{\mathrm{ep}} = \mathscr{L}^{n+1} - \frac{\left(\mathscr{L}^{n+1} : \frac{\partial \Phi^{n+1}}{\partial \boldsymbol{\sigma}} \right) \otimes \left(\mathscr{L}^{n+1} : \frac{\partial \Phi^{n+1}}{\partial \boldsymbol{\sigma}} \right)}{\frac{\partial \Phi^{n+1}}{\partial \boldsymbol{\sigma}} : \mathscr{L}^{n+1} : \frac{\partial \Phi^{n+1}}{\partial \boldsymbol{\sigma}} + {H_{n+1}}'} . \tag{3.172}$$

3.3.10 Complete Abaqus/UMAT implementation

Box. 3.5: Algorithmic steps implemented in UMAT.

1. The following quantities are provided in Abaqus UMAT at the start of increment for each integration point:

    - Deformation gradients $\mathbf{F}^n$ and $\mathbf{F}^{n+1}$
    - Cauchy stress tensor in the global frame $\boldsymbol{\sigma}^n$
    - Rotation tensor $\mathbf{R}^n$
    - Incremental consistency parameter $\Delta\gamma^n$
    - Equivalent plastic strain $(\bar{\varepsilon}^{\mathrm{p}})^n$
    - Plastic strain increment in global frame $(\Delta\boldsymbol{\varepsilon}^{\mathrm{p}})^n$

    It should be noted that some of the quantities are defined by the user as the state variables (SDVs). More importantly, the superscript n and $n+1$ denote the quantities at the start and end of the increment, respectively. Moreover, quantities in the rotated coordinate frame are characterized by ˆ over their respective symbols in order to separate them from the quantities defined in the global coordinate frame. It should be noted that in Abaqus UMAT, the updated stress tensor and the CEPT have to be returned in the global coordinate frame.

2. The velocity gradient increment is calculated using the deformation gradient tensors $\mathbf{F}^n$ and $\mathbf{F}^{n+1}$ combined with the approximation derived in [134]. Afterwards, the velocity gradient tensor is split into its symmetric and antisymmetric parts:

    $$\Delta\mathbf{L}^{n+1} = \Delta\mathbf{D}^{n+1} + \Delta\mathbf{W}^{n+1} . \tag{3.173}$$

3. In order to calculate the rotation tensors $\mathbf{R}^{n+\frac{1}{2}}$ and $\mathbf{R}^{n+1}$, first, the incremental plastic spin tensor $(\Delta\mathbf{W}^{\mathrm{p}})^{n+1}$ has to be determined. This is achieved

by using the plastic strain increment $(\Delta\boldsymbol{\varepsilon}^{\mathrm{p}})^n$ and the incremental consistency parameter $\Delta\gamma^n$ combined with the expressions derived in section 3.3.7.2 and 3.4.2.4. Afterwards, with

$$(\Delta\mathbf{W}^{\mathrm{e}})^{n+1} = \Delta\mathbf{W}^{n+1} - (\Delta\mathbf{W}^{\mathrm{p}})^{n+1} \,, \tag{3.174}$$

and the integration algorithms presented in section 3.3.4 all rotation matrices can be easily calculated, which are required for the transformation of the quantities between the locally rotating CCO and global frame. Moreover, by making use of the relations derived in section 3.3.4, it is then possible to rotate the vectors and tensors. The following transformation is shown as an example:

$$\hat{\boldsymbol{\sigma}}^n = (\mathbf{R}^n)^{\mathrm{T}} \cdot \boldsymbol{\sigma}^n \cdot \mathbf{R}^n \,. \tag{3.175}$$

4. The trial stress $\hat{\boldsymbol{\sigma}}^{\mathrm{tr}}$ in the rotated coordinate frame is calculated using the algorithm derived in section 3.3.4. The eq. (3.103) is adopted, which makes use of the midpoint rule:

   $$\hat{\boldsymbol{\sigma}}^{\mathrm{tr}} = \hat{\boldsymbol{\sigma}}_n + \Delta t\, \mathbb{C} : \hat{\mathbf{D}}_{n+\frac{1}{2}} \,. \tag{3.176}$$

5. After calculating the trial stress $\hat{\boldsymbol{\sigma}}^{\mathrm{tr}}$ in the rotated coordinate frame, the yield condition is checked:

   $$f(\hat{\boldsymbol{\sigma}}^{\mathrm{tr}}, \bar{\varepsilon}^{\mathrm{p}}_n) = \Phi\left(\hat{\boldsymbol{\sigma}}^{\mathrm{tr}}\right) - \sigma_{\mathrm{y}}\left(\bar{\varepsilon}^{\mathrm{p}}_n\right) \,. \tag{3.177}$$

   If $f(\hat{\boldsymbol{\sigma}}^{\mathrm{tr}}, \bar{\varepsilon}^{\mathrm{p}}_n) \leq 0$, then the strain increment is elastic. In such a case, the end of increment is reached, and the quantities can be updated as follows $\hat{\boldsymbol{\sigma}}^{n+1} = \hat{\boldsymbol{\sigma}}^{\mathrm{tr}}$ and $\bar{\varepsilon}^{\mathrm{p}}_{n+1} = \bar{\varepsilon}^{\mathrm{p}}_n$. If $f(\hat{\boldsymbol{\sigma}}^{\mathrm{tr}}, \bar{\varepsilon}^{\mathrm{p}}_n) > 0$ holds true, then plastic deformation has occurred, and a return mapping algorithm is employed. The iterative procedure afterward is exactly as described in the box 3.3 and 3.4.

6. The iterative process in the last step comes to an end if convergence is reached. If this is the case, then the quantities in the rotated coordinate frame are updated for the last time, and the required CEPT is calculated as shown in eq. (3.172):

   $$\hat{\mathbb{C}}^{\mathrm{ep}} = \hat{\mathscr{L}}^{n+1} - \frac{\left(\hat{\mathscr{L}}^{n+1} : \frac{\partial\Phi^{n+1}}{\partial\hat{\boldsymbol{\sigma}}}\right) \otimes \left(\hat{\mathscr{L}}^{n+1} : \frac{\partial\Phi^{n+1}}{\partial\hat{\boldsymbol{\sigma}}}\right)}{\frac{\partial\Phi^{n+1}}{\partial\hat{\boldsymbol{\sigma}}} : \hat{\mathscr{L}}^{n+1} : \frac{\partial\Phi^{n+1}}{\partial\hat{\boldsymbol{\sigma}}} + {H_{n+1}}'} \,. \tag{3.178}$$

7. In the last step, all the quantities are rotated back to the global frame using the relations in section 3.3.4 and are either returned as output ($\boldsymbol{\sigma}^{n+1}$ and $\mathbb{C}^{\mathrm{ep}}$) to Abaqus or stored as SDVs ($\Delta\gamma^{n+1}$, $\mathbf{R}^{n+1}$, $(\bar{\varepsilon}^{\mathrm{p}})^{n+1}$, and $(\Delta\boldsymbol{\varepsilon}^{\mathrm{p}})^{n+1}$) for the next increment. It should be noted that even though $\boldsymbol{\sigma}^{n+1}$ is returned

to Abaqus in the global frame, in the next increment, the stress tensor $\boldsymbol{\sigma}^n$ is rotated internally by Abaqus using the Hughes-Winget approximation shown in eq. (3.109). This is the case when `NLGEOM=ON` and has to be accounted for. For more details, see Abaqus documentation [171].

3.3.11 A summary of the macroscale model equations

The continuum mechanics elastoplasticity model consists of the following system of governing equations

$$\begin{cases} \mathbf{F} = \mathbf{F}^{\mathrm{e}} \cdot \mathbf{F}^{\mathrm{p}} & \text{Multiplicative decomposition} \\ \nabla \cdot \boldsymbol{\sigma} = 0 & \text{Mechanical equilibrium} \\ \dot{\hat{\boldsymbol{\sigma}}} = \mathbb{C} : \left[\hat{\mathbf{D}} - \hat{\mathbf{D}}^{\mathrm{p}}\right] & \text{Hypoelastic stress-strain relation} \\ \dot{\hat{\boldsymbol{\sigma}}} = \mathbf{R}^{\mathrm{T}} \cdot \overset{\triangledown}{\boldsymbol{\sigma}} \cdot \mathbf{R}, \overset{\triangledown}{\boldsymbol{\sigma}} = [\dot{\boldsymbol{\sigma}} + \boldsymbol{\sigma} \cdot \mathbf{W} - \mathbf{W} \cdot \boldsymbol{\sigma}] & \text{Corotational formulation} \\ f(\hat{\boldsymbol{\sigma}}, \bar{\varepsilon}^{\mathrm{p}}) = \Phi\left(\hat{\boldsymbol{\sigma}}\right) - \sigma_{\mathrm{y}}\left(\bar{\varepsilon}^{\mathrm{p}}\right) & \text{Yield function} \\ f(\hat{\boldsymbol{\sigma}}, \bar{\varepsilon}^{\mathrm{p}}) = 0 & \text{Yield condition} \\ \hat{\mathbf{D}}^{\mathrm{p}} = \dot{\gamma} \frac{\partial f}{\partial \hat{\boldsymbol{\sigma}}} & \text{Plastic flow rule} \\ \dot{\boldsymbol{\alpha}} = \dot{\gamma} \frac{\partial f}{\partial \boldsymbol{A}} & \text{Hardening rule} \\ \hat{\mathbf{W}}^{\mathrm{p}} = \text{Function}(\hat{\mathbf{D}}^{\mathrm{p}}, \dot{\gamma}) & \text{Plastic spin evolution} \\ \mathbf{W}^{\mathrm{e}} = \mathbf{W} - \mathbf{W}^{\mathrm{p}}\,, \dot{\mathbf{R}} = \mathbf{W}^{\mathrm{e}} \cdot \mathbf{R}, \mathbf{R}|_{t=0} = \mathbf{I} & \text{Rotation matrix evolution} \\ \dot{\gamma} \geq 0\,, f \leq 0\,, \dot{\gamma} f = 0 & \text{KKT conditions} \end{cases} \tag{3.179}$$

that employs for the constitutive model the following specifications
(a) for the effective stress:

$$\Phi\left(\boldsymbol{\sigma}\right) = \left\{ \frac{1}{4} \left[|s_1' - s_1''|^a + |s_1' - s_2''|^a + |s_1' - s_3''|^a + |s_2' - s_1''|^a + \right.\right.$$

$$\left.\left. |s_2' - s_2''|^a + |s_2' - s_3''|^a + |s_3' - s_1''|^a + |s_3' - s_2''|^a + |s_3' - s_3''|^a \right] \right\}^{1/a} . \tag{3.180}$$

where s_i' and s_j'' $(i, j = 1, 2, 3)$ are the principal values of tensors $\mathbf{s}'$ and $\mathbf{s}''$.

$$\mathbf{s}' = \mathbf{C}' : \mathbf{s}\,, \qquad \mathbf{s}'' = \mathbf{C}'' : \mathbf{s}\,, \qquad \mathbf{s} = \sigma - \frac{1}{3}(\mathbf{I} : \sigma)\mathbf{I}. \tag{3.181}$$

and
(b) for the hardening function:

$$\sigma_{\mathrm{y}}\left(\bar{\varepsilon}^{\mathrm{p}}\right) = \begin{cases} \sigma_0 + K\left(\bar{\varepsilon}^{\mathrm{p}}\right)^n & \text{for } \bar{\varepsilon}^{\mathrm{p}} \leq \bar{\varepsilon}_{\mathrm{L1}} \\ \sigma_{\mathrm{y}}\left(\bar{\varepsilon}_{\mathrm{L1}}\right) + L\left(\bar{\varepsilon}^{\mathrm{p}} - \bar{\varepsilon}_{\mathrm{L1}}\right)\left(1 - \frac{\bar{\varepsilon}^{\mathrm{p}} - \bar{\varepsilon}_{\mathrm{L1}}}{2(\bar{\varepsilon}_{\mathrm{L2}} - \bar{\varepsilon}_{\mathrm{L1}})}\right) & \text{for } \bar{\varepsilon}_{\mathrm{L1}} < \bar{\varepsilon}^{\mathrm{p}} \leq \bar{\varepsilon}_{\mathrm{L2}} \\ \sigma_{\mathrm{y}}\left(\bar{\varepsilon}_{\mathrm{L2}}\right) & \text{for } \bar{\varepsilon}^{\mathrm{p}} > \bar{\varepsilon}_{\mathrm{L2}} \end{cases} . \tag{3.182}$$

3.3.11.1 Incremental form

$$\mathbf{L}_{n+\frac{1}{2}} = \mathbf{D}_{n+\frac{1}{2}} + \mathbf{W}_{n+\frac{1}{2}} \,. \tag{3.183}$$

$$\mathbf{W}^{\mathrm{p}}{}_{n+\frac{1}{2}} = \mathrm{Function}(\mathbf{D}^{\mathrm{p}}_{n}, \Delta\gamma_n) \,. \tag{3.184}$$

$$\mathbf{W}^{\mathrm{e}}{}_{n+\frac{1}{2}} = \mathbf{W}_{n+\frac{1}{2}} - \mathbf{W}^{\mathrm{p}}{}_{n+\frac{1}{2}} \,. \tag{3.185}$$

$$\mathbf{R}_{n+\frac{1}{2}} = \exp\left[\frac{\Delta t}{2}\mathbf{W}^{\mathrm{e}}_{n+\frac{1}{2}}\right]\cdot\mathbf{R}_n \,, \qquad \mathbf{R}_{n+1} = \exp\left[\Delta t\mathbf{W}^{\mathrm{e}}_{n+\frac{1}{2}}\right]\cdot\mathbf{R}_n \,. \tag{3.186}$$

$$\hat{\mathbf{D}}_{n+\frac{1}{2}} = \mathbf{R}^{\mathrm{T}}_{n+\frac{1}{2}} \cdot \mathbf{D}_{n+\frac{1}{2}} \cdot \mathbf{R}_{n+\frac{1}{2}} \,. \tag{3.187}$$

$$\Delta\hat{\boldsymbol{\varepsilon}} = \Delta t \, \hat{\mathbf{D}}_{n+\frac{1}{2}} \,. \tag{3.188}$$

$$\hat{\boldsymbol{\sigma}}_n = \mathbf{R}^{\mathrm{T}}_n \cdot \boldsymbol{\sigma}_n \cdot \mathbf{R}_n \,. \tag{3.189}$$

$$\hat{\boldsymbol{\sigma}}_{n+1} = \mathbf{R}^{\mathrm{T}}_{n+1} \cdot \boldsymbol{\sigma}_{n+1} \cdot \mathbf{R}_{n+1} \,. \tag{3.190}$$

$$\Delta\hat{\boldsymbol{\varepsilon}}^{\mathrm{p}} = \Delta\gamma_{n+1}\frac{\partial f}{\partial\hat{\boldsymbol{\sigma}}_{n+1}} \,. \tag{3.191}$$

$$\hat{\boldsymbol{\sigma}}_{n+1} = \hat{\boldsymbol{\sigma}}_n + \mathbb{C} : \left(\Delta\hat{\boldsymbol{\varepsilon}} - \Delta\hat{\boldsymbol{\varepsilon}}^{\mathrm{p}}\right) \,. \tag{3.192}$$

The following expressions define a non-linear system of equations for the determination of the unknown $\hat{\boldsymbol{\sigma}}_{n+1}$ and $\Delta\gamma_{n+1}$.

$$f(\hat{\boldsymbol{\sigma}}_{n+1}, \Delta\gamma_{n+1}) = \Phi\left(\hat{\boldsymbol{\sigma}}_{n+1}\right) - \sigma_{\mathrm{y}}\left(\bar{\varepsilon}^{\mathrm{p}}_n + \Delta\gamma_{n+1}\right) = 0 \,, \tag{3.193}$$

$$\mathbf{G}(\hat{\boldsymbol{\sigma}}_{n+1}, \Delta\gamma_{n+1}) = \hat{\boldsymbol{\sigma}}_{n+1} - \hat{\boldsymbol{\sigma}}_n - \mathbb{C} : (\Delta\hat{\varepsilon}_{n+\frac{1}{2}} - \Delta\gamma_{n+1}\frac{\partial f}{\partial\hat{\boldsymbol{\sigma}}_{n+1}}) = \mathbf{0} \,, \tag{3.194}$$

with

$$\Delta\bar{\varepsilon}^{\mathrm{p}} = \Delta\gamma_{n+1} \,, \tag{3.195}$$

$$\Delta\gamma_{n+1} \geq 0 \,, \tag{3.196}$$

$$f\Delta\gamma_{n+1} = 0 \,. \tag{3.197}$$

3.3.11.2 Return mapping algorithm

(i) Calculate trial stress $\hat{\boldsymbol{\sigma}}^{\mathrm{tr}}$:

$$\hat{\boldsymbol{\sigma}}^{\mathrm{tr}} = \hat{\boldsymbol{\sigma}}^{n} + \mathbb{C} : \Delta\hat{\boldsymbol{\varepsilon}} \,. \tag{3.198}$$

(ii) Check yield condition:

$$f(\hat{\boldsymbol{\sigma}}^{\mathrm{tr}}, \bar{\varepsilon}^{\mathrm{p}}_{n}) = \Phi\left(\hat{\boldsymbol{\sigma}}^{\mathrm{tr}}\right) - \sigma_{\mathrm{y}}\left(\bar{\varepsilon}^{\mathrm{p}}_{n}\right) \,. \tag{3.199}$$

(iii) If $f(\hat{\boldsymbol{\sigma}}^{\mathrm{tr}}, \bar{\varepsilon}^{\mathrm{p}}_{n}) \leq 0$, then the strain increment is elastic:

$$\hat{\boldsymbol{\sigma}}^{n+1} = \hat{\boldsymbol{\sigma}}^{\mathrm{tr}} \,, \tag{3.200}$$

$$\bar{\varepsilon}^{\mathrm{p}}_{n+1} = \bar{\varepsilon}^{\mathrm{p}}_{n} \,. \tag{3.201}$$

(iv) If $f(\hat{\boldsymbol{\sigma}}^{\mathrm{tr}}, \bar{\varepsilon}^{\mathrm{p}}_{n}) > 0$, then iterate over ${}^{(k)}$:

$$f^{(k)} = \Phi\left(\hat{\boldsymbol{\sigma}}^{(k)}\right) - \sigma_{\mathrm{y}}\left(\bar{\varepsilon}^{\mathrm{p}}_{n} + \Delta\gamma^{(k)}\right) \,, \tag{3.202}$$

$$\mathbf{G}^{(k)} = -\mathbb{C}^{-1} : (\boldsymbol{\sigma}^{(k)} - \boldsymbol{\sigma}^{\mathrm{tr}}) - \Delta\gamma^{(k)} \frac{\partial f^{(k)}}{\partial \hat{\boldsymbol{\sigma}}} \,, \tag{3.203}$$

$$\psi^{(k)} = \frac{1}{2}\left[\mathbf{G}^{(k)} : \mathbf{G}^{(k)} + \left(\frac{f^{(k)}}{2\mu}\right)^{2}\right] \,. \tag{3.204}$$

If $\psi^{(k)} \leq \varepsilon^{\mathrm{Tol}}$ go to (v), otherwise continue:

$$\mathscr{L}^{(k)^{-1}} = \mathbb{C}^{-1} + \Delta\gamma^{(k)} \frac{\partial f^{(k)}}{\partial \hat{\boldsymbol{\sigma}} \partial \hat{\boldsymbol{\sigma}}} \,, \tag{3.205}$$

$$H_{(k)}{}' = \frac{\mathrm{d}\sigma_{\mathrm{y}}}{\mathrm{d}\bar{\varepsilon}^{\mathrm{p}}}\left(\bar{\varepsilon}^{\mathrm{p}}_{n} + \Delta\gamma^{(k)}\right) \,, \tag{3.206}$$

$$\Delta(\Delta\gamma) = \frac{f^{(k)} - \mathbf{G}^{(k)} : \mathscr{L}^{(k)} : \frac{\partial f^{(k)}}{\partial \hat{\boldsymbol{\sigma}}}}{\frac{\partial f^{(k)}}{\partial \hat{\boldsymbol{\sigma}}} : \mathscr{L}^{(k)} : \frac{\partial f^{(k)}}{\partial \hat{\boldsymbol{\sigma}}} + H_{(k)}{}'} \,, \tag{3.207}$$

$$\Delta\boldsymbol{\sigma} = -\mathscr{L}^{(k)} : \left(\mathbf{G}^{(k)} + \Delta(\Delta\gamma) \frac{\partial \Phi^{(k)}}{\partial \boldsymbol{\sigma}}\right) \,, \tag{3.208}$$

$$\Delta\gamma^{(k+1)} = \Delta\gamma^{(k)} + \Delta(\Delta\gamma) \,, \tag{3.209}$$

$$\boldsymbol{\sigma}^{(k+1)} = \boldsymbol{\sigma}^{(k)} + \Delta\boldsymbol{\sigma} \,. \tag{3.210}$$

Go to (iv).

(v) End of increment is reached and all quantities are updated.

3.3.11.3 The incremental finite element formulation

The Newton-Raphson scheme used for the solution of the incremental nonlinear finite element formulation based on [132]:

(i) Calculate internal and external forces used for the calculation of the residual vector:

$$\mathbf{f}_{(\mathrm{e})}^{\mathrm{int}} = \int_{\Omega_\mathrm{e}} \mathbf{B}^\mathrm{T}\, \boldsymbol{\sigma}_{n+1}\, \mathrm{d}V\,, \tag{3.211}$$

$$\mathbf{f}_{(\mathrm{e})}^{\mathrm{ext}} = \int_{\partial\Omega_\mathrm{e}} \mathbf{N}^\mathrm{T}\, \mathbf{t}_{n+1}\, \mathrm{d}A\,, \tag{3.212}$$

$$\mathbf{r} = \mathbf{f}^{\mathrm{int}} - \mathbf{f}^{\mathrm{ext}}\,. \tag{3.213}$$

(ii) Determine element tangent stiffness matrices:

$$\mathbf{K}_{\mathrm{Tan}}^{(\mathrm{e})} = \int_{\Omega_\mathrm{e}} \mathbf{B}^\mathrm{T}\, \mathbb{C}_{n+1}^{\mathrm{ep}}\, \mathbf{B}\, \mathrm{d}V\,, \tag{3.214}$$

using CEPT:

$$\frac{\mathrm{d}\boldsymbol{\sigma}^{n+1}}{\mathrm{d}\boldsymbol{\varepsilon}^{n+1}} = \mathbb{C}_{n+1}^{\mathrm{ep}} = \mathscr{L}^{n+1} - \frac{\left(\mathscr{L}^{n+1} : \frac{\partial\Phi^{n+1}}{\partial\boldsymbol{\sigma}}\right) \otimes \left(\mathscr{L}^{n+1} : \frac{\partial\Phi^{n+1}}{\partial\boldsymbol{\sigma}}\right)}{\frac{\partial\Phi^{n+1}}{\partial\boldsymbol{\sigma}} : \mathscr{L}^{n+1} : \frac{\partial\Phi^{n+1}}{\partial\boldsymbol{\sigma}} + {H_{n+1}}'}\,. \tag{3.215}$$

(iii) Determine increment of the displacement vector:

$$\mathbf{K}_{\mathrm{Tan}}\, \delta\mathbf{u}^{(k+1)} = -\mathbf{r}^{(k)}\,. \tag{3.216}$$

(iv) Update the displacement vector:

$$\mathbf{u}_{n+1}^{(k+1)} = \mathbf{u}_{n+1}^{(k)} + \delta\mathbf{u}^{(k+1)}\,. \tag{3.217}$$

(v) Update all other quantities using the new displacement vector and go to (i). Repeat these steps until $\frac{||\mathbf{r}||}{||\mathbf{f}^{\mathrm{ext}}||} \leq \varepsilon^{\mathrm{Tol}}$.

3.4 Scale bridging approach and the calibration procedure

In this section, the calibration process and the fusion of the micro and macroscale model are discussed. The main motivations behind this multi-scale approach are increasing the simulation accuracy and, at the same time, reducing all the experimental efforts. These goals are achieved by the determination of the required material parameters of the macroscale model using the calibrated and validated CP model. This is possible since the CP model is capable of capturing the underlying physical phenomena at the microscale and, thus, can be used to conduct virtual experiments. The parameters required for the microscale simulations are as follows:

1. The SCECs of LPBF316L, which are taken from literature [172].
2. The parameters of the phenomenological CP model (section 3.2.3), which are calibrated using tensile tests.

The macroscale model explained in section 3.3 requires the following parameters for the simulation:

1. Homogenized elastic stiffness tensor $\mathbb{C}$.
2. Parameters for the chosen hardening model.
3. Parameters of the Barlat yield function Yld2004-18p.
4. Parameters of the plastic spin model $\hat{\mathbf{W}}^{\mathrm{p}}$.

The parameters for the macroscale model can also be obtained by making use of actual experiments. However, this approach would require a significant increase in the number of experiments and would render this material model impractical because of the immense cost and time required for conducting such investigations. However, by using virtual experiments, these complex models regain their strength since the calibration process is no longer a strong barrier. It should be noted that the four parameter sets for the macroscale model are extracted from different CP simulations. Consequently, these virtual experiments automatically establish a link between micro and macroscale. In the following sections, the necessary steps required to extract all model parameters are explained in detail.

3.4.1 Estimating the elastic properties of a polycrystal

The first step in establishing a link between micro and macroscale is the determination of the homogenized elastic properties of LPBF316L. This step is crucial since predicting the anisotropic material behavior of LPBF316L at the macroscale is one of the main objectives of this work and is strongly influenced by its elastic response. Thus, the elastic anisotropy has to be determined with high accuracy for the whole multi-scale framework to succeed. Experimentally, this goal can be achieved using the resonance method [108]. However, for the determination of the entire elastic stiffness tensor, the resonance method requires many samples with different inclinations, which is not feasible, especially for AM materials. Fortunately, there is where the multi-scale simulation approach shines since by only having the initial crystallographic texture and SCEC, this issue can be solved.

The elastic properties of the grains inside of a FCC single-phase polycrystalline material can be described using three elastic constants, C_{11}, C_{12}, and C_{44}, which are also called the SCEC. These values can be used to assemble the elastic tensor $\mathbb{C}_{\text{crystal}}$. Using this tensor, one can predict the anisotropic elastic response of a single crystal for any desired loading direction. However, as mentioned before, a polycrystalline material contains a large number of grains. These grains each have a specific orientation and act as a single crystal. To predict the elastic response of a polycrystalline material, different methods were developed, which use the crystallographic texture and the single crystal elastic constants as input data and deliver the homogenized elastic stiffness tensor $\mathbb{C}_{\text{polycrystal}}$ for the whole polycrystal [173]. The difference between these methods is that each of them uses different assumptions for the calculation of the average properties. Besides the CP model explained in section 3.2.3, three famous approaches exist for this purpose, namely Voigt [174], Hill [175], and Reuss [176]. The Voigt model is based on the assumption that everywhere the strain field is homogeneous and is equal to the macroscopic strain tensor. This assumption implicates that the same strain field is applied to all of the grains. Thus, the volume average is defined as follows [173]:

$$\left\langle \mathbf{T}^{\text{Voigt}} \right\rangle = \sum_{m=1}^{M} V_m \mathbf{T}(g_m^c)\,. \tag{3.218}$$

$\mathbf{T}^{\text{Voigt}}$, V_m, and $\mathbf{T}(g_m^c)$ are the average tensor, the volume fraction of the grain m, and the individual tensor with crystal orientation g_m^c, respectively. In the Reuss model, on the other hand, it is assumed that the stress field is constant in the specimen. Thus, the same stress tensor is applied to all of the grains. The average tensor is then calculated by averaging the inverses of the individual tensors [173]:

$$\left\langle \mathbf{T}^{\text{Reuss}} \right\rangle = \left[\sum_{m=1}^{M} V_m \mathbf{T}^{-1}(g_m^c) \right]^{-1}\,. \tag{3.219}$$

Both these assumptions do not represent reality and describe the average bounds. The experimentally determined elastic properties usually lie in between the estimated values for these models. In the Hill model, the average tensor from the Voigt and Reuss models is calculated:

$$\left\langle \mathbf{T}^{\text{Hill}} \right\rangle = \frac{1}{2}\left(\left\langle \mathbf{T}^{\text{Voigt}} \right\rangle + \left\langle \mathbf{T}^{\text{Reuss}} \right\rangle \right)\,. \tag{3.220}$$

Note that the Hill model is much closer to reality but has no theoretical justification [173]. All of these models are implemented in the software MTEX [147]. The following elastic stiffness tensor $\mathbb{C}$ written in Voigt notation is used for all Abaqus simulations (same x, y, and z coordinate system as in fig. 2.1):

$$\mathbb{C} = \begin{bmatrix} 268 & 93 & 110 & 0 & 0 & 0 \\ 93 & 269 & 110 & 0 & 0 & 0 \\ 110 & 110 & 252 & 0 & 0 & 0 \\ 0 & 0 & 0 & 76 & 0 & 0 \\ 0 & 0 & 0 & 0 & 76 & 0 \\ 0 & 0 & 0 & 0 & 0 & 62 \end{bmatrix} \text{ in GPa}\,. \tag{3.221}$$

The above homogenized elastic stiffness tensor $\mathbb{C}$ is determined using the EBSD measurement from Tower 45° combined with the SCECs of LPBF316L taken from [172]. Moreover, the above elastic stiffness tensor $\mathbb{C}$ is the result of the Hill model.

3.4.2 Parameter identification procedure

To have accurate simulation results, the simulation softwares (DAMASK [71] and Abaqus [171]) have to be supplied with the correct input parameters. Each of them requires a different set of parameters, which have to be determined by either using the results from real or virtual experiments. Thus, in this section, a general calibration procedure is presented, which is then employed in the following sections. The identification of these parameters is achieved utilizing least-squares-based regression analysis. After defining the residual

$$\begin{aligned} &\text{minimize } \mathcal{F}(\mathbf{p}) = \frac{1}{2}\sum_{i=1}^{N} w_i (f_i(\mathbf{p}) - y_i)^2\,, \\ &\text{by changing } \mathbf{p} \in S\,, \\ &\text{such that } g_j(\mathbf{p}) \leq 0, j = 1, ..., n_{\mathrm{g}}\,, \end{aligned} \tag{3.222}$$

the Levenberg-Marquardt scheme [177, 178] is used to minimize it. $\mathcal{F}$, g_j, $\mathbf{p}$, and w_i are the residual function, the vector of constraints, the vector containing the parameters to be optimized, and the weight associated with the experiment i, respectively. Moreover, $f_i(\mathbf{p})$ and y_i are the values extracted from the numerical simulations and the corresponding target values. These can for example be the simulated ($f_i(\mathbf{p})$) and the experimental (y_i) stress-strain values. Depending on the parameters which have to be optimized, the vector $\mathbf{p}$ contains, for example, the CP model parameters n, h_0, a, τ_0, and τ_∞.

3.4.2.1 Parameters of the crystal plasticity model

The software DAMASK [71] has to be supplied with the SCEC, C_{11}, C_{12}, and C_{44}, for an FCC crystal and the five parameters (n, h_0, a, τ_0, and τ_∞) for the phenomenological CP model explained in section 3.2.3. The calibration of the CP model is straightforward, assuming that the RVE generated from texture data correctly represents the whole microstructure. One or more experimental data sets can be included during the calibration process. However, it should be noted that some data sets are also needed for the validation of these parameters. Therefore, for the CP model, only one tensile test (Tower 45°) and one EBSD measurement (Tower 45°) were used. Moreover, the strain was limited to the range between 0 and 1.5 %. The calibrated parameters are listed in table 3.1. In fig. 3.11, the accuracy of the calibration procedure is shown. It is evident that the CP model can at least capture the yield behavior of LPBF316L for this particular sample (Tower 45°). The validation and implication of these results are discussed in section 4. The parameters q and $\dot{\gamma}_0$ were set to a fixed value of 1.

Table 3.1: Calibrated parameters of the CP model for the 50 µm specimens.

n	h_0 (MPa)	a	τ_0 (MPa)	τ_∞ (MPa)
38	3160	9	263	1130

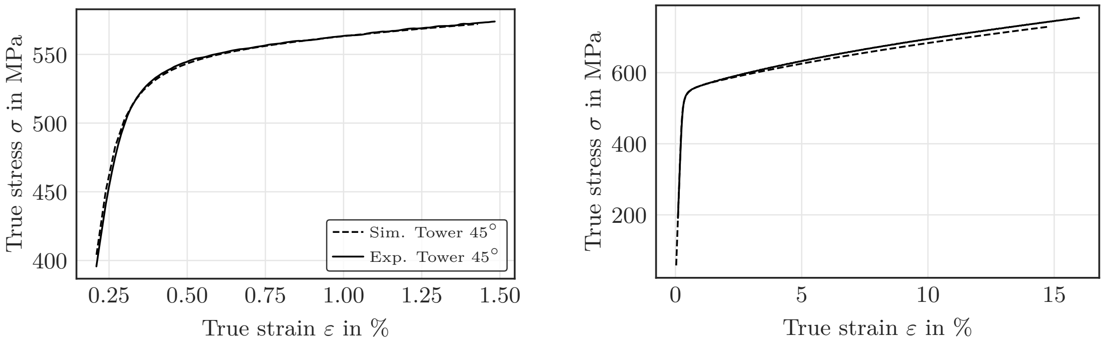

Figure 3.11: Comparison between stress-strain curves obtained experimentally from the 50 µm specimens and from the calibrated CP model.

It should be noted that for the numerical analysis of the lattice strain evolution, the CP model parameters are re-calibrated using the ex-situ stress-strain curves obtained for two 30 µm specimens instead of one 50 µm specimen. The re-calibrated stress-strain curves are shown in fig. 3.12. The parameters of the CP model are listed in table 3.2, which are only used for the simulation of the lattice evolution, see section 4.4. All other numerical simulations are conducted using the results for the 50 µm specimens.

Table 3.2: Calibrated parameters of the crystal plasticity model for the 30 µm specimens.

n	h_0 (MPa)	a	τ_0 (MPa)	τ_∞ (MPa)
79	1676	9	246	1227

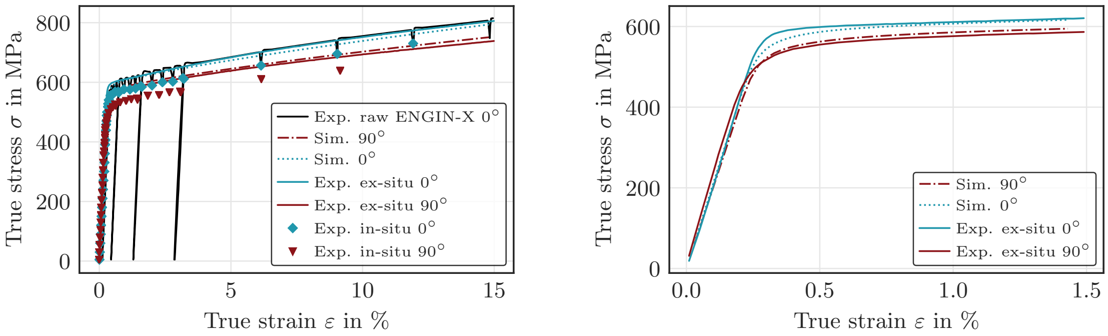

Figure 3.12: Comparison between experimental and numerical stress-strain curves obtained for tensile specimens manufactured from 30 µm walls. The crystal plasticity model was calibrated using the ex-situ tensile test results, see fig. 4.11.

3.4.2.2 Parameters of the Barlat yield function Yld2004-18p

The parameters of the Yld2004-18p model can be calibrated using the results from tension, shear, and bi-axial tests. With a growing number of experiments, the accuracy of the calibrated parameters increases. However, this comes at a cost. Both aspects, time and cost, have to be considered when planning and conducting such experiments. In recent years and with increasing accuracy of the numerical models, an alternative way of calibrating the yield function has emerged. The main idea is to use virtual experiments instead of real ones. For this purpose, a calibrated model is needed which is capable of accurately predicting the material response for any desired loading direction. In the last sections, it was explained that the CP model employed in this work is capable of both describing and predicting the elastic and plastic anisotropy. Thus, the same CP model can be used to conduct the necessary virtual experiments for extracting the parameters of the Barlat yield function Yld2004-18p. These efforts are necessary since due to the high computational cost, the CP model can only be used to accurately simulate the deformation behavior in small regions, such as the RVE employed in this work. However, additively manufactured parts are orders of magnitude larger than these RVEs. To overcome this constraint, such virtual-lab frameworks were developed [86,88], which allow these results to be transferred to the macroscale retaining high simulation accuracy with reduced computational cost.

In such a framework, the same RVE is subjected to many different random loading conditions, which cover the stress space with a sufficient number of resulting yield points. With these boundary conditions, it is possible to simulate tension, shear, and bi-axial tests or also construct loading conditions, which can not be tested in an actual experiment. However, it should be noted that the accuracy of the calibrated yield surface is heavily dependent on the accuracy of the CP model. After each simulation, the results are then averaged over the whole RVE. Furthermore, the average stress tensor at a specific value of plastic work per unit volume is used to determine the yield loci. The plastic work per unit volume can be experimentally determined, where its value is equal to the area under the true stress-strain curve obtained from a uniaxial tensile test [179, 180]. In this work, this value is set to 5 MPa, which corresponds to roughly 1 percent plastic strain. On the other hand, the plastic work per unit volume is numerically calculated using the eqs. (3.18) and (3.20) [86, 139, 181]:

$$\dot{w}^{\mathrm{p}} = \sum_{\alpha=1}^{N} \tau^{\alpha} \dot{\gamma}^{\alpha}, \tag{3.223}$$

where τ^{α}, $\dot{\gamma}^{\alpha}$, and N are the resolved shear stress, the slip rate, and the total number of slip systems, respectively. Hence, with a sufficient number of virtual experiments, the yield loci can be determined with a fraction of the experimental cost. The calibrated parameters are listed in table 3.3 for 1000 virtual experiments. Furthermore, the shape of the yield surface together with the yield loci extracted from CP simulations are shown in fig. 3.13, where the anisotropy of LPBF316L can be seen. It is worth noting that the yield loci in fig. 3.13 are presented using their corresponding σ_{11} and σ_{33} stress components. Therefore, many yield loci are located within the yield surface since other components, such as shear components, contribute to the calculation of the effective stress, but aren't visible in this particular plot. This is evident in the plot with varying contours of shear stress, where the yield surface gets smaller as the shear components get larger. Moreover, the boundary conditions are generated randomly to ensure that as many different loading conditions are covered during the simulations, which means that many different stress states are generated for the determination of the yield surface.

Table 3.3: Calibrated parameters of the yield function Yld2004-18p.

c'_{12}	c'_{21}	c'_{23}	c'_{32}	c'_{31}	c'_{13}	c'_{44}	c'_{55}	c'_{66}
0.844	0.928	0.807	1.06	0.86	0.146	1.03	0.711	0.955
c''_{12}	c''_{21}	c''_{23}	c''_{32}	c''_{31}	c''_{13}	c''_{44}	c''_{55}	c''_{66}
1.17	0.674	1.0	0.435	0.827	0.976	0.799	1.28	0.927

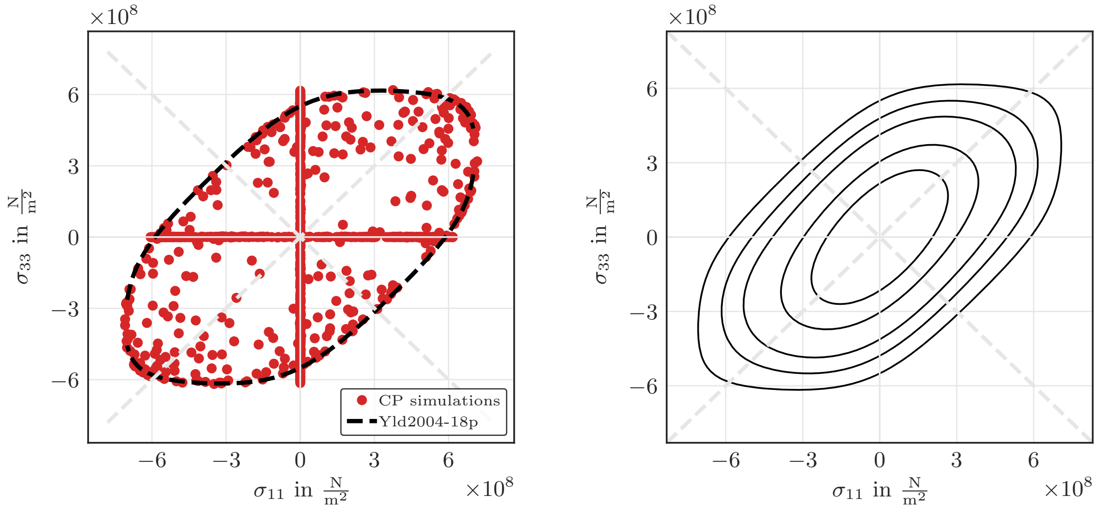

Figure 3.13: Calibration of the Barlat yield function using 1000 virtual experiments shown on the left. The same yield surface is shown on the right for varying contours of shear stress.

3.4.2.3 Parameters of the macroscopic hardening model

After calibrating the parameters of the Barlat yield function Yld2004-18p using the virtual experiments, the parameters of the hardening model described in section 3.3.6 have to be calibrated. This is necessary since the Barlat yield function Yld2004-18p only captures the initial anisotropic response of the material. Thus, a hardening model has to be chosen and calibrated to fully describe the anisotropic yield behavior of the material at the macroscale. This is also straightforward since the parameters are determined with the same tensile test, which was used to calibrate the CP model in section 3.4.2.1. In this case, there is no need for a RVE since the influence of texture is captured by the homogenized elastic stiffness tensor and the Barlat yield function Yld2004-18p, see sections 3.4.1 and 3.4.2.2. However, there is one problem that has to be addressed. The experimentally obtained stress-strain curves are only valid until necking sets in, which is a localized phenomenon that arises from a instability during tensile deformation. This issue prohibits the usage of the experimental results beyond the necking since they don’t reflect the actual stress-strain response of the material. Thus, the experimental results have to be extrapolated beyond the necking for them to be used as input data for simulation softwares.

In this work, the extrapolation is carried out using three different assumptions, which are graphically shown in fig. 3.14. The reason for having different extrapolations is that in absence of experimental results it is impossible to accurately describe the material response beyond the necking point. However, by comparing the experimental torsion and shear results against the simulations conducted for these different hardening assumptions, it is possible to estimate the hardening behavior, which is closer to the actual material behavior. Moreover, these results could also serve as a sensitivity analysis. The hardening behaviors shown in fig. 3.14 are the same up to 25 % strain. After that, in the simplest case, a linear extrapolation function is used to describe the hardening behavior from 25 % strain, which closely follows the actual material behavior up to the necking point. However, such behavior is not realistic for larger strain values. Thus, two other extrapolations are shown, which deviate at 25 % strain from the linear extrapolation and converge to two different saturation values, after which the yield stress remains constant, which represents the material state before failure. The saturation values 110 % and 140 % are chosen arbitrarily.

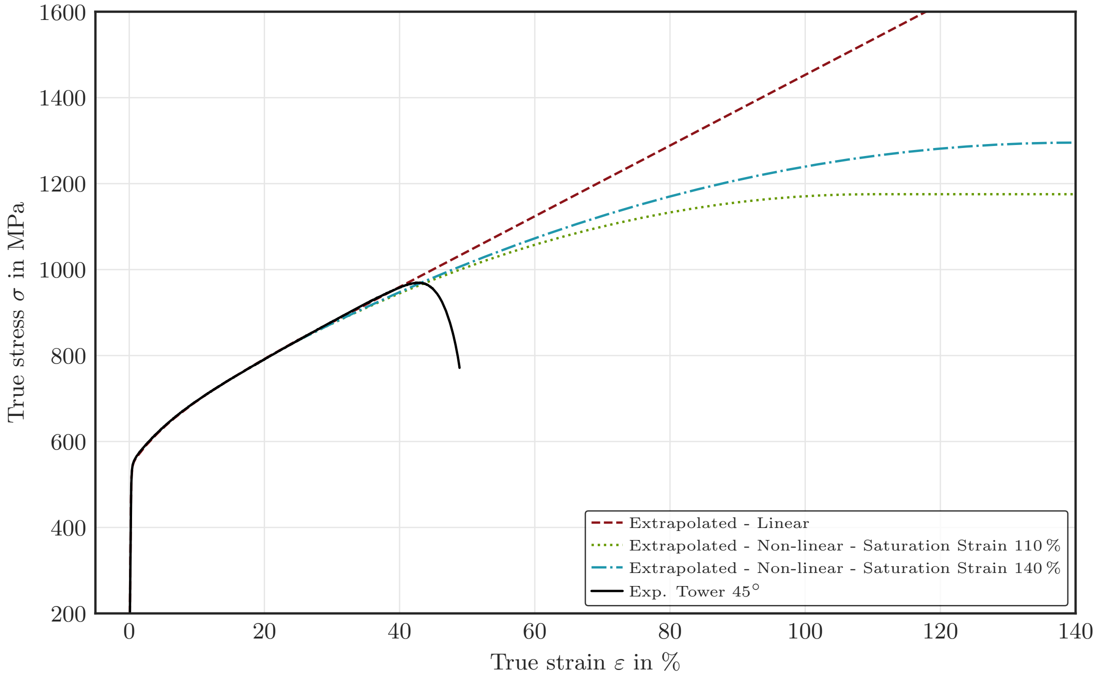

Figure 3.14: Extrapolation of the experimentally obtained stress-strain curves beyond the necking instability.

Afterward, the extrapolated data are used to calibrate the hardening models. As explained in section 3.3.6, a single hardening model is often not capable of accurately capturing the hardening behavior of a material over a very large strain range. This is specially true for the extrapolated stress-strain curves shown in fig. 3.14. It is worth noting, that the Ludwik law alone is also capable of extrapolating the stress-strain results beyond the necking point. However, the extrapolation behavior of the Ludwik law is different to the behavior shown in fig. 3.14 and it can't be used to have a linear extrapolation. Thus, the following models are proposed, which are constructed by dividing the whole strain range into smaller regions:

- Model 1 - Ludwik law combined with linear extrapolation:

$$\sigma_{\mathrm{y}}\left(\bar{\varepsilon}^{\mathrm{p}}\right)=\begin{cases}\sigma_0+K\left(\bar{\varepsilon}^{\mathrm{p}}\right)^n & \text{for } \bar{\varepsilon}^{\mathrm{p}} \leq \bar{\varepsilon}_{\mathrm{L1}} \\ \sigma_{\mathrm{y}}\left(\bar{\varepsilon}_{\mathrm{L1}}\right)+L\left(\bar{\varepsilon}^{\mathrm{p}}-\bar{\varepsilon}_{\mathrm{L1}}\right) & \text{for } \bar{\varepsilon}^{\mathrm{p}} > \bar{\varepsilon}_{\mathrm{L1}}\end{cases},$$

$$\frac{\partial \sigma_{\mathrm{y}}\left(\bar{\varepsilon}^{\mathrm{p}}\right)}{\partial \bar{\varepsilon}^{\mathrm{p}}}=\begin{cases}-nK(\bar{\varepsilon}^{\mathrm{p}})^{n-1} & \text{for } \bar{\varepsilon}^{\mathrm{p}} \leq \bar{\varepsilon}_{\mathrm{L1}} \\ L & \text{for } \bar{\varepsilon}^{\mathrm{p}} > \bar{\varepsilon}_{\mathrm{L1}}\end{cases}. \tag{3.224}$$

- Model 2 and 3 - Ludwik law combined with non-linear extrapolation:

$$\sigma_{\mathrm{y}}\left(\bar{\varepsilon}^{\mathrm{p}}\right)=\begin{cases}\sigma_0+K\left(\bar{\varepsilon}^{\mathrm{p}}\right)^n & \text{for } \bar{\varepsilon}^{\mathrm{p}} \leq \bar{\varepsilon}_{\mathrm{L1}} \\ \sigma_{\mathrm{y}}\left(\bar{\varepsilon}_{\mathrm{L1}}\right)+L\left(\bar{\varepsilon}^{\mathrm{p}}-\bar{\varepsilon}_{\mathrm{L1}}\right)\left(1-\frac{\bar{\varepsilon}^{\mathrm{p}}-\bar{\varepsilon}_{\mathrm{L1}}}{2(\bar{\varepsilon}_{\mathrm{L2}}-\bar{\varepsilon}_{\mathrm{L1}})}\right) & \text{for } \bar{\varepsilon}_{\mathrm{L1}} < \bar{\varepsilon}^{\mathrm{p}} \leq \bar{\varepsilon}_{\mathrm{L2}} \\ \sigma_{\mathrm{y}}\left(\bar{\varepsilon}_{\mathrm{L2}}\right) & \text{for } \bar{\varepsilon}^{\mathrm{p}} > \bar{\varepsilon}_{\mathrm{L2}}\end{cases},$$

$$\frac{\partial \sigma_{\mathrm{y}}\left(\bar{\varepsilon}^{\mathrm{p}}\right)}{\partial \bar{\varepsilon}^{\mathrm{p}}}=\begin{cases}-nK(\bar{\varepsilon}^{\mathrm{p}})^{n-1} & \text{for } \bar{\varepsilon}^{\mathrm{p}} \leq \bar{\varepsilon}_{\mathrm{L1}} \\ L\left(1-\frac{\bar{\varepsilon}^{\mathrm{p}}-\bar{\varepsilon}_{\mathrm{L1}}}{\bar{\varepsilon}_{\mathrm{L2}}-\bar{\varepsilon}_{\mathrm{L1}}}\right) & \text{for } \bar{\varepsilon}_{\mathrm{L1}} < \bar{\varepsilon}^{\mathrm{p}} \leq \bar{\varepsilon}_{\mathrm{L2}} \\ 0 & \text{for } \bar{\varepsilon}^{\mathrm{p}} > \bar{\varepsilon}_{\mathrm{L2}}\end{cases}. \tag{3.225}$$

The stress-strain curves extracted from the calibrated hardening models are compared to the experimental stress-strain response of the material in fig. 3.15, which show the high accuracy of the simulation results. The corresponding calibrated parameters of the three hardening models are listed in table 3.4, which are required as input for Abaqus UMAT.

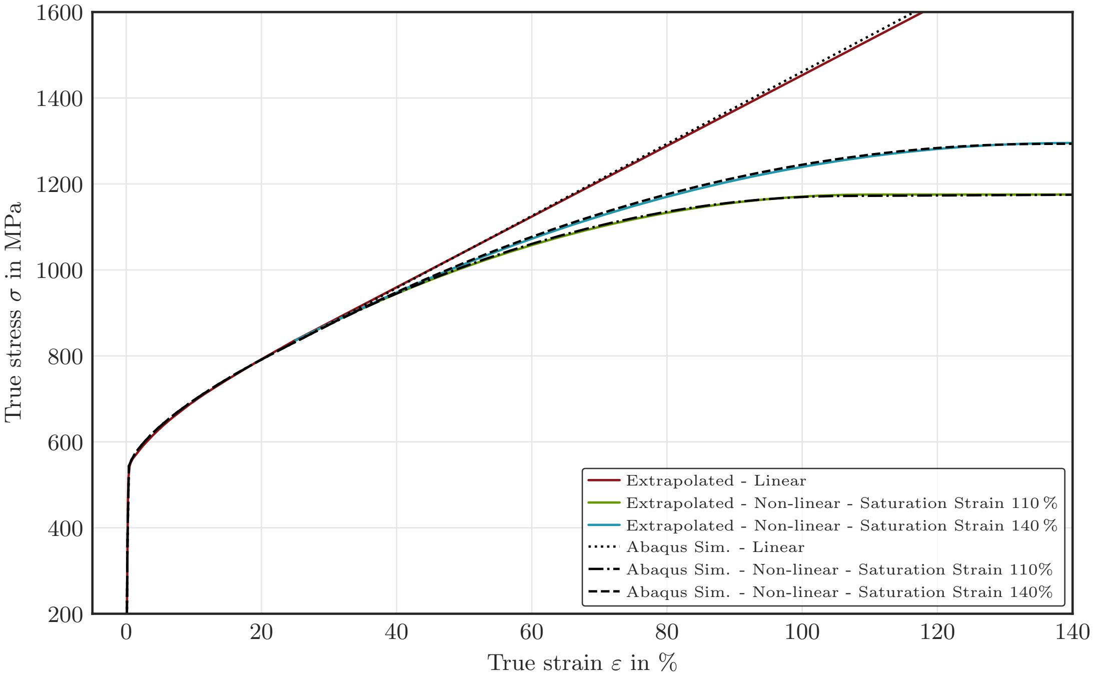

Figure 3.15: Comparison between the extrapolated stress-strain curves with the calibrated hardening models.

Table 3.4: Calibrated parameters of the macroscopic hardening models. Model 1 captures the material behavior corresponding to the linearly extrapolated curve. Similarly, Model 2 and 3 are used to calculate the yield strength of the material in the case of non-linear extrapolation with saturation strains of 110 % and 140 %, respectively.

	σ_0 (MPa)	K (MPa)	n	$\bar{\varepsilon}_{\mathrm{L1}}$	L (MPa)	$\bar{\varepsilon}_{\mathrm{L2}}$
Model 1	516	697	0.648	0.25	785	-
Model 2	516	697	0.648	0.25	785	1.1
Model 3	516	697	0.648	0.25	785	1.4

3.4.2.4 Parameters for the novel plastic spin model

The parameters of the plastic spin functions $\hat{\mathbf{W}}^{\mathrm{p}}_{\mathrm{TC}}$ and $\hat{\mathbf{W}}^{\mathrm{p}}_{\mathrm{S}}$ are calibrated using a different set of virtual experiments. Both are required for the final plastic spin model $\hat{\mathbf{W}}^{\mathrm{p}}$ shown in eq. (3.148). As explained in section 3.3.7.2, the tensor $\hat{\mathbf{W}}^{\mathrm{p}}_{\mathrm{TC}}$ describes the plastic spin caused by deformations, which correspond either to uni-axial tension or compression. On the other hand, the tensor $\hat{\mathbf{W}}^{\mathrm{p}}_{\mathrm{S}}$ is needed when the deformation represents simple or pure shear. Thus, it is necessary to calibrate these two parts separately using appropriate virtual experiments. Naturally, the parameters of the tensor $\hat{\mathbf{W}}^{\mathrm{p}}_{\mathrm{TC}}$ are calibrated using virtual experiments, which describe uni-axial tension in different directions. Uni-axial compression experiments are unnecessary since they produce the same results as uni-axial tension but with a reversed sign. Consequently, the tensor $\hat{\mathbf{W}}^{\mathrm{p}}_{\mathrm{S}}$ is calibrated using virtual experiments, which describe pure shear in different directions. Simple shear experiments are neglected since they are the superposition of the simple shear with a rigid body rotation. Thus, it is assumed that they both result in the same plastic spin tensor.

The calibration procedure for both $\hat{\mathbf{W}}^{\mathrm{p}}_{\mathrm{TC}}$ and $\hat{\mathbf{W}}^{\mathrm{p}}_{\mathrm{S}}$ is the same. After each virtual experiment corresponding to one specific loading direction, the result of the CP simulation is analyzed. More specifically, the results are used to determine the final crystallographic texture at the end of the deformation process. Afterward, similar to the approach presented in section 3.4.1, the software MTEX [147] (combined with the SCEC of LPBF316L and the Hill model) is used to determine the elastic stiffness tensor of the deformed material at the end of simulation. Furthermore, it is assumed that the change of elastic stiffness tensor is directly the result of rotation caused by plastic spin. It should be noted that the change of elastic stiffness tensor due to the evolution of microstructure is neglected since this aspect is not a part of the investigation in this work. Finally, after calculating the deformed elastic stiffness tensor $\mathbb{C}^{\mathrm{deformed}}$, it is possible to determine a rotation tensor $\mathbf{R}^{\mathrm{C}}$ by making use of the Frobenius norm of a $m \times n$ matrix $\mathbf{A}$ [182, 183]:

$$||\mathbf{A}||_{\mathrm{F}} = \sqrt{\sum_{i}^{m}\sum_{j}^{n} |\mathrm{A}_{ij}|^2} \,. \tag{3.226}$$

Using the above norm, a residual can be defined, which has to be minimized in order to obtain the proper $\mathbf{R}^{\mathrm{C}}$ as follows:

$$\begin{aligned} &\text{minimize } \mathcal{F}(\hat{\mathbb{C}}, \mathbb{C}^{\text{deformed}}) = ||\hat{\mathbb{C}} - \mathbb{C}^{\text{deformed}}||_{\mathrm{F}}\,, \\ &\text{with } \hat{\mathrm{C}}_{ijkl} = \mathrm{R}^{\mathrm{C}}_{ia}\,\mathrm{R}^{\mathrm{C}}_{jb}\,\mathrm{R}^{\mathrm{C}}_{kc}\,\mathrm{R}^{\mathrm{C}}_{ld}\,\mathrm{C}_{abcd}\,. \end{aligned} \tag{3.227}$$

$\mathbb{C}$ is the initial elastic stiffness tensor before any deformation has occurred. Moreover, $\hat{\mathbb{C}}$ is the rotated elastic stiffness tensor using the rotation matrix $\mathbf{R}^{\mathrm{C}}$. And $\mathbb{C}^{\text{deformed}}$ is the deformed elastic stiffness tensor. The rotation matrix $\mathbf{R}^{\mathrm{C}}$ has nine components. However, it can be represented with only three independent angles using the Euler representation [184]. Thus, the residual $\mathcal{F}(\hat{\mathbb{C}}, \mathbb{C}^{\text{deformed}})$ is minimized by varying these three independent angles. After the minimization process is completed, the rotation matrix $\mathbf{R}^{\mathrm{C}}$ is uniquely determined, which is then used for the calibration of the parameters of the plastic spin tensor $\hat{\mathbf{W}}^{\mathrm{p}}$. In the final step, all the rotation matrices are converted to incremental spin tensors using the logarithm map as follows [185]:

$$\Delta\hat{\mathbf{W}}^{\mathrm{p}} = -\log\left(\mathbf{R}^{\mathrm{C}}\right) = -\frac{\theta}{2\sin(\theta)}\left[\left(\mathbf{R}^{\mathrm{C}}\right)^{\mathrm{T}} - \mathbf{R}^{\mathrm{C}}\right]\,, \tag{3.228}$$

with

$$\theta = \arccos\left(\frac{\operatorname{trace}\left(\mathbf{R}^{\mathrm{C}}\right) - 1}{2}\right)\,, \qquad \theta \neq 0\,, \qquad -\pi < \theta < \pi\,. \tag{3.229}$$

If $\theta = 0$, then one has the trivial case where $\mathbf{R}^{\mathrm{C}} = \mathbf{I}$ and $\log\left(\mathbf{R}^{\mathrm{C}}\right) = \mathbf{0}$. It is worth noting that the minus sign in eq. (3.228) comes from the following expression, defined in section 3.3.7:

$$\mathbf{W}^{\mathrm{e}} = \mathbf{W} - \mathbf{W}^{\mathrm{p}}\,. \tag{3.230}$$

In an uni-axial tensile test, the spin tensor $\mathbf{W}$ is equal to zero. Thus, the above equation reduces to:

$$\mathbf{W}^{\mathrm{e}} = -\mathbf{W}^{\mathrm{p}} \qquad \text{or equivalently} \qquad \mathbf{W}^{\mathrm{p}} = -\mathbf{W}^{\mathrm{e}}\,. \tag{3.231}$$

Based on the assumptions made in section 3.3.7.2, the material axes and, consequently, the elastic stiffness tensor rotate with $\mathbf{W}^{\mathrm{e}}$. More importantly, the plastic spin model $\mathbf{W}^{\mathrm{p}}$ is calibrated using the rotation of the elastic stiffness tensor calculated from the initial and final texture, directly caused by $\mathbf{W}^{\mathrm{e}}$. But from eq. (3.231) it is clear that $\mathbf{W}^{\mathrm{p}}$ and $\mathbf{W}^{\mathrm{e}}$ have opposite sign. Therefore, if the rotation of the elastic stiffness tensor is caused by $\mathbf{W}^{\mathrm{e}}$ and we capture this behavior using $\mathbf{W}^{\mathrm{p}}$, then, $\mathbf{W}^{\mathrm{p}}$ has to be multiplied with a minus sign to result in the same final rotation. The resulting incremental spin tensors must also be divided by the value of the equivalent plastic strain since the rotation matrices are determined from CP simulations after 30% strain. This has to be done in order to account for the incremental nature of the simulations conducted in Abaqus UMAT. Hence, the correct value of equivalent plastic strain can be easily determined using corresponding Abaqus simulations mimicking the same loading conditions as in the CP simulations. The Abaqus simulations are run only using one integration point.

This process is repeated for all the loading directions defined in the SPC space. The number of the loading directions are reduced utilizing the symmetric properties of the LPBF316L texture investigated in this work. More specifically, the angles φ^{p} and θ^{p} are restricted as graphically demonstrated in fig. 3.16. The creation of a proper boundary condition for the CP simulations in DAMASK was presented in section 3.2.6. As an example, the boundary condition for the simulation of uni-axial tension in 11 direction was shown to be:

$$\dot{\mathbf{F}}_{\mathrm{BC}} = \begin{pmatrix} a & 0 & 0 \\ 0 & * & 0 \\ 0 & 0 & * \end{pmatrix} \text{ and } \mathbf{P}_{\mathrm{BC}} = \begin{pmatrix} * & * & * \\ * & 0 & * \\ * & * & 0 \end{pmatrix}. \tag{3.232}$$

a stands for the loading rate. It was also explained that the software DAMASK allows for the definition of rotation matrices, which can be applied to the above tensors to define other loading directions. Using this method, the boundary condition tensors $\dot{\mathbf{F}}_{\mathrm{BC}}$ and $\mathbf{P}_{\mathrm{BC}}$ are the same for one type of deformation, such as uni-axial tension. Only the rotation matrix belonging to the specific loading directions defined in fig. 3.16 changes.

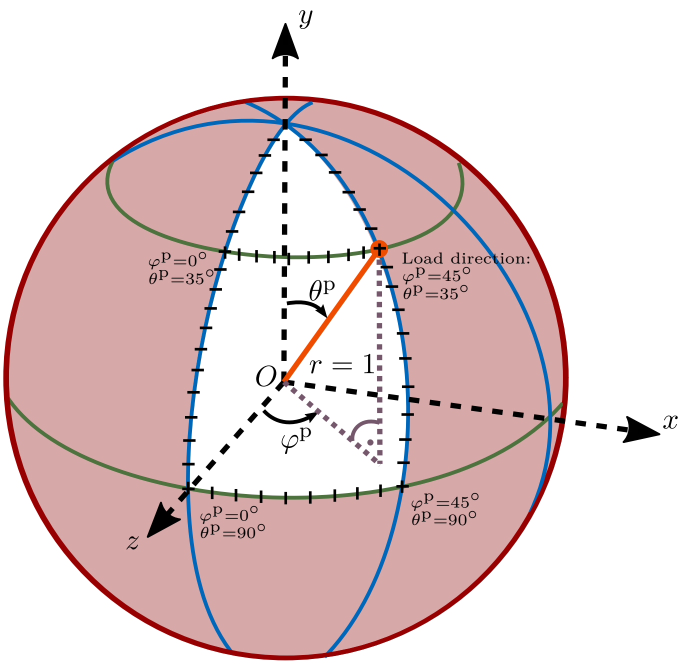

Figure 3.16: Loading directions are defined using the angles φ^{p} and θ^{p} restricted to $0^\circ - 45^\circ$ and $0^\circ - 90^\circ$, respectively. Each of the angles are varied in steps of 5°

As explained in section 3.3.7.2, the mathematical expressions for the calculation of the plastic spin components only depend on the angles θ^{p} and φ^{p}. The same general expression is chosen to describe the plastic spin components during tension/compression and shear deformation. This novel expression is constructed by the author using mainly trigonometric functions with different amplitudes and frequencies. The frequencies are chosen such that the periodic behavior of each component is captured correctly and is consistent with the symmetries observed in the crystallographic texture. The periodicity in the crystallographic texture is also used to simplify the calibration procedure by reducing and limiting the number of virtual texture evolution experiments. The initial symmetric crystallographic textures and their evolution at their different strain levels for the load direction $\varphi^{\mathrm{p}} = 90\,^\circ$ and $\theta^{\mathrm{p}} = 75\,^\circ$ are shown in figs. 3.17 and 3.18.

It is worth noting that this symmetric initial texture is idealized by rotating the texture extracted from the side of Tower 45° by 90 °, 180 °, and 270 ° and averaging them together. This step isn't always necessary or even possible. However, due to the symmetric scan strategies employed during the production of LPBF316L samples in this work, the experimentally measured crystallographic textures exhibit these symmetric properties. The texture analysis is presented in detail in section 4.2. However, due to different sources of uncertainty in actual measurements, the experimentally determined crystallographic textures aren't always perfectly symmetric. Thus, the idealization step is used to get rid of the measurement inaccuracies and also to simplify the calibration procedure. It is also possible to treat the crystallographic texture as anistropic. In that case, more virtual experiments are needed. Moreover, the expressions for the plastic spin components have to be adjusted.

The figs. 3.17 and 3.18 reveal that the presented texture is symmetric along the XY, YZ, and XZ planes. Moreover, the texture is also symmetric with respect to the XZ plane rotated along the Z-axis by ±45 °. Thus, the whole region can be reduced, for example, to $\varphi^{\mathrm{p}} = 0^\circ - 45^\circ$ and $\theta^{\mathrm{p}} = 0^\circ - 90^\circ$, see fig. 3.16. As an example, it is possible to look at the texture evolution results shown in figs. 3.17 and 3.18 to better understand the evolution of the plastic spin components for the tension case. In this particular example, the load direction is $\varphi^{\mathrm{p}} = 90\,^\circ$ and $\theta^{\mathrm{p}} = 75\,^\circ$. This load direction is in the XZ-plane, 15 ° rotated from the X-axis towards the Z-axis. In the presented results it is easy to see that the initial texture is slowly rotating towards the load direction. More importantly, the rotation axis is the Y-axis, which is logical since the load direction is in the XZ symmetry plane. From these results it is obvious that only one component should exist for the plastic spin tensor, which is the component acting in the symmetry plane. This is also evident in the results shown in fig. 3.19 for the calibrated plastic spin components, where for $\varphi^{\mathrm{p}} = 0\,^\circ$ and $\theta^{\mathrm{p}} = 75\,^\circ$, which is equivalent to $\varphi^{\mathrm{p}} = 90\,^\circ$ and $\theta^{\mathrm{p}} = 75\,^\circ$ (Only X- and Y-axis are swapped), only one component acting in the symmetry plane is non-zero.

Such case studies are used to construct the general expressions for the plastic spin components. They can be used both in 2D and 3D domains and can be easily adjusted for other textures and symmetry properties. The expressions for the tension/compression and shear deformation are formulated based on the virtual experiment results shown in figs. 3.19, 3.20, 3.21, and 3.22. It is worth noting that the expressions for the tension/compression and shear deformation are calibrated using different set of virtual experiments, which results in a unique set of parameters for each deformation condition. Thus, the final expressions for these different loading conditions are similar but not identical. The parameters are listed in tables 3.5 and 3.6. The exact mathematical expressions for the plastic spin components $\tilde{\mathrm{W}}^{\mathrm{p}}_{\theta r}$, $\tilde{\mathrm{W}}^{\mathrm{p}}_{\varphi r}$, and $\tilde{\mathrm{W}}^{\mathrm{p}}_{\varphi\theta}$ in the SPC frame are as follows:

$$\begin{aligned}
\tilde{\mathrm{W}}^{\mathrm{p}}_{\theta r} =&\, \dot{\bar{\varepsilon}}^{\mathrm{p}} \left[\beta_1 \sin\left(2\theta^{\mathrm{p}}\right) + \beta_2 \sin\left(4\theta^{\mathrm{p}}\right) + \beta_3 \sin\left(6\theta^{\mathrm{p}}\right) + \beta_4 \sin\left(8\theta^{\mathrm{p}}\right) + \beta_5 \sin\left(10\theta^{\mathrm{p}}\right)\right] \cdot \\
&\cdot \left[1 - \beta_{11}\left|\sin\left(2\varphi^{\mathrm{p}}\right)\right| - \beta_{12}\left|\sin\left(4\varphi^{\mathrm{p}}\right)\right|\right] + \\
&\left[\beta_6 \sin\left(2\theta^{\mathrm{p}}\right) + \beta_7 \sin\left(4\theta^{\mathrm{p}}\right) + \beta_8 \sin\left(6\theta^{\mathrm{p}}\right) + \beta_9 \sin\left(8\theta^{\mathrm{p}}\right) + \beta_{10} \sin\left(10\theta^{\mathrm{p}}\right)\right] \cdot \\
&\cdot \left[\beta_{13}\left|\sin\left(2\varphi^{\mathrm{p}}\right)\right| + \beta_{14}\left|\sin\left(4\varphi^{\mathrm{p}}\right)\right|\right] \,, \\[2ex]
\tilde{\mathrm{W}}^{\mathrm{p}}_{\varphi r} =&\, \dot{\bar{\varepsilon}}^{\mathrm{p}}\, \beta_1 \sin\left(4\varphi^{\mathrm{p}}\right) \left[\beta_2 \sin\left(\theta^{\mathrm{p}}\right) + \beta_3 \sin\left(3\theta^{\mathrm{p}}\right) + \beta_4 \sin\left(5\theta^{\mathrm{p}}\right) + \beta_5 \sin\left(7\theta^{\mathrm{p}}\right)\right] \,, \\[2ex]
\tilde{\mathrm{W}}^{\mathrm{p}}_{\varphi\theta} =&\, \dot{\bar{\varepsilon}}^{\mathrm{p}}\, \beta_1 \sin\left(4\varphi^{\mathrm{p}}\right) \left[\beta_2 \sin\left(2\theta^{\mathrm{p}}\right) + \beta_3 \sin\left(4\theta^{\mathrm{p}}\right) + \beta_4 \sin\left(6\theta^{\mathrm{p}}\right) + \right. \\
&\left. + \beta_5 \sin\left(8\theta^{\mathrm{p}}\right) + \beta_6 \sin\left(10\theta^{\mathrm{p}}\right)\right] . \qquad (3.233)
\end{aligned}$$

For the sake of completeness, the whole procedure for calculating the plastic spin tensor $\hat{\mathbf{W}}^{\mathrm{p}}$ is explained and summarized again as follows:

1. After any plastic deformation has occurred, the eigenvalues and eigenvectors of the rate of plastic deformation tensor $\hat{\mathbf{D}}^{\mathrm{p}}$ are determined.
2. The eigenvector belonging to the largest eigenvalue is chosen.
3. The polar angles θ^{p} and φ^{p} of the chosen eigenvector are calculated, see fig. 3.16.
4. The angles θ^{p} and φ^{p} combined with the equivalent plastic strain rate $\dot{\bar{\varepsilon}}^{\mathrm{p}}$ are then used to calculate the components $\tilde{\mathrm{W}}^{\mathrm{p}}_{\theta r}$, $\tilde{\mathrm{W}}^{\mathrm{p}}_{\varphi r}$, and $\tilde{\mathrm{W}}^{\mathrm{p}}_{\varphi\theta}$ of the tensors $\tilde{\mathbf{W}}^{\mathrm{p}}_{\mathrm{TC}}$ and $\tilde{\mathbf{W}}^{\mathrm{p}}_{\mathrm{S}}$, which are the plastic spin tensors for tension/compression and shear deformations in the SPC frame. It is worth noting that for each of the tensors $\tilde{\mathbf{W}}^{\mathrm{p}}_{\mathrm{TC}}$ and $\tilde{\mathbf{W}}^{\mathrm{p}}_{\mathrm{S}}$, three separate components $\tilde{\mathrm{W}}^{\mathrm{p}}_{\theta r}$, $\tilde{\mathrm{W}}^{\mathrm{p}}_{\varphi r}$, and $\tilde{\mathrm{W}}^{\mathrm{p}}_{\varphi\theta}$ are calculated, which results in a total of six independent components.
5. $\tilde{\mathbf{W}}^{\mathrm{p}}_{\mathrm{TC}}$ and $\tilde{\mathbf{W}}^{\mathrm{p}}_{\mathrm{S}}$ are transformed back to the rotating CCO frame, to get the tensors $\hat{\mathbf{W}}^{\mathrm{p}}_{\mathrm{TC}}$ and $\hat{\mathbf{W}}^{\mathrm{p}}_{\mathrm{S}}$
6. The lode parameter μ_{L} is calculated using the determined eigenvalues of $\hat{\mathbf{D}}^{\mathrm{p}}$.
7. With the lode parameter μ_{L} and the calculated tensors $\hat{\mathbf{W}}^{\mathrm{p}}_{\mathrm{TC}}$ and $\hat{\mathbf{W}}^{\mathrm{p}}_{\mathrm{S}}$, the final plastic spin tensor $\hat{\mathbf{W}}^{\mathrm{p}}$ is determined by simply inserting these terms in the following equation, derived in section 3.3.7.2:

$$\hat{\mathbf{W}}^{\mathrm{p}} = \mu_{\mathrm{L}} \hat{\mathbf{W}}^{\mathrm{p}}_{\mathrm{TC}} + \left(1 - |\mu_{\mathrm{L}}|\right) \left(\hat{\mathbf{W}}^{\mathrm{p}}_{\mathrm{S}}\right) . \qquad (3.234)$$

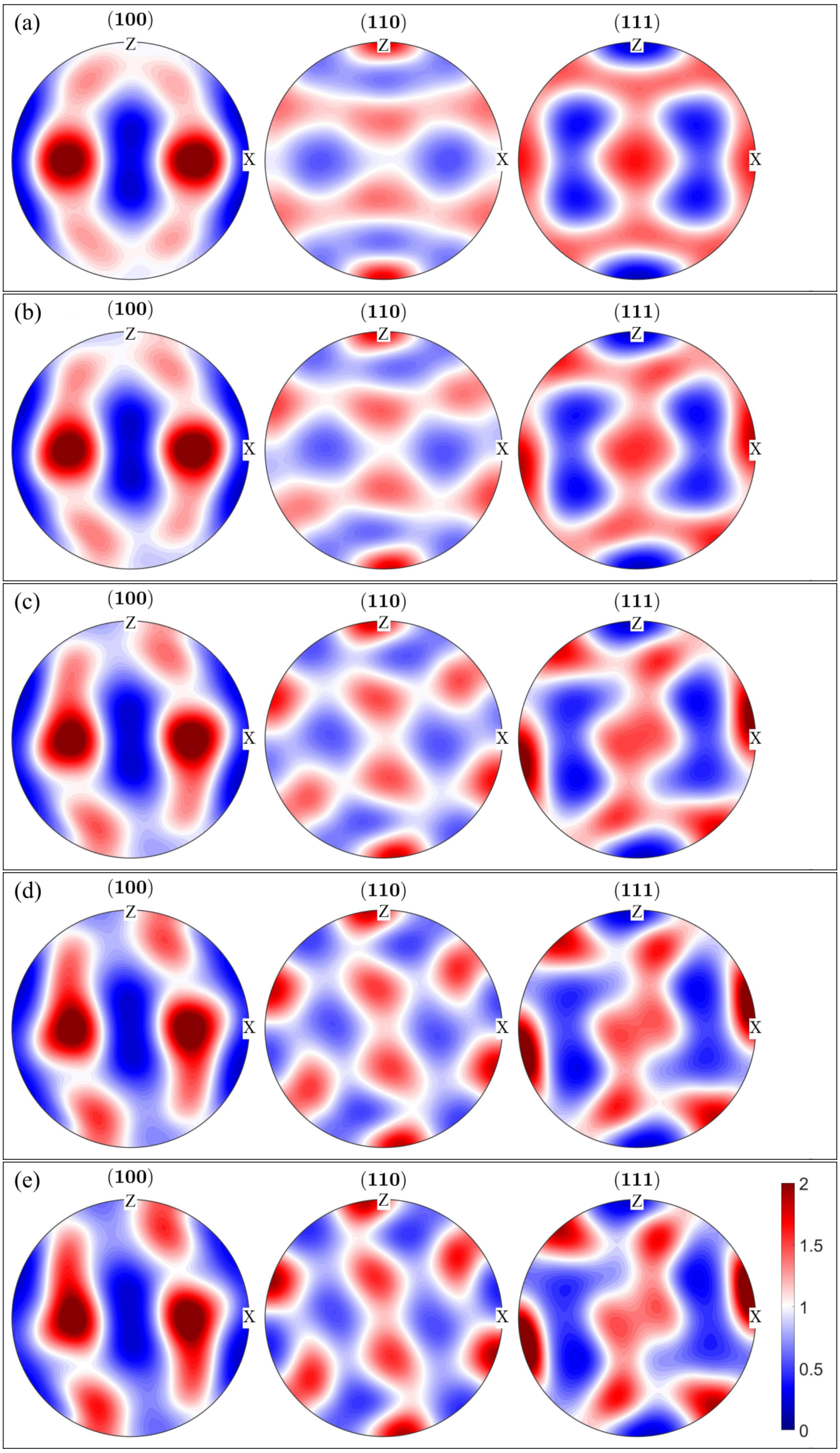

Figure 3.17: Pole figures in (X,Z) coordinate frame at different strain levels (a) 0 %, (b) 20 %, (c) 40 %, (d) 60 %, and (e) 80 % strain, which show the evolution of the texture during tensile deformation. The initial texture is from the side of Tower 45°, which is idealized by rotating the initial texture by 90 °, 180 °, and 270 ° and averaging them together. The load direction for this virtual experiment is $\varphi^{\mathrm{p}} = 90\,^{\circ}$ and $\theta^{\mathrm{p}} = 75\,^{\circ}$, see fig. 3.16 for more details.

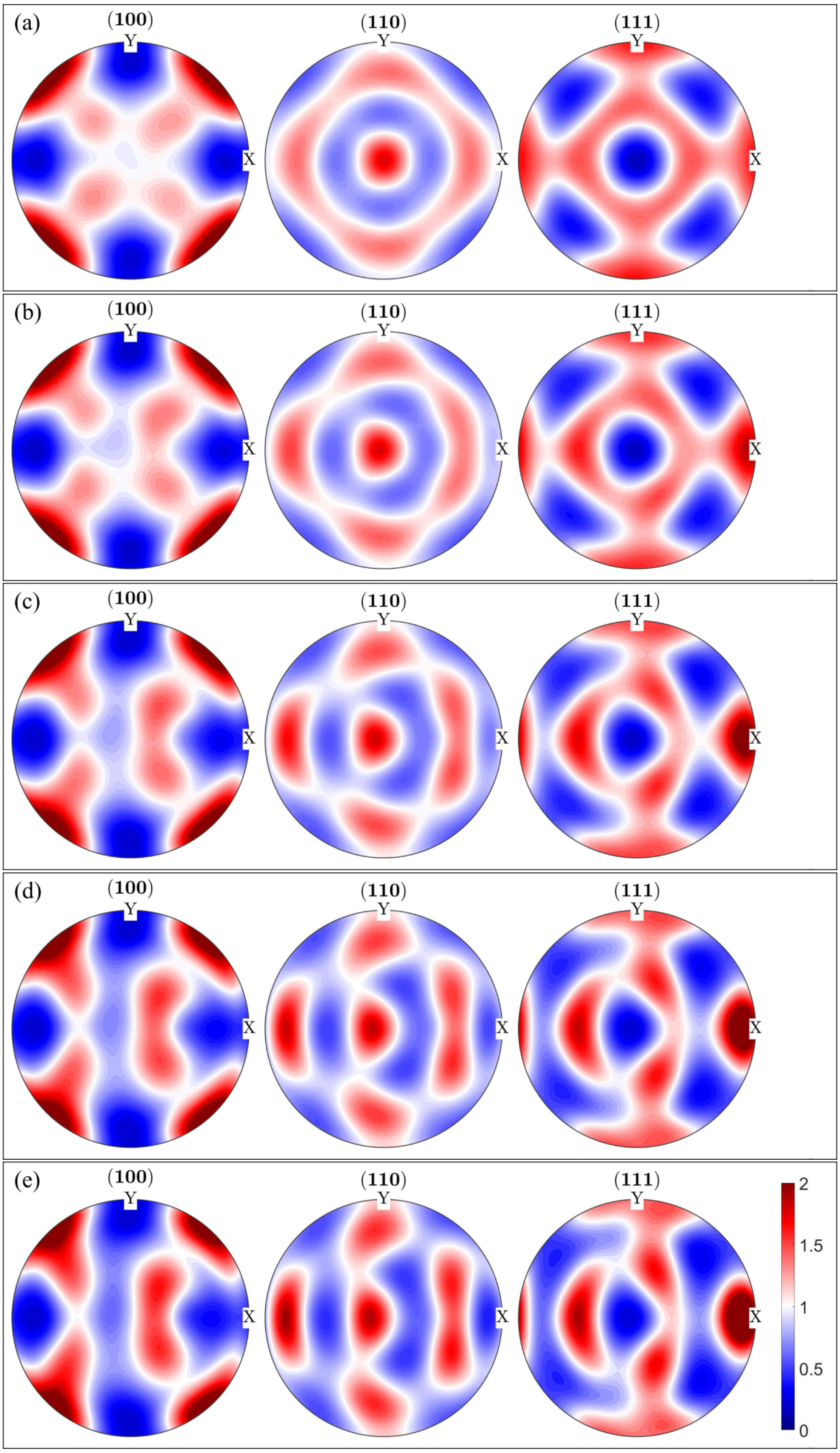

Figure 3.18: Pole figures in (X,Y) coordinate frame at different strain levels (a) 0 %, (b) 20 %, (c) 40 %, (d) 60 %, and (e) 80 % strain, which show the evolution of the texture during tensile deformation. The initial texture is from the side of Tower 45°, which is idealized by rotating the initial texture by 90 °, 180 °, and 270 ° and averaging them together. The load direction for this virtual experiment is $\varphi^{\mathrm{p}} = 90\,^\circ$ and $\theta^{\mathrm{p}} = 75\,^\circ$, see fig. 3.16 for more details.

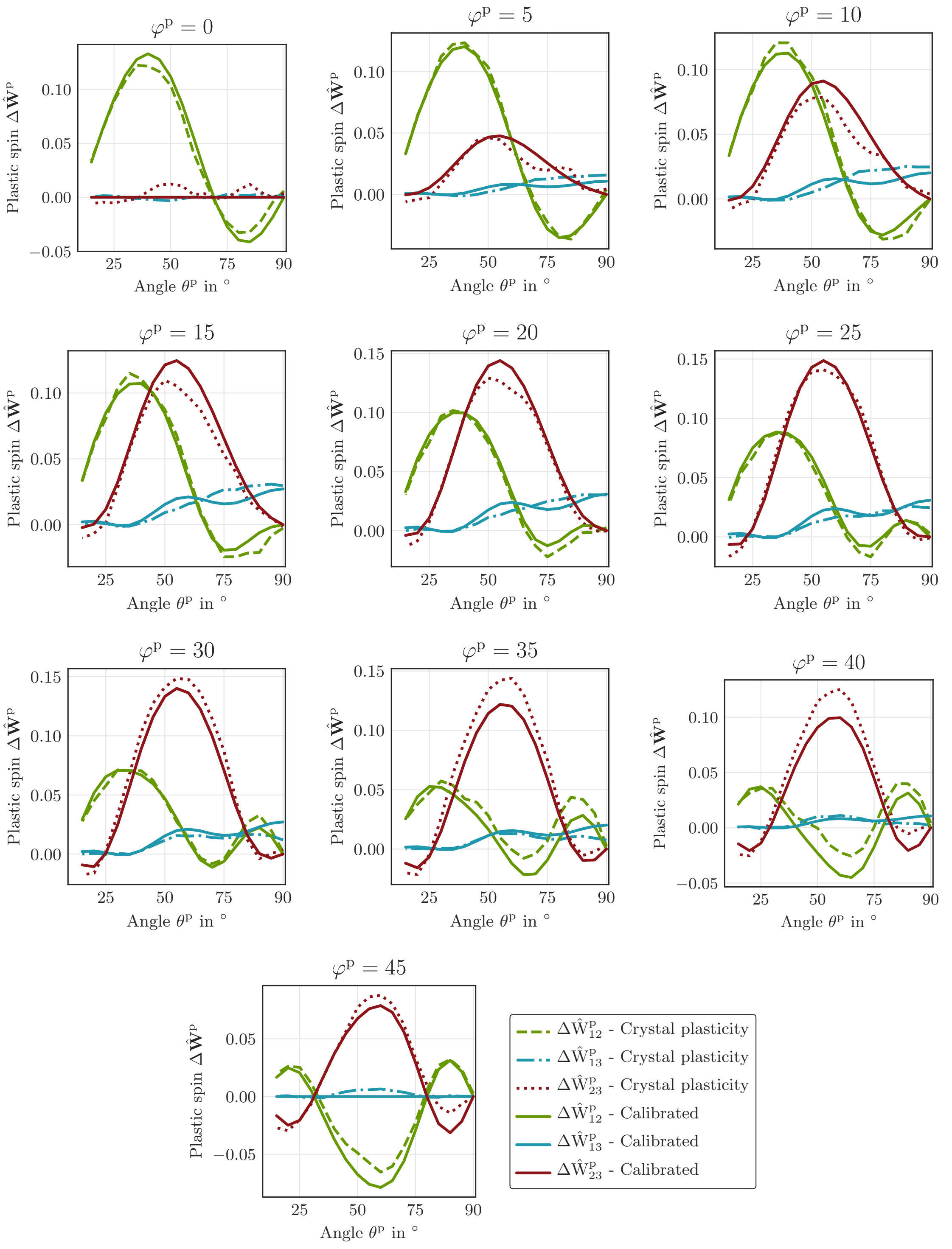

Figure 3.19: Calibrated plastic spin model $\hat{\mathbf{W}}^p_{TC}$.

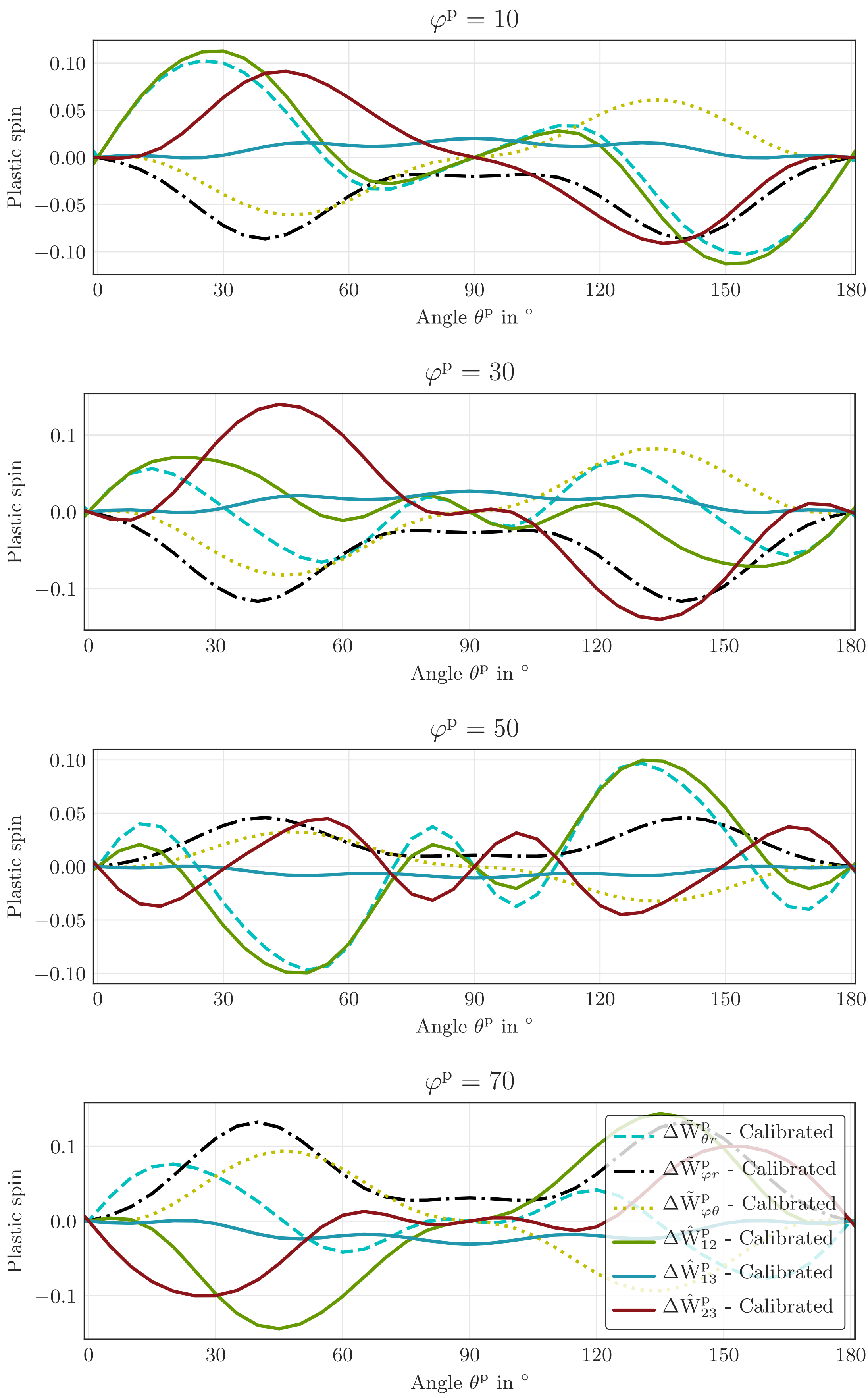

Figure 3.20: Comparison between plastic spin components in CCO ($\hat{\mathbf{W}}^p_{TC}$) and SPC ($\tilde{\mathbf{W}}^p_{TC}$).

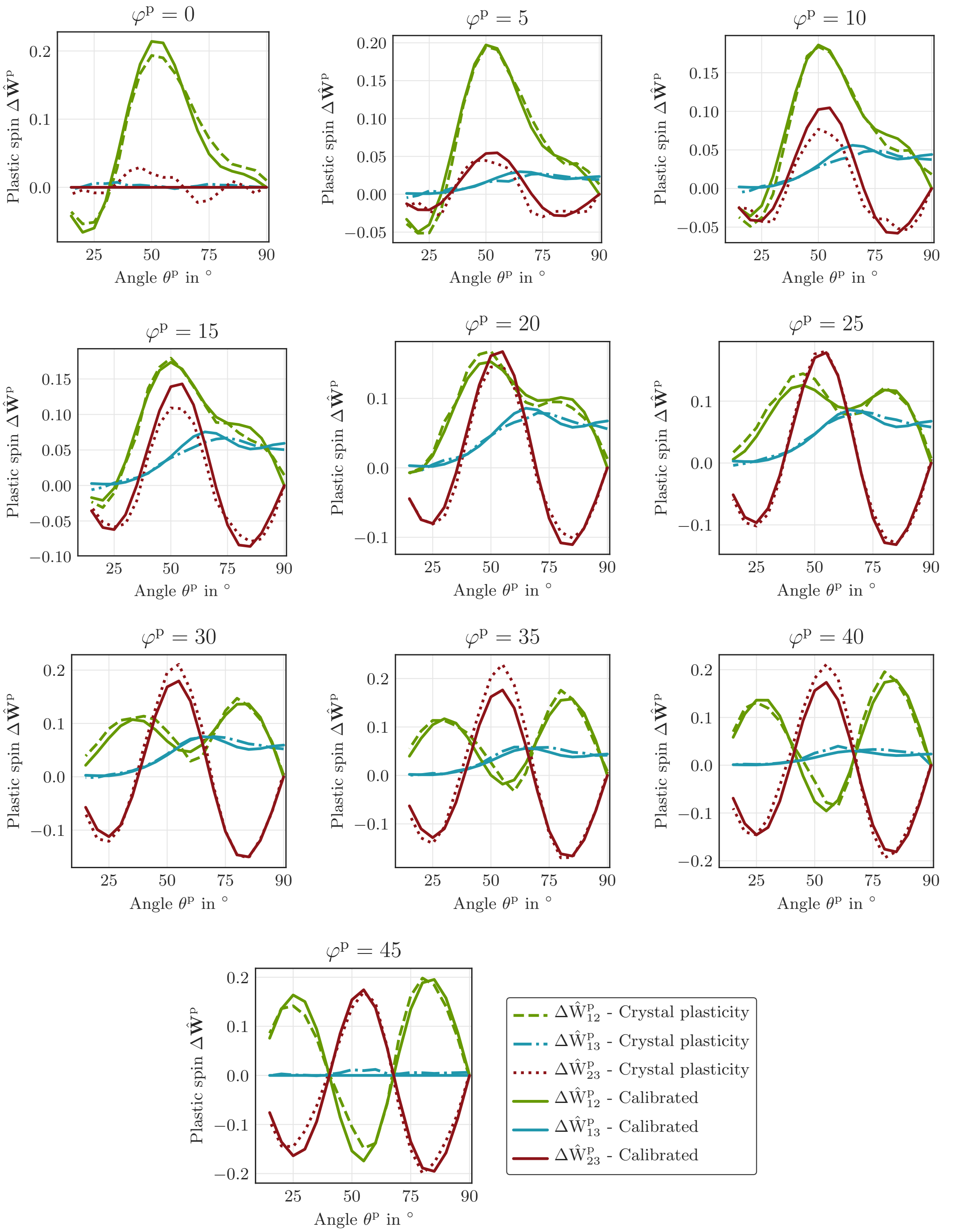

Figure 3.21: Calibrated plastic spin model $\hat{\mathbf{W}}^{\mathrm{p}}_{\mathrm{S}}$.

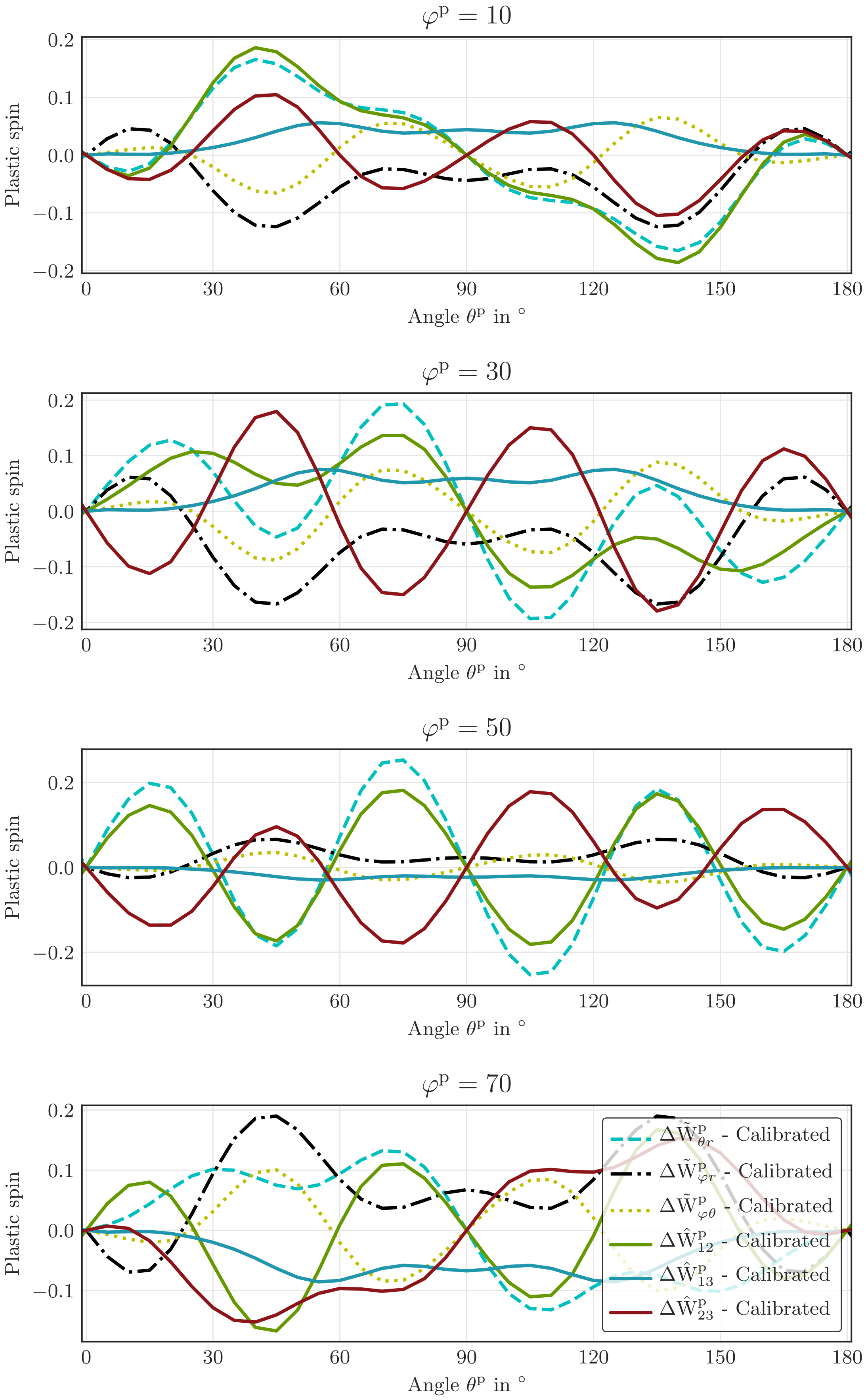

Figure 3.22: Comparison between plastic spin components in CCO ($\hat{\mathbf{W}}^{\mathrm{p}}_{\mathrm{S12}}$) and SPC ($\tilde{\mathbf{W}}^{\mathrm{p}}_{\mathrm{S}}$).

Table 3.5: Calibrated parameters of the plastic spin model $\tilde{\mathbf{W}}^{\mathrm{p}}_{\mathrm{TC}}$.

	β_1	β_2	β_3	β_4	β_5	β_6	β_7	β_8	β_9	β_{10}	β_{11}	β_{12}	β_{13}	β_{14}
$\tilde{\mathrm{W}}^{\mathrm{p}}_{\theta r}$	0.25	0.26	-0.04	0.0	0.0	0.75	0.35	-0.4	0.04	-0.07	0.16	-0.14	-0.56	0.11
$\tilde{\mathrm{W}}^{\mathrm{p}}_{\varphi r}$	-0.4	-0.3	0.05	0.1	0.7	—	—	—	—	—	—	—	—	—
$\tilde{\mathrm{W}}^{\mathrm{p}}_{\varphi\theta}$	0.75	-0.05	-0.22	-0.01	-0.02	0.33	—	—	—	—	—	—	—	—

Table 3.6: Calibrated parameters of the plastic spin model $\tilde{\mathbf{W}}^{\mathrm{p}}_{\mathrm{S}}$.

	β_1	β_2	β_3	β_4	β_5	β_6	β_7	β_8	β_9	β_{10}	β_{11}	β_{12}	β_{13}	β_{14}
$\tilde{\mathrm{W}}^{\mathrm{p}}_{\theta r}$	0.41	-0.05	-0.28	-0.12	0.02	1.27	-0.25	0.3	-0.32	-0.02	3.2	-1.01	0.77	-0.19
$\tilde{\mathrm{W}}^{\mathrm{p}}_{\varphi r}$	-0.55	-0.22	0.32	0.35	0.63	—	—	—	—	—	—	—	—	—
$\tilde{\mathrm{W}}^{\mathrm{p}}_{\varphi\theta}$	-0.96	-1.64	3.36	-0.16	-0.65	-0.07	—	—	—	—	—	—	—	—

4 Final results and discussion

The results of the experimental characterization and the numerical simulations are presented in this chapter with the following structure:

- In section 4.1, the defect and residual stress state analysis is presented for several LPBF316L specimens.
- In section 4.2, the morphological and crystallographic texture of the LPBF316L material is studied using several EBSD measurements for both 30 µm and 50 µm specimens.
- In section 4.3, the main contributing factor to the mechanical anisotropy of LPBF316L is determined with the help of experimental and numerical results.
- In section 4.4, the microscale model and previous findings are validated utilizing the data obtained during in-situ neutron diffraction experiments. Moreover, an inverse analysis is conducted to determine the accuracy of the SCEC used in crystal plasticity simulations.
- In section 4.5, the capabilities the macroscale model are presented and its accuracy is compared against the data obtained during torsion and shear tests.
- In section 4.6, the calibrated and validated macroscale model is used in different virtual experiments to verify the findings in previous sections and also determine the critical aspects of the model, that have the highest impact on the simulation results.

4.1 Defects and residual stresses

To investigate the influence of defects and residual stresses on the anisotropic behavior of LPBF316L samples, six tensile specimens (Tower 0 °, Tower 45 °, Tower 90 °, Wall 0 °, Wall 45 °, and Wall 90 °) were chosen. These samples were then analyzed using µCT and neutron diffraction. µCT was used to identify the microstructural defects, whereas neutron diffraction was employed to measure the residual stresses inside of these six tensile specimens since both of them can have an impact on the material performance of LPBF316L specimens [33, 186, 187]. The measured porosity for the six different samples is displayed in table 4.1. The detected pores during the µCT measurements are believed to be gas pores since they all were of spherical shape. Moreover, it is safe to assume that the anisotropic behavior of the tested tensile specimens in this work is not affected by the very low porosity, which is much smaller than 0.01% for all tested specimens. Thus, the defects are omitted during the numerical analysis.

It is emphasized once more that all the detected pores in this analysis are bigger than 20 µm since the achieved voxel size was 10 µm, as explained in section 2.5. Thus, it is possible that pores smaller than 20 µm have another shape. However, even if the number of smaller undetected pores is high in the LPBF316L, it is very unlikely that the anisotropy is affected by it in a meaningful way since simple modeling assumptions (without considering the porosity) are enough to accurately predict the material behavior, as it will be shown in following sections. But it is worth noting that other testing conditions, such as creep, and cyclic loading, are much more sensitive to the existence of pores inside the material.

Table 4.1: Porosity measured by µCT for six tensile specimens. These results implicate that the porosity is not a contributing factor to the mechanical anisotropy of LPBF316L specimens since the measured porosity is much smaller than 0.01% for all specimens.

	Tower 0°	**Tower 45°**	**Tower 90°**	**Wall 0°**	**Wall 45°**	**Wall 90°**
Analyzed vol. (mm^3)	443.1586	443.7266	442.5135	443.1867	445.1126	444.6265
Vol. of pores (mm^3)	0.0005	0.0015	0.0009	0.0007	0.0013	0.0010
Number of pores	28	73	42	43	59	57
Porosity	$< 0.01\%$	$< 0.01\%$	$< 0.01\%$	$< 0.01\%$	$< 0.01\%$	$< 0.01\%$

During the AM process, the part which is being built is subjected to rapid heating-cooling thermal cycles, which result in RSs in the final part. This mechanisms which are very similar to those during the welding process are explained in this section. The process starts with the heat source melting the feed stock powder, which results in thermal expansion of the material. However, this thermal expansion is very localized and is restrained by the cooler surrounding material. Thus, compressive RSs are formed, which can cause the material to plastically deform. In the following step and by the removal of the localized heat source, the heated material starts to cool down, which results in a shrinkage of the material. However, because of the plastic deformation field, the shrinkage of the material is partially restrained. As a result compressive RSs are formed in the surrounding region of the heating zone accompanied by tensile RSs the middle of the heating zone. It should be noted that in the final stage, the tensile and compressive RSs are balanced out by each other and are thus, in an equilibrium state. In addition to this mechanism, the layer wise nature of the AM process can introduce RSs in the final part through shrinkage of the newly deposited layer during the solidification and cooling phase restrained by the previous layers [110].

To have a better understanding of the RS distribution inside of the tensile specimens, for each specimen, the RSs were determined on three different planes along its height. On each plane, five measurement points were chosen. In total, 15 measurements were conducted for each sample. In each measurement point, RS components for three perpendicular directions were determined. The RSs in normal direction ($\overline{\mathrm{Z}}$), transverse ($\overline{\mathrm{X}}$), and longitudinal ($\overline{\mathrm{Y}}$) are displayed in figs. 4.1, 4.2, and 4.3, respectively. In all these measurements, the highest observed RS range was 142 MPa, with an average error of approximately 20 MPa. The distributions of the RSs for the wall specimens are very similar for each stress component but appear not to be symmetric with respect to the normal axis of the investigated specimens. The minor deviations observed in these results are considered to be connected to the varying extraction locations and orientations within the wall. Comparing the tower and wall specimens reveals that the tower specimens also exhibit a very similar RS distribution.

It is evident from the results that the RSs in Tower 90 ° tend to be compressive. This deviation can be attributed to the fact that the experimental data for this particular specimen were acquired during two separate measurements, which could have resulted in an offset for the stress-free reference. This explanation is very plausible since the absolute values determined for the RSs, and consequently, the compressive and tensile RS profiles are directly linked to the stress-free reference [188]. However, irrespective of the absolute values, the RS distributions and ranges remain unaltered by choice of the stress-free reference, which allows the experimental data to be compared to each other even if the stress-free reference values are not identical.

The experimentally determined RS ranges in these six tensile specimens are listed in table 4.2, which are low compared to the values obtained for net-shape geometries [115,189,190]. This can be attributed to the mechanical relaxation of the RSs due to the machining process [114]. It is highlighted that the RS profile in each sample is a direct result of its thermal and manufacturing history. Thus, deviations in the experimental results are expected since these specimens were extracted from walls and towers, which had different geometries and, consequently, thermal histories. Yet, despite the observed variations in the experimental results, the stress-strain curves obtained during the tensile tests, in particular for the 0 ° direction, are nearly identical, see section 4.3.1. Moreover, the RSs are low when compared to the yield strength of the LPBF316L investigated in this work, see section 4.3.1. These observations indicate that the RSs are not contributing to the mechanical anisotropy in a significant way and are therefore not taken into account during the numerical analysis.

Table 4.2: Maximum residual stress range measured in 6 tensile specimens for three orthogonal directions, see fig. 2.6 for the used coordinate system. All values are in MPa.

	Tower 0°	**Tower 45°**	**Tower 90°**	**Wall 0°**	**Wall 45°**	**Wall 90°**
Normal direction ($\overline{\mathbf{Z}}$)	89.98	117.64	142.68	109.5	96.81	107.49
In-plane direction ($\overline{\mathbf{X}}$)	118.06	84.66	160.78	147.43	106.33	169.34
In-plane direction ($\overline{\mathbf{Y}}$)	109.3	130.75	149.92	115.31	104.87	159.31

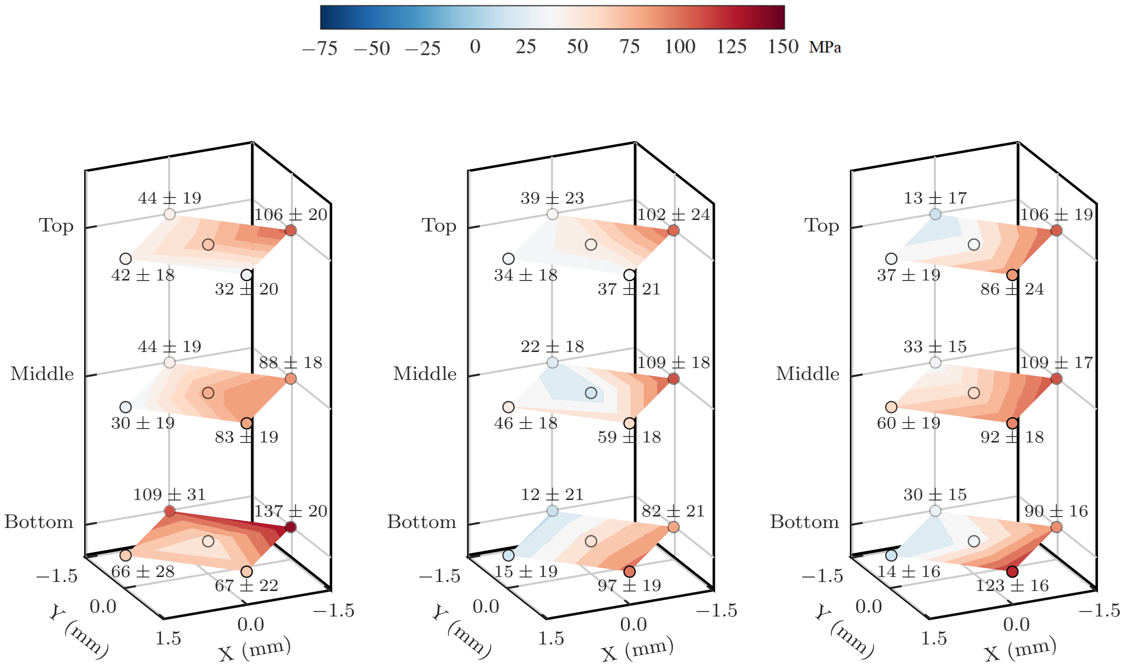

(a) Wall 90° **(b)** Wall 45° **(c)** Wall 0°

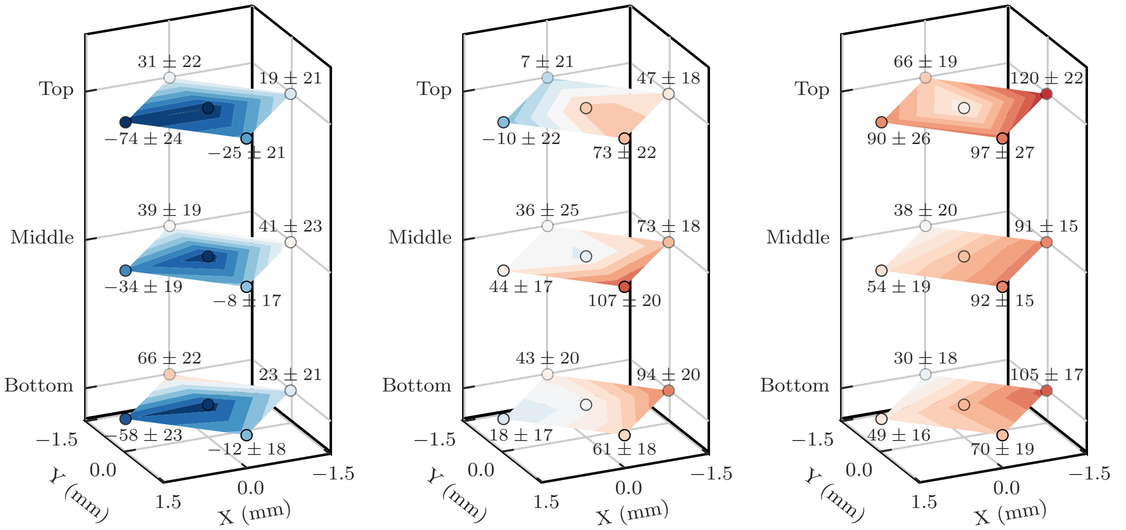

(d) Tower 90° **(e)** Tower 45° **(f)** Tower 0°

Figure 4.1: RSs in the normal direction ($\overline{\mathrm{Z}}$) measured at three different heights, named Bottom, Middle, and Top. The pictures on the top row show RSs for three inclinations in the wall specimens and the pictures on the bottom row show RSs in the tower specimens. The coordinate system ($\overline{\mathrm{X}}$, $\overline{\mathrm{Y}}$, and $\overline{\mathrm{Z}}$) is shown in fig. 2.6. The highest value of measured RS is 137 MPa in Wall 90 ° specimen and the lowest value is −76 MPa in Tower 90 ° specimen. Once more it is highlighted that the compressive nature of RSs in Tower 90 ° specimen are likely due to an offset for the stress-free reference diffraction values, as explained before.

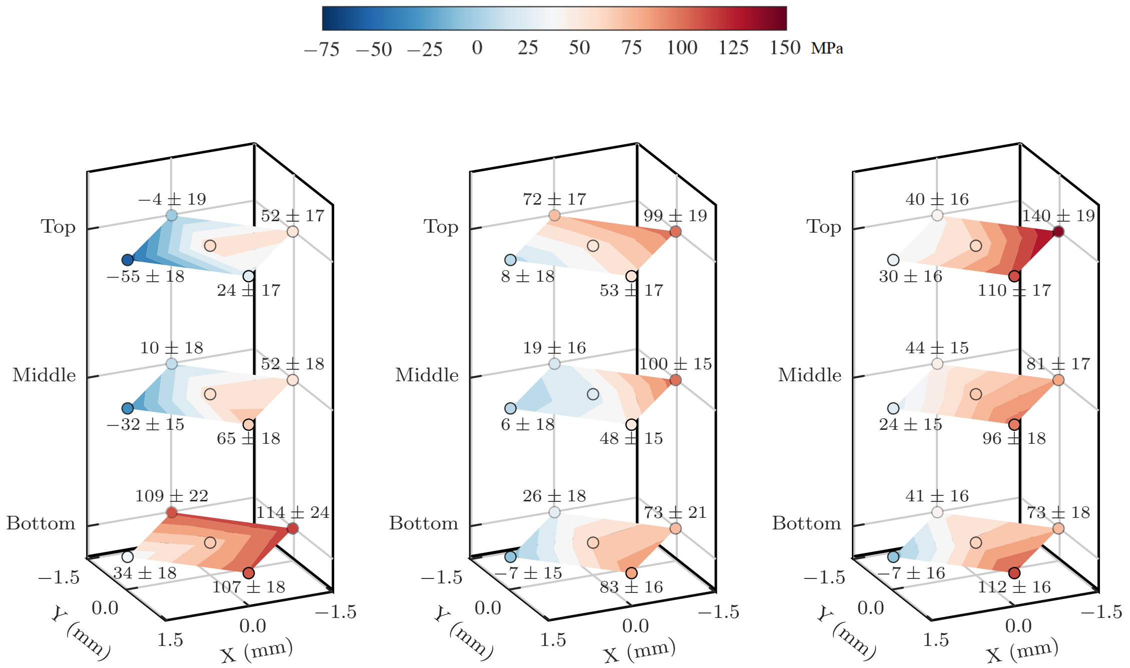

(a) Wall 90° **(b)** Wall 45° **(c)** Wall 0°

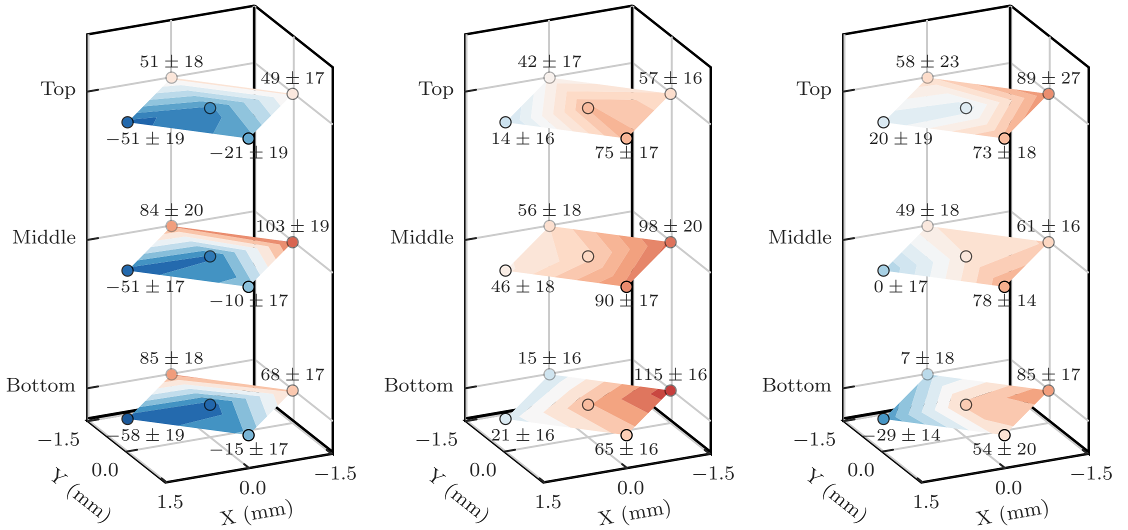

(d) Tower 90° **(e)** Tower 45° **(f)** Tower 0°

Figure 4.2: RSs in the transverse direction ($\overline{\mathrm{X}}$) measured at three different heights, named Bottom, Middle, and Top. The pictures on the top row show RSs for three inclinations in the wall specimens and the pictures on the bottom row show RSs in the tower specimens. The coordinate system ($\overline{\mathrm{X}}$, $\overline{\mathrm{Y}}$, and $\overline{\mathrm{Z}}$) is shown in fig. 2.6. The highest value of measured RS is 140 MPa in Wall 0 ° specimen and the lowest value is −58 MPa in Tower 90 ° specimen. Once more it is highlighted that the compressive nature of RSs in Tower 90 ° specimen are likely due to an offset for the stress-free reference diffraction values, as explained before.

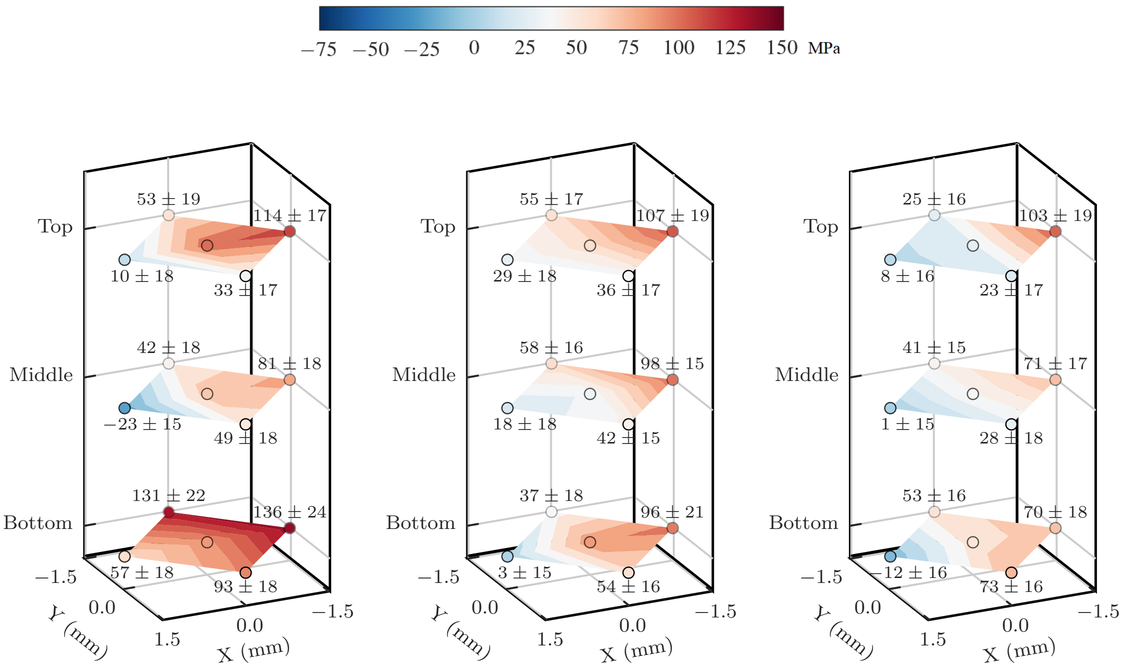

(a) Wall 90° **(b)** Wall 45° **(c)** Wall 0°

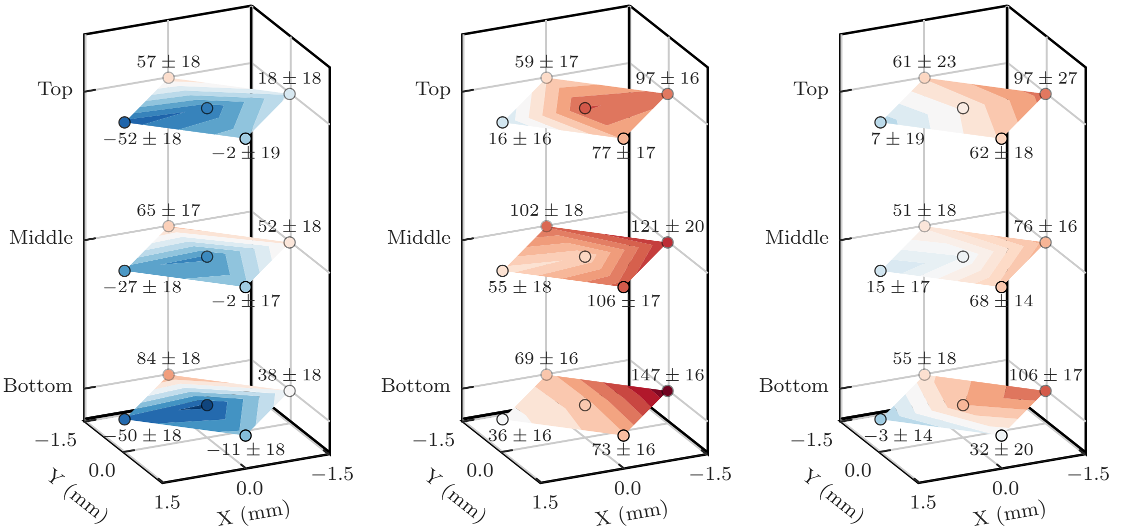

(d) Tower 90° **(e)** Tower 45° **(f)** Tower 0°

Figure 4.3: RSs in the longitudinal direction ($\overline{\mathrm{Y}}$) measured at three different heights, named Bottom, Middle, and Top. The pictures on the top row show RSs for three inclinations in the wall specimens and the pictures on the bottom row show RSs in the tower specimens. The coordinate system ($\overline{\mathrm{X}}$, $\overline{\mathrm{Y}}$, and $\overline{\mathrm{Z}}$) is shown in fig. 2.6. The highest value of measured RS is 147 MPa in Tower 45 ° specimen and the lowest value is −65 MPa in Tower 90 ° specimen. Once more it is highlighted that the compressive nature of RSs in Tower 90 ° specimen are likely due to an offset for the stress-free reference diffraction values, as explained before.

4.2 Texture analysis

The mechanical performance of a metallic material is directly linked to its microstructure. In this work, the crystallographic and morphological textures are analyzed using EBSD measurements from five different specimens. Two of the 30 µm Walls, one 50 µm Tower 90 °, one 50 µm Tower 45 °, and one 50 µm Wall were used for the experimental investigation. All measurements were designed to ensure that the retrieved microstructural data, especially the crystallographic texture, is as representative as possible for both the 30 µm and 50 µm specimens. The EBSD maps, the extracted crystallographic textures, and the grain size distribution for the 50 µm specimens, which were extracted from five different regions, are displayed in figs. 4.4, 4.5, and 4.6. The results for the 30 µm specimens (extracted from four different regions) are shown in figs. 4.8, 4.8, and 4.9. The total scanned area for these measurements equals $132 + 192\,\mathrm{mm}^2$. The measurements from both the 30 µm and 50 µm walls, each consisting of four smaller EBSD maps, are merged using the software MTEX [147,173].

Note that the EBSD maps for the 30 µm and 50 µm specimens were post-processed in the software MTEX [147, 173]. The unindexed measurement points were corrected during this procedure, and an average orientation was determined for each grain. The average grain orientation has been used to replace the gradients measured in each grain to reduce the noise in the displayed data. The displayed EBSD maps reveal the unusual grain morphology, which is characterized by the checkerboard pattern in the cross-section measurements and columnar structures in the measurements from the side of specimens. This grain morphology is a direct result of the employed scan strategy. More interestingly, there is no sign of melt pool boundaries in the measurements from the specimens' side. This indicates that remelted zones have epitaxial grain growth. Besides the unusual morphological texture, the LPBF316L specimens exhibit a two to three times random {110} texture in the build direction visible in the pole figures for the 30 µm and 50 µm specimens, see fig. 4.5. These results match the findings in other studies [16,39,191] and will be used as an input for the CP simulations.

It is worth noting that for the determination of the grain boundaries in the software MTEX [147,173], the misorientation value has been set to 15 °. These EBSD measurements show that crystallographic and morphological textures are comparable in all manufactured specimens despite the different geometries and modified processing parameters. The most significant difference is observed in the grain size distributions, whereby 65 µm and 25.4 µm are the mean values extracted from the grain size distributions of the 50 µm and 30 µm specimens. These results show that reducing the layer thickness from 50 µm to 30 µm reduces the average grain size substantially, which could have an impact on the overall mechanical performance of the specimens. However, this aspect is not analyzed in depth in this work since due to the limited number of produced specimens, the 30 µm and 50 µm specimens are used for different purposes. Therefore, most of the findings can't be compared to each other directly. Such comparison is only available for the tensile results shown in section 4.3.1.

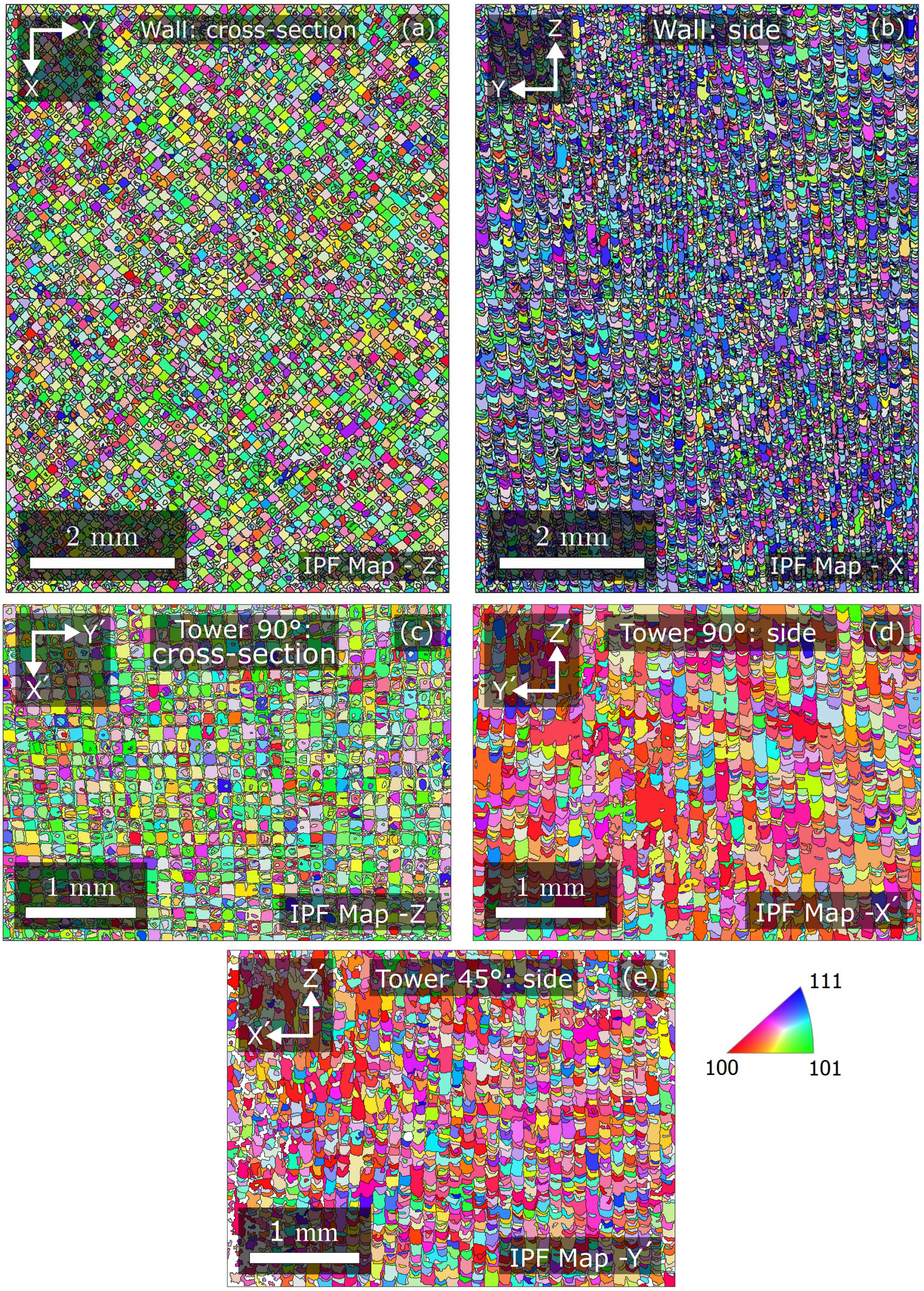
Y
X
Wall: cross-section
(a)
2 mm
IPF Map - Z
Z
Y
Wall: side
(b)
2 mm
IPF Map - X
Y´
X´
Tower 90°: cross-section
(c)
1 mm
IPF Map -Z´
Z´
Y´
Tower 90°: side
(d)
1 mm
IPF Map -X´
Z´
X´
Tower 45°: side
(e)
1 mm
IPF Map -Y
111
100
101

Figure 4.4: EBSD measurements from cross-section of wall (a), side of wall (b), cross-section of Tower 90° (c), side of Tower 90° (d) and side of Tower 45° (e). Note that the coordinate systems (X, Y, Z) and (X′, Y′, Z′) are different, for more details see fig. 2.1. The corresponding pole figures are shown in fig. 4.5.

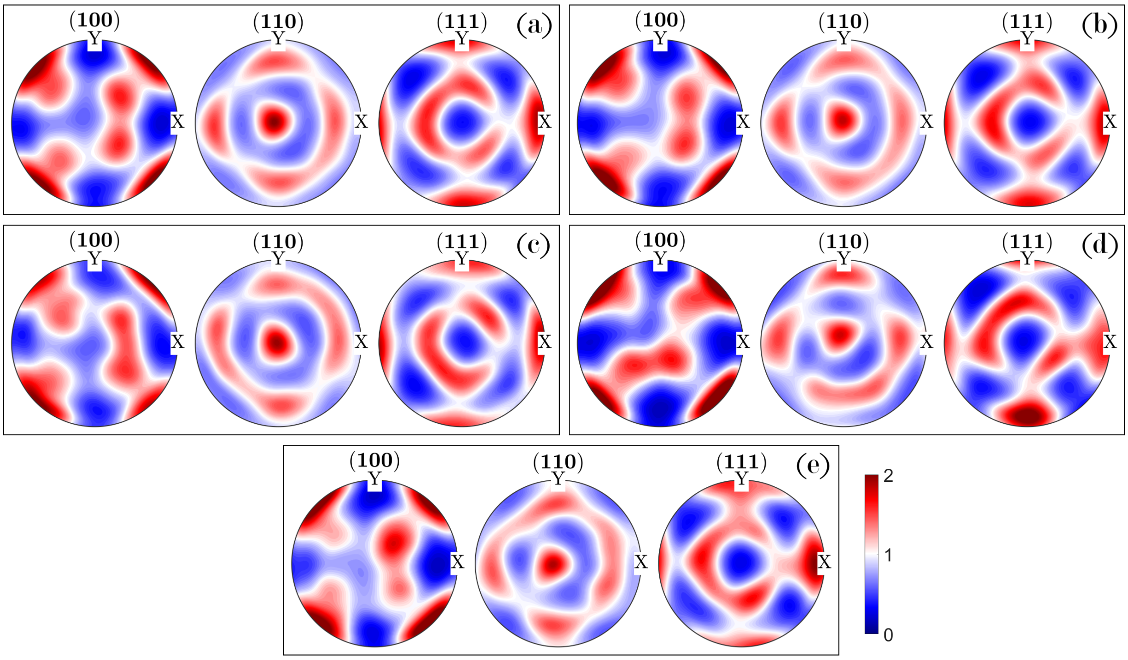

Figure 4.5: Pole figures from cross-section of wall (a), side of wall (b), cross-section of Tower 90° (c), side of Tower 90° (d) and side of Tower 45° (e). Note that for an easier comparison, all pole figures (a, b, c, d, e) are shown in the same coordinate system (X, Y, Z) and not the coordinate system of their corresponding EBSD map in fig. 4.4. It is evident from the results that all specimens have a very similar $\{110\}$ texture in the build direction.

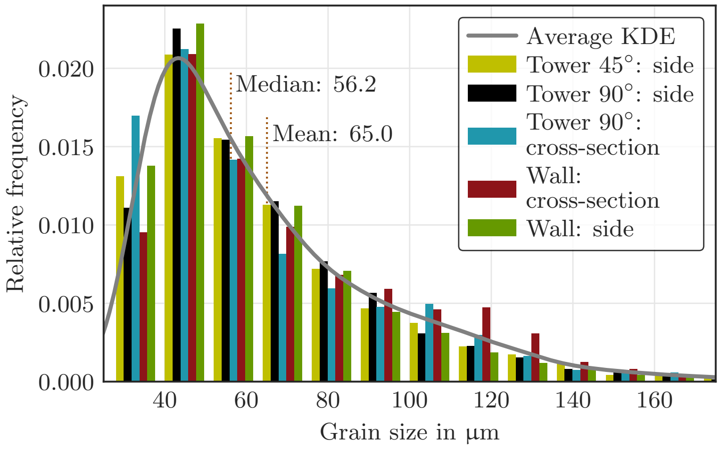

Figure 4.6: Grain size distributions determined from five EBSD measurements, see fig. 4.4. The grain size is calculated from the grain area assuming a rectangular grain shape. The kernel density estimation (KDE) visible in the plot is the average KDE of all five grain size distributions.

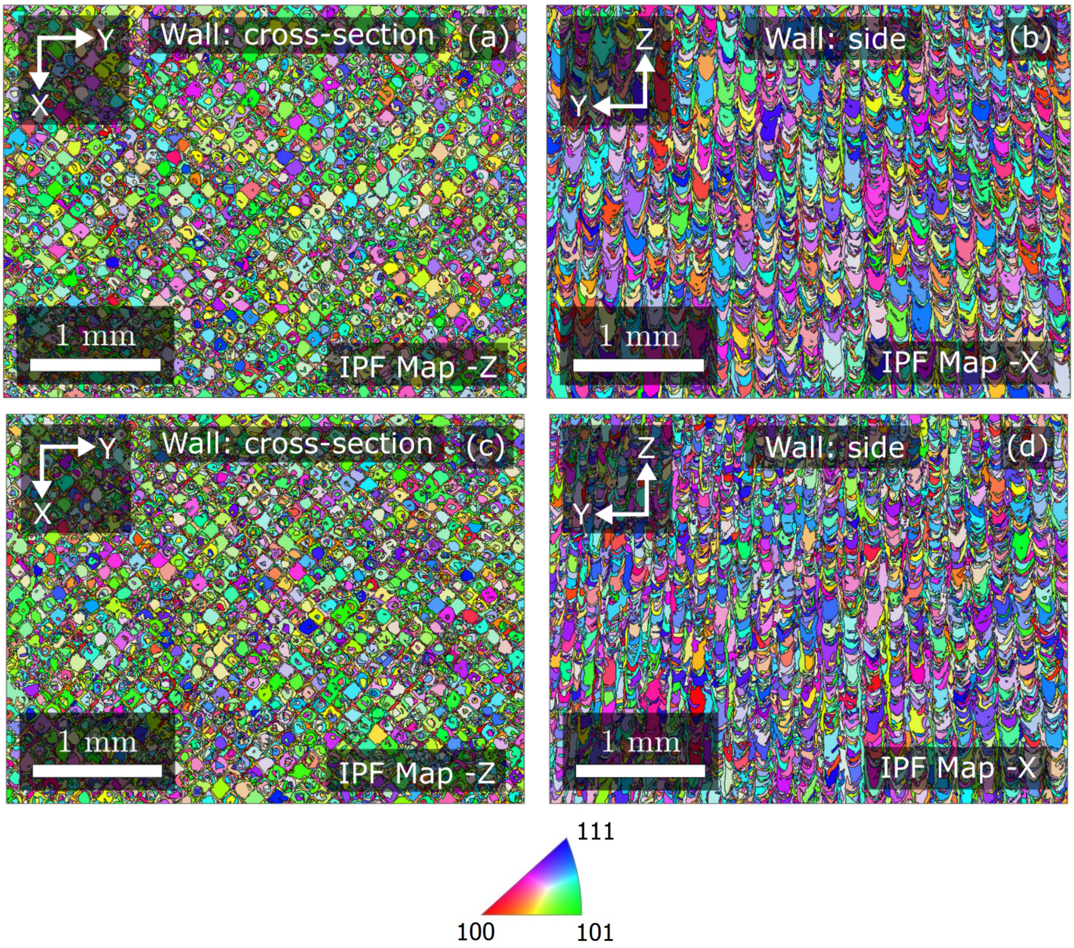
Y
X
Wall: cross-section
(a)
1 mm
IPF Map -Z
Z
Y
Wall: side
(b)
1 mm
IPF Map -X
Y
X
Wall: cross-section
(c)
1 mm
IPF Map -Z
Z
Y
Wall: side
(d)
1 mm
IPF Map -X
111
100
101

Figure 4.7: EBSD measurements from cross-section of 30 µm wall 1 (a), side of 30 µm wall 1 (b), cross-section of 30 µm wall 2 (c), and side of 30 µm wall 2 (d). The coordinate system is shown in fig. 2.1. The corresponding pole figures are shown in fig. 4.8.

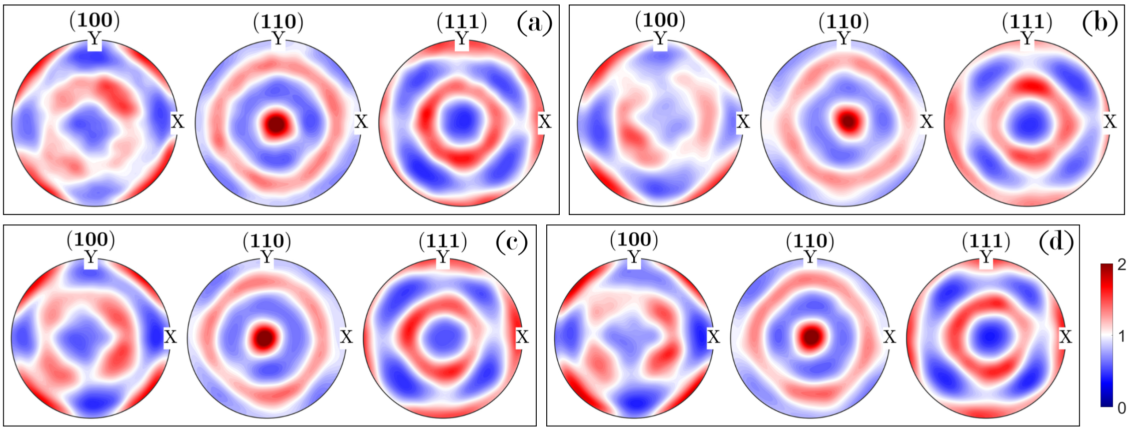

Figure 4.8: Pole figures from cross-section of 30 µm wall 1 (a), side of 30 µm wall 1 (b), cross-section of 30 µm wall 2 (c), and side of 30 µm wall 2 (d). All pole figures (a, b, c, d) are shown in the same coordinate system (X, Y, Z). All specimens have a very similar {110} texture in the build direction, comparable to the results in fig. 4.5.

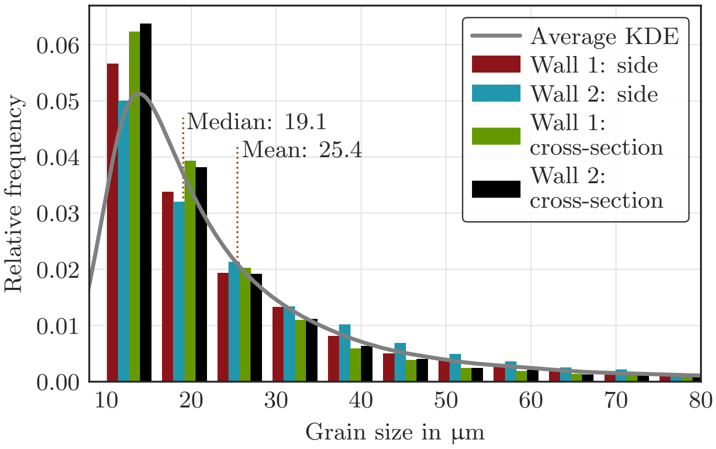

Figure 4.9: Grain size distributions determined from five EBSD measurements, see fig. 4.8. The grain size is calculated from the grain area assuming a rectangular grain shape. The kernel density estimation (KDE) visible in the plot is the average KDE of all four grain size distributions.

4.3 Understanding the mechanical anisotropy in LPBF316L

4.3.1 Tensile test results

As explained in section 2.3, the specimens from the 50 µm plates and towers were investigated using both tensile tests and the resonance method. For the specimens from the 30 µm plates, only tensile tests were conducted. The characteristic values for the 50 µm specimens, determined from the tensile tests, are listed in table 4.3. The corresponding stress-strain curves are plotted in fig. 4.10 for different stress and strain ranges. It is evident from these results that, in general, for the 50 µm specimens, the characteristic strength parameters (E, $R_{p0.2}$, and R_m) increase as the build angle decreases. Furthermore, the specimens from the plates and towers exhibit very similar behaviors, except for the 45 ° orientation, which is caused by the rotated scan strategy (see fig. 2.1). However, this is not the case for 90 ° specimens since the rotation and loading axes coincide. The percentage elongation after fracture (A), which is calculated by carefully fitting back together the broken pieces after fracture and measuring the gauge length, and reduction of area (Z) seem to be independent of the build orientation. Moreover, it is highlighted that the tensile test results for the 50 µm specimens, in general, display a low scatter. Only the stress-strain curves for 90° specimens exhibit a small deviation. Comparison between these stress-strain curves also reveals the fact that each direction exhibits a slightly different yield behavior, which is most notable during the transition from purely elastic to plastic deformation. The sharpest transition behavior belongs to the 0° direction, contrary to the 90° specimens, which have a more diffused transition behavior.

Table 4.3: Tensile test results for the 50 µm specimens according to DIN EN ISO 6892-1.

			0°		**45°**		**90°**	
			Spec. 1	**Spec. 2**	**Spec. 1**	**Spec. 2**	**Spec. 1**	**Spec. 2**
$R_{p0.2}$	MPa	Tower	583	583	540	537	500	– –
		Wall	581	581	564	563	514	506
R_m		Tower	692	692	652	653	619	– –
		Wall	689	691	670	671	620	611
A	%	Tower	54	55.5	56.5	56.5	60	– –
		Wall	56.5	56.5	56.5	53	59.5	53.5
Z		Tower	72.2	71.3	73.3	71.5	72.2	– –
		Wall	73	72.5	71	70.6	72.5	72.3
E	GPa	Tower	212	218	196	199	198	– –
		Wall	213	218	194	210	194	181

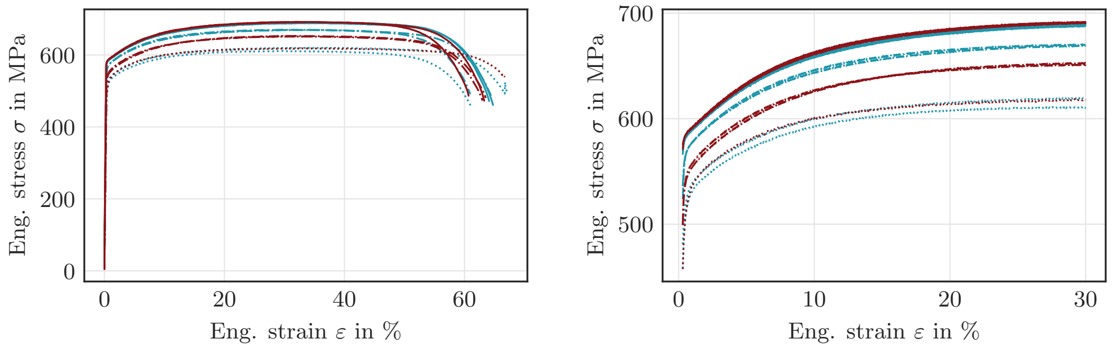

(a) Complete stress-strain range.

(b) Hardening behavior from 0 to 0.3 strain.

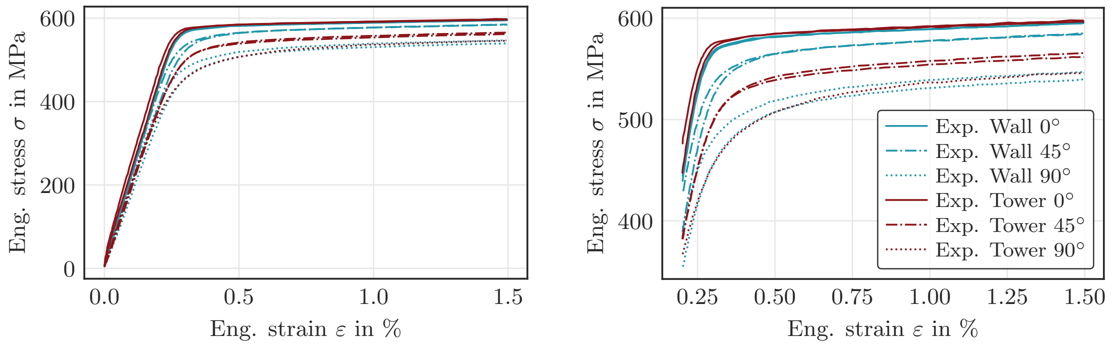

(c) Anisotropy during elastic deformation.

(d) Start of yielding.

Figure 4.10: Stress-strain curves obtained during the tensile tests for the 50 µm specimens. The plots (a, b, c, d) display the same results within different stress and strain ranges. Tower 45 ° and Wall 45 ° stress-strain curves are shifted relative to each other, which is due to the rotated scan strategy, see fig. 2.1. Therefore, the analysis in subsequent sections is conducted by grouping the specimens in 0 °, Tower 45 °, Wall 45 ° and 90 ° to account for the effect of the scan strategy.

The tensile test results for the 30 µm specimens are shown in fig. 4.11, highlighting that the 30 µm specimens exhibit a higher yield strength but an ever so slightly flatter hardening behavior compared to the 50 µm specimens. These results match the findings in section 4.2, where it was shown that the 30 µm specimens have smaller grains compared to the 50 µm specimens. This fact alone could explain the differences observed in the yield strength of these specimens. Moreover, higher yield strength is usually accompanied by a higher dislocation density, which in turn can reduce the workability of the material, evident from the flatter hardening behavior combined with the lower ultimate tensile strength. However, these results are not sufficient to definitely prove these claims since only two 30 µm specimens could be tested due to limitations during the manufacturing process. Overall, it can be concluded that despite the differences observed in tensile behavior, mostly the yield strength, the underlying deformation mechanisms in both the 30 µm and 50 µm specimens are very similar since both the anisotropy and the hardening behavior are very close to each other. This is also in line with the findings presented in section 4.2, where it was shown that both the 30 µm and 50 µm specimens have a very comparable {110} texture in the build direction.

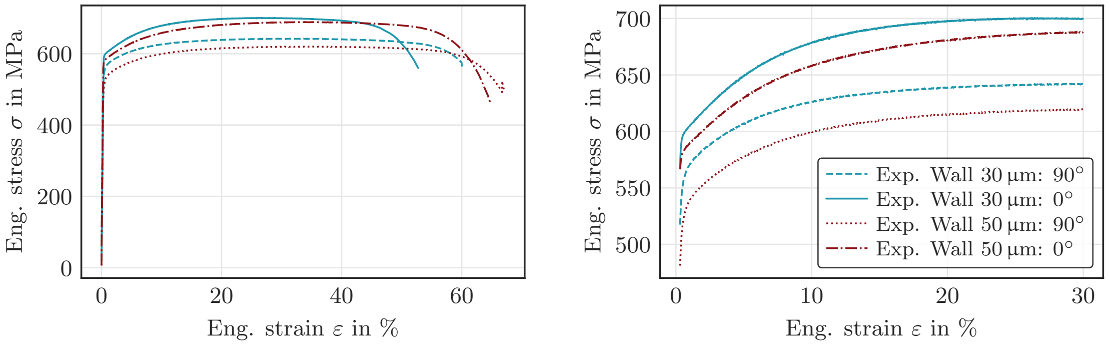

(a) Complete stress-strain range.

(b) Hardening behavior from 0 to 30 % strain.

Figure 4.11: Comparison between stress-strain curves obtained during the tensile tests for the 30 µm and 50 µm specimens. The plots (a, b) display the same results within different stress and strain ranges.

Similar trends to the results shown in this section were also reported in [192–194]. However, it is worth noting that it is hard to directly compare the results in this section with the findings in other studies since these results are linked to the specific microstructure shown in section 4.2, which is in turn a direct result of the chosen parameters during the manufacturing process. Different parameters result in different microstructures with different material and mechanical properties, as shown in this section and section 4.2. The severity of these differences are dependent on the chosen parameters and the final texture of the material. This property of the AM process is what allows the tailoring of specific microstructures with certain desired properties. However, it also makes it nearly impossible to compare such results directly to each other. This is also one of the reasons why in [32] it was shown that the reported directional dependency of LPBF316L in different studies differed significantly and even contradictory in some cases.

4.3.2 Elastic anisotropy

The extensometer utilized in this work during the tensile testing is not particularly suitable for determining Young's moduli since it was designed to capture the stress-strain behavior of the specimens for an extensive strain range. Therefore, the stress-strain results at the beginning of a tensile test aren't as accurate as those obtained by some other extensometers designed explicitly for smaller strain ranges. That is why the resonance method [108] was employed to accurately determine the dynamic Young's moduli of three specimens that were cut out from one of the 50 µm AM walls for three different inclinations. The fundamental flexural resonance frequencies obtained from in-plane and out-of-plane flexure were then used to calculate the dynamic Young's moduli. The measurement error is determined to be around 1 % by inter-laboratory studies using other materials. The experimental results are listed in table 4.4. Compared to Young's moduli determined in tensile tests, the values from the resonance method cover a wider range for the chosen inclinations, which is graphically shown in fig. 4.12.

Table 4.4: Results from resonance method according to ASTM E1876 [108].

			0°		**45°**		**90°**	
			Spec. 1	**Spec. 2**	**Spec. 1**	**Spec. 2**	**Spec. 1**	**Spec. 2**
E	GPa	Tower	−−	−−	−−	−−	−−	−−
		Wall	225	−−	206	−−	180	−−

The elastic response of a polycrystalline material, such as LPBF316L (see fig. 4.4), is directly coupled with the elastic properties of its grains, more specifically, the single-crystal elastic anisotropy. The elastic stiffness tensor belonging to a single-crystal can be uniquely specified using three elastic constants, C_{11}, C_{12}, and C_{44}, also called SCEC. If these values are known, then the elastic behavior can be predicted in any desired direction. It is worth noting that SCEC are dependent on the crystallographic orientation of the single-crystal. A polycrystalline material consists of many such grains. And it is logical that the resulting average behavior of all grains determines the macroscopic elastic behavior. That is also why the mechanical properties of a polycrystalline material depend on the crystallographic texture since it gives insight into the arrangement of the grains. Thus, changes in the crystallographic texture mean that the grains are rearranged, which in turn directly impacts the average mechanical properties.

The Young's moduli determined from eleven tensile tests are averaged for loading directions 0°, Wall 45°, Tower 45°, and 90° and measured to be 215 ± 3 GPa, 202 ± 8 GPa, 198 ± 2 GPa, and 192 ± 7 GPa, respectively. As explained in previous sections, Wall 45° and Tower 45° specimens are separated from each other to account for the influence of the rotated scan strategy during specimen production, see fig. 2.1 and 4.10. The measured dynamic Young's moduli for Wall 0°, Wall 45°, and Wall 90° specimens are 225 GPa, 206 GPa, and 180 GPa, respectively. For the numerical analysis, the softwares DAMASK [71] and MTEX [147] are utilized. Both of them require the crystallographic texture with the SCEC to output the averaged elastic properties, see sections 3.4.1 and 3.2.3. Voigt, Hill, Reuss are the three available methods in MTEX for the estimation of the macroscopic elastic behavior [173].

The crystallographic textures for the 50 µm specimens, shown in fig. 4.4, were from five different regions, which are also used for the numerical calculation of Young's moduli. In this way, the accuracy and sensitivity of the models are assessed easily since variations in ODFs could influence the numerical results. In fig. 4.12, all experimental and numerical results are compared to each other. The numerical results cover the range between the minimum and maximum values obtained for all five crystallographic textures and are displayed in different colors. The most accurate models for the numerical estimation of Young's moduli are revealed to be the Hill model in MTEX and the CP model. The differences observed between tensile tests and resonance method are likely due to measurement inaccuracies since the employed extensometer for the tensile tests was calibrated in the range of −10 % to 50 % percent strain. As explained previously, such a wide range is not ideally suited for precise measurements of Young's moduli. In summary, despite the observed differences, it can be argued that for the tested specimens, the crystallographic texture and the SCEC are sufficient to predict the elastic response of LPBF316L with good accuracy. These results are also in line with the findings in [195, 196], where the authors arrived at the same conclusions for their AM Inconel 718 specimens. These results are a strong indication that the crystallographic texture predominately controls the mechanical anisotropy of LPBF316L.

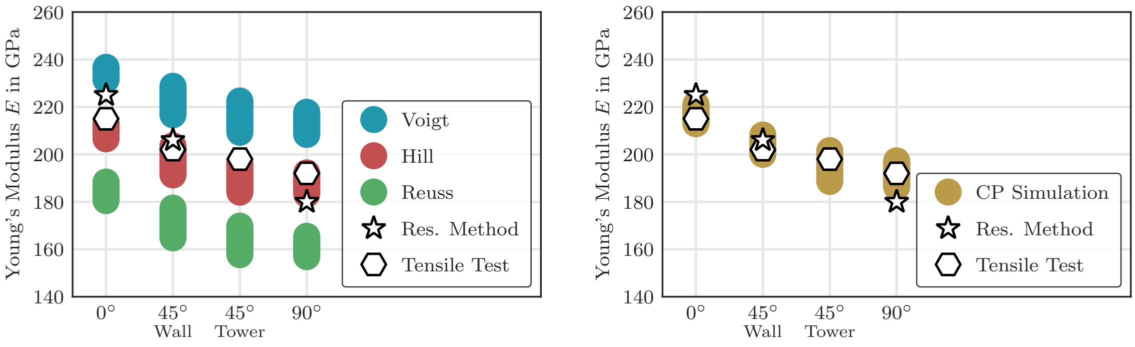

(a) (b)

Figure 4.12: Comparison between experimentally measured and numerically estimated Young's moduli using softwares MTEX (a) and DAMASK (b). Each color, which corresponds to a different estimation method, renders the range between the minimum and maximum value obtained for five separate extracted crystallographic textures, see fig. 4.5. The SCEC are taken from [172].

4.3.3 Numerical modeling of anisotropic yield behavior

The most important findings in the former sections are as follows:

- The LPBF316L tensile specimens exhibit anisotropic behavior during elastic and plastic deformation.
- Microstructural defects are not a contributing factor to the mechanical anisotropy of LPBF316L since the measured porosity is much smaller than 0.01 % in six different 50 µm specimens.
- RSs in the 50 µm tensile specimens are much lower compared to net-shape geometries due to mechanical relaxation. Furthermore, it was concluded that the RSs don't contribute to the mechanical anisotropy of LPBF316L in any significant way.
- Both the 30 µm and 50 µm specimens have a very similar {110} texture in the build direction.
- The elastic anisotropy in the 50 µm specimens is mainly controlled by the crystallographic texture and can be predicted using the CP model very accurately.

With these findings, the next logical step is the numerical analysis of the anisotropic yield behavior of LPBF316L using the CP model. The calibration of the model was carried out using only one tensile test and one EBSD measurement (both from Tower 45°) according to the procedure explained in section 3.4.2.1 to demonstrate the efficiency and reliability of the numerical method. As such, the remaining tensile tests and EBSD measurements were utilized for the validation and sensitivity analysis of the model. The simulated stress-strain curves for all loading directions and crystallographic textures, along with their corresponding experimental results, are shown in fig. 4.13 and 4.14. The numerical curves cover the range between the minimum and maximum value obtained during the simulations for all five experimentally determined crystallographic textures, see fig. 4.5. Thus, the numerical stress-strain curves show the sensitivity of the CP model with respect to the variations in the crystallographic texture.

The CP model is capable of predicting the anisotropic yield behavior of LPBF316L with high accuracy, as evident from the error analysis presented in fig. 4.15, which shows the maximum deviation between the simulations and experiments as %-error. The accuracy of the numerical model is shown to be high since %-error is below 5% after only 0.4 % strain and stays under 3% after 2.5 % strain. Considering the difficulties of extracting the crystallographic texture from a 2D surface area and all possible sources of measurement error, such as surface finish, beam shift, and texture gradients in the material, the variations observed in the simulation results are very tolerable. It is highlighted once more that the parameter calibration was based on the results from a single test specimen, and in all subsequent simulations, the same parameter set was used. This means that the final simulation results shown in this section can be further optimized since the other tensile tests and EBSD measurements were not part of the calibration process, see fig. 4.16. However, this optimization is not part of this work since the remaining experimental data were used to demonstrate the sensitivity and reliability of this approach.

By close inspection of the results shown in fig. 4.13, it becomes clear that there is a variation in the yield behavior for each loading direction, which is not captured in the CP simulations. The transition from purely elastic to plastic deformation is sharper in the 0° direction, whereas the 90° specimens have a more diffused transition behavior. This behavior leads to a greater deviation between the simulations and experiments, most notably in the region where yielding starts. There is no specific explanation for this observation since no further experimental analysis was conducted. However, different competing deformation mechanisms for each loading direction might be responsible for it. For example, nano twinning has been observed in AM metals and is believed to be contributing to the mechanical behavior [16,22,25,40]. Other contributing factors, such as melt pool boundaries and cellular structures, might also play a role. However, these mechanisms aren't included in the currently used CP model since dislocation slip is sufficient to capture the main underlying physical phenomena. These results strongly indicate that the crystallographic texture is mainly responsible for the mechanical anisotropy of LPBF316L.

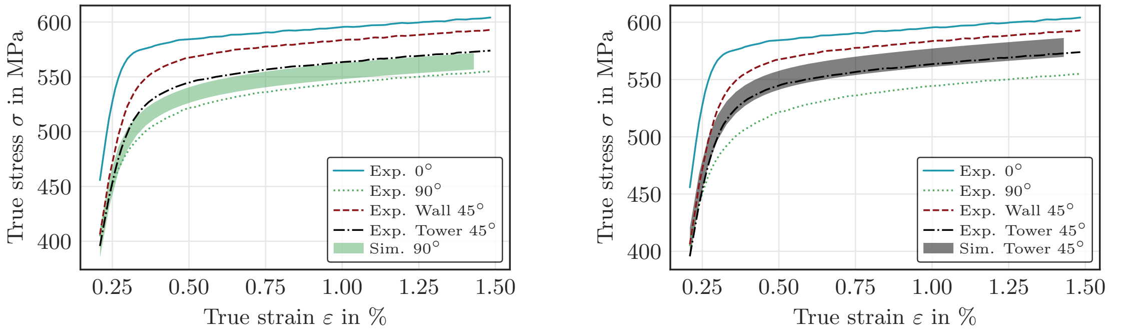

(a) Simulations results for 90° samples. **(b)** Simulations results for Tower 45° samples.

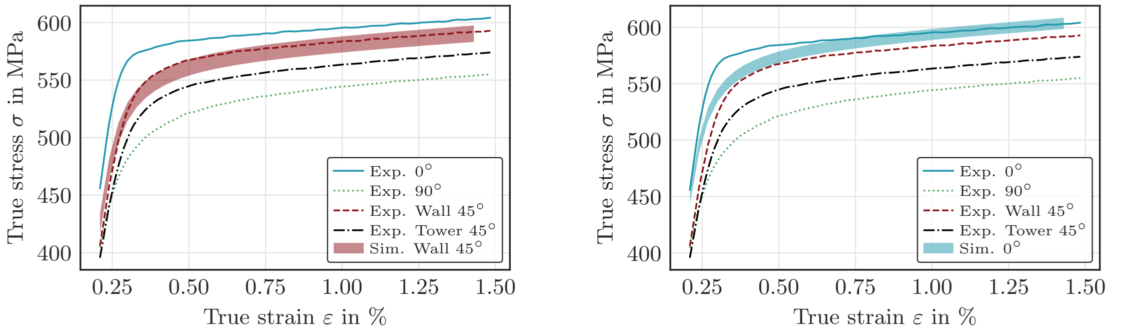

(c) Simulations results for Wall 45° samples. **(d)** Simulations results for 0° samples.

Figure 4.13: Comparison between experimental and numerical (CP) stress-strain response in the strain range of 0.002 to 0.015. The plots (a, b, c, d) each contain the simulation results for one specific loading direction. The simulation results cover the range between minimum and maximum value obtained for all five extracted crystallographic textures, see fig. 4.4.

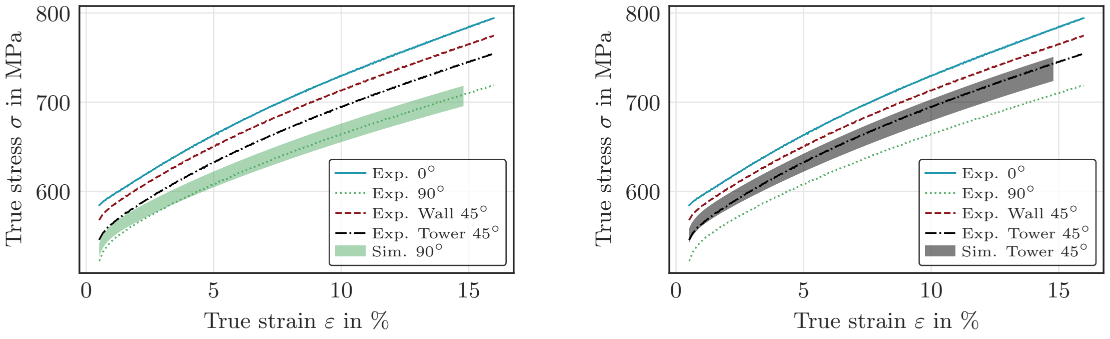

(a) Simulations results for 90° samples. **(b)** Simulations results for Tower 45° samples.

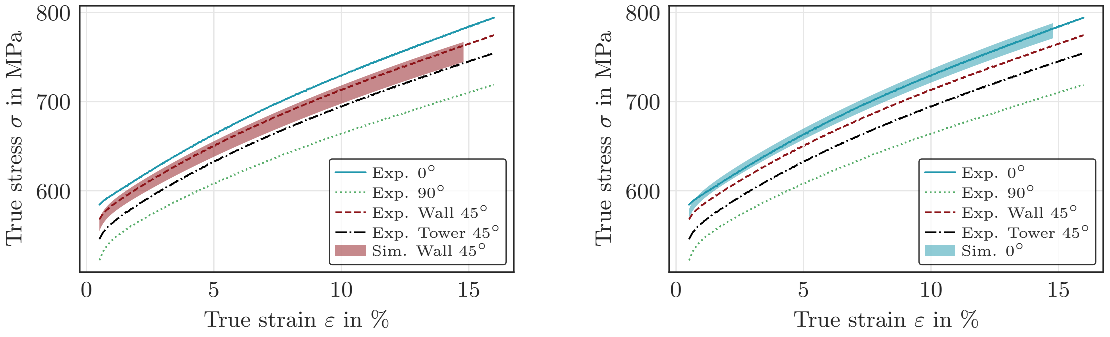

(c) Simulations results for Wall 45° samples. **(d)** Simulations results for 0° samples.

Figure 4.14: Experimental and numerical results for all extracted crystallographic textures displayed in the strain range of 0.005 to 0.16, which demonstrate the accuracy of the CP model outside of its calibration range. Note that the strain range for the calibration process was between 0 and 0.015.

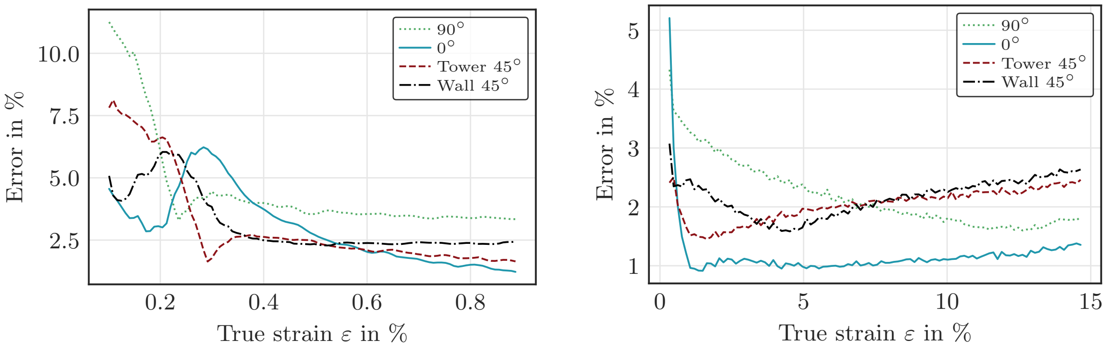

Figure 4.15: Maximum deviation between the experimental and numerical stress-strain curves (fig. 4.13 and 4.14) presented as %-Error.

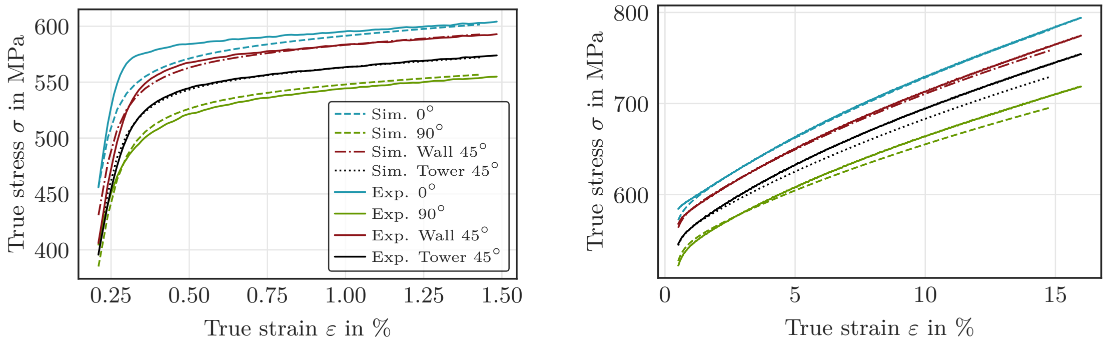

(a) Inside calibration range: 0 to 1.5 % strain. **(b)** Outside calibration range: 0 to 15 % strain.

Figure 4.16: CP model calibration results for the Tower 45° specimen.

4.4 Micromechanical validation

As explained in section 2.8, the in-situ neutron diffraction experiments were conducted to determine the lattice strain evolution during two separate tensile tests, one for the 0° and the other one for the 90° direction. Both tensile specimens were manufactured from 30 µm walls. In section 4.3.3, it was demonstrated that the CP model is capable of predicting the anisotropy observed in LPBF316L if the model is provided with the correct crystallographic texture and the SCEC of the material. Thus, it was concluded that the anisotropy is mainly controlled by crystallographic texture and dislocation slip is the dominant deformation mechanism. However, these findings were based on the average stress-strain response determined over the entire RVE consisting of many smaller grains. Through this averaging procedure, it is possible that some unique physical phenomena remain undetected. Thus, in this section, the deformation behavior of these grains is inspected more closely. The experimental and numerical lattice strain evolution results shown in this work serve the following purposes:

- Validate the main conclusions in section 4.3.3 by comparing the CP model predictions with the experimental results at the grain scale.
- Identify possible shortcomings of the CP and isolate deformation mechanisms not captured by it.

The experimental data presented in this work are a small part of a much bigger ongoing work package aimed at characterizing AM metals. And they are only used in this section for the validation of the CP model. Therefore, the experimental results aren't analyzed on their own since that would require expertise and further testing, which are outside of the scope of this investigation. It is noted that the 30 µm and 50 µm specimens possess slightly different crystallographic textures and that the stress-strain response of these specimens varies, as evident from fig. 4.11. However, these differences are not significant, and it is assumed that the findings for the 30 µm specimens are also valid for the 50 µm specimens.

4.4.1 Numerical simulation of the lattice strain evolution

In total, two 30 µm tensile specimens were investigated during the in-situ neutron diffraction experiments. For each specimen, the lattice strains were measured in two directions. The first direction, called the normal direction, was along the height of the tensile specimens, which is also aligned with the loading axis. Therefore, the lattice strains in this particular direction are positive. The second one, called the radial direction, was perpendicular to the normal direction, as shown in fig. 2.8. As a consequence, the lattice strains in the radial direction are negative since they describe the lateral contraction.

The CP simulation results, along with the experimentally measured lattice strains, are shown in figs. 4.17 and 4.18. The experimental values are plotted using different markers. The numerically calculated lattice strains include the CP results for four different RVEs. Therefore, they cover the range between the minimum and maximum lattice strain value at each stress level, and the lines mark the average value. These four RVEs are created using the EBSD measurements shown in fig. 4.7 and the ODFs in fig. 4.8. In this way, it can be ensured that CP simulation results are representative of the whole sample since the model's sensitivity due to variations in the crystallographic texture can be analyzed directly. The results are plotted in two different stress ranges to separate the elastic region (400 MPa upper limit). The results in the elastic region reveal that all trends are predicted correctly by the CP model. This shows that the extracted crystallographic textures are representative of the whole specimen. However, the elastic behavior belonging to the {100} and {111} reflections show greater deviation, which, interestingly, characterize the most compliant and stiffest responses. This could be a result of incorrect SCEC since, in this work, they are taken from [106], which belong to conventional stainless steel 316L. Moreover, the elastic properties of the single crystals also influence the material behavior after the yielding starts. This is evident from the lattice strains plotted in the whole stress range. The discrepancy between the simulated and experimental results is carried over from the elastic region. The influence of SCEC is further analyzed in the next section. Similar to the elastic region, even during plastic deformation, the accuracy of the CP model in predicting the lattice strain evolution varies for different grain families. Interestingly, the severe loading and unloading behavior observed for the {200} grain family in the radial direction is captured by the CP model, which shows the highest sensitivity to texture variations.

Overall, the results shown in this section are also in line with the findings presented in [142], where the authors investigated the influence of microscale or intergranular residual stresses on the lattice strain evolution of AM 316L. The authors in [142] employed a crystal plasticity finite element model to simulate the lattice strain evolution. They showed that the intergranular residual stresses played an important role on the yield and hardening behavior of their AM specimens. However, even with the incorporated residual stresses, their simulation accuracy wasn't much higher than the results shown in this section. Thus, it is highlighted once more that LPBF316L has a very complex substructure. Higher dislocation densities, cellular substructures, melt-pool boundaries, different types of residual stresses, and very unusual grain morphologies are some of the features of LPBF316L, which could have an impact on the results. However, due to the simplifications made during the numerical modeling in this work, the effects of these features and their interactions are not included in the utilized CP model. But based on the simulation results, it is clear that, overall, the present CP model captures the most critical underlying physical deformation mechanisms. These results validate the main modeling assumptions and the findings in section 4.3.3.

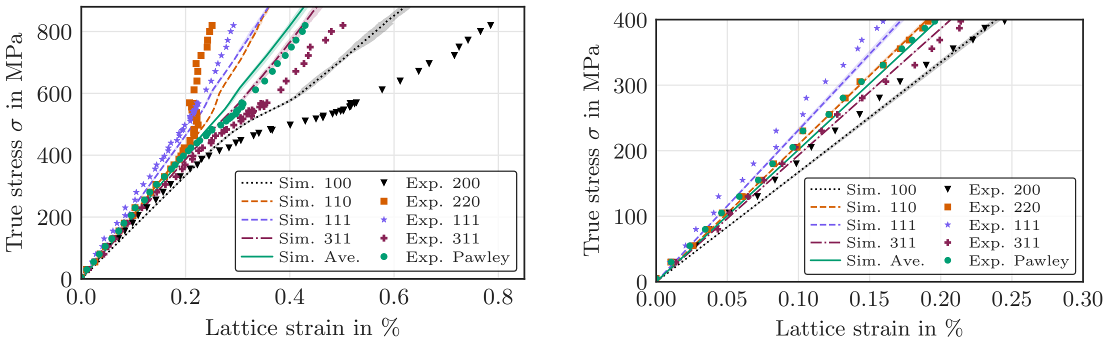

(a) Normal direction.

(b) Normal direction in elastic region.

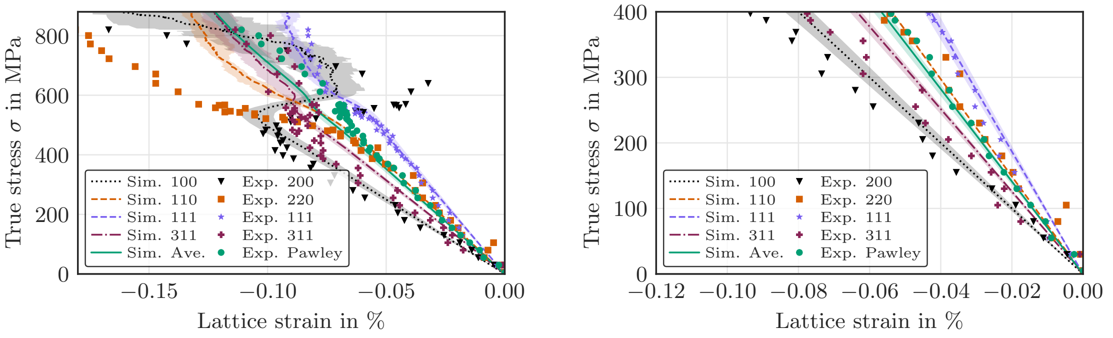

(c) Radial direction.

(d) Radial direction in the elastic region.

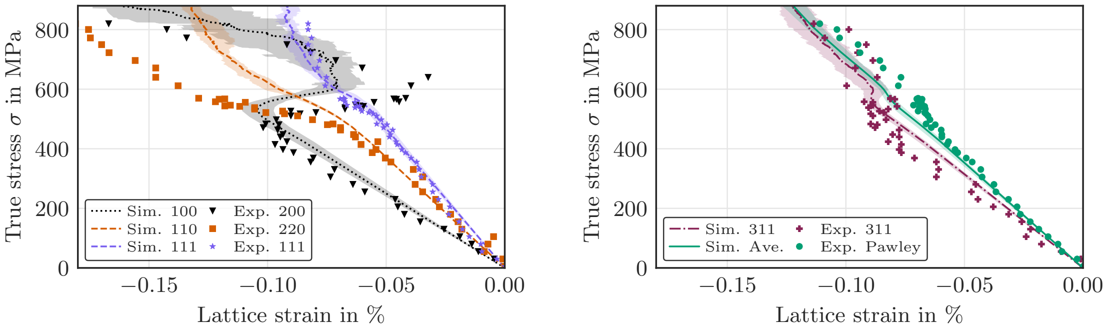

(e) Radial direction splitted: part 1.

(f) Radial direction splitted: part 2.

Figure 4.17: Comparison between experimentally measured and numerically calculated lattice strains for the 90° tensile specimen manufactured from 30 µm wall.

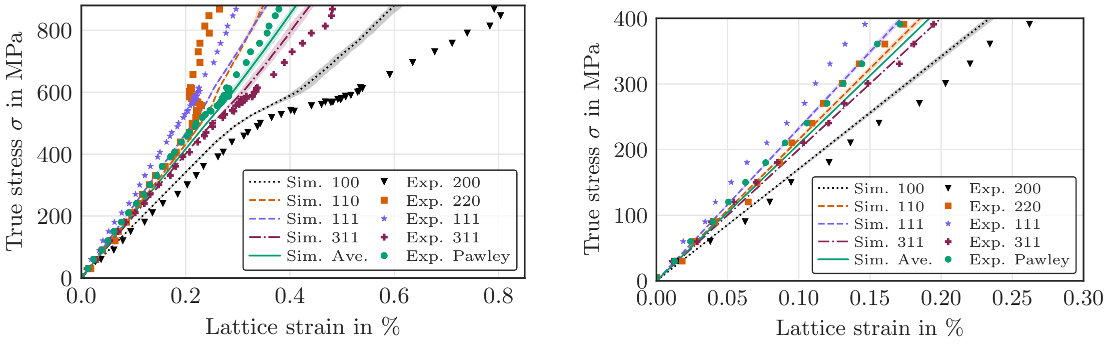

(a) Normal direction.

(b) Normal direction in elastic region.

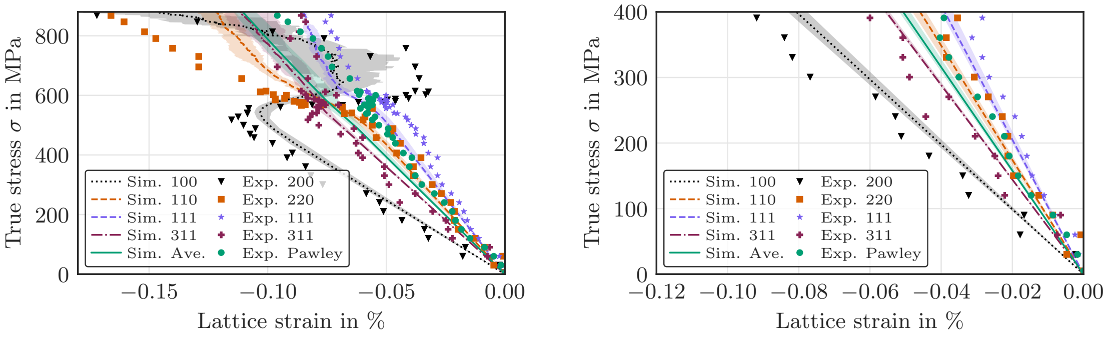

(c) Radial direction.

(d) Radial direction in the elastic region.

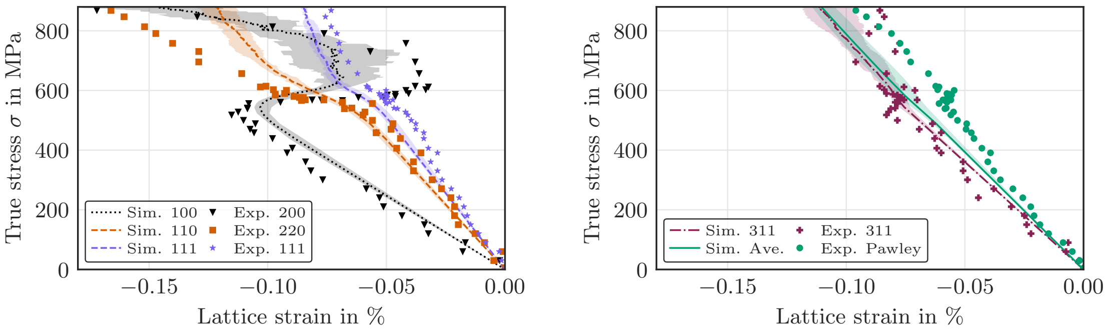

(e) Radial direction splitted.

(f) Radial direction splitted.

Figure 4.18: Comparison between experimentally measured and numerically calculated lattice strain for the 0 ° tensile specimen manufactured from 30 µm wall.

4.4.2 Optimized single crystal elastic constants

In the prior section, it was shown that the CP model was able to successfully capture the trends observed in the in-situ neutron diffraction experiments. However, the lattice strain evolution was not predicted correctly for certain grain families. These deviations can be caused by several different factors and features of LPBF316L, mentioned in prior section. The experimental and numerical analysis of most of these factors is outside of the scope of this investigation. The CP model employed in this work is mainly influenced by the SCEC and crystallographic texture. However, as evident from the results shown in figs. 4.17 and 4.18, the crystallographic texture couldn't be the cause of the deviations observed in the final results since the CP simulation results display very low scatter. This shows that the crystallographic textures in four RVEs are very similar and representative of the whole specimen. Therefore, only the influence of the SCEC on the simulation results is analyzed in this section.

The analysis is conducted as follows. First, the SCEC are re-calibrated using all experimental data. During the re-calibration process, the SCEC are varied until the deviation between the experimentally measured and numerically calculated lattice strains in the elastic region is minimized. All lattice strain values below 400 MPa are assumed to belong to the elastic region. This calibration procedure is described in section 3.4.2. The re-calibrated SCEC are listed in table 4.5 for four different crystallographic textures shown in fig. 4.8. Interestingly, all re-calibrated SCEC are higher compared to the original SCEC. After this step, the CP simulations are rerun for these four different crystallographic textures using the new average SCEC. Theoretically, the accuracy of the simulation results should improve significantly if the observed deviations were caused by incorrect SCEC values.

The new simulation results are plotted in figs. 4.19 and 4.20, which show an overall improvement in the elastic region. However, this is expected since these data were used during the re-calibration process. The trends during the plastic deformation are not as clear. Therefore, an error analysis is conducted for the original and re-calibrated SCEC, and the outcomes are compared to each other in fig. 4.21. The error analysis reveals that the results in the normal direction for both the 0 ° and 90 ° specimens are clearly improved with regard to simulation accuracy. However, in the radial direction, the average error is even increased slightly, which is primarily due to the error caused by the {200} grain family. This increase in % error is simply explained by comparing the results shown in figs. 4.17, 4.18, 4.19, and 4.20. The results for the {200} grain family using the original SCEC appear to be better during the plastic deformation. However, this is caused by the unloading behavior for this particular grain family combined with the stiffer response in the elastic region.

Concluding the analysis in this section, it is clear that re-calibrated SCEC did improve the overall accuracy of the simulation results, which indicate that the actual SCEC of LPBF316L are closer to the re-calibrated values than of the conventional stainless steel 316L. However, these findings have to be validated using other experimental methods outside of the scope of this investigation. More importantly, it is clear that the discrepancies observed between the numerical and experimental values are not solely because of the SCEC. With these results, it is safe to assume that other factors mentioned at the beginning of this section also contribute to the simulation inaccuracies, which must be incorporated into the numerical model for further improvements.

Table 4.5: Recalibrated SCEC.

	C_{11} in GPa	C_{12} in GPa	C_{44} in GPa
BD01	225	170	141
BD03	235	180	137
CS01	221	166	143
CS03	217	166	143
Average	225 ± 6.7	170.5 ± 5.7	141 ± 2.4
SCEC from [172]	206	133	119

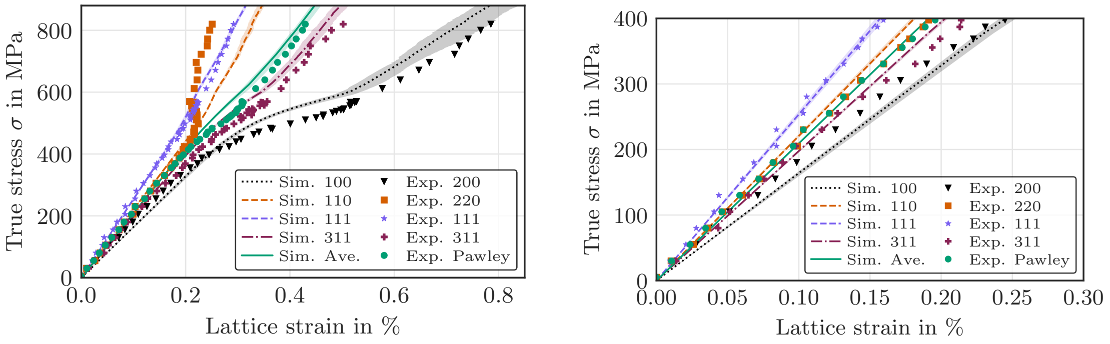

(a) Normal direction. **(b)** Normal direction in elastic region.

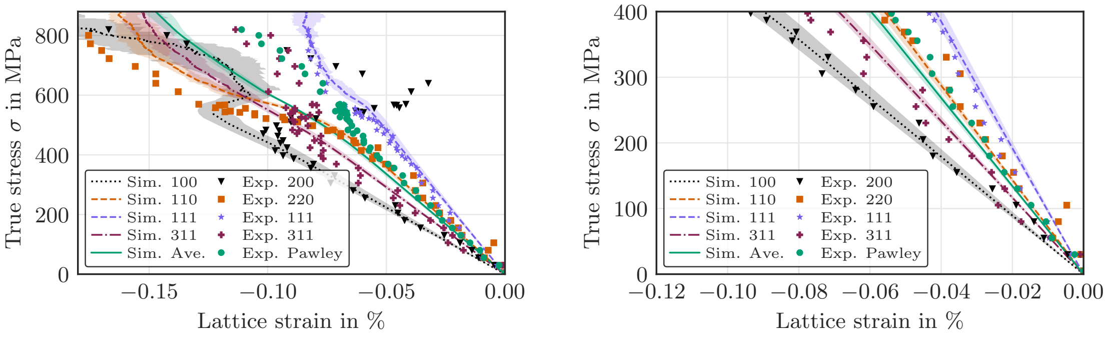

(c) Radial direction. **(d)** Radial direction in the elastic region.

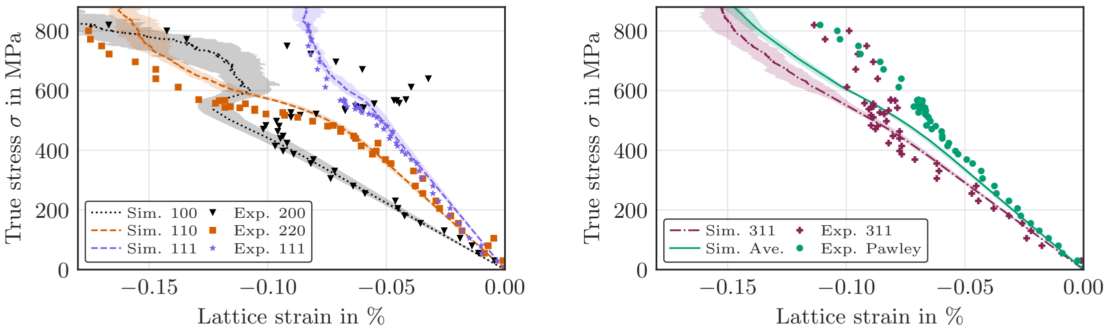

(e) Radial direction splitted. **(f)** Radial direction splitted.

Figure 4.19: Comparison between experimentally measured and numerically calculated lattice strain for the 90 ° tensile specimen manufactured from 30 µm wall.

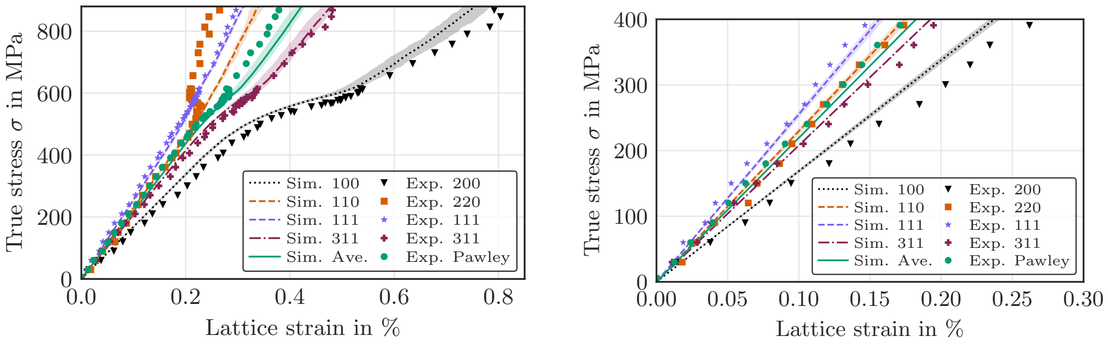

(a) Normal direction.

(b) Normal direction in elastic region.

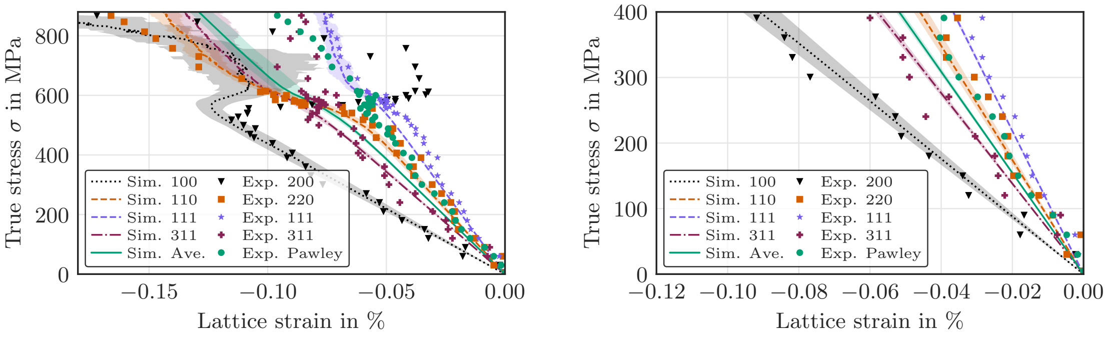

(c) Radial direction.

(d) Radial direction in the elastic region.

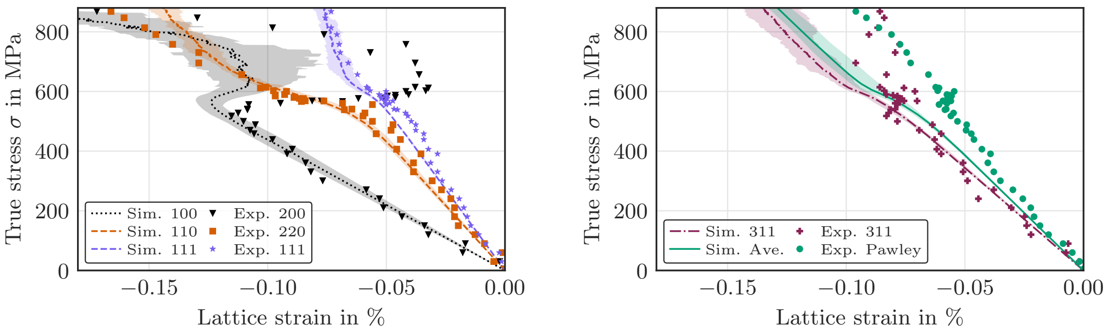

(e) Radial direction splitted.

(f) Radial direction splitted.

Figure 4.20: Comparison between experimentally measured and numerically calculated lattice strain for the 0° tensile specimen manufactured from 30 µm wall.

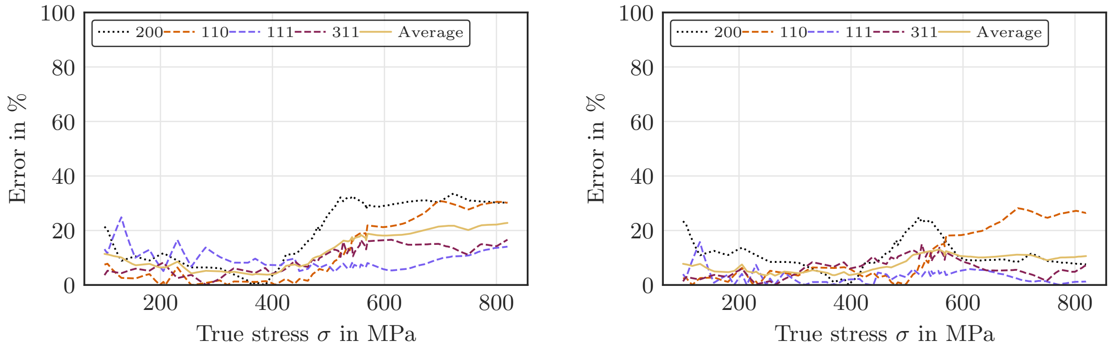

(a) Normal direction 90 ° - original.

(b) Normal direction 90 ° - re-calibrated.

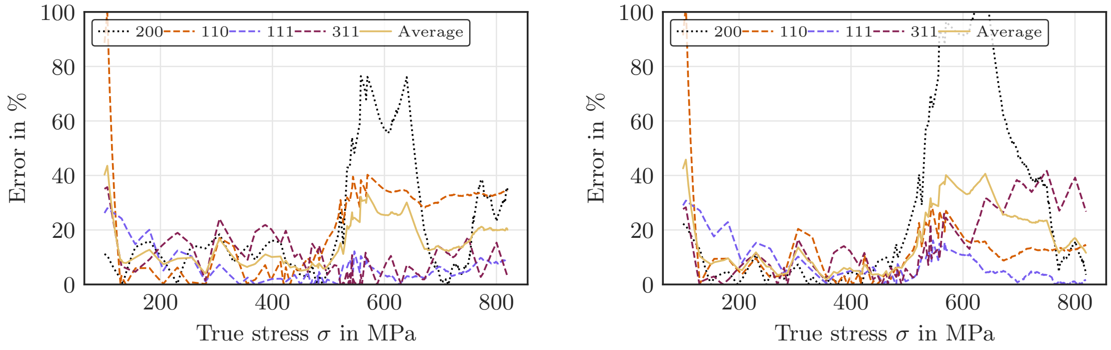

(c) Radial direction 90 ° - original.

(d) Radial direction 90 ° - re-calibrated.

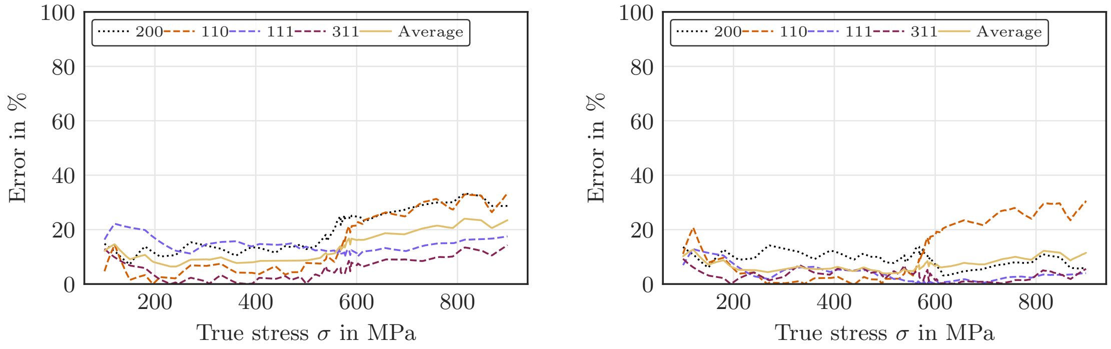

(e) Normal direction 0 ° - original.

(f) Normal direction 0 ° - re-calibrated.

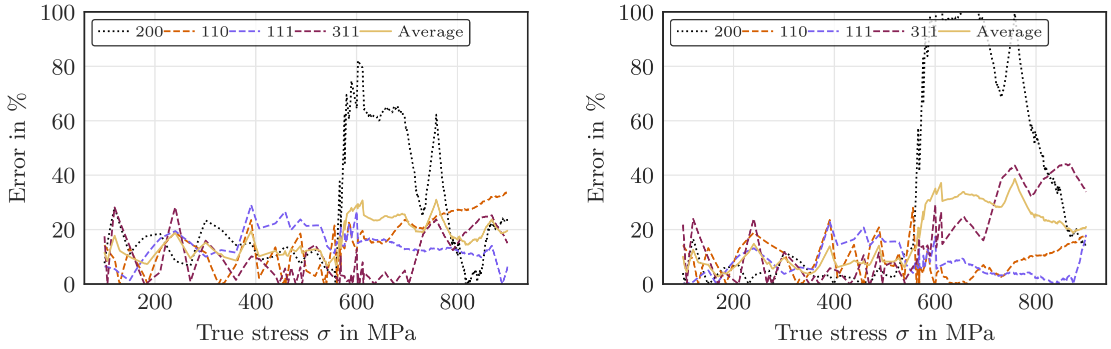

(g) Radial direction 0 ° - original.

(h) Radial direction 0 ° - re-calibrated.

Figure 4.21: Error analysis between original and re-calibrated SCEC for the 0 ° and 90 ° tensile specimens manufactured from 30 µm wall.

4.5 Macromechanical validation

Transferring the micromechanical results to the macroscale is the final step in the multi-scale simulation approach employed in this work. The findings discussed in the prior section validated the initial assumption that the mechanical anisotropy of LPBF316L can be predicted using a CP model. The scale-bridging approach connecting the micro and macroscale together is explained in detail in section 3.4. In summary, the CP model is used to calibrate the macroscale model in a virtual-lab framework, which eliminates the need for further experimental material characterization by using virtual experiments instead of real ones. The calibrated macroscale model, presented in section 3.3, allows the use of finite element softwares for simulating the deformation behavior of additively manufactured parts with complex geometries. The results presented in this section serve as the validation of the entire multi-scale framework. One shear and one torsion test are used for this purpose. It is highlighted that the macroscale model is calibrated entirely by using the CP model, which means that the shear and torsion test results were not part of the calibration process. Therefore, the validation is successful if the simulated shear and torsion tests correctly predict the experimental data. Moreover, the accuracy of different numerical implementations, derived in section 3.3, together with the influence of the plastic spin on the final results, are analyzed for both test conditions.

4.5.1 Abaqus model creation

The shear and torsion simulations are conducted in the software Abaqus using the UMAT interface, which allows the implementation of new constitutive models, such as the corotational formulation, presented in section 3.3.10. The shear and torsion specimens are recreated in Abaqus CAE. The part geometries and corresponding meshes are shown in figs. 4.22 and 4.23. For the torsion specimen, only half of the geometry is used since it is possible to make use of anti-symmetric boundary conditions in Abaqus. Moreover, the grip portion of the torsion specimen is neglected during the torsion test to decrease the computational cost. Both of these simplifications don't influence the final results. For the torsion specimen, the simulations are conducted using two different meshes to analyze the numerical convergence behavior. The meshes, including the number of elements and the element type, are shown in fig. 4.22. The boundary conditions are applied to the top and bottom portions of the torsion specimen. The anti-symmetric boundary conditions are applied at the bottom, which prohibit the rotation of the sample along its height. At the top, a torsional rotation of 360° is applied to a reference point, which is connected to the upper surface utilizing a kinematic coupling constraint. Because of the anti-symmetric boundary condition, the total torsional rotation is double the amount applied to the reference point, equaling to 720°. The geometry belonging to the shear specimen and two different meshes are shown in fig. 4.23. The shear simulations are conducted using the complete geometry. The boundary conditions are applied at the bottom and top surfaces of the shear specimen. The lower part is held in place, whereas a total displacement of 1.4 mm is applied to the upper surface. All simulations are conducted using Abaqus standard with `Nlgeom = ON`.

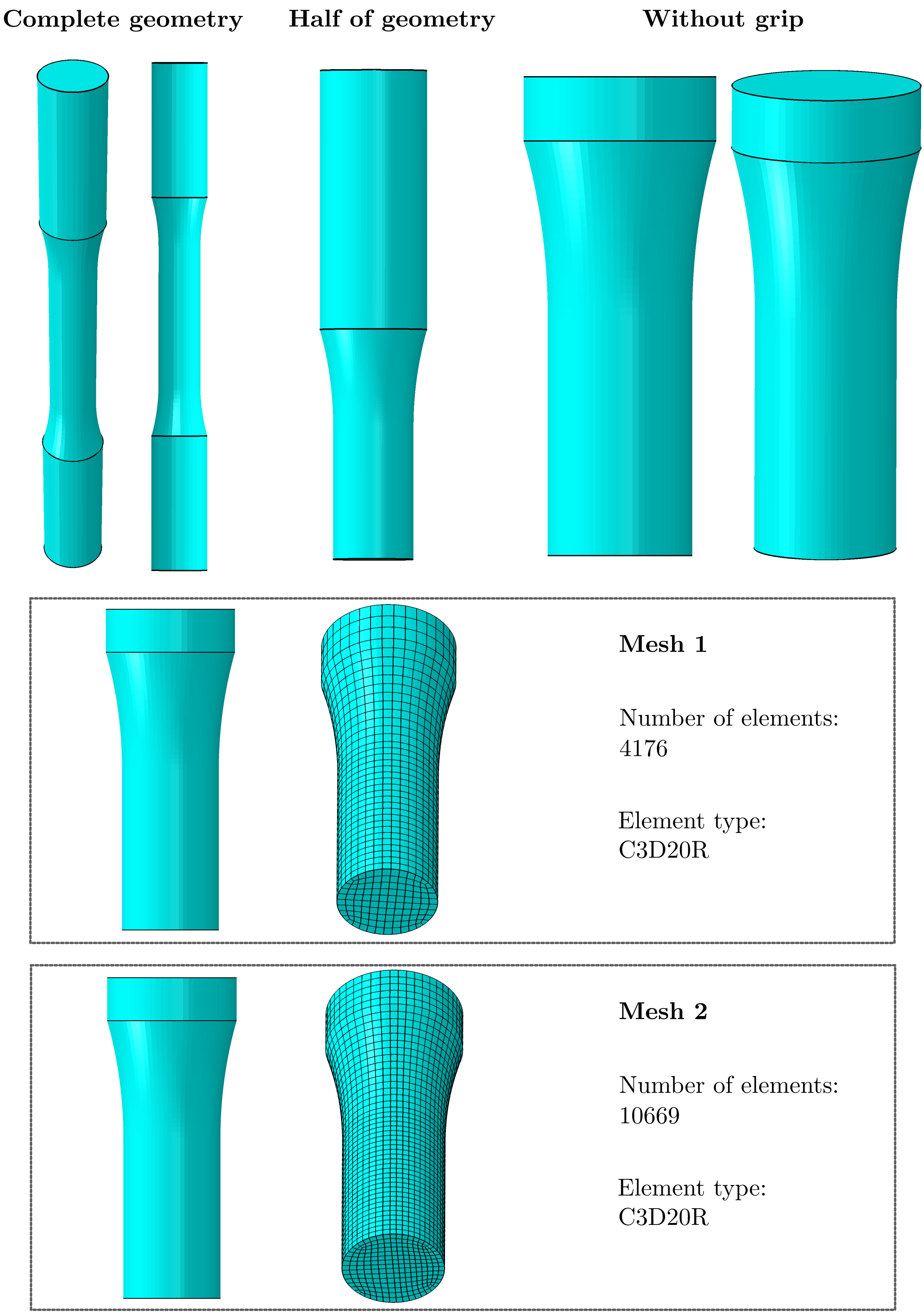
Complete geometry
Half of geometry
Without grip
Mesh 1
Number of elements:
4176
Element type:
C3D20R
Mesh 2
Number of elements:
10669
Element type:
C3D20R

Figure 4.22: Abaqus geometry and mesh for the torsion specimen

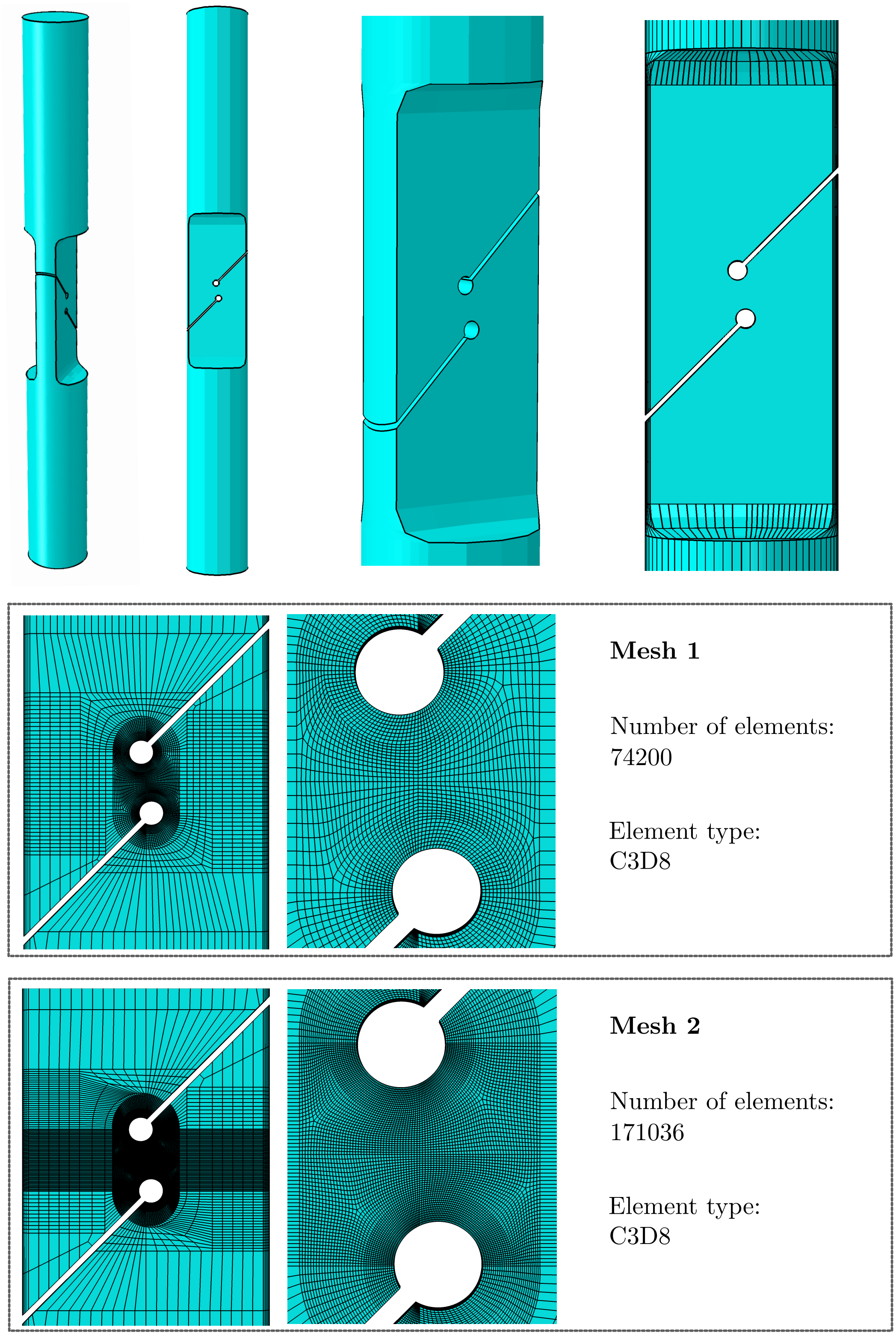
Mesh 1
Number of elements:
74200
Element type:
C3D8
Mesh 2
Number of elements:
171036
Element type:
C3D8

Figure 4.23: Abaqus geometry and mesh for the shear specimen

4.5.2 Torsion test: comparison between simulation and experiment

The numerical results obtained from torsion simulations in Abaqus are shown in fig. 4.24. The simulation results are split and shown in different subfigures since the simulations are repeated for each of the three hardening behaviors. The issue of the hardening behavior beyond the necking point in tensile tests is explained in section 3.4.2.3. The torsion simulations serve two purposes. First, they are used to validate the macroscale model and its correct implementation in the software Abaqus. Second, they are used to determine the hardening behavior closest to the real experiment. Looking at the simulation results makes it clear that the plastic spin contribution is negligible for the torsion specimen with this particular orientation. Moreover, there is a significant difference between the corotational implementation and the Abaqus standard implementation. The corotational implementation is much closer to the experimental results, irrespective of the hardening behavior. This is more evident in fig. 4.25, where the error between the experimentally measured and numerically calculated torsion moment is presented. In figs. 4.24 and 4.25, it is evident that the hardening behavior with a saturation strain of 110 % is closest to the actual experiment. Hence, only this hardening behavior is used for the numerical simulations in all subsequent sections.

The results of the FE convergence study are shown in fig. 4.26. Each line in this figure displays the relative error between the torsion moment obtained from two different Abaqus simulations conducted using the exact same parameters. However, each simulation is performed using different meshes, as shown in fig. 4.22. This procedure is repeated for all the simulations shown in fig. 4.24, which results in nine separate lines. For all the simulations, the relative error is smaller than 0.35 %. Moreover, the error decreases with higher torsion angles and remains under 0.1 % after 300° torsion angle. Thus, it is concluded from these results that the utilized meshes and element type are adequate for the conducted simulations.

It is highlighted that the parameters of the macroscale model are calibrated using virtual experiments shown in section 3.4. In total, a single tensile test and one EBSD measurement were used to extract the necessary material properties. Hence, it is safe to conclude that the approach presented in this work is well suited for modeling the anisotropic yield behavior of the LPBF316L since the results of the torsion experiment are accurately predicted by the macroscale model. Moreover, this approach can be used for other materials and can also be adjusted to include other deformation mechanisms such as twinning and phase transformation. Furthermore, it is clear from the simulation results that for large deformations and rotations, the standard Abaqus implementation is not sufficient, which is also correctly emphasized in its users manual [171]. It appears that for such conditions, the corotational formulation is a more appropriate choice. From these results, it may seem that it is not necessary to include the plastic spin model in the final implementation. However, this is not always the case since, depending on the orientation of the test specimen, the contribution of the plastic spin tensor could become significant. Such conditions will be presented in the following sections.

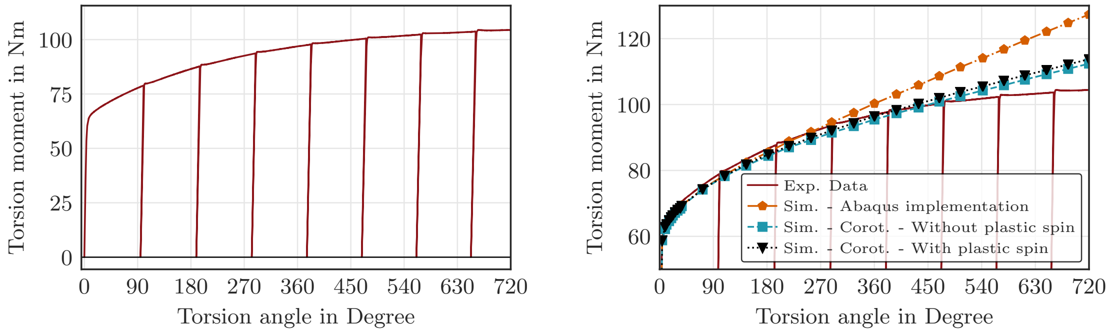

(a) Torsion experiment.

(b) Hardening with linear extrapolation.

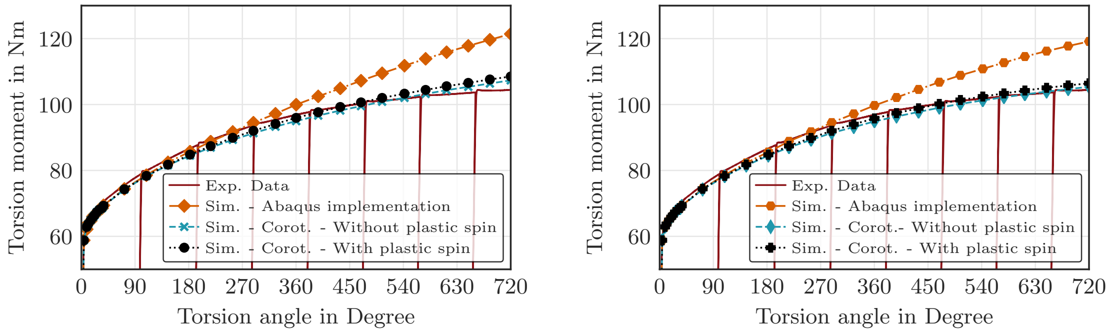

(c) Hardening with saturation strain 140 %.

(d) Hardening with saturation strain 110 %.

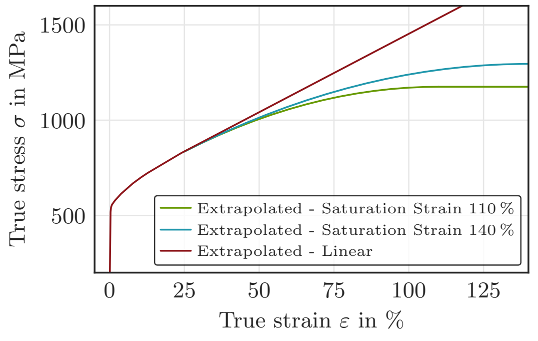

(e) Calibrated stress-strain curves for three different hardening behaviors, see section 3.4.2.3.

Figure 4.24: Comparison between experimentally measured and numerically calculated torsion moment. In fig. (a) the experimental results are shown for torsion angle between 0° and 720°. In figs. (b,c,d) the simulation results are compared to the experimental data. In each of the figures (b,c,d), the simulation results are shown for the three different implementations. Lastly, in fig. (e) the stress-strain curves corresponding to three different hardening behaviors are shown again.

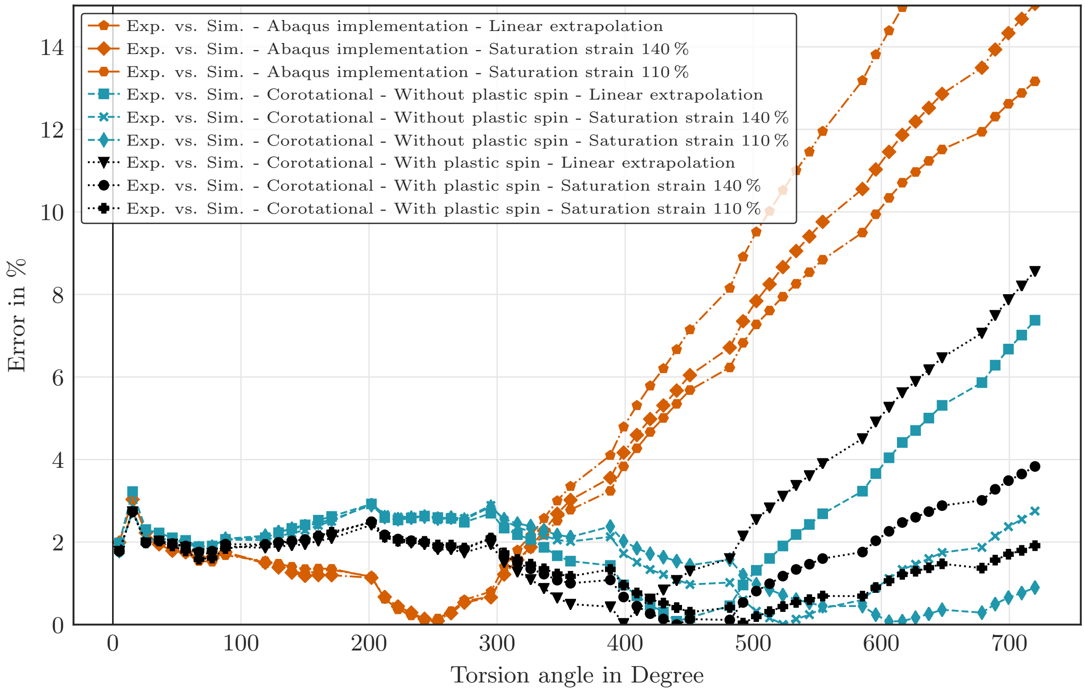

Figure 4.25: Error analysis for all torsion simulations, which clearly shows that the corotational formulation with saturation strain 110 % is the most accurate combination.

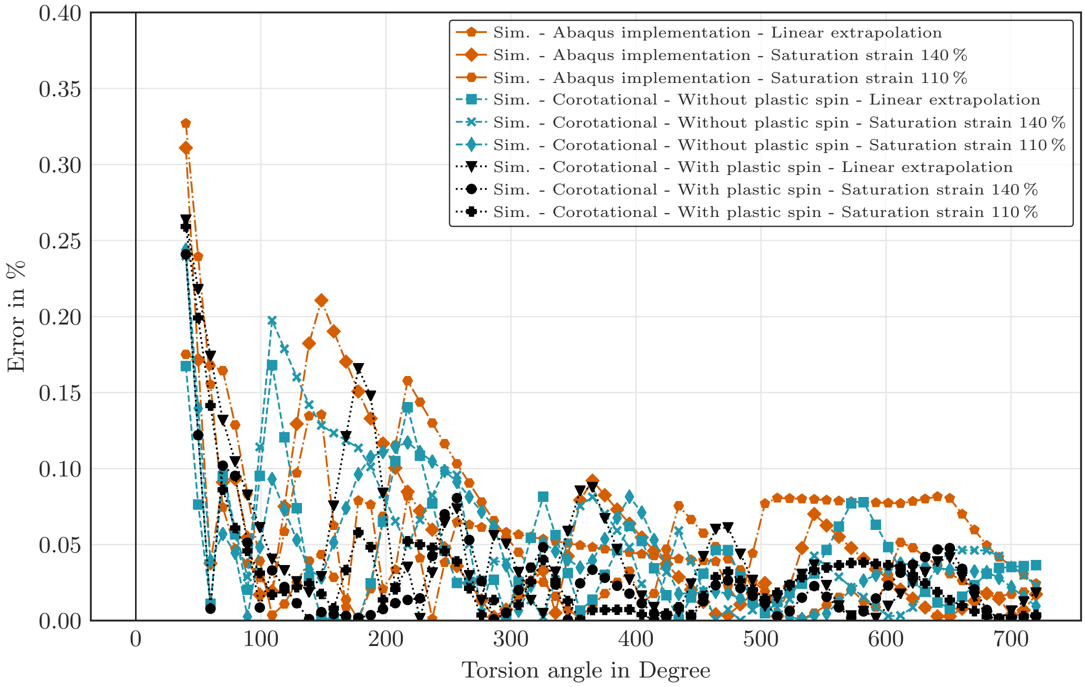

Figure 4.26: The results of the convergence study, which clearly demonstrate that the chosen mesh and element type are adequate for the simulation of the torsion experiment.

4.5.3 Shear test: comparison between simulation and experiment

Continuing the numerical analysis, the macroscale model is also used to predict the material behavior of LPBF316L during the shear tests. As explained in the prior section, only a single hardening behavior is used for the simulation of the shear tests, which is chosen based on the results of the torsion experiments and is assumed to be closest to the actual hardening behavior of LPBF316L. The simulation results, along with the experimental data, are shown in fig. 4.27. The experimental results consist of two separate shear tests. Both of them behave nearly identical in the elastic region. After yielding starts, the experimental results are very similar up until the very end, shortly before the specimens are broken.

Comparing the simulation results with the experiments makes it clear that the standard Abaqus implementation delivers inaccurate results, similar to the torsion simulation. This becomes more evident in fig. 4.28, where the error analysis is presented for each of the implementations. It should be noted that the %-error is the average error between the numerical results and each of the shear tests. Moreover, the influence of the plastic spin is visible both in figs. 4.27 and 4.28. The simulation results for the corotational formulation with the plastic spin model are more accurate compared to the model without it. Although the differences observed for the models with and without plastic spin are not very significant, it is still possible to see that the plastic spin model improves the simulation accuracy. However, even without the plastic spin model, the corotational formulation is still far superior to the standard Abaqus implementation.

Similar to the prior section, the FE convergence analysis is conducted for all simulations using two separate meshes shown in fig. 4.23. The relative error between the numerically obtained shear force is plotted in fig. 4.29. It is clear from these results that the employed meshes and element type are adequate for this kind of simulation since the relative error is smaller than 0.25 % for all simulations during the whole deformation process. It is highlighted that achieving convergence for the shear tests is more challenging compared to the torsion tests since shear tests produce a much more localized deformation field, which significantly affects the numerical accuracy and, consequently, the mesh dependency.

Overall, the simulation results show that, again, the corotational formulation offers the best accuracy when dealing with large deformations and rotations. More importantly, with these results, it is safe to assume that the macroscale model and the approach presented in this work are well suited for the simulation of yield behavior of LPBF316L for any desired loading condition since the model was accurate during tensile, torsion, and shear tests. Thus, the validation of the macroscale model is complete. It is important to note that the average error between the shear experiments and the corotational formulation with the plastic spin is mostly under 2 %. This accuracy is very high considering the difficulties and uncertainties during the AM process, specimen manufacturing, mechanical testing, and also numerical modeling. These aspects, along with the fact that only one single tensile test and one EBSD measurement were used to calibrate the macroscale model, show the power of the virtual experiments when employed with the correct modeling assumptions. However, the importance of the plastic spin model is still not very clear from the presented results since, even for the shear tests, the impact of the plastic spin model on the final results is not very significant. This issue and other aspects are analyzed in the following section.

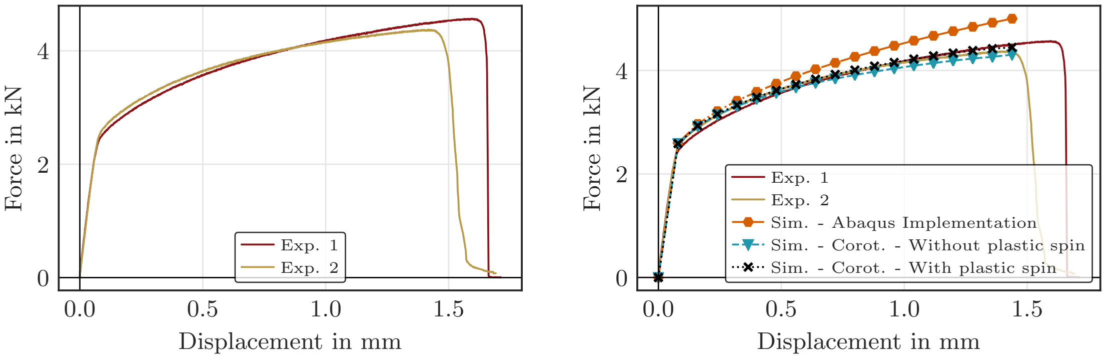

(a) Torsion experiment.

(b) Comparison between simulation and exp.

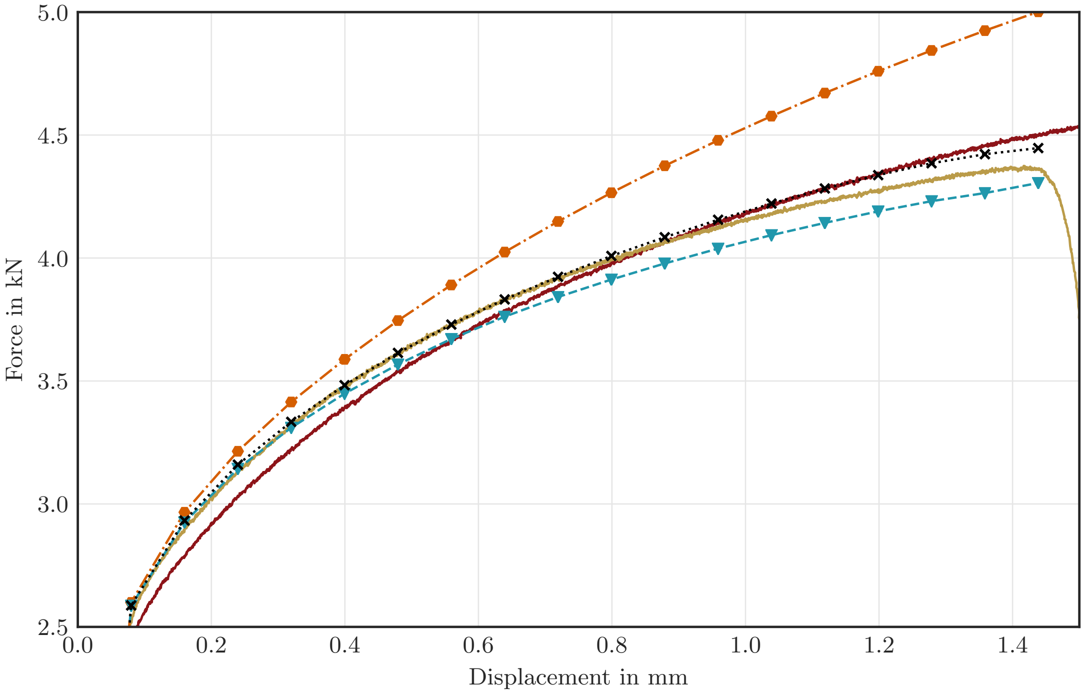

(c) Comparison between simulation and experiment.

Figure 4.27: Comparison between experimentally measured and numerically calculated shear force. In fig. (a) the experimental results are shown for two separate specimens. In fig. (b,c) the simulation results are compared to the experimental data, whereby the simulation results are shown for the three different implementations.

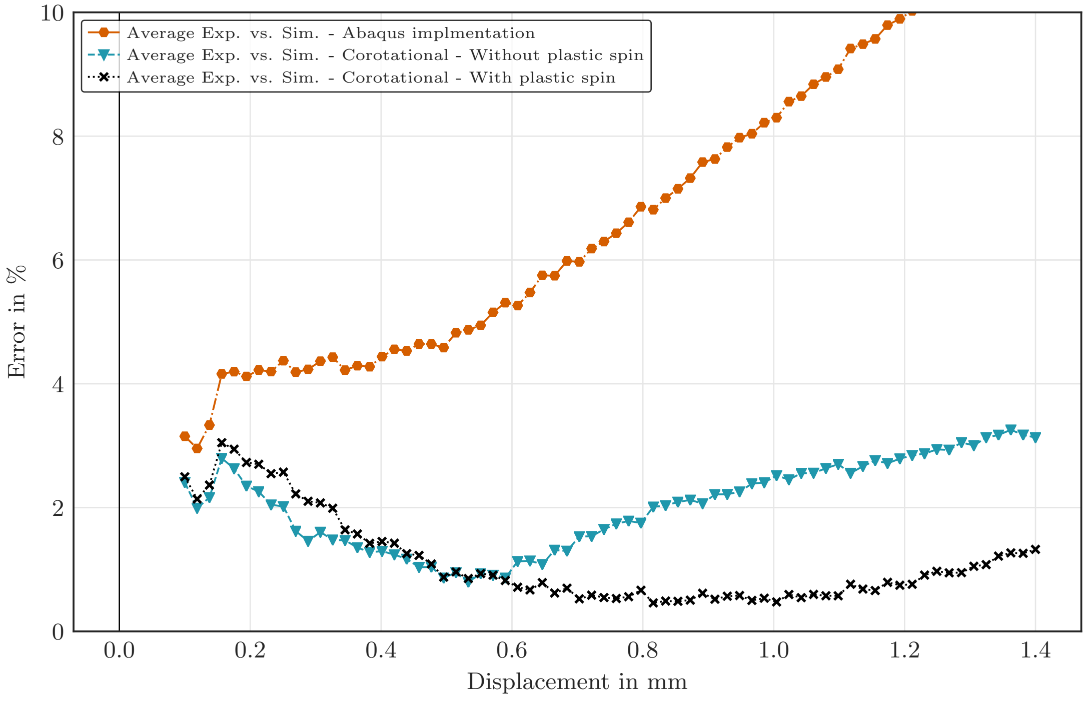

Figure 4.28: The error analysis for three different implementations, which clearly shows that the corotational formulation with plastic spin delivers the most accurate results.

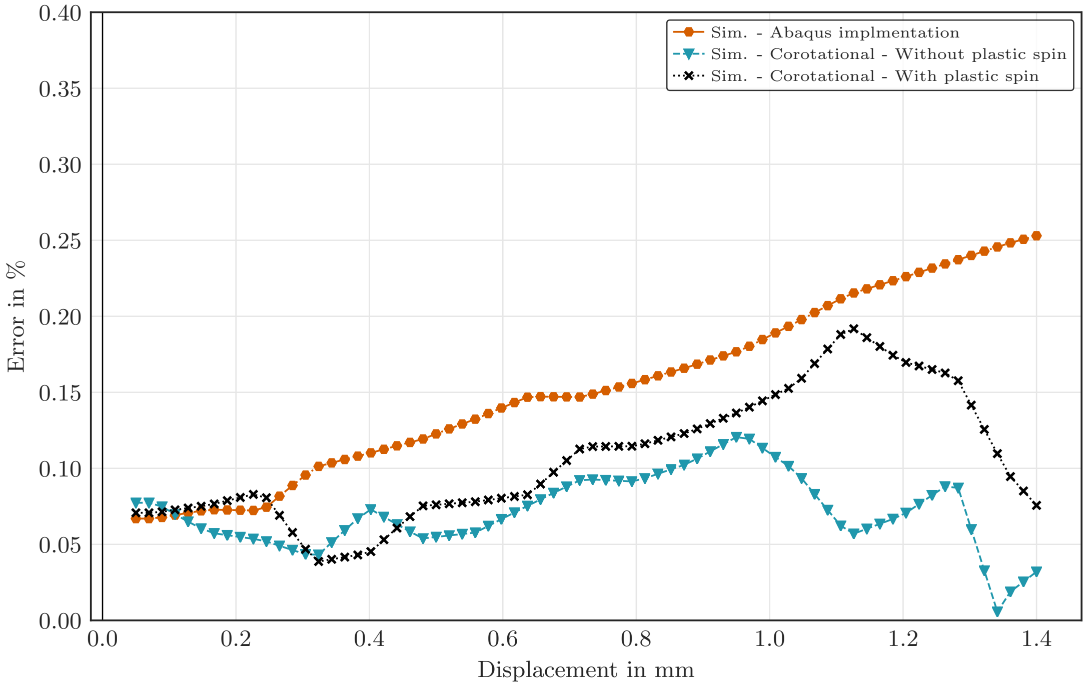

Figure 4.29: The results of the convergence study, which clearly demonstrate that the chosen mesh and element type are adequate for the simulation of the shear experiment.

4.6 Influence of anisotropy, numerical algorithm, and plastic spin on macroscale results

As explained in the prior section, it is not easy to separate the influence of different factors on the final results since elastic anisotropy, anisotropic yield behavior, numerical algorithm, and the plastic spin simultaneously influence the final outcome. Moreover, due to the limited number of samples, it isn't possible to experimentally analyze the material behavior for other specimen orientations. Therefore, virtual experiments are used in this section to tackle this issue. The torsion and shear simulations are repeated using the same specimen geometry, boundary condition, and material parameters. The only difference is the orientation of the new specimens in the virtual experiments, which is directly linked to the orientation of the actual specimens in the LPBF system during the manufacturing process. Thus, changing the orientation of the virtual specimens is the same as producing specimens with different orientations using the same scan strategy. More importantly, these virtual and actual specimens all share the same crystallographic texture since the scan strategy and all other parameters are kept unchanged, see section 4.2 for the texture analysis results. For each type torsion and shear specimens, two more orientations are tested. These results will be used to identify the the most important factors, which are necessary for accurately simulating the material behavior of LPBF316L for large plastic deformations. For simplicity and ease of comparison, the same CCO is employed as in fig. 2.1. The new configurations for the torsion and shear specimens are shown in figs. 4.30 and 4.31. In these figures, the orientation during the actual experiment is clearly visible. The new orientations called test orientation 1 and test orientation 2 are not unique in any way and are simply created by rotating the original configuration using two different axes. It is emphasized that the only difference between these tests is the adjusted loading condition relative to the material texture, analyzed in section 4.2.

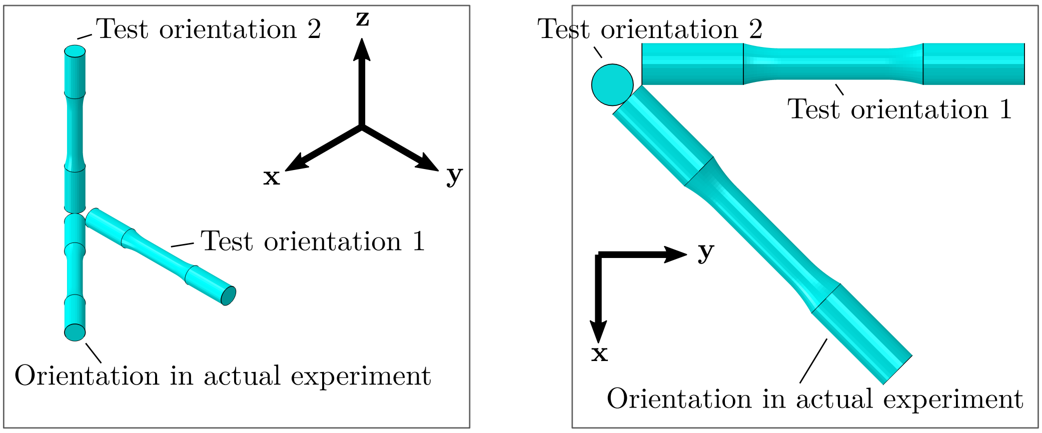

Figure 4.30: Orientation of three torsion specimens shown relative to each other and with respect to the same CCO as in fig. 2.1.

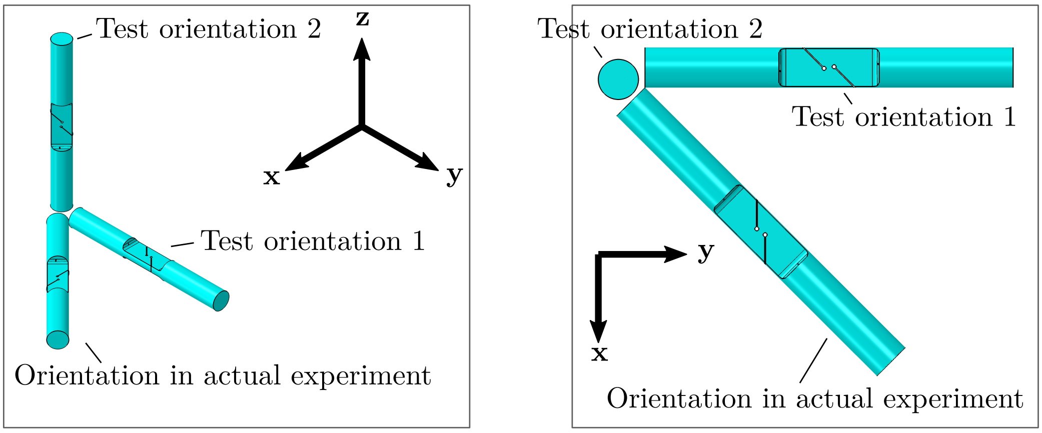

Figure 4.31: Orientation of three shear specimens shown relative to each other and with respect to the same CCO as in fig. 2.1.

4.6.1 Virtual torsion experiments

The simulation results for the test orientations 1 and 2 are shown in figs. 4.32 and 4.33. It is worth noting that in figs. 4.32 and 4.33, the experimental result is the same as in fig. 4.24, which belongs to the specimen tested in the prior section, and is only shown for easier comparison between different orientations. Moreover, only one hardening behavior is chosen, which is closest to the actual experiment with 110 % saturation strain. The following details become more clear analyzing all simulation results side by side. First, the anisotropy of LPBF316L can't be neglected and has to be taken into account even if deformations are small since it has a substantial effect on the initial and subsequent yield behavior of the material. Second, the standard Abaqus implementation isn't always stiffer than the corotational formulation, which makes it even more crucial to employ the corotational formulation to correctly capture the effect of large deformations and rotations. Third, the plastic spin can significantly impact the final results, depending on the anisotropy of the material and the actual orientation of the test specimen. Fourth, the effect of anisotropy becomes even more apparent when the torsion moments for these three simulations at the start of yielding and at the end of the simulation are compared side by side. Even though the employed stress-strain hardening behavior is identical in these simulations, the response of the torsion specimen under the same loading condition is entirely different. Most importantly, from these results, it can be safely concluded that neglecting the anisotropy of the material and reducing the problem to an isotropic case leads to substantial error in most cases. The simulation results shown in this section are not unique in any way. Other specimen orientations could result in even more pronounced differences.

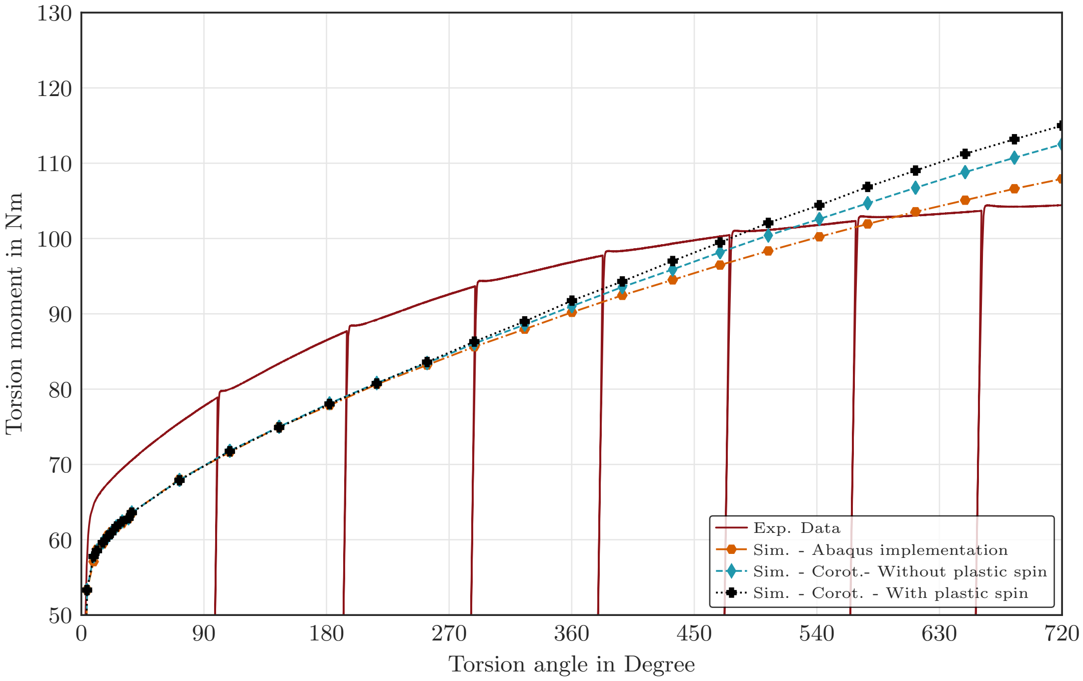

Figure 4.32: Torsion simulation results for the test orientation 1.

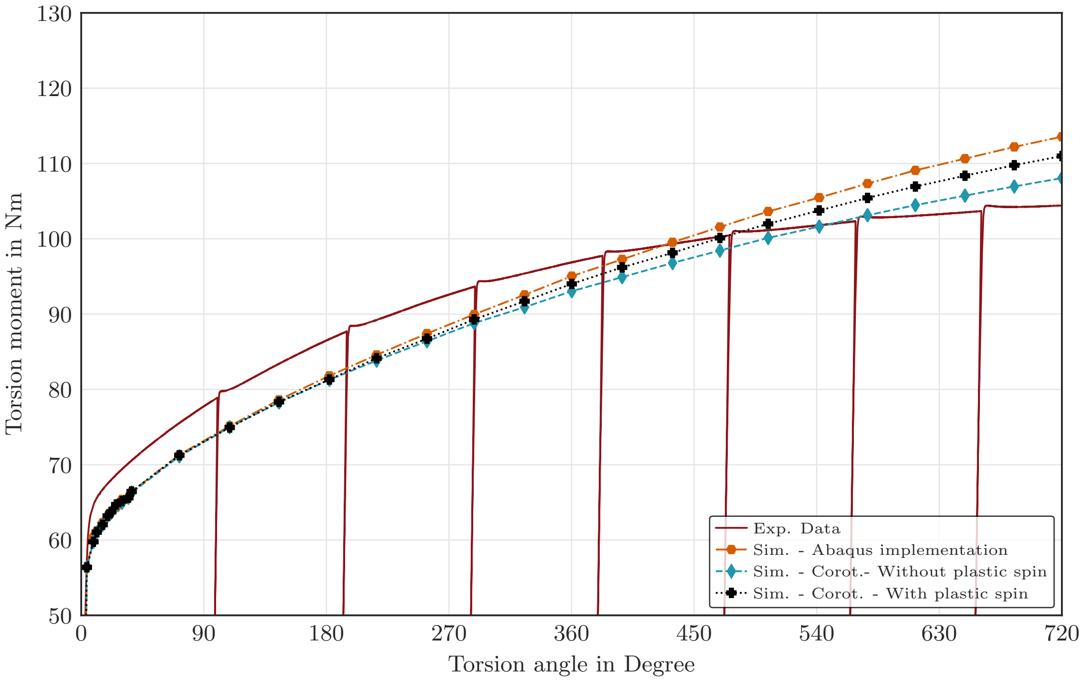

Figure 4.33: Torsion simulation results for the test orientation 2.

4.6.2 Virtual shear experiments

The shear test results for orientations 1 and 2 are shown in figs. 4.34 and 4.35. The experimental curves shown in these figures belong to the specimen tested in the actual experiment and are the same as in fig. 4.27. These results are only included for comparison purposes. The hardening behavior and all simulation parameters are the same as the torsion simulations. The shear force/displacement curves for the newly tested orientations validate the same findings as for the torsion specimens, which are summarized again as follows:

- The anisotropy of LPBF316L can't be neglected even for small strain simulations since it affects both the initial and subsequent yield behavior of the specimens.
- For large deformations and rotations, the standard Abaqus implementation is not sufficient and a correct numerical implementation such as the corotational formulation has to be utilized.
- The plastic spin contribution to the final simulation results is heavily dependent on the initial texture of the material and the orientation of the test specimens. Under certain conditions, the plastic spin could result in significant differences.

In these simulations, it appears that the influence of the numerical algorithm is more significant than plastic spin. However, it is highlighted that these tested orientations are not unique in any way and don't serve as lower and upper bounds. It is possible that for other orientations, the influence of the plastic spin becomes greater than other factors. However, the simulations for the chosen orientations are sufficient to prove that accurate simulation results are obtained only if the contributions of anisotropy, numerical algorithm, and plastic spin are correctly calculated.

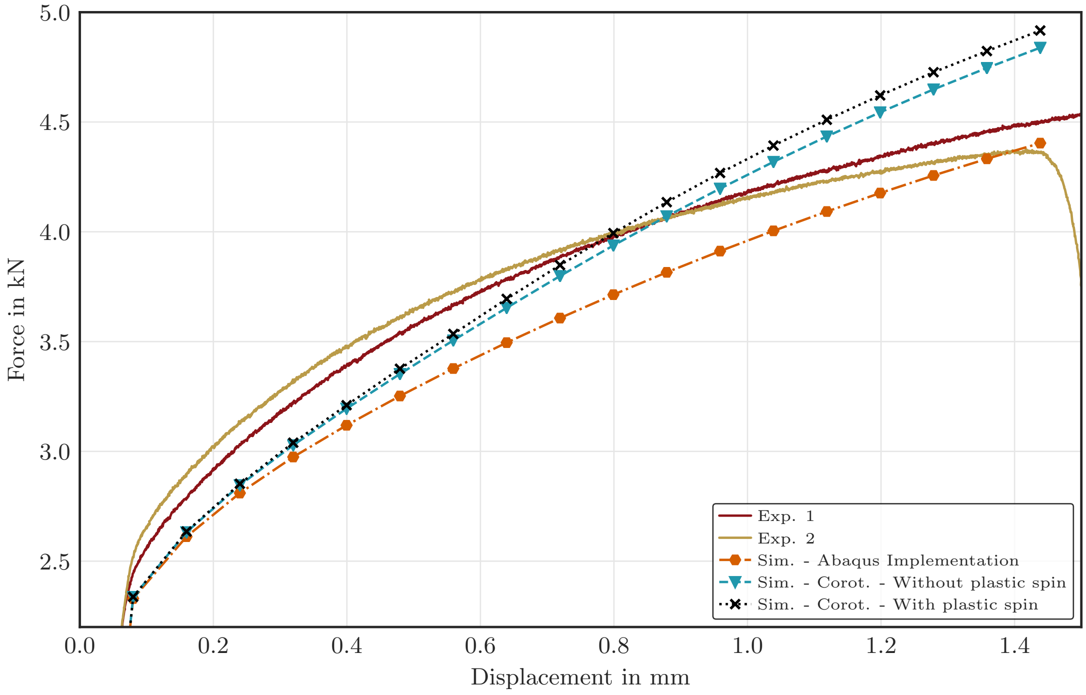

Figure 4.34: Shear simulation results for the test orientation 1.

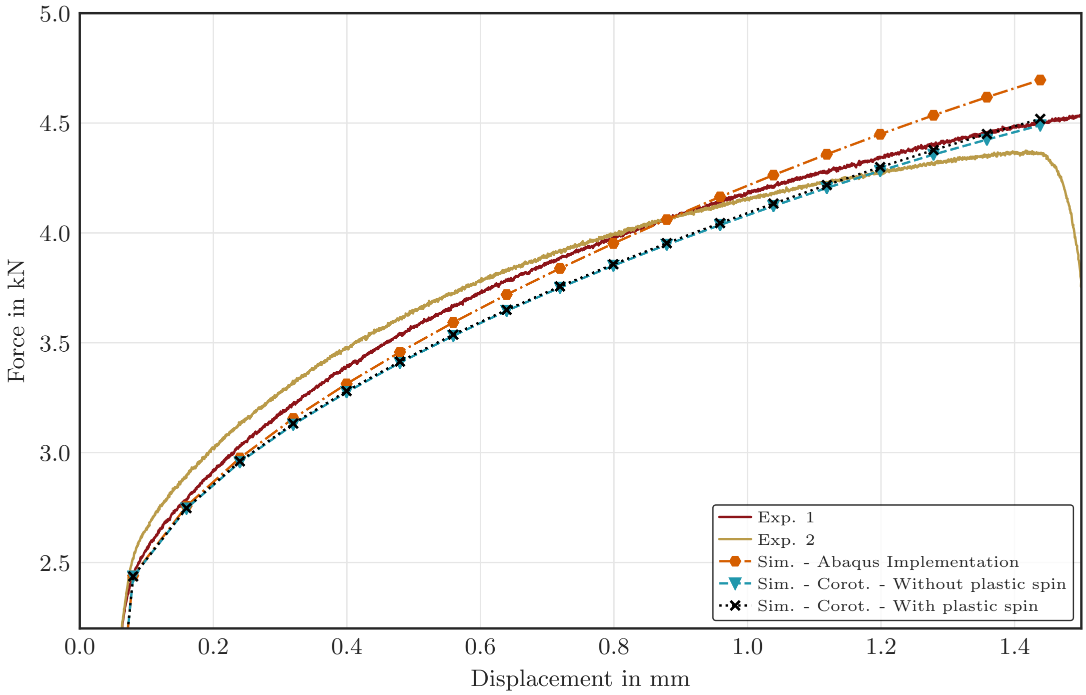

Figure 4.35: Shear simulation results for the test orientation 2.

4.7 Conclusion and outlook

The main objectives in this work can be summarized as follows:

1. How can the mechanical anisotropy be understood and is it possible to isolate the fundamental mechanisms that are the main contributing factors to the mechanical anisotropy of LPBF316L?
2. Is it possible to predict the anisotropic response of LPBF316L using a CP model?
3. Is it possible to create a multiscale simulation framework to accurately simulate the material response of LPBF316L at the macroscale by transferring the results from the microscale without the need for extensive experimental testing procedures?
4. What are the necessary requirements for the correct implementation of the macroscale model and accurate simulation of the LPBF316L material response undergoing large plastic deformations and microstructure evolution?

Thus, the analysis in this work can be categorized in mainly four parts. The first part consists of the findings obtained during the experimental material characterization, which are as follows:

- The measured porosity of LPBF316L was much smaller than 0.01 % in six different tensile specimens, which indicated that the porosity isn't relevant when analyzing the anisotropy of LPBF316L.
- The residual stress distributions determined via neutron diffraction experiments were very similar in all six tensile specimens. Moreover, the RS ranges were low compared to the values obtained for net-shape geometries. With these observations, it was concluded that the RSs were not contributing to the mechanical anisotropy of LPBF316L in a significant way. Thus, both the porosity and residual stresses were omitted during the numerical analysis.
- Texture analysis conducted using EBSD measurements revealed that both the 30 µm and 50 µm specimens had a very similar {110} texture in the build direction but with an unusual grain morphology, which was directly the result of the utilized scan strategy and was recognizable as a checkerboard pattern in cross-section measurements. Moreover, it was concluded that reducing the layer thickness from 50 µm to 30 µm leads to a substantial decrease in the average grain size.
- Finally, the resonance method and tensile tests revealed the anisotropic response of the LPBF316L specimens both for the elastic and plastic deformations, whereby the vertical specimens had the lowest, and the horizontal specimens had the highest Young's moduli and yield stress.

In the second part, and with the experimental findings at hand, a CP model was employed to simulate the anisotropic response of the LPBF316L at the microscale and determine the most critical factor controlling the mechanical anisotropy of LPBF316L. To simplify the procedure and isolate the main contributing factor, the actual grain morphology and grain size distributions were replaced with a RVE having a fixed grain size. The following steps roughly summarize the second part of the analysis conducted in this work:

- The RVE was created based on the ODF extracted from a single EBSD measurement and a very simple grain morphology. The CP model was then calibrated using this RVE, and the results from only one tensile test.
- The remaining tensile test results were used to validate the CP model. The phenomenological CP was capable of accurately predicting the anisotropic response of LPBF316L both in the elastic and plastic regions. With these results, it was concluded that dislocation slip is the primary underlying deformation mechanism in LPBF316L, and that the crystallographic texture is the main contributing factor to the mechanical anisotropy of LPBF316L.

After the successful calibration and validation of the CP model and identifying the primary source of the mechanical anisotropy in LPBF316L, the next step was to simulate the material response at the macroscale. High computational costs of the CP simulations rendered it impractical for such use cases. Therefore, a multiscale simulation approach was utilized to overcome this limitation. This scale-bridging procedure is summarized as follows:

- The homogenized elastic stiffness tensor for the macroscale simulations was determined using the Hill estimation method, and the crystallographic texture of the material was determined using one EBSD measurement.
- The Barlat analytical yield function was utilized to capture the initial anisotropic yield behavior of the LPBF316L at the macroscale. However, instead of real experiments, virtual experiments were conducted using the calibrated and validated CP model. The hardening behavior of the LPBF316L was modeled separately using Ludwik's law combined with different extrapolation techniques.
- Moreover, it was shown that it is necessary to include the microstructure evolution in the macroscale simulations to retain the accuracy observed in CP simulations. Therefore, a novel and general plastic spin model was formulated in 3D using the eigenvalues and eigenvectors of the plastic deformation tensor.
- Finally, the results of the previous steps were merged together in a corotational framework suited for simulating large deformations and rotations. This formulation was implemented in the UMAT subroutine of the program Abaqus standard.

This multiscale simulation approach eliminated the need for more experimental material characterization while retaining the high simulation accuracy observed in CP simulations. Moreover, the micro and macroscale simulation results were validated using different experiments, which were conducted on two separate scales:

- Using neutron diffraction experiments, the results of the CP model were validated again, separate from the tensile experiments since, during tensile experiments, only the average response of the polycrystal is determined. However, during the neutron diffraction experiments, the elastic response of specific grain families was analyzed. These results were then subsequently compared against the CP simulations, where it was shown that the phenomenological CP was able to capture the trends observed in the experiments. This analysis reconfirmed the conclusions based on the comparison between the tensile test results and the CP simulations.
- The macroscale simulation results were validated using torsion and shear tests. In both cases, the predictions of the macroscale model were very accurate, which demonstrated the capabilities of the corotational formulation and the scale-bridging approach presented in this work. Moreover, it was shown that the standard Abaqus implementation shouldn't be used for simulating large deformations and rotations.
- Furthermore, the torsion and shear tests were repeated using virtual experiments for other specimen orientations. This was done to analyze the contribution of different factors to the final simulation results. In summary, it was shown that the elastic and plastic anisotropy, corotational formulation, and plastic spin are crucial for accurate simulations of large deformations and rotations. Finally, it should be noted that the LPBF316L in this work doesn't have a strong initial texture. For materials with even more noticeable textures, the contributions of these factors become even more pronounced.

Although the approach presented in this work was successful and the macroscale model performed very well in both torsion and shear tests, some aspects require further investigation, which are listed as follows:

- The comparison between the neutron diffraction experiments and the CP simulations revealed some uncertainties concerning the SCEC of LPBF316L, which have to be analyzed using other experimental methods such as nano-indentation.
- The plastic spin only accounts for the rotational part of the microstructure evolution in the present macroscale model. However, in some cases, the rotational part is negligible, but the microstructure changes completely, which drastically alters the yield surface's shape. This aspect has to be taken into account to increase the numerical accuracy.
- The present microscale model is formulated and tested for monotonic loading conditions. Further improvements could include the extension of the model to cyclic loading conditions.
- The validation of the macroscale model was achieved using torsion and shear tests. However, the performance of the macroscale model for actual parts in real-life loading conditions is still unknown.

References

[1] S. M. Yusuf and N. Gao, "Influence of energy density on metallurgy and properties in metal additive manufacturing," *Materials Science and Technology*, vol. 33, no. 11, pp. 1269–1289, 2017.

[2] W. E. Frazier, "Metal Additive Manufacturing: A Review," *Journal of Materials Engineering and Performance*, vol. 23, no. 6, pp. 1917–1928, 2014.

[3] T. DebRoy, H. L. Wei, J. S. Zuback, T. Mukherjee, J. W. Elmer, J. O. Milewski, A. M. Beese, A. Wilson-Heid, A. De, and W. Zhang, "Additive manufacturing of metallic components – Process, structure and properties," *Progress in Materials Science*, vol. 92, pp. 112–224, 2018.

[4] P. C. Collins, D. A. Brice, P. Samimi, I. Ghamarian, and H. L. Fraser, "Microstructural Control of Additively Manufactured Metallic Materials," *Annual Review of Materials Research*, vol. 46, no. 1, pp. 63–91, 2016.

[5] J. J. Lewandowski and M. Seifi, "Metal Additive Manufacturing: A Review of Mechanical Properties," *Annual Review of Materials Research*, vol. 46, no. 1, pp. 151–186, 2016.

[6] M. Seifi, A. Salem, J. Beuth, O. Harrysson, and J. J. Lewandowski, "Overview of Materials Qualification Needs for Metal Additive Manufacturing," *JOM*, vol. 68, no. 3, pp. 747–764, 2016.

[7] B. Blakey-Milner, P. Gradl, G. Snedden, M. Brooks, J. Pitot, E. Lopez, M. Leary, F. Berto, and A. du Plessis, "Metal additive manufacturing in aerospace: A review," *Materials & Design*, vol. 209, p. 110008, 2021.

[8] W. E. King, A. T. Anderson, R. M. Ferencz, N. E. Hodge, C. Kamath, S. A. Khairallah, and A. M. Rubenchik, "Laser powder bed fusion additive manufacturing of metals; physics, computational, and materials challenges," *Applied Physics Reviews*, vol. 2, no. 4, 2015.

[9] I. Yadroitsev, I. Yadroitsava, A. Du Plessis, and E. Macdonald, *Fundamentals of Laser Powder Bed Fusion of Metals*. Elsevier, 03 2021.

[10] Y. M. Wang, T. Voisin, J. T. McKeown, J. Ye, N. P. Calta, Z. Li, Z. Zeng, Y. Zhang, W. Chen, T. T. Roehling, R. T. Ott, M. K. Santala, P. J. Depond, M. J. Matthews, A. V. Hamza, and T. Zhu, "Additively manufactured hierarchical stainless steels with high strength and ductility," *Nature Materials*, vol. 17, no. 1, p. 63, 2018.

[11] E. Liverani, S. Toschi, L. Ceschini, and A. A. Fortunato, "Effect of selective laser melting (SLM) process parameters on microstructure and mechanical properties of 316L austenitic stainless steel," *Journal of Materials Processing Technology*, vol. 249, pp. 255–263, 2017.

[12] Y. Kok, X. P. Tan, P. Wang, M. Nai, N. H. Loh, E. Liu, and S. B. Tor, "Anisotropy and heterogeneity of microstructure and mechanical properties in metal additive manufacturing: A critical review," *Materials & Design*, vol. 139, pp. 565–586, 2018.

[13] R. Casati, J. Lemke, and M. Vedani, "Microstructure and Fracture Behavior of 316L Austenitic Stainless Steel Produced by Selective Laser Melting," *Journal of Materials Science & Technology*, vol. 32, no. 8, pp. 738–744, 2016.

[14] J. Suryawanshi, K. G. Prashanth, and U. Ramamurty, "Mechanical behavior of selective laser melted 316L stainless steel," *Materials Science and Engineering: A*, vol. 696, pp. 113–121, 2017.

[15] D. Kong, X. Ni, C. Dong, L. Zhang, C. Man, X. Cheng, and X. Li, "Anisotropy in the microstructure and mechanical property for the bulk and porous 316L stainless steel fabricated via selective laser melting," *Materials Letters*, vol. 235, pp. 1–5, 2019.

[16] Y.-D. Im, K.-H. Kim, K.-H. Jung, Y.-K. Lee, and K.-H. Song, "Anisotropic Mechanical Behavior of Additive Manufactured AISI 316L Steel," *Metallurgical and Materials Transactions A*, vol. 50, no. 4, pp. 2014–2021, 2019.

[17] S. Bahl, S. Mishra, K. U. Yazar, I. R. Kola, K. Chatterjee, and S. Suwas, "Non-equilibrium microstructure, crystallographic texture and morphological texture synergistically result in unusual mechanical properties of 3D printed 316L stainless steel," *Additive Manufacturing*, vol. 28, pp. 65–77, 2019.

[18] T. Niendorf, S. Leuders, A. Riemer, H. A. Richard, T. Tröster, and D. Schwarze, “Highly Anisotropic Steel Processed by Selective Laser Melting,” *Metallurgical and Materials Transactions B*, vol. 44, no. 4, pp. 794–796, 2013.

[19] E. O. Hall, “The Deformation and Ageing of Mild Steel: III Discussion of Results,” *Proceedings of the Physical Society, Section A*, vol. 64, no. 9, pp. 747–753, 1951.

[20] Petch, N. J., “The Cleavage Strength of Polycrystals,” *The Journal of the Iron and Steel Institute, London*, vol. 174, pp. 25–28, 1953.

[21] G. T. Gray, V. Livescu, P. A. Rigg, C. P. Trujillo, C. M. Cady, S. R. Chen, J. S. Carpenter, T. J. Lienert, and S. J. Fensin, “Structure/property (constitutive and spallation response) of additively manufactured 316L stainless steel,” *Acta Materialia*, vol. 138, pp. 140–149, 2017.

[22] C. Qiu, M. Al Kindi, A. S. Aladawi, and I. Al Hatmi, “A comprehensive study on microstructure and tensile behaviour of a selectively laser melted stainless steel,” *Scientific Reports*, vol. 8, no. 1, p. 7785, 2018.

[23] H. Sohrabpoor, V. Salarvand, R. Lupoi, Q. Chu, W. Li, B. Aldwell, W. Stanley, S. O’Halloran, R. Raghavendra, C.-H. Choi, *et al.*, “Microstructural and mechanical evaluation of post-processed ss 316l manufactured by laser-based powder bed fusion,” *Journal of Materials Research and Technology*, vol. 12, pp. 210–220, 2021.

[24] U. S. Bertoli, B. E. MacDonald, and J. M. Schoenung, “Stability of cellular microstructure in laser powder bed fusion of 316L stainless steel,” *Materials Science and Engineering: A*, vol. 739, pp. 109–117, 2019.

[25] M. S. Pham, B. Dovgyy, and P. A. Hooper, “Twinning induced plasticity in austenitic stainless steel 316L made by additive manufacturing,” *Materials Science and Engineering: A*, vol. 704, pp. 102–111, 2017.

[26] X. Wang, J. A. Muñiz-Lerma, O. Sánchez-Mata, M. Attarian Shandiz, and M. Brochu, “Microstructure and mechanical properties of stainless steel 316L vertical struts manufactured by laser powder bed fusion process,” *Materials Science and Engineering: A*, vol. 736, pp. 27–40, 2018.

[27] M. Zietala, T. Durejko, M. Polański, I. Kunce, T. Płociński, W. Zieliński, M. Łazińska, W. Stepniowski, T. Czujko, K. Kurzydłowski, and Z. Bojar, “The microstructure, mechanical properties and corrosion resistance of 316L stainless steel fabricated using laser engineered net shaping,” *Materials Science and Engineering: A*, vol. 677, pp. 1–10, 2016.

[28] Y. Zhong, L. Liu, S. Wikman, D. Cui, and Z. Shen, “Intragranular cellular segregation network structure strengthening 316L stainless steel prepared by selective laser melting,” *Journal of Nuclear Materials*, vol. 470, pp. 170–178, 2016.

[29] Y. Tomota, P. Lukáš, D. Neov, S. Harjo, and Y. R. Abe, “In situ neutron diffraction during tensile deformation of a ferrite-cementite steel,” *Acta Materialia*, vol. 51, no. 3, pp. 805–817, 2003.

[30] B. Vrancken, V. Cain, R. Knutsen, and J. van Humbeeck, “Residual stress via the contour method in compact tension specimens produced via selective laser melting,” *Scripta Materialia*, vol. 87, pp. 29–32, 2014.

[31] J. V. Gordon, C. V. Haden, H. F. Nied, R. P. Vinci, and D. G. Harlow, “Fatigue crack growth anisotropy, texture and residual stress in austenitic steel made by wire and arc additive manufacturing,” *Materials Science and Engineering: A*, vol. 724, pp. 431–438, 2018.

[32] L. Hitzler, J. Hirsch, B. Heine, M. Merkel, W. Hall, and A. Öchsner, “On the Anisotropic Mechanical Properties of Selective Laser-Melted Stainless Steel,” *Materials*, vol. 10, no. 10, p. 1136, 2017.

[33] W. Chen, T. Voisin, Y. Zhang, J.-B. Florien, C. M. Spadaccini, D. L. McDowell, T. Zhu, and Y. M. Wang, “Microscale residual stresses in additively manufactured stainless steel,” *Nature Communications*, vol. 10, no. 1, pp. 1–12, 2019.

[34] W. Shifeng, L. Shuai, W. Qingsong, C. Yan, Z. Sheng, and S. Yusheng, “Effect of molten pool boundaries on the mechanical properties of selective laser melting parts,” *Journal of Materials Processing Technology*, vol. 214, no. 11, pp. 2660–2667, 2014.

[35] D. J. Jensen and N. Hansen, “Flow stress anisotropy in aluminium,” *Acta metallurgica et Materialia*, vol. 38, no. 8, pp. 1369–1380, 1990.

[36] J. Hirsch, “Texture and anisotropy in industrial applications of aluminium alloys,” *Archives of Metallurgy and Materials*, vol. 50, no. 1, pp. 21–34, 2005.

[37] P. Dawson, S. MacEwen, and P. Wu, “Advances in sheet metal forming analyses: dealing with mechanical anisotropy from crystallographic texture,” *International Materials Reviews*, vol. 48, no. 2, pp. 86–122, 2003.

[38] J. M. Jeon, J. M. Park, J.-H. Yu, J. G. Kim, Y. Seong, S. H. Park, and H. S. Kim, “Effects of microstructure and internal defects on mechanical anisotropy and asymmetry of selective laser-melted 316L austenitic stainless steel,” *Materials Science and Engineering: A*, vol. 763, p. 138152, 2019.

[39] Z. Sun, X. Tan, S. B. Tor, and C. K. Chua, “Simultaneously enhanced strength and ductility for 3D-printed stainless steel 316L by selective laser melting,” *NPG Asia Materials*, vol. 10, no. 4, pp. 127–136, 2018.

[40] X. Wang, J. A. Muñiz-Lerma, M. Attarian Shandiz, O. Sanchez-Mata, and M. Brochu, “Crystallographic-orientation-dependent tensile behaviours of stainless steel 316L fabricated by laser powder bed fusion,” *Materials Science and Engineering: A*, vol. 766, p. 138395, 2019.

[41] Y. Yin, J. Sun, J. Guo, X. Kan, and D. Yang, “Mechanism of high yield strength and yield ratio of 316 l stainless steel by additive manufacturing,” *Materials Science and Engineering: A*, vol. 744, pp. 773–777, 2019.

[42] L. N. S. Chiu, B. Rolfe, X. Wu, and W. Yan, “Effect of stiffness anisotropy on topology optimisation of additively manufactured structures,” *Engineering Structures*, vol. 171, pp. 842–848, 2018.

[43] C. Dapogny, R. Estevez, A. Faure, and G. Michailidis, “Shape and topology optimization considering anisotropic features induced by additive manufacturing processes,” *Computer Methods in Applied Mechanics and Engineering*, vol. 344, pp. 626–665, 2019.

[44] A. M. Vilardell, A. Takezawa, A. Du Plessis, N. Takata, P. Krakhmalev, M. Kobashi, I. Yadroitsava, and I. Yadroitsev, “Topology optimization and characterization of Ti6Al4V ELI cellular lattice structures by laser powder bed fusion for biomedical applications,” *Materials Science and Engineering: A*, vol. 766, p. 138330, 2019.

[45] L. Cheng, X. Liang, J. Bai, Q. Chen, J. Lemon, and A. To, “On utilizing topology optimization to design support structure to prevent residual stress induced build failure in laser powder bed metal additive manufacturing,” *Additive Manufacturing*, vol. 27, pp. 290–304, 2019.

[46] G. Dong, Y. Tang, and Y. F. Zhao, “A survey of modeling of lattice structures fabricated by additive manufacturing,” *Journal of Mechanical Design*, vol. 139, no. 10, p. 100906, 2017.

[47] A. du Plessis, I. Yadroitsava, and I. Yadroitsev, “Ti6Al4V lightweight lattice structures manufactured by laser powder bed fusion for load-bearing applications,” *Optics & Laser Technology*, vol. 108, pp. 521–528, 2018.

[48] J. Zhang, B. Song, L. Yang, R. Liu, L. Zhang, and Y. Shi, “Microstructure evolution and mechanical properties of TiB/Ti6Al4V gradient-material lattice structure fabricated by laser powder bed fusion,” *Composites Part B: Engineering*, vol. 202, p. 108417, 2020.

[49] C. Meier, R. W. Penny, Y. Zou, J. S. Gibbs, and A. J. Hart, “Thermophysical phenomena in metal additive manufacturing by selective laser melting: fundamentals, modeling, simulation, and experimentation,” *Annual Review of Heat Transfer*, vol. 20, 2017.

[50] P. Promoppatum and V. Uthaisangsuk, “Part scale estimation of residual stress development in laser powder bed fusion additive manufacturing of Inconel 718,” *Finite Elements in Analysis and Design*, vol. 189, p. 103528, 2021.

[51] K. Carpenter and A. Tabei, “On residual stress development, prevention, and compensation in metal additive manufacturing,” *Materials*, vol. 13, no. 2, p. 255, 2020.

[52] M. Megahed, H.-W. Mindt, N. N’Dri, H. Duan, and O. Desmaison, “Metal additive-manufacturing process and residual stress modeling,” *Integrating Materials and Manufacturing Innovation*, vol. 5, no. 1, pp. 61–93, 2016.

[53] L. Lizzul, M. Sorgato, R. Bertolini, A. Ghiotti, and S. Bruschi, “Influence of additive manufacturing-induced anisotropy on tool wear in end milling of ti6al4v,” *Tribology International*, vol. 146, p. 106200, 2020.

[54] J. Kang, E. Dong, D. Li, S. Dong, C. Zhang, and L. Wang, “Anisotropy characteristics of microstructures for bone substitutes and porous implants with application of additive manufacturing in orthopaedic,” *Materials & Design*, vol. 191, p. 108608, 2020.

[55] B. Wysocki, P. Maj, R. Sitek, J. Buhagiar, K. J. Kurzydłowski, and W. Święszkowski, “Laser and electron beam additive manufacturing methods of fabricating titanium bone implants,” *Applied Sciences*, vol. 7, no. 7, p. 657, 2017.

[56] L. Ladani, J. Razmi, and S. Farhan Choudhury, “Mechanical anisotropy and strain rate dependency behavior of Ti6Al4V produced using E-beam additive fabrication,” *Journal of Engineering Materials and Technology*, vol. 136, no. 3, 2014.

[57] D. Herzog, V. Seyda, E. Wycisk, and C. Emmelmann, “Additive manufacturing of metals,” *Acta Materialia*, vol. 117, pp. 371–392, 2016.

[58] F. Caiazzo, V. Alfieri, G. Corrado, and P. Argenio, “Laser powder-bed fusion of Inconel 718 to manufacture turbine blades,” *The International Journal of Advanced Manufacturing Technology*, vol. 93, no. 9, pp. 4023–4031, 2017.

[59] L. A. Zepeda-Ruiz, A. Stukowski, T. Oppelstrup, and V. V. Bulatov, “Probing the limits of metal plasticity with molecular dynamics simulations,” *Nature*, vol. 550, no. 7677, pp. 492–495, 2017.

[60] A. Arsenlis, W. Cai, M. Tang, M. Rhee, T. Oppelstrup, G. Hommes, T. G. Pierce, and V. V. Bulatov, “Enabling strain hardening simulations with dislocation dynamics,” *Modelling and Simulation in Materials Science and Engineering*, vol. 15, no. 6, p. 553, 2007.

[61] V. Bulatov and W. Cai, *Computer simulations of dislocations*, vol. 3. OUP Oxford, 2006.

[62] J. A. Moriarty, V. Vitek, V. V. Bulatov, and S. Yip, “Atomistic simulations of dislocations and defects,” *Journal of computer-aided materials design*, vol. 9, no. 2, pp. 99–132, 2002.

[63] B. Devincre and L. P. Kubin, “Mesoscopic simulations of dislocations and plasticity,” *Materials Science and Engineering: A*, vol. 234, pp. 8–14, 1997.

[64] L. A. Zepeda-Ruiz, A. Stukowski, T. Oppelstrup, N. Bertin, N. R. Barton, R. Freitas, and V. V. Bulatov, “Atomistic insights into metal hardening,” *Nature materials*, vol. 20, no. 3, pp. 315–320, 2021.

[65] S. Bargmann, B. Klusemann, J. Markmann, J. E. Schnabel, K. Schneider, C. Soyarslan, and J. Wilmers, “Generation of 3D representative volume elements for heterogeneous materials: A review,” *Progress in Materials Science*, vol. 96, pp. 322–384, 2018.

[66] M. Diehl, M. Groeber, C. Haase, D. A. Molodov, F. Roters, and D. Raabe, “Identifying structure–property relationships through DREAM. 3D representative volume elements and DAMASK crystal plasticity simulations: an integrated computational materials engineering approach,” *Jom*, vol. 69, no. 5, pp. 848–855, 2017.

[67] F. Fritzen, T. Böhlke, and E. Schnack, “Periodic three-dimensional mesh generation for crystalline aggregates based on voronoi tessellations,” *Computational Mechanics*, vol. 43, no. 5, pp. 701–713, 2009.

[68] F. Roters, P. Eisenlohr, L. Hantcherli, D. D. Tjahjanto, T. R. Bieler, and D. Raabe, “Overview of constitutive laws, kinematics, homogenization and multiscale methods in crystal plasticity finite-element modeling: Theory, experiments, applications,” *Acta materialia*, vol. 58, no. 4, pp. 1152–1211, 2010.

[69] M. Knezevic and D. J. Savage, “A high-performance computational framework for fast crystal plasticity simulations,” *Computational materials science*, vol. 83, pp. 101–106, 2014.

[70] D. Raabe and F. Roters, “Using texture components in crystal plasticity finite element simulations,” *International Journal of Plasticity*, vol. 20, no. 3, pp. 339–361, 2004.

[71] F. Roters, M. Diehl, P. Shanthraj, P. Eisenlohr, C. Reuber, S. L. Wong, T. Maiti, A. Ebrahimi, T. Hochrainer, H.-O. Fabritius, S. Nikolov, M. Friák, N. Fujita, N. Grilli, K. G. F. Janssens, N. Jia, P. J. J. Kok, D. Ma, F. Meier, E. Werner, M. Stricker, D. Weygand, and D. Raabe, “DAMASK – The Düsseldorf Advanced Material Simulation Kit for modeling multi-physics crystal plasticity, thermal, and damage phenomena from the single crystal up to the component scale,” *Computational Materials Science*, vol. 158, pp. 420–478, 2019.

[72] P. R. Dawson, “Computational crystal plasticity,” *International journal of solids and structures*, vol. 37, no. 1-2, pp. 115–130, 2000.

[73] E. B. Marin, “On the formulation of a crystal plasticity model.,” tech. rep., Sandia National Laboratories (SNL), Albuquerque, NM, and Livermore, CA (United States), 2006.

[74] C. Miehe, J. Schröder, and J. Schotte, “Computational homogenization analysis in finite plasticity simulation of texture development in polycrystalline materials,” *Computer methods in applied mechanics and engineering*, vol. 171, no. 3-4, pp. 387–418, 1999.

[75] D. Banabic, H. Aretz, D. Comsa, and L. Paraianu, “An improved analytical description of orthotropy in metallic sheets,” *International Journal of Plasticity*, vol. 21, no. 3, pp. 493–512, 2005.

[76] F. Barlat, H. Aretz, J. W. Yoon, M. E. Karabin, J. C. Brem, and R. E. Dick, “Linear transfomation-based anisotropic yield functions,” *International Journal of Plasticity*, vol. 21, no. 5, pp. 1009–1039, 2005.

[77] O. Cazacu, B. Plunkett, and F. Barlat, “Orthotropic yield criterion for hexagonal closed packed metals,” *International Journal of Plasticity*, vol. 22, no. 7, pp. 1171–1194, 2006.

[78] D. Banabic, F. Barlat, O. Cazacu, and T. Kuwabara, “Advances in anisotropy and formability,” *International journal of material forming*, vol. 3, no. 3, pp. 165–189, 2010.

[79] D. L. McDowell, “A perspective on trends in multiscale plasticity,” *International Journal of Plasticity*, vol. 26, no. 9, pp. 1280–1309, 2010.

[80] J. Segurado, R. A. Lebensohn, J. LLorca, and C. N. Tomé, “Multiscale modeling of plasticity based on embedding the viscoplastic self-consistent formulation in implicit finite elements,” *International Journal of Plasticity*, vol. 28, no. 1, pp. 124–140, 2012.

[81] H. M. Zbib and T. D. de la Rubia, “A multiscale model of plasticity,” *International Journal of Plasticity*, vol. 18, no. 9, pp. 1133–1163, 2002.

[82] D. Banabic, *Multiscale modelling in sheet metal forming.* Springer, 2016.

[83] K. Inal, R. K. Mishra, and O. Cazacu, “Forming simulation of aluminum sheets using an anisotropic yield function coupled with crystal plasticity theory,” *International Journal of Solids and Structures*, vol. 47, no. 17, pp. 2223–2233, 2010.

[84] F. Roters, M. Diehl, P. Eisenlohr, and D. Raabe, “Crystal plasticity modeling,” *Microstructural Design of Advanced Engineering Materials*, pp. 41–67, 2013.

[85] M. Baiker, D. Helm, and A. Butz, “Determination of mechanical properties of polycrystals by using crystal plasticity and numerical homogenization schemes,” *steel research international*, vol. 85, no. 6, pp. 988–998, 2014.

[86] J. Gawad, D. Banabic, A. Van Bael, D. S. Comsa, M. Gologanu, P. Eyckens, P. Van Houtte, and D. Roose, “An evolving plane stress yield criterion based on crystal plasticity virtual experiments,” *International Journal of Plasticity*, vol. 75, pp. 141–169, 2015.

[87] K. Zhang, B. Holmedal, O. S. Hopperstad, S. Dumoulin, J. Gawad, A. Van Bael, and P. Van Houtte, “Multi-level modelling of mechanical anisotropy of commercial pure aluminium plate: crystal plasticity models, advanced yield functions and parameter identification,” *International Journal of Plasticity*, vol. 66, pp. 3–30, 2015.

[88] H. Zhang, M. Diehl, F. Roters, and D. Raabe, “A virtual laboratory using high resolution crystal plasticity simulations to determine the initial yield surface for sheet metal forming operations,” *International Journal of Plasticity*, vol. 80, pp. 111–138, 2016.

[89] B. Berisha, S. Hirsiger, H. Hippke, P. Hora, A. Mariaux, D. Leyvraz, and C. Bezençon, “Modeling of anisotropic hardening and grain size effects based on advanced numerical methods and crystal plasticity,” *Arch Mech*, vol. 71, no. 4-5, pp. 489–505, 2019.

[90] M. Kraska, M. Doig, D. Tikhomirov, D. Raabe, and F. Roters, “Virtual material testing for stamping simulations based on polycrystal plasticity,” *Computational materials science*, vol. 46, no. 2, pp. 383–392, 2009.

[91] W. Liu, B. K. Chen, Y. Pang, and A. Najafzadeh, “A 3D phenomenological yield function with both in and out-of-plane mechanical anisotropy using full-field crystal plasticity spectral method for modelling sheet metal forming of strong textured aluminum alloy,” *International Journal of Solids and Structures*, vol. 193, pp. 117–133, 2020.

[92] H. Ma, Y. Li, H. Zhang, Q. Li, F. Chen, and Z. Cui, “A virtual laboratory based on full-field crystal plasticity simulation to characterize the multiscale mechanical properties of AHSS,” *Scientific reports*, vol. 12, no. 1, pp. 1–16, 2022.

[93] J. Kochmann, S. Wulfinghoff, L. Ehle, J. Mayer, B. Svendsen, and S. Reese, “Efficient and accurate two-scale FE-FFT-based prediction of the effective material behavior of elasto-viscoplastic polycrystals,” *Computational Mechanics*, vol. 61, no. 6, pp. 751–764, 2018.

[94] C. Gierden, J. Kochmann, J. Waimann, T. Kinner-Becker, J. Sölter, B. Svendsen, and S. Reese, “Efficient two-scale FE-FFT-based mechanical process simulation of elasto-viscoplastic polycrystals at finite strains,” *Computer Methods in Applied Mechanics and Engineering*, vol. 374, p. 113566, 2021.

[95] F. Han, F. Roters, and D. Raabe, “Microstructure-based multiscale modeling of large strain plastic deformation by coupling a full-field crystal plasticity-spectral solver with an implicit finite element solver,” *International Journal of Plasticity*, vol. 125, pp. 97–117, 2020.

[96] F. Han, M. Diehl, F. Roters, and D. Raabe, “Using spectral-based representative volume element crystal plasticity simulations to predict yield surface evolution during large scale forming simulations,” *Journal of Materials Processing Technology*, vol. 277, p. 116449, 2020.

[97] Y. Dafalias, “The plastic spin,” *Journal of Applied Mechanics*, vol. 52, no. 4, pp. 865–871, 1985.

[98] J. L. Bassani and H. Pan, “A phenomenological model for microstructural evolution during plastic flow,” *Comptes Rendus Mecanique*, vol. 340, no. 4-5, pp. 369–377, 2012.

[99] C. P. Kohar, J. L. Bassani, A. Brahme, W. Muhammad, R. K. Mishra, and K. Inal, “A new multi-scale framework to incorporate microstructure evolution in phenomenological plasticity: theory, explicit finite element formulation, implementation and validation,” *International Journal of Plasticity*, vol. 117, pp. 122–156, 2019.

[100] G. Mohr, S. J. Altenburg, and K. Hilgenberg, “Effects of inter layer time and build height on resulting properties of 316L stainless steel processed by laser powder bed fusion,” *Additive Manufacturing*, p. 101080, 2020.

[101] G. Mohr, S. J. Altenburg, A. Ulbricht, P. Heinrich, D. Baum, C. Maierhofer, and K. Hilgenberg, “In-situ defect detection in laser powder bed fusion by using thermography and optical tomography—comparison to computed tomography,” *Metals*, vol. 10, no. 1, p. 103, 2020.

[102] *Metallic materials - Tensile testing - Part 1: Method of test at room temperature*. Berlin, Germany, Feb. 2017.

[103] *Metallic materials - Calibration and verification of static uniaxial testing machines - Part 1: Tension/compression testing machines - Calibration and verification of the force-measuring system*. Berlin, Germany, June 2018.

[104] *Metallic materials - Calibration of extensometer systems used in uniaxial testing*. Berlin, Germany, May 2013.

[105] A. Wolfenden, M. Harmouche, G. Blessing, Y. Chen, P. Terranova, V. Dayal, V. Kinra, J. Lemmens, R. Phillips, J. Smith, *et al.*, “Dynamic young’s modulus measurements in metallic materials: results of an interlaboratory testing program,” *Journal of Testing and Evaluation*, vol. 17, no. 1, pp. 2–13, 1989.

[106] H. M. Ledbetter, “Dynamic vs. static young’s moduli: a case study,” *Materials Science and Engineering: A*, vol. 165, no. 1, pp. L9–L10, 1993.

[107] M. Radovic, E. Lara-Curzio, and L. Riester, “Comparison of different experimental techniques for determination of elastic properties of solids,” *Materials Science and Engineering: A*, vol. 368, no. 1-2, pp. 56–70, 2004.

[108] *Standard Test Method for Dynamic Young's Modulus, Shear Modulus, and Poisson's Ratio by Impulse Excitation of Vibration.* West Conshohocken, PA, USA, May 2015.

[109] H. M. Ledbetter and R. P. Reed, "Elastic Properties of Metals and Alloys, I. Iron, Nickel, and Iron–Nickel Alloys," *Journal of Physical and Chemical Reference Data*, vol. 2, no. 3, pp. 531–618, 1973.

[110] C. Li, Z. Liu, X. Fang, and Y. Guo, "Residual stress in metal additive manufacturing," *Procedia Cirp*, vol. 71, pp. 348–353, 2018.

[111] T. Poeste, R. C. Wimpory, and R. Schneider, "The New and Upgraded Neutron Instruments for Materials Science at HMI - Current Activities in Cooperation with Industry," *Materials Science Forum*, vol. 524-525, pp. 223–228, 2006.

[112] M. R. Daymond, M. A. M. Bourke, R. B. von Dreele, B. Clausen, and T. Lorentzen, "Use of Rietveld refinement for elastic macrostrain determination and for evaluation of plastic strain history from diffraction spectra," *Journal of Applied Physics*, vol. 82, no. 4, pp. 1554–1562, 1997.

[113] F. Bayerlein, F. Bodensteiner, C. Zeller, M. Hofmann, and M. F. Zaeh, "Transient development of residual stresses in laser beam melting – A neutron diffraction study," *Additive Manufacturing*, vol. 24, pp. 587–594, 2018.

[114] E. Polatidis, J. Čapek, A. Arabi-Hashemi, C. Leinenbach, and M. Strobl, "High ductility and transformation-induced-plasticity in metastable stainless steel processed by selective laser melting with low power," *Scripta Materialia*, vol. 176, pp. 53–57, 2020.

[115] M. Ghasri-Khouzani, H. Peng, R. Rogge, R. Attardo, P. Ostiguy, J. Neidig, R. Billo, D. Hoelzle, and M. R. Shankar, "Experimental measurement of residual stress and distortion in additively manufactured stainless steel components with various dimensions," *Materials Science and Engineering: A*, vol. 707, pp. 689–700, 2017.

[116] P. Rangaswamy, M. Griffith, M. Prime, T. Holden, R. Rogge, J. Edwards, and R. Sebring, "Residual stresses in lens® components using neutron diffraction and contour method," *Materials Science and Engineering: A*, vol. 399, no. 1-2, pp. 72–83, 2005.

[117] E. Kröner, "Berechnung der elastischen konstanten des vielkristalls aus den konstanten des einkristalls," *Zeitschrift für Physik*, vol. 151, no. 4, pp. 504–518, 1958.

[118] C. Randau, U. Garbe, and H.-G. Brokmeier, "StressTextureCalculator: A software tool to extract texture, strain and microstructure information from area-detector measurements," *Journal of Applied Crystallography*, vol. 44, no. 3, pp. 641–646, 2011.

[119] A. J. Schwartz, M. Kumar, B. L. Adams, and D. P. Field, *Electron backscatter diffraction in materials science*, vol. 2. Springer, 2009.

[120] W. H. Bragg and W. L. Bragg, "The reflection of X-rays by crystals," *Proceedings of the Royal Society of London. Series A, Containing Papers of a Mathematical and Physical Character*, vol. 88, no. 605, pp. 428–438, 1913.

[121] J. Santisteban, L. Edwards, A. Steuwer, and P. Withers, "Time-of-flight neutron transmission diffraction," *Journal of applied crystallography*, vol. 34, no. 3, pp. 289–297, 2001.

[122] L. Lutterotti, S. Matthies, H.-R. Wenk, A. Schultz, and J. Richardson Jr, "Combined texture and structure analysis of deformed limestone from time-of-flight neutron diffraction spectra," *Journal of Applied Physics*, vol. 81, no. 2, pp. 594–600, 1997.

[123] M. Sprengel, A. Charmi, A. Evans, A. Ulbricht, A. Kromm, S. Kabra, J. Kelleher, J. Schroeder, R. Saliwan-Neumann, L. Ávila Calderón, R. Falkenburg, G. Bruno, and T. Kannengiesser, "Evolution of lattice strains in laser powder bed fused stainless steel 316L," *Materials Science and Engineering: A*, 2022.

[124] G. Pawley, "Unit-cell refinement from powder diffraction scans," *Journal of Applied Crystallography*, vol. 14, no. 6, pp. 357–361, 1981.

[125] M. Sprengel, G. Mohr, S. J. Altenburg, A. Evans, I. Serrano-Munoz, A. Kromm, T. Pirling, G. Bruno, and T. Kannengiesser, "Triaxial residual stress in laser powder bed fused 316L: Effects of interlayer time and scanning velocity," *Advanced Engineering Materials*, p. 2101330, 2022.

[126] J. Santisteban, M. Daymond, J. James, and L. Edwards, "ENGIN-X: a third-generation neutron strain scanner," *Journal of Applied Crystallography*, vol. 39, no. 6, pp. 812–825, 2006.

[127] C. Moreton-Smith, S. Johnston, and F. Akeroyd, "Open genie—a generic multi-platform program for the analysis of neutron scattering data," *Journal of Neutron Research*, vol. 4, no. 1-4, pp. 41–47, 1996.

[128] O. Kolditz, *Computational methods in environmental fluid mechanics.* Springer Science & Business Media, 2002.

[129] P. Haupt, *Continuum Mechanics and Theory of Materials.* Springer Berlin Heidelberg, 2002.

[130] F. Roters, P. Eisenlohr, T. R. Bieler, and D. Raabe, *Crystal plasticity finite element methods: in materials science and engineering.* John Wiley & Sons, 2011.

[131] A. Bertram, *Elasticity and Plasticity of Large Deformations: An Introduction.* Springer Berlin Heidelberg, 2011.

[132] E. A. de Souza Neto, D. Peric, and D. R. Owen, *Computational methods for plasticity: theory and applications.* John Wiley & Sons, 2011.

[133] F. Dunne and N. Petrinic, *Introduction to computational plasticity.* Oxford University Press on Demand, 2005.

[134] J. C. Simo and T. J. Hughes, *Computational inelasticity*, vol. 7. Springer Science & Business Media, 2006.

[135] E. H. Lee, "Elastic-Plastic Deformation at Finite Strains," *Journal of Applied Mechanics*, vol. 36, no. 1, pp. 1–6, 1969.

[136] W. Müller, *An Expedition to Continuum Theory.* Solid Mechanics and Its Applications, Springer Netherlands, 2014.

[137] D. Hull and D. J. Bacon, *Introduction to dislocations*, vol. 37. Elsevier, 2011.

[138] A. Abu-Odeh, M. Cottura, and M. Asta, "Insights into dislocation climb efficiency in fcc metals from atomistic simulations," *Acta Materialia*, vol. 193, pp. 172–181, 2020.

[139] A. Saai, S. Dumoulin, O. S. Hopperstad, and O.-G. Lademo, "Simulation of yield surfaces for aluminium sheets with rolling and recrystallization textures," *Computational Materials Science*, vol. 67, pp. 424–433, 2013.

[140] J. W. Hutchinson, "Bounds and self-consistent estimates for creep of polycrystalline materials," *Proceedings of the Royal Society A*, vol. 348, no. 1652, pp. 101–127, 1976.

[141] T. O. Erinosho, D. M. Collins, A. J. Wilkinson, R. I. Todd, and F. Dunne, "Assessment of X-ray diffraction and crystal plasticity lattice strain evolutions under biaxial loading," *International Journal of Plasticity*, vol. 83, pp. 1–18, 2016.

[142] W. Chen, T. Voisin, Y. Zhang, J.-B. Florien, C. M. Spadaccini, D. L. McDowell, T. Zhu, and Y. M. Wang, "Microscale residual stresses in additively manufactured stainless steel," *Nature communications*, vol. 10, no. 1, pp. 1–12, 2019.

[143] M. V. Upadhyay, S. van Petegem, T. Panzner, R. A. Lebensohn, and H. van Swygenhoven, "Study of lattice strain evolution during biaxial deformation of stainless steel using a finite element and fast Fourier transform based multi-scale approach," *Acta Materialia*, vol. 118, pp. 28–43, 2016.

[144] P. Shanthraj, M. Diehl, P. Eisenlohr, F. Roters, D. Raabe, C. Chen, K. Chawla, N. Chawla, W. Chen, and Y. Kagawa, "Spectral solvers for crystal plasticity and multi-physics simulations," *Handbook of Mechanics of Materials*, pp. 978–981, 2019.

[145] J. P. Boyd, *Chebyshev and Fourier spectral methods.* Courier Corporation, 2001.

[146] R. Quey, P. R. Dawson, and F. Barbe, “Large-scale 3D random polycrystals for the finite element method: Generation, meshing and remeshing,” *Computer Methods in Applied Mechanics and Engineering*, vol. 200, no. 17-20, pp. 1729–1745, 2011.

[147] F. Bachmann, R. Hielscher, and H. Schaeben, “Texture analysis with MTEX – free and open source software toolbox,” *Solid State Phenomena*, vol. 160, pp. 63–68, 2010.

[148] P. Eisenlohr and F. Roters, “Selecting a set of discrete orientations for accurate texture reconstruction,” *Computational Materials Science*, vol. 42, no. 4, pp. 670–678, 2008.

[149] P. Eisenlohr, M. Diehl, R. A. Lebensohn, and F. Roters, “A spectral method solution to crystal elasto-viscoplasticity at finite strains,” *International Journal of Plasticity*, vol. 46, pp. 37–53, 2013.

[150] G. Dhondt, *The finite element method for three-dimensional thermomechanical applications*. John Wiley & Sons, 2004.

[151] O. C. Zienkiewicz, R. L. Taylor, R. L. Taylor, and R. L. Taylor, *The finite element method: solid mechanics*, vol. 2. Butterworth-heinemann, 2000.

[152] O. C. Zienkiewicz, C. Humpheson, and R. Lewis, “Associated and non-associated visco-plasticity and plasticity in soil mechanics,” *Geotechnique*, vol. 25, no. 4, pp. 671–689, 1975.

[153] W. M. Scherzinger, “A return mapping algorithm for isotropic and anisotropic plasticity models using a line search method,” *Computer Methods in Applied Mechanics and Engineering*, vol. 317, pp. 526–553, 2017.

[154] H. Mei, L. Lang, K. Liu, and X. Yang, “Evaluation study on iterative inverse modeling procedure for determining post-necking hardening behavior of sheet metal at elevated temperature,” *Metals*, vol. 8, no. 12, p. 1044, 2018.

[155] K. Kim and J. Yin, “Evolution of anisotropy under plane stress,” *Journal of the Mechanics and Physics of Solids*, vol. 45, no. 5, pp. 841–851, 1997.

[156] Y. Dafalias, “Corotational rates for kinematic hardening at large plastic deformations,” *Journal of Applied Mechanics*, vol. 50, no. 3, pp. 561–565, 1983.

[157] Y. F. Dafalias, “The plastic spin concept and a simple illustration of its role in finite plastic transformations,” *Mechanics of Materials*, vol. 3, no. 3, pp. 223–233, 1984.

[158] Y. F. Dafalias, “Plastic spin: necessity or redundancy?,” *International Journal of Plasticity*, vol. 14, no. 9, pp. 909–931, 1998.

[159] M. H. Ulz and C. C. Celigoj, “A uniquely defined multiplicative elasto-plasticity model with orthotropic yield function and plastic spin,” *Computer Methods in Applied Mechanics and Engineering*, vol. 374, p. 113565, 2021.

[160] T. Kaiser, J. Lu, A. Menzel, and P. Papadopoulos, “A covariant formulation of finite plasticity with plasticity-induced evolution of anisotropy: Modeling, algorithmics, simulation, and comparison to experiments,” *International Journal of Solids and Structures*, vol. 185, pp. 116–142, 2020.

[161] G. Smith, “On isotropic functions of symmetric tensors, skew-symmetric tensors and vectors,” *International Journal of Engineering Science*, vol. 9, no. 10, pp. 899–916, 1971.

[162] Q.-S. Zheng, “Theory of representations for tensor functions—a unified invariant approach to constitutive equations,” *Appl. Mech. Rev. Nov*, vol. 47, no. 11, pp. 545–485, 1994.

[163] H. Pan, *Problems of orthotropic plastic constitutive models: Non-associated flow and evolution of anisotropy*. PhD thesis, University of Pennsylvania, 2009.

[164] R. M. Brannon, *Elements of Phenomenological Plasticity: Geometrical Insight, Computational Algorithms, and Topics in Shock Physics*, pp. 225–274. Berlin, Heidelberg: Springer Berlin Heidelberg, 2007.

[165] K. Danas and P. P. Castañeda, “Influence of the lode parameter and the stress triaxiality on the failure of elasto-plastic porous materials,” *International Journal of Solids and Structures*, vol. 49, no. 11-12, pp. 1325–1342, 2012.

[166] I. Barsoum and J. Faleskog, "Rupture mechanisms in combined tension and shear—experiments," *International journal of solids and structures*, vol. 44, no. 6, pp. 1768–1786, 2007.

[167] C. Soyarslan, H. Richter, and S. Bargmann, "Lode parameter dependence and quasi-unilateral effects in continuum damage mechanics: Models and applications in metal forming," in *Key Engineering Materials*, vol. 651, pp. 187–192, Trans Tech Publ, 2015.

[168] C. Soyarslan, H. Richter, and S. Bargmann, "Variants of lemaitre's damage model and their use in formability prediction of metallic materials," *Mechanics of Materials*, vol. 92, pp. 58–79, 2016.

[169] A. Kumar and P. R. Dawson, "Dynamics of texture evolution in face-centered cubic polycrystals," *Journal of the Mechanics and Physics of Solids*, vol. 57, no. 3, pp. 422–445, 2009.

[170] J.-W. Yoon, F. Barlat, R. E. Dick, K. Chung, and T. J. Kang, "Plane stress yield function for aluminum alloy sheets—part ii: Fe formulation and its implementation," *International Journal of Plasticity*, vol. 20, no. 3, pp. 495–522, 2004.

[171] M. Smith, *ABAQUS/Standard User's Manual, Version 6.9.* United States: Dassault Systèmes Simulia Corp, 2009.

[172] H. M. Ledbetter, "Predicted single-crystal elastic constants of stainless-steel 316," *British journal of non-destructive testing*, vol. 23, no. 6, pp. 286–287, 1981.

[173] D. Mainprice, R. Hielscher, and H. Schaeben, "Calculating anisotropic physical properties from texture data using the MTEX open-source package," *Geological Society, London, Special Publications*, vol. 360, no. 1, pp. 175–192, 2011.

[174] W. Voigt, *Lehrbuch der kristallphysik:(mit ausschluss der kristalloptik)*, vol. 34. BG Teubner, 1910.

[175] R. Hill, "The elastic behaviour of a crystalline aggregate," *Proceedings of the Physical Society. Section A*, vol. 65, no. 5, p. 349, 1952.

[176] A. Reuß, "Berechnung der fließgrenze von mischkristallen auf grund der plastizitätsbedingung für einkristalle.," *ZAMM-Journal of Applied Mathematics and Mechanics/Zeitschrift für Angewandte Mathematik und Mechanik*, vol. 9, no. 1, pp. 49–58, 1929.

[177] K. Levenberg, "A method for the solution of certain non-linear problems in least squares," *Quarterly of Applied Mathematics*, vol. 2, no. 2, pp. 164–168, 1944.

[178] J. J. Moré, "The levenberg-marquardt algorithm: implementation and theory," in *Numerical analysis*, pp. 105–116, Springer, 1978.

[179] R. Kapoor and S. Nemat-Nasser, "Determination of temperature rise during high strain rate deformation," *Mechanics of materials*, vol. 27, no. 1, pp. 1–12, 1998.

[180] L. Xu, L. Chen, B. De Cooman, D. Steglich, and F. Barlat, "Hole expansion of advanced high strenth steel sheet sample," *International Journal of Material Forming*, vol. 3, no. 1, pp. 247–250, 2010.

[181] S. Dumoulin, O. Engler, O. Hopperstad, and O. Lademo, "Description of plastic anisotropy in AA6063-T6 using the crystal plasticity finite element method," *Modelling and Simulation in Materials Science and Engineering*, vol. 20, no. 5, p. 055008, 2012.

[182] R. A. Horn and C. R. Johnson, *Matrix analysis.* Cambridge university press, 2012.

[183] G. H. Golub and C. F. Van Loan, *Matrix computations.* JHU press, 2013.

[184] D. Rowenhorst, A. Rollett, G. Rohrer, M. Groeber, M. Jackson, P. J. Konijnenberg, and M. De Graef, "Consistent representations of and conversions between 3D rotations," *Modelling and Simulation in Materials Science and Engineering*, vol. 23, no. 8, p. 083501, 2015.

[185] J. R. Cardoso and F. S. Leite, "Exponentials of skew-symmetric matrices and logarithms of orthogonal matrices," *Journal of computational and applied mathematics*, vol. 233, no. 11, pp. 2867–2875, 2010.

[186] M. Taheri Andani, M. Ghodrati, M. R. Karamooz-Ravari, R. Mirzaeifar, and J. Ni, “Damage modeling of metallic alloys made by additive manufacturing,” *Materials Science and Engineering: A*, vol. 743, pp. 656–664, 2019.

[187] A. Ahmadi, R. Mirzaeifar, N. S. Moghaddam, A. S. Turabi, H. E. Karaca, and M. Elahinia, “Effect of manufacturing parameters on mechanical properties of 316L stainless steel parts fabricated by selective laser melting: A computational framework,” *Materials & Design*, vol. 112, pp. 328–338, 2016.

[188] T. Thiede, S. Cabeza, T. Mishurova, N. Nadammal, A. Kromm, J. Bode, C. Haberland, and G. Bruno, “Residual Stress in Selective Laser Melted Inconel 718: Influence of the Removal from Base Plate and Deposition Hatch Length,” *Materials Performance and Characterization*, vol. 7, no. 4, p. 20170119, 2018.

[189] A. S. Wu, D. W. Brown, M. Kumar, G. F. Gallegos, and W. E. King, “An Experimental Investigation into Additive Manufacturing-Induced Residual Stresses in 316L Stainless Steel,” *Metallurgical and Materials Transactions A*, vol. 45, no. 13, pp. 6260–6270, 2014.

[190] P. Mercelis and J.-P. Kruth, “Residual stresses in selective laser sintering and selective laser melting,” *Rapid Prototyping Journal*, vol. 12, no. 5, pp. 254–265, 2006.

[191] O. Andreau, I. Koutiri, P. Peyre, J.-D. Penot, N. Saintier, E. Pessard, T. De Terris, C. Dupuy, and T. Baudin, “Texture control of 316L parts by modulation of the melt pool morphology in selective laser melting,” *Journal of Materials Processing Technology*, vol. 264, pp. 21–31, 2019.

[192] B. Barkia, P. Aubry, P. Haghi-Ashtiani, T. Auger, L. Gosmain, F. Schuster, and H. Maskrot, “On the origin of the high tensile strength and ductility of additively manufactured 316l stainless steel: Multiscale investigation,” *Journal of Materials Science & Technology*, vol. 41, pp. 209–218, 2020.

[193] L. Wiesent, U. Schultheiß, P. Lulla, A. Nonn, and U. Noster, “Mechanical properties of small structures built by selective laser melting 316 l stainless steel–a phenomenological approach to improve component design,” *Materialwissenschaft und Werkstofftechnik*, vol. 51, no. 12, pp. 1615–1629, 2020.

[194] X. Li, D. Yi, X. Wu, J. Zhang, X. Yang, Z. Zhao, J. Wang, B. Liu, and P. Bai, “Study on mechanism of structure angle on microstructure and properties of slm-fabricated 316l stainless steel,” *Frontiers in Bioengineering and Biotechnology*, vol. 9, 2021.

[195] F. Geiger, K. Kunze, and T. Etter, “Tailoring the texture of IN738LC processed by selective laser melting (SLM) by specific scanning strategies,” *Materials Science and Engineering: A*, vol. 661, pp. 240–246, 2016.

[196] K. Kunze, T. Etter, J. Grässlin, and V. Shklover, “Texture, anisotropy in microstructure and mechanical properties of IN738LC alloy processed by selective laser melting (SLM),” *Materials Science and Engineering: A*, vol. 620, pp. 213–222, 2015.